Measurement of the WZ Production Cross Section in Proton-Proton Collision at \(\sqrt s = 7 TeV\) and Limits on Anomalous Triple Gauge Couplings with the ATLAS Detector

Measurement of the WZ production cross section in proton-proton collision at $\sqrt{s} = 7$ TeV and limits on anomalous triple gauge couplings with the ATLAS detector

A dissertation presented

by

Laura Elizabeth Jeanty

to

The Department of Physics

in partial fulfillment of the requirements

for the degree of

Doctor of Philosophy

in the subject of

Physics

Harvard University

Cambridge, Massachusetts

May 2013

Thesis advisor

Melissa Franklin

Author

Laura Elizabeth Jeanty

Measurement of the WZ production cross section in proton-proton collision at $\sqrt{s} = 7$ TeV and limits on anomalous triple gauge couplings with the ATLAS detector

Abstract

In this dissertation, we present a study of WZ production in proton-proton collisions at a center-of-mass energy of 7 TeV. The data analyzed was collected by the ATLAS detector and corresponds to an integrated luminosity of 4.6 fb^{-1} provided by the Large Hadron Collider in 2011. We select WZ events in the fully leptonic decay mode with electrons, muons, and missing transverse energy in the final state.

Events are required to have three isolated leptons with significant transverse momentum, a large missing transverse energy, a Z candidate reconstructed from two of the selected leptons, and a W candidate reconstructed from the missing transverse energy and third lepton. The major backgrounds to the WZ signal in the leptonic decay channel are Z+jets events, ZZ production, Z+photon events, and events with top quarks. We estimate the Z+jets and top quark background contributions from data and take the expected contribution for the other background processes from simulation.

We observe 317 WZ candidates in data, with a background expectation of 68 ± 10 events. The total production cross section is extracted from the selected sample using

a maximum likelihood method and is determined to be $19.0^{+1.4}_{-1.3}$ (stat) ± 0.9 (syst) ± 0.4 (lumi) pb, which is consistent with the next-to-leading Standard Model prediction of $17.6^{+1.1}_{-1.0}$ pb.

WZ production in the Standard Model includes a contribution from the WWZ triple gauge boson vertex. If new physics beyond the Standard Model exists and interacts with W and Z bosons, the coupling of the WWZ vertex could differ from the Standard Model prediction. We set limits on anomalous triple gauge boson couplings using the transverse momentum spectrum of Z bosons in the selected sample. We derive the 95% confidence interval for three model-independent anomalous triple gauge couplings using a frequentist approach and set the most stringent bounds to date on two of the three parameters.

Contents

List of Figures

List of Tables

Acknowledgments

Melissa Franklin: thank you for teaching me particle physics and for making an experimentalist out of me. Thank you always asking difficult questions, and for teaching me to ask the right ones myself. Thank you for your advice, your care, your time. I am honored to be your student.

Masahiro Morii: you were a second advisor to me. I learned a tremendous amount from you while working on the WZ analysis. Thank you for answering all my questions thoughtfully, for your patience, and for your insights.

Joao Guimaraes da Costa, John Huth, Paolo Giromini, George Brandenburg, Gary Feldman, and Frank Taylor: thank you for sharing with me your expertise on everything from detectors to statistics to the internal workings of the ATLAS management, and for your advice, feedback, and encouragement.

Howard Georgi: thank you for your comments, questions, and support.

Alexander Oh, Adam Yurkewicz, and the WZ analysis team: thank you for your leadership, collaboration, and interesting discussions.

Ludo Pontecorvo and the muon spectrometer community: thank you for teaching me about the detector, and for your guidance.

My partner on team WZ, Michael Kagan: thank you for your enthusiasm, dedication, and everything you taught me while we worked together. While working with you, analysis was engaging and fun.

Giovanni Zevi Della Porta: thank you for your friendship, generosity, and for sharing so much of this experience with me. I am grateful to have had a graduate school buddy as awesome as you.

Ben Smith, Kevin Black, Shulamit Moed Sher, Corrinne Mills, Alberto Belloni,

Srivas Prasad and Verena Martinez Outschoorn: thank you for showing me how to be a useful member of the group, and for answering my many questions.

Bart Butler, Pierluigi Catastini, Geraldine Conti, David Lopez Mateos, and Hugh Skottowe: thank you for sharing your expertise with me, and for interesting and varied discussions.

My fellow graduate students Kevin Mercurio, William Spearman, Andy Yen, Tomo Lazovich, Siyuan Sun, Emma Tolley, Jake Connors, Tony Tong, and Stephen Chan: thank you for your help and for making both 188 and Palfrey fun places to work.

Bonnie Fleming, Colin Gay, and Charles Bailyn: thank you for introducing me to particle physics, ATLAS, and the art of doing research. Thank you for your encouragement and support.

Josh Bridger: thank you for making physics fun and interesting from the very first.

The UPenn ATLAS group, in particular Brig Williams and Mike Hance: thank you for adopting me during my first year on ATLAS.

Angela Allen, Robyn Provost, Carol Davis, Sheila Ferguson, and Lisa Cacciabaudo: thank you for all of your help and support throughout graduate school, and for being so on top of everything, always.

The Harvard computing team, in particular John Brunelle: thank you for taking care of Odyssey and for your extremely prompt replies to computing crises large and small.

The Harvard physics custodians and building staff: thank you for making the

physics department and Palfrey great places to work.

The staff at the Northwest Cafeteria, the Science Center, the Lise Buckminster Cafe, and various Mass Ave restaurants: thank you for many tasty and quick lunches, and for always being cheerful.

Brian Shuve, Clay Cordova, David Simmons-Duffin, and Yang-Ting Chien: thank you for answering my theory questions, no matter how strange.

Sofia Magkiriadou, Nick Hutzler, Jack DiSciacca, Renee Sher, Tina Lin, Eleanor Millman, Yiwen Chu, Michael Gullans, Chin Lin Wong, Eli Visbal, Ben Feldman, Julia Rasmussen and Eddie Schlafly: thank you for teaching me about other fields of physics, but more importantly, for our many shared adventures throughout the last 6 years. You made graduate school fun.

My CERN friends: thank you for making CERN an amazing place to work, for teaching me about other analyses and parts of the detector, for delicious culinary expeditions, and for adventures in Geneva, the Jura, the Alps, and beyond.

Thank you to my friends, near and far, for your encouragement, generosity, and love. Thank you to the Yale Physics Posse for being awesome.

Thank you to my family for their encouragement, love and support from many corners of the world, especially my uncle Corey and my aunt Kelly for their interest in my work.

To my sister, Aja, my amazing parents, and my partner Jayson: thank you, for everything, and more. Including the cup of tea you just made for me so I could finish this.

Chapter 1

Overview

In this dissertation, we present a study of WZ production in proton-proton collisions at $\sqrt{s} = 7$ TeV. The data analyzed was collected by the ATLAS detector in 2011 and corresponds to an integrated luminosity of 4.6 fb^{-1} provided by the Large Hadron Collider. We select WZ events in the fully leptonic decay mode, with electrons, muons, and missing transverse energy in the final state. We extract the WZ production cross section from the observed events and derive limits on anomalous triple gauge boson couplings using the transverse momentum spectrum of Z bosons in the selected sample.

The thesis is organized as follows. In Chapter 2, we motivate the study of WZ events at the LHC and introduce anomalous triple gauge couplings. Previous measurements of WZ physics at both the LEP and Tevatron accelerators are summarized, and the theoretical background behind WZ production at the LHC is presented. Chapter 3 summarizes the LHC design and performance and describes how we measure the integrated luminosity delivered by the accelerator. In Chapter 4, we give a brief

overview of the ATLAS detector, focusing on the parts of the detector which are used in identifying and reconstructing $WZ \to \ell\nu\ell\ell$ events.

We describe the reconstruction of electrons, muons, and missing transverse energy, used in selecting WZ events, in Chapter 5. The ATLAS trigger system and the triggers used to select the WZ data sample are presented in Chapter 6. In Chapter 7, we describe the simulation of the WZ events used for the analysis.

We select WZ events by requiring three isolated leptons, each with significant transverse momentum, and missing transverse energy in the event, as described in Chapter 8. Events from other physics processes which pass our event selection include Z+jets, ZZ, $Z + \gamma$, and top quark events. We estimate the expected contribution of Z+jets and top quark events from data, as discussed in Chapter 9. The expected contributions from ZZ and $Z+\gamma$ events are taken from simulation. In Chapter 10, we present the measurement of the WZ production cross section. Using the transverse momentum of the Z boson in the selected WZ events, we extract the 95% confidence interval for values of the anomalous triple gauge couplings. The method for setting limits on the anomalous couplings and the results are presented in Chapter 11.

The analysis presented in this thesis is published in an abbreviated form by the ATLAS Collaboration [37]. An internal ATLAS note [34], from which parts of this thesis are adapted, provides more detail than the paper.

Chapter 2

Motivation and Background

2.1 Introduction to Electroweak Physics

For more than 50 years, understanding electroweak interactions has been a major goal of particle physics. In 1957, Schwinger first suggested the existence of a triplet of vector bosons whose couplings could generate both the weak interactions and electromagnetism [137]. In 1961, Glashow showed that by adding an additional vector boson to the theory, the electromagnetic and weak interactions could be linked with underlying symmetries [92]. With major contributions from Weinberg [145], Salam [136], Higgs [104], and others, the unified electroweak theory was fully established by 1968.

The electroweak theory predicts the existence of three massive gauge bosons: the W^+, W^-, and Z^0 bosons, in addition to the massless photon. Additionally, the theory requires at least one more particle to break the high energy symmetry of the electromagnetic and weak forces and to give mass to the W^+, W^-, and Z^0 bosons. In the simplest model of symmetry breaking, the additional particle is the scalar

Higgs boson, which gives mass to the W and Z bosons in the process of electroweak symmetry breaking. In addition to the new particles, the electroweak theory predicts a host of interactions, from neutral current interactions of fermions to interactions between the W and Z bosons themselves, that were not yet observed at the time of the theory's development.

Experimental support of the unified electroweak theory first came in 1973 from the Gargamelle bubble chamber at CERN. Experimenters observed the scattering of muon antineutrinos off electrons, a neutral current interaction mediated by the Z boson [103]. In 1983, the UA1 and UA2 experiments observed the direct production of the W and Z bosons from proton-antiproton collisions provided by the Super Proton Synchrotron accelerator at CERN [14, 45]. Experiments on the Large Electron Positron (LEP) collider at CERN (1989-2000) as well as the Tevatron at Fermilab (1983-2011) continued to verify predictions of the electroweak theory and made precision measurements of many of its parameters.

The electroweak theory is a cornerstone of the Standard Model of particle physics. Combined with quantum chromodynamics, which describes the interactions of the strong force, the model describes three of the four fundamental forces in nature. Gravity is not included in the Standard Model. The Standard Model has 19 parameters and 17 particles which are the excited states of underlying fields. The fundamental particles consist of 3 charged leptons, 3 neutrinos, 6 quarks, 4 gauge bosons, and the Higgs boson. Through interactions with the leptons and quarks, the Higgs boson can also give those particles an effective mass. One of the important features of the Standard Model is that the fields respect local gauge symmetry, and any measurable

quantity of a particle is independent of the local phase of its field. The existence of the gauge bosons is a direct consequence of requiring the theory to respect local gauge invariance. Additionally, interactions described by the electromagnetic and the strong force respect charge (C) and parity (P) symmetries. Electroweak interactions violate both symmetries maximally and show small violation of the combined CP symmetry. Detailed introductions to the Standard Model, including full descriptions of the electroweak theory, are available in References [97, 133, 101]. An interesting discussion of the importance of the values of the parameters of the Standard Model is available in Reference [54]. For a full presentation of the field theory formulation of the Standard Model, see Reference [134].

2.2 Motivation for studying WZ production

Before the Large Hadron Collider began colliding protons in 2010, several important questions about electroweak physics remained unanswered. To answer many of these questions, studying diboson production at the LHC is essential. Among these remaining questions, three significant ones are:

1. Is there a scalar Higgs boson as predicted by the simplest model of electroweak symmetry breaking?

2. What do vector boson interactions at the TeV scale look like?

3. Is there evidence of new interactions or particles hiding in the interactions or production of W and Z bosons?

In July 2012 both the CMS and ATLAS experiments announced the discovery of a new particle consistent with the Higgs boson, observed primarily in final states consisting of pairs of photons, pairs of W bosons, and pairs of Z bosons [38, 72]. Now that a new particle has been found, we must measure its mass and its couplings to the gauge bosons to confirm that it behaves as predicted by the electroweak theory. We must also check whether or not its couplings to fermions are consistent with the model in which its interactions with fermions give them mass. Much work remains, but the answer to the first question looks affirmative from the 2011 and 2012 LHC dataset.

The discovery of a particle consistent with the Higgs boson also begins to answer the second question in the list above, but the full answer must come from more detailed studies of vector boson interactions. There are two separate issues. First, without the Higgs boson or another new particle, the scattering of vector boson pairs off each other grows as a function of the center-of-mass energy, $\sqrt{\hat{s}}$, of the interaction and begins to violate unitarity at the TeV scale. The Feynman diagrams illustrating WW and WZ scattering in the Standard Model are shown in Figure 2.1. In the simplest model, the Higgs boson is responsible not only for breaking electroweak symmetry but also for regularizing vector boson scattering by introducing another diagram whose contribution cancels the divergences from the pure vector boson diagrams. Diagrams showing the Higgs boson contribution to WW and WZ scattering are shown in Figure 2.2. Even if the production and decay rates of the new particle look consistent with a Standard Model Higgs boson, it will be necessary to measure the rates of diboson production to extract the small signal of diboson scattering and

confirm that the rate is consistent with the addition of diagrams that include the Higgs boson. Measuring the vector boson scattering processes will require 100s of fb^{-1} of data at $\sqrt{s} = 14$ TeV.

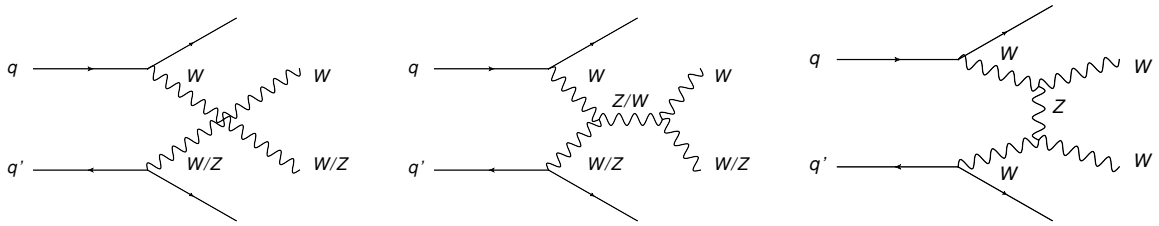

(a) (b) (c)

Figure 2.1: WW and WZ scattering diagrams at the LHC. The virtual Z in diagrams (b) and (c) could be replaced by a photon as well.

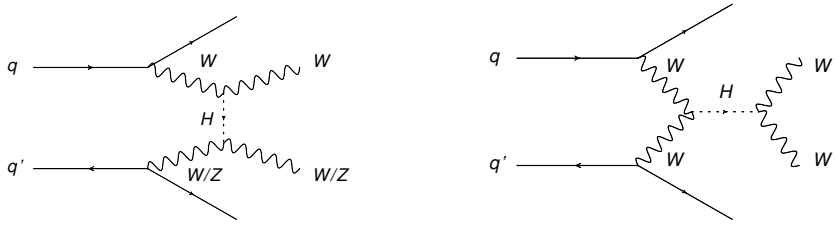

(a) (b)

Figure 2.2: WW and WZ scattering diagrams, at the LHC, which include a Higgs boson contribution.

The second distinctive feature of vector diboson production at the TeV scale is the accessibility to vertices involving three and four gauge bosons. The three leading order diagrams that contribute to Standard Model WZ production at the LHC are shown in Figure 2.3, and the triple gauge coupling at the WWZ vertex can be seen in Figure 2.3(c).

The existence of these vertices is a direct consequence of gauge invariance; moreover, the values of the triple gauging couplings (TGCs) and quartic gauge couplings

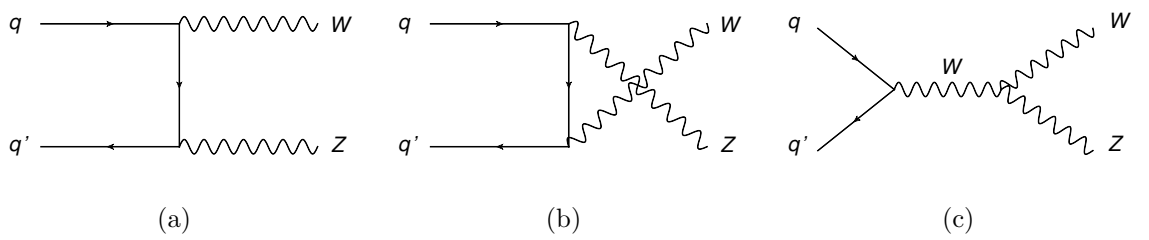

Figure 2.3: Leading order WZ production at the LHC. Figure (c) shows the WWZ triple gauge coupling vertex.

(QGCs) are fixed exactly by gauge symmetry. Measuring these couplings is an important confirmation of the full implications of gauge symmetry in electroweak physics.

Measuring the triple and quartic gauge couplings via diboson production is important not only as a confirmation of electroweak physics and gauge invariance, but also because the uncertainty on the couplings measured values leaves open the possibility that the couplings differ from the Standard Model predictions. If the couplings do differ, it could point to the interaction of new, heavy particles at the vertices. The new particles could be heavier than the LHC is able to directly produce. The new particles could be from any model of physics beyond the Standard Model; the only requirement is that they must couple to the vector bosons. A Feynman diagram illustrating the interaction of new particles at the WWZ vertex that would lead to non-Standard Model triple gauge couplings is shown in Figure 2.4(a).

Section 2.3 briefly motivates the search for physics beyond the standard model. New physics could alter diboson production in other ways. Several theories predict new particles which could be directly produced at the LHC which would decay to diboson pairs. Diboson pair production from the decay of heavy particles is a prediction of certain parameter spaces of Supersymmetry [135, 128, 94, 144, 146],

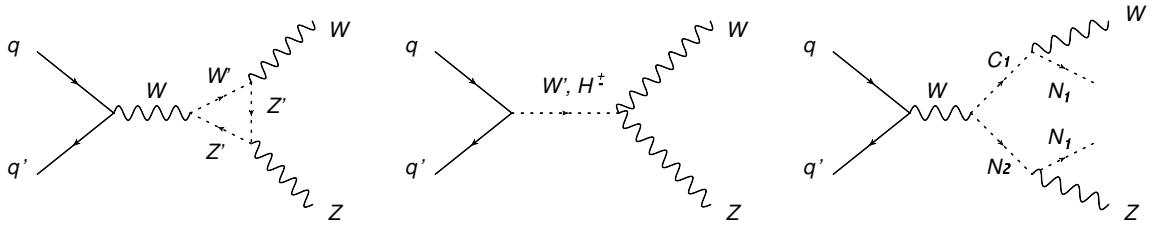

(a) (b) (c)

Figure 2.4: Potential new physics contributions to WZ production. In Figure a, new physics contributes at the WWZ vertex and alters the triple gauge coupling. The W' and Z' particles shown here could be SUSY or Technicolor particles, or particles from any new theory as long as they couple to W and Z bosons. They can be too heavy to be directly produced by the LHC. In Figure (b), a strongly produced W' (including technirhos, for example) or charged Higgs boson could decay to a WZ pair. In Figure (c), weakly-produced supersymmetric neutralinos (N_2) and charginos (C_1) in certain parameter spaces of SUSY could decay to a pair of lightest neutralinos (N_1) and W and Z bosons.

Technicolor [85], and generic W' and Z' models [111].

It is important to measure the production of all vector boson pairs. In this thesis, we focus on the measurement of WZ production. While WW and ZZ final states are crucial decay modes of the Higgs boson, the WZ final state cannot be the decay product of a neutral Higgs. Therefore, measuring WZ production at the LHC serves as an essential cross check on diboson production as a background to the Higgs searches and measurements.

Measuring WZ production is also important because it allows us to look for the direct production of new, heavy, charged particles to which WW and ZZ production are not sensitive. New physics which could decay to WZ pairs include charged Higgs bosons [132] and particles in certain phase spaces of Supersymmetry (SUSY), Technicolor, and generic W' models [131]. Figure 2.4(b) shows an example of WZ production from the decay of a strongly-produced charged Higgs, W', or charged

technicolor particle such as a technirhos. Figure 2.4(c) shows how a weakly-produced chargino, C_1, and neutralino, N_2, could decay to a pair of W and Z bosons and a pair of the lightest neutralinos, N_1, in certain parameter sets of SUSY. Weakly-produced neutralinos and charginos are favored in some models of SUSY in which the squarks and gauginos are heavy [44].

Finally, WZ production serves as a background to several important searches for new physics. $WZ \to \ell\nu\ell\ell$ production is the largest source of Standard Model events with three, isolated, high p_T leptons, so it serves as a major background to multi-lepton SUSY analyses. It also contributes background to analyses that look for final states with two leptons and missing transverse energy, including $WW \to \ell\nu\ell\nu$ production, $ZZ \to \ell\ell\nu\nu$ production, and many models of new physics.

WW production was first observed with the LEP accelerator by the DELPHI experiment in 1996 [80]. WZ production, as a charged final state, could not be produced by electron-positron collisions; WZ production was first observed at the Tevatron in 2007 [3].

Experimental efforts at the LEP and at the Tevatron have measured predictions and parameters of electroweak physics to high accuracy. The mass of the W boson was measured to 0.02% by the CDF experiment [58]. The couplings between the vector bosons and the fermions was measured by the experiments on LEP to accuracies ranging from 0.01% to 1%, depending on the assumptions made about the relationship between the couplings [8]. Constraining the triple and quartic gauge couplings has remained difficult, however, because of the high center-of-mass energies necessary to probe the vertex. As discussed in Section 2.6, low energy measurements of precision

electroweak quantities provide some indirect constraints on triple gauge couplings, but these constraints assume certain relationships between the different coupling. LEP provided the first direct measurements of triple gauge couplings in the WW final state and experiments at the Tevatron improved these measurements, but in general the values of the couplings are only known within 1%-30% accuracy.

2.3 Motivation for Looking for New Physics

The Standard Model has proved enormously successful in describing the interactions of fundamental particles at energies we have been able to test. The relationship between the electron spin magnetic moment and the value of the fine structure constant is measured to agree with the Standard Model prediction within one part per billion [102]. So far, there has been no conclusive experimental evidence that any of the predictions of the Standard Model are incorrect. Among the most compelling exceptions to this statement are the following experimental results:

1. *Neutrino Masses* – The observation of neutrino oscillations requires that the neutrinos have non-zero mass [95]. In the Standard Model, neutrinos are massless. To give the neutrinos mass, several extensions are proposed. The simplest extensions, including right handed sterile neutrinos or heavy Majorana neutrinos, only affect the neutrino sector.

2. *Measurement of $\bar{B} \to D^{(*)}\tau^-\bar{\nu_\tau}$ decays* – The BaBar experiment observes a three sigma disagreement with the Standard Model predictions of the branching ratio comparison of $BR(\bar{B} \to D^{(*)}\tau^-\bar{\nu_\tau})$ to $BR(\bar{B} \to D^{(*)}\ell^-\bar{\nu_\ell})$, where ℓ is an

electron or muon and both D and D^* decays are measured [113]. These ratios are sensitive to new physics such as a charged Higgs boson (which couples more strongly to the tau than to the electron or muon), but the results are not compatible with the simplest two Higgs-doublet model that includes a charged Higgs boson.

3. *Measurement of $\bar{\nu_\mu} \to \bar{\nu_e}$ oscillations* – The MiniBooNE experiment observes an excess of anti-electron neutrino events in a measurement of the $\bar{\nu_\mu} \to \bar{\nu_e}$ oscillation probability [123]. No such excess is observed in electron neutrino events, suggesting that anti-neutrinos might oscillate to a new type of sterile anti-neutrinos; if so, CP symmetry is broken and no such oscillation occurs for the neutrinos.

There is also strong observational evidence the Standard Model may not be a complete description of matter in the universe, even if it is internally consistent. To the previous list we add perhaps the most compelling experimental support for extensions to the Standard Model:

1. *Dark Matter* – there is an abundance of astronomical evidence for matter interacting gravitationally at cosmological scales that is not made up of Standard Model particles [140]. There are compelling theoretical calculations arguing that the dark matter might be composed of heavy particles that interact with Standard Model particles at roughly the weak scale [48]. Supersymmetry and other theories provide candidates for dark matter particles. However, the only non-controversial experimental evidence that dark matter interacts with Standard Model particles is indirect, and, at this stage, the possibility that the signal

could be due to astronomical sources, such as pulsars, is not yet ruled out [12].

There are also theoretical arguments for the existence of physics beyond the Standard Model. We briefly mention a few of the questions which motivate many models of new physics:

1. Why is the Higgs mass of order 100 GeV when there are arguments [120] for its natural mass to be on the order of the Planck scale, 10^{19} GeV?

2. Why is there no CP violation in quantum chromodynamics when it exists in the electroweak sector?

3. What is the physics behind the form of the Higgs potential?

4. Is there a universal symmetry which unites all three forces described by the Standard Model? Can the symmetry be extended to include gravity?

5. What happens at the Planck scale, when gravity becomes incompatible with the Standard Model?

6. Why are there 3 families of particles that appear identical except for their masses?

Possible solutions to these questions motivate an expanse of theoretical models describing new physics, from Supersymmetry [120] to Technicolor [85] to Kaluza Klein Bosons [10] to Grand Unified Theories [91] to many more, that predict signatures that may be observable at the LHC. These questions leave open the possibility that the Standard Model, as successful as it is, is not the complete description of the interactions of fundamental particles. As it has been so successful in describing interactions

up to the TeV scale, the Standard Model must be a low energy approximation of any new physics model. The data so far has shown no evidence for any particular model of new physics, so it is reasonable to look for new interactions or new particles in a model-independent way.

New particles or interactions could show up anywhere. As shown in Figure 2.4(a) and discussed in Section 2.2, looking for anomalous triple gauge couplings in WZ production allows us to look for new particles that interact with only the W and Z weak gauge bosons; these new particles can be heavier than those that the LHC could produce directly.

2.4 WZ Production at the LHC

The leading order contributions to WZ production at the LHC are shown in Figure 2.3. The contributions that are next-to-leading order (NLO) in the strong coupling, α_s, are shown in Figure 2.5. Leading-order WZ production is possible only through quark-antiquark interaction, but the next-to-leading order terms include production from quark-gluon interactions. As the gluon content of the proton is significant at LHC, the NLO contributions are important. Indeed, at $\sqrt{s} = 7$ TeV the NLO terms nearly double the cross-section calculated at leading-order [46, 56].

The details of the theoretical WZ Standard Model cross section used in this analysis are discussed in Section 10.1. The total cross section at $\sqrt{s} = 7$ TeV calculated to next-to-leading order with MCFM [55] is:

$$\sigma_{WZ}^{tot} = 17.6^{+1.1}_{-1.0} \text{ pb} \tag{2.1}$$

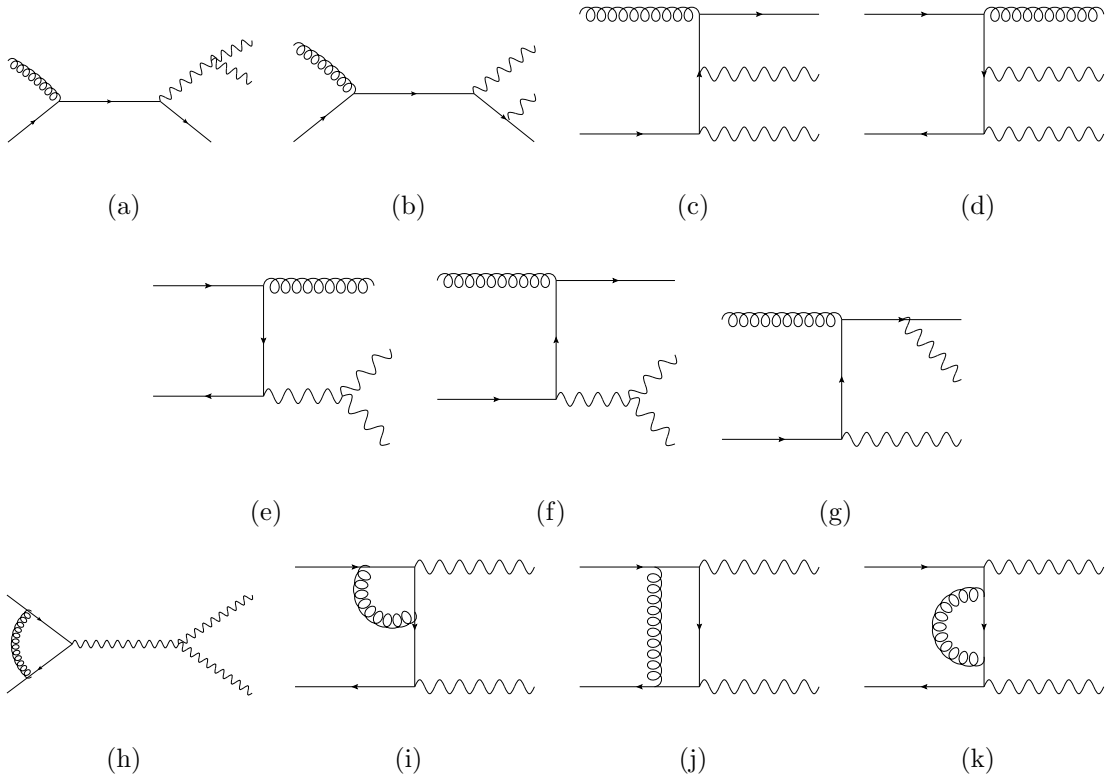

Figure 2.5: NLO Feynman diagrams for WZ production. These are the next-to-leading order QCD terms which contribute to WZ production [108]. Straight lines represent quarks, gluons are shown by spiraling lines, and wavy lines correspond to W or Z bosons.

The largest sources of theoretical uncertainty on the predicted cross section are due to uncertainties on the parton distribution functions and on the choice of QCD renormalization and factorization scale.

The production cross section of various vector boson processes at the LHC is shown in Figure 2.6. The cross section times branching ratio to leptons, $\sigma \times BR(W \to \ell\nu, Z \to \ell\ell)$, is shown for processes including W, Z, and γ bosons for proton-proton collisions with center-of-mass energies between 7 and 14 TeV, from simulation [56]. The cross sections shown include decays of both the W and Z bosons to one lepton species, as this is the most common decay channel in which we observe these processes. For the $W\gamma$ and $Z\gamma$ processes, the photon is required to have $p_T > 25$ GeV. For the $\gamma\gamma$ cross section, one photon must have $p_T > 25$ GeV and the second photon must fulfill $p_T > 10$ GeV. These selections are reasonable requirements for identifying photons in the detector.

After production, the W and Z bosons decay in 10^{-25} seconds. Using the decay branching fractions as reported in the Particle Data Group [127], the expected fraction of WZ decays to each channel are reported in Table 2.1. The branching ratio for the $WZ \to \ell\nu\ell\ell$ process is 0.365% for each leptonic decay channel. There are four combinations that include final states with electrons and muons: $e\nu ee$, $e\nu\mu\mu$, $\mu\nu ee$, and $\mu\nu\mu\mu$. In total, these decay processes constitute 1.5% of all WZ decays. Decays including hadrons make up 90.3% of all decays. We will not consider these decays in this analysis.

While the fully leptonic mode $WZ \to \ell\nu\ell\ell$ is a small subset of all WZ events, it has the advantage that relatively few other processes produce three isolated, high p_T

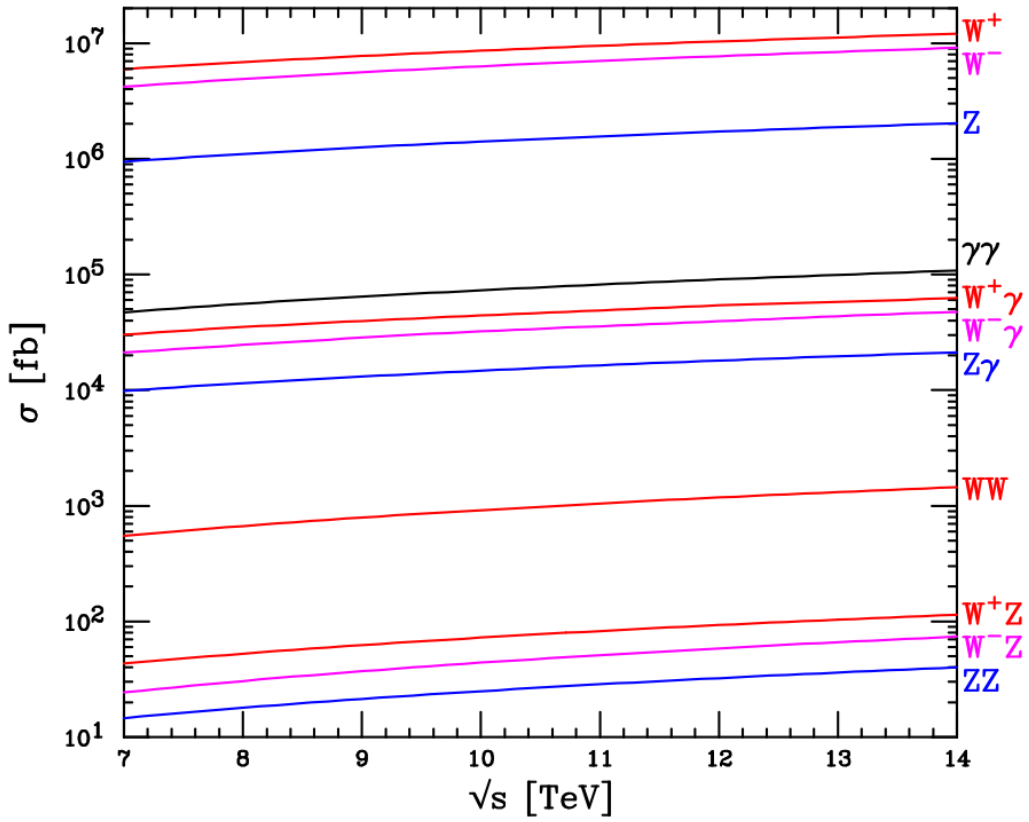

Figure 2.6: NLO boson production in proton-proton collisions for collisions with a center-of-mass energy ranging from 7 to 14 TeV. The cross section shown includes the branching fraction to one lepton type. Photon cross sections impose $p_T^\gamma > 25$ GeV on the first photon and $p_T^\gamma > 10$ GeV on the second photon (only applicable to $\gamma\gamma$.) [56]

Table 2.1: WZ branching fractions. In the table, ℓ includes electron and muon decays; τ decays are included separately.

Decay mode	Fraction of Decays
$WZ \to \ell\nu\ell\ell$	1.5%
$WZ \to \ell\nu\nu\nu$	4.3%
$WZ \to \ell\nu\tau\tau$	0.7%
$WZ \to \ell\nu jj$	15.1%
$WZ \to \tau\nu\ell\ell$	0.7%
$WZ \to \tau\nu\nu\nu$	2.2%
$WZ \to \tau\nu\tau\tau$	0.4%
$WZ \to \tau\nu jj$	7.5%
$WZ \to jj\ell\ell$	4.5%
$WZ \to jj\nu\nu$	2.4%
$WZ \to jj\tau\tau$	13.5%
$WZ \to jjjj$	47.3%

leptons and missing transverse energy from the neutrino. After the full event selection used in this analysis, $WZ \to \ell\nu\ell\ell$ events constitute 77% of all expected events. With a clean sample, we can make a precise measurement of the WZ cross section.

By contrast, selecting WZ events with a hadronic decay in either the W or Z boson does not yield a clean sample. For example, selecting WZ events with a leptonically decaying W boson and a hadronically decaying Z boson includes 15% of all WZ events. However, the inclusive W production cross section is 95 nb, a factor of 5,000 larger than the predicted WZ cross section, and many of the W events include two or more jets that will pass the $WZ \to \ell\nu jj$ selection. The measurement of $WZ \to \ell\nu jj$ was recently performed by ATLAS [36]. After all selections, WZ events contribute 0.28% of all expected events. The WW diboson processes can also contribute $\ell\nu jj$ events that are indistinguishable from WZ events; it contributes 1.25% of all expected events. The uncertainty on the measurement of the combined $WW+WZ$ cross section in the $\ell\nu jj$ final state is 30% and is dominated by systematic

uncertainty. For comparison, the measurement of the WZ cross section in the fully leptonic decay mode presented in this thesis has a total uncertainty of 9% and is dominated by statistical uncertainty.

Additionally, we can select a sample of $WZ \to \ell\nu\ell\ell$ events with straightforward selection requirements, which gives us an inclusive sample with relatively little reliance on theoretical predictions for event acceptance. In contrast, to select $WZ \to \ell\nu jj$ events, more aggressive selection requirements, including vetoes on additional jets in the events, are necessary. This requires a stronger reliance on the Standard Model predictions of event acceptance, and therefore the semi-leptonic channel is less useful in looking for beyond the Standard Model physics which might be produced with additional jets or leptons in the event.

2.5 Triple Gauge Couplings

2.5.1 Standard Model Triple and Quartic Gauge Couplings

Several years before the W and Z bosons were discovered, the importance of measuring the heavy vector boson self couplings was already identified as an important test of the gauge nature of the weak bosons [50]. In the Standard Model, electromagnetism is described by the Abelian gauge symmetry $U(1)$. Due to the Abelian nature of the symmetry, the quanta of the electromagnetic field, the photon, can not couple to itself. This can be also be understood another way: the photon only interacts with particles with electric charge, and because the photon itself is electrically neutral, it can't interact with itself.

Before symmetry breaking, however, the electroweak interaction is described by the gauge symmetry $SU(2) \times U(1)$, which is non-Abelian. To preserve gauge invariance under this symmetry group, the electroweak Lagrangian must include specific terms that correspond to self-couplings between the gauge bosons. These terms include both interactions among three gauge bosons (triple gauge couplings) and among four gauge bosons (quartic gauge couplings.) After symmetry breaking, these interaction terms describe interactions among the W^+, W^-, Z, and γ bosons. The triple gauge couplings are described by a term of the electroweak Lagrangian which takes the following form:

$$\begin{aligned} L_{WWV} = &- ig[(W^+_{\mu\nu}W^{-\mu} - W^{+\mu}W^-_{\mu\nu})(A^\nu \sin\theta_W - Z^\nu \cos\theta_W) \\ &+ W^-_\nu W^+_\mu (A^{\mu\nu} \sin\theta_W - Z^{\mu\nu} \cos\theta_W)] \end{aligned} \tag{2.2}$$

where $W^\pm_\mu$ represents the gauge field corresponding to the W boson, Z_μ represents the Z boson field, A_μ represents the photon field, θ_W is the weak mixing angle or Weinberg angle, and $X_{\mu\nu}$ is defined as:

$$X_{\mu\nu} \equiv \partial_u X_\nu - \partial_\nu X_\mu \tag{2.3}$$

where X represents any of the W, Z, or A fields. The coupling g is the $SU(2)$ weak coupling parameter and it is related to the electric charge e and θ_W by:

$$g = \frac{e}{\sin\theta_W} \tag{2.4}$$

For a complete explanation of the Lagrangian description of the Standard Model, see Reference [134]. To see the triple gauge coupling term before electroweak symmetry breaking, see Reference [108].

The Standard Model includes all self-interactions of the gauge bosons that are consistent with gauge invariance, symmetric under $SU(2)\times U(1)$, and renormalizable. Equation 2.2 shows that the allowed triple gauge vertices in the Standard Model are the W^+W^-Z and $W^+W^-\gamma$ vertices. Moreover, the strength of the couplings at the vertices is fixed by gauge invariance as well. These can also be extracted from equation 2.2 and they are:

$$\begin{aligned} g_{WW\gamma} &= -e \\ g_{WWZ} &= -e\cot\theta_W \end{aligned} \tag{2.5}$$

where e is the electric charge. The allowed triple gauge interactions are illustrated in Figure 2.7.

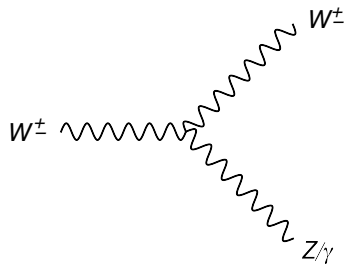

Figure 2.7: The triple gauge boson vertices that exist in the Standard Model.

The contribution to the electroweak Lagrangian that describes the quartic couplings between gauge bosons is:

$$\begin{aligned} L_{WWVV} = -\frac{g^2}{4}\Big\{ & [2W_\mu^+W^{-\mu} + (A^\mu\sin\theta_W - Z^\mu\cos\theta_W)^2]^2 \\ & - [W_\mu^+W_\nu^- + W_\nu^+W_\mu^- + (A^\mu\sin\theta_W - Z^\mu\cos\theta_W)(A^\nu\sin\theta_W - Z^\nu\cos\theta_W)]^2\Big\} \end{aligned} \tag{2.6}$$

and the allowed vertices are $W^+W^+W^-W^-$, $W^+W^-\gamma\gamma$, $W^+W^-Z\gamma$, and W^+W^-ZZ.

The coupling values are:

$$\begin{aligned} g_{WWWW} &= -\frac{e^2}{\sin^2\theta_W} \\ g_{WW\gamma\gamma} &= e^2 \\ g_{WWZ\gamma} &= e^2\cot\theta_W \\ g_{WWZZ} &= e^2\cot^2\theta_W \end{aligned} \tag{2.7}$$

and the vertices corresponding to these quartic gauge couplings are shown in Figure 2.8.

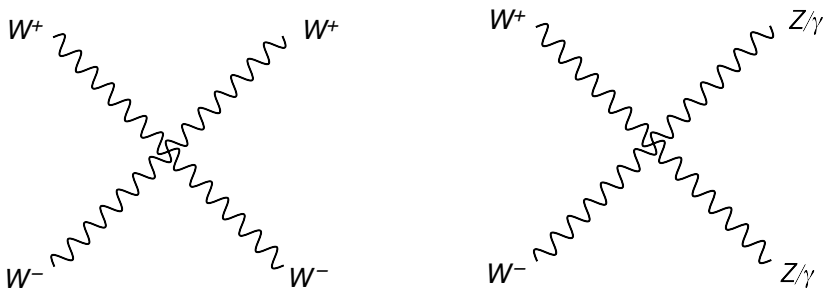

(a) (b)

Figure 2.8: The quartic gauge boson vertices that exist in the Standard Model.

2.5.2 Anomalous Triple Gauge Couplings

As discussed in Section 2.3, it is interesting to look for new physics in a model independent way. The effective Lagrangian method is one such model-independent approach [6]. The effective Lagrangian parametrization represents the dynamical content of a new theory in the low energy limit, which must be consistent with the Standard Model. By including the most general set of terms consistent with the symmetries of Standard Model, the approach is independent of the details of the

new physics at higher energies, and therefore model-independent. The assumption is made that the energy scale of new physics, Λ, is above the energy scale probed by the experiment [83]. Therefore, the new physics model under consideration only appears in virtual interactions at vertices where the incoming and out-going particles belong to the Standard Model. All possible vertex terms involving the Standard Model particles, which respect the symmetries of the Standard Model, are written down in an expansion in powers of $1/\Lambda$. As Λ is assumed to be large relative to all external momenta, the series can be truncated at some small power and a finite number of new interactions with arbitrary couplings can be studied. For a formal overview of the effective Lagrangian approach, see Reference [148]. For its specific application to the anomalous triple gauge couplings, see References [6, 83, 149].

We can use the effective Lagrangian approach to model any set of interactions. In this thesis, we are interested in studying the high energy behavior of electroweak physics and in looking for new physics that interacts with W and Z bosons. This corresponds to the effective Lagrangian terms which describe the general triple gauge boson vertex. The relevant terms of the effective Lagrangian that describe the WWV vertex, where $V = Z$ or γ, are [83, 149]:

$$\begin{aligned} L_{WWV} = g_{WWV}\Big\{ & ig_1^V(W^\dagger_{\mu\nu}W^\mu V^\mu - W^\dagger_\mu V_\nu W^{\mu\nu}) + i\kappa_V W^\dagger_\mu W_\nu V^{\mu\nu} \\ & + i\frac{\lambda_V}{m_W^2}W^\dagger_{\lambda\mu}W^\mu_\nu V^{\nu\lambda} - g_4^V W^\dagger_\mu W_\nu(\partial^\mu V^\nu + \partial^\nu V^\mu) \\ & + g_5^V\epsilon^{\mu\nu\lambda\rho}(W^\dagger_\mu\partial_\lambda W_\nu - \partial_\lambda W^\dagger_\mu W_\nu)V_\rho \\ & + i\tilde{\kappa}_V W^\dagger_\mu W_\nu \tilde{V}^{\mu\nu} + i\frac{\tilde{\lambda}_V}{m_W^2}W^\dagger_{\lambda\mu}W^\mu_\nu\tilde{V}^{\nu\lambda}\Big\} \end{aligned} \tag{2.8}$$

where g_{WWV} are the value of the Standard Model couplings described by equation 2.5, and $\tilde{X}_{\mu\nu} = \frac{1}{2}\epsilon_{\mu\nu\lambda\rho}X^{\lambda\rho}$. This expansion does not include operators of dimension 8 and

higher, which are small if Λ is large relative to the momentum of the initial and final state particles. With $V = Z$ or γ, the 14 parameters g_1^V, κ_V, λ_V, g_4^V, g_5^V, $\tilde{\kappa_V}$, and $\tilde{\lambda_V}$ are the most general model-independent couplings associated to the WWV vertex. To recover the Standard Model triple gauge vertices in equation 2.2, the general couplings must take the values:

$$\begin{aligned} g_1^V &= \kappa_V = 1 \\ \lambda_V &= g_4^V = g_5^V = \tilde{\kappa_V} = \tilde{\lambda_V} = 0 \end{aligned} \tag{2.9}$$

Any deviation from the coupling values in equation 2.9 are called *anomalous triple gauge couplings* (aTGCs). Measuring non-zero anomalous coupling values would be direct evidence of new physics beyond the Standard Model.

The interactions associated to the g_4^V, $\tilde{\kappa_V}$, and $\tilde{\lambda_V}$ couplings in equation 2.8 violate CP invariance. To simplify the search for anomalous couplings, we drop these terms and assume that the new physics does not produce additional sources of CP violation at low energies. Moreover, measurements of the electron electric dipole moment might offer more constraining limits than measurements at the LHC on the existence of CP-violating terms [107]. Following the procedure set by LEP and the Tevatron, we also do not further consider the g_5^V coupling, which violates charge conjugation symmetry. That leaves us with six couplings describing the general WWV vertex, three of which belong to the WWZ vertex and three of which belong to the $WW\gamma$ vertex.

The same approach can be applied to couplings describing a triple gauge vertex involving only neutral gauge bosons, the Z and photon, as shown in Figure 2.9. The couplings associated to terms with one on-shell Z boson, one on-shell photon, and an off-shell photon or Z denoted by V are parametrized by eight couplings: h_1^V, h_2^V, h_3^V,

and h_4^V. Interactions associated with the first two couplings violate CP invariance, whereas the latter two respect it. The vertex with two on-shell Z bosons and an off-shell photon or Z boson, denoted by V, is described by four couplings: f_4^V and f_5^V. All four couplings violate charge conjugation, and the two f_4^V couplings do not respect CP invariance. For a full description of neutral triple gauge couplings, see Reference [96].

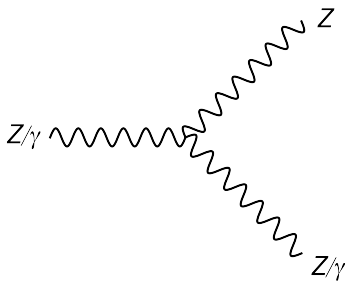

Figure 2.9: Neutral triple gauge vertices, which do not exist in the Standard Model.

Several of the coupling parameters can be expressed in terms of physical quantities of the W and Z bosons, in particular the magnetic and electric dipole and quadrupole moments of the W and Z bosons. For details, see Reference [83].

Theoretical arguments about the structure of the terms in equation 2.8, assuming weak coupling to the vector bosons from the new physics, and assuming that the Higgs boson or another scalar field breaks electroweak symmetry, leads to a theoretical upper bound on the values of the anomalous couplings on the order of $\mathcal{O}(\frac{m_W^2}{\Lambda^2})$ [83]. Therefore, if the scale of new physics is $\Lambda = 1$ TeV, the largest reasonable value of the couplings would be around $\mathcal{O}(10^{-2})$. However, if electroweak symmetry is strongly broken or if the new physics couples strongly to the W and Z bosons, these upper limits are not valid.

Measurements based on different final states are sensitive to different anomalous couplings. WW production is sensitive to all the terms in equation 2.8, $W\gamma$ production is sensitive only to the vertices involving a photon, and WZ production is sensitive only to the WWZ terms. To extract information from WW production about the six couplings to which it is sensitive, assumptions about the relationship between the photon couplings and the Z couplings must be made.

Anomalous couplings increase the production cross section for these processes for most values of the couplings, although for a narrow range of couplings the production cross section actually decreases. The presence of anomalous couplings can also affect kinematic distributions sensitive to the $\sqrt{\hat{s}}$ of the interaction, including the p_T distributions of the bosons or the diboson invariant mass. More information about the effect of anomalous couplings for the WZ system is provided in Section 11.2.

The approach begun by the LEP experiments and continued at the Tevatron is to use measurements of diboson production to set limits on the values of the anomalous couplings. We follow this approach in this analysis. Considering only terms which conserve C, P, and CP, and keeping only couplings that contribute to WZ production, equation 2.8 reduces to:

$$\frac{\mathcal{L}_{WWZ}}{g_{WWZ}} = ig_1^Z(W^\dagger_{\mu\nu}W^\mu Z^\mu - W^\dagger_\mu Z_\nu W^{\mu\nu}) + i\kappa_Z W^\dagger_\mu W_\nu Z^{\mu\nu} + i\frac{\lambda_Z}{m_W^2}W^\dagger_{\lambda\mu}W^\mu{}_\nu Z^{\nu\lambda} \quad (2.10)$$

Therefore, WZ production is sensitive to the couplings g_1^Z, κ_Z, and λ_Z. We search for deviations from the Standard Model values reported in equation 2.9 by defining:

$$\begin{aligned} \Delta g_1^Z &\equiv g_1^Z - 1 \\ \Delta\kappa_Z &\equiv \kappa_Z - 1 \end{aligned} \quad (2.11)$$

In this analysis, we set limits on the values of Δg_1^Z, $\Delta\kappa_Z$, and λ_Z. The limit setting procedure is discussed in Section 11.6. Searching for direct production of any specific particles, including technirhos or neutralinos or charginos, would require tuning the selection requirements toward the specific model. In this analysis, we make an inclusive measurement of WZ production, and use our selected sample to search for model independent anomalous couplings.

The terms in equation 2.10 that are associated to Δg_1^Z and λ_Z are proportional to $\hat{s}$, the square of the center-of-mass energy of the interaction, in WZ production. The terms associated to $\Delta\kappa_Z$ are proportional to $\sqrt{\hat{s}}$. Therefore, WZ production is more sensitive to anomalous values of Δg_1^Z and λ_Z than to anomalous values of $\Delta\kappa_Z$, because the former will have more impact on the cross section and kinetic distributions.

The effective Lagrangian approach assumes that the scale of new physics is large relative to the center-of-mass energy of the experiment. If this assumption is not true, then the higher order terms in $1/\Lambda$ that were neglected in equation 2.8 become as important as the terms that were kept. The finite series shows pathologies and, in particular, can violate unitary as energy increases.

To enforce unitary, either the full Lagrangian of the higher energy physics must be written down, or a form factor can be added to the effective couplings that cuts off the effect of the new interactions above a certain energy scale. Both of these approaches introduce assumptions about the type or scale of new physics, and do not preserve the model-independent nature of the effective Lagrangian approach. Introducing a form factor is the simpler of the two approaches and can be done by replacing the

anomalous couplings introduced in equation 2.8 with energy-dependent couplings:

$$\alpha \rightarrow \alpha(\hat{s}) \equiv \frac{\alpha}{(1 + \hat{s}/\Lambda_{FF}^2)^n} \tag{2.12}$$

where α represents any of the anomalous coupling parameters, n is the exponent chosen to ensure unitarity, and Λ_{FF} is the form-factor or cut-off scale above which the effect of the anomalous couplings is negligible. The cut-off scale Λ_{FF} is set by the new physics scale Λ, but they do not have to be equivalent. For the WWZ vertex, a choice of $n = 2$ is sufficient to ensure unitarity [83].

The advantage of using a form factor is that it guarantees that the model we are studying respects unitarity at all energies. There are two main disadvantages. First, the choice of form factor scale no longer makes the approach completely independent, and the measurement of anomalous couplings will depend on the choice of form factor. Second, the choice of form factor may make it harder to see the effects of new physics. For example, if there is new physics around 2 TeV, or higher, and a cut-off scale of 2 TeV is chosen to damp the anomalous contributions at this scale, then it will be harder to see the signal of the new physics.

For our analysis, we have chosen to search for anomalous WWZ couplings in two scenarios:

1. $\Lambda_{FF} = 2$ TeV

2. no form factor

The first condition nominally allows us to compare our results with measurements made at LEP and at the Tevatron. However, using the same cutoff scale as these experiments prevents us from exploiting the gain in sensitivity from the higher center

of mass energy at the LHC. In reporting our results with no form factor, we report the most model independent limits on the values of the anomalous couplings. Moreover, if the theoretical arguments that the maximum value of the couplings should be order $\mathcal{O}(10^{-2})$ hold true, then unitary violation would only occur at center of mass energies significantly above the LHC energy, and the form-factor becomes unnecessary [83].

Section 11.2 discusses the effect of anomalous couplings in the WZ system at $\sqrt{s} =$ 7 TeV at the LHC. To compare the effect of the couplings at different center-of-mass energies and in proton-antiproton versus proton-proton collisions, see Figures 2.10 and 2.11. These distributions show the ratio of the WZ production cross section with a specific value of one anomalous coupling to the WZ Standard Model cross section, for anomalous values of Δg_1^Z in Figure 2.10 and $\Delta\kappa_Z$ and λ_Z in Figure 2.11. The specific value of the couplings simulated is chosen to correspond to either the lower or upper bound of the 99% expected Confidence Interval (see Section 11.7.1) for the anomalous coupling analysis presented in this thesis. The ratio between anomalous and Standard Model WZ production is shown for two values of the cut-off scale and for both proton-proton and proton-antiproton collisions, as a function of the center-of-mass energy of the collider. The results were simulated with MCFM [55].

As seen in Figure 2.10 and 2.11, the presence of anomalous couplings usually increases the WZ production cross section, although for certain values of Δg_1^Z the cross section decreases. As mentioned previously, λ_Z and Δg_1^Z are more sensitive to the collision energy than $\Delta\kappa_Z$, as the latter grows as $\sqrt{\hat{s}}$ while the former grow as $\hat{s}$. For the same hadron energy, proton-antiproton collisions are more sensitive to the presence of anomalous couplings than proton-proton collisions. As seen in

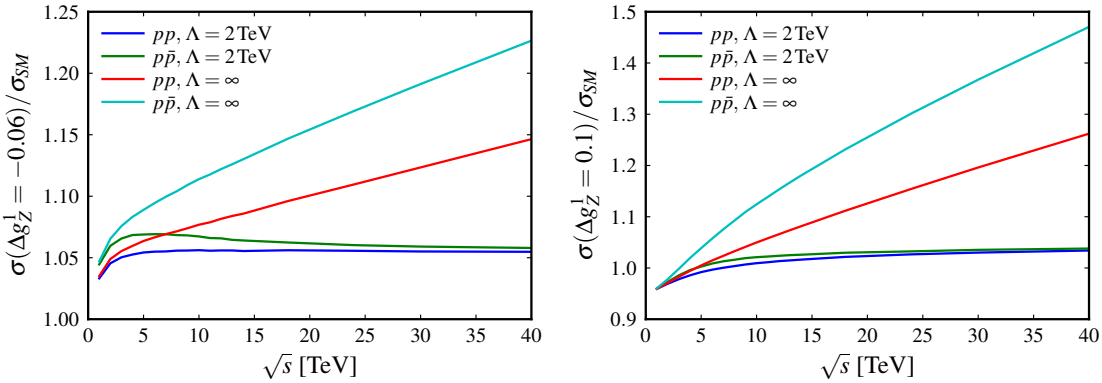

Figure 2.10: WZ production with anomalous Δg_1^Z couplings as a function of $\sqrt{s}$. The ratio between the WZ cross section where $\Delta g_1^Z = -0.06$ (left) and the Standard Model WZ cross section, for both pp and $p\bar{p}$ collisions, is shown for two different values of the cut-off scale Λ. The right plot shows the same quantity, for $\Delta g_1^Z = 0.1$

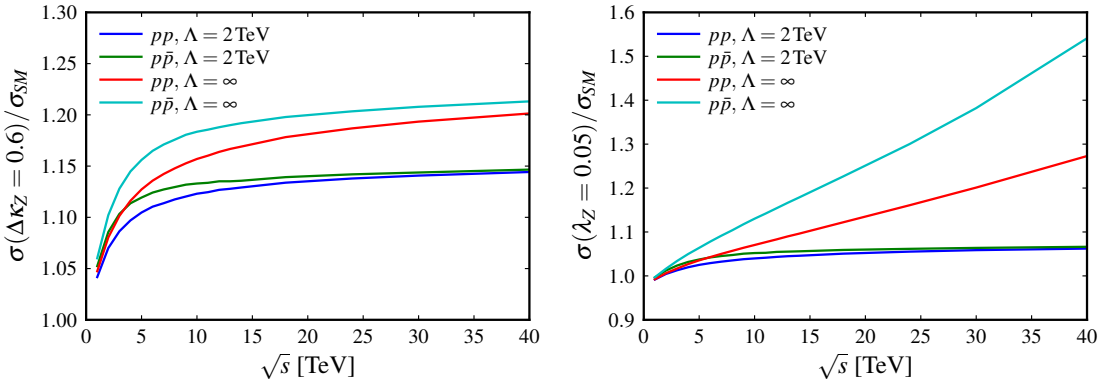

Figure 2.11: WZ production with anomalous $\Delta\kappa_Z$ and λ_Z couplings as a function of $\sqrt{s}$. The ratio between the WZ cross section where $\Delta\kappa_Z = 0.6$ and the Standard Model WZ cross section, for both pp and $p\bar{p}$ collisions, is shown for two different values of the cut-off scale Λ. The right plot shows the same quantity, for $\lambda_Z = 0.05$.

Figure 2.3, the leading order diagram with the triple gauge vertex is from quark-antiquark annihilation, for which the proton-antiproton parton distributions are more favorable than the proton-proton parton distribution functions.

The effect of the cut-off scale Λ is also evident in Figures 2.10 and 2.11. In fact, including a form factor of 2 TeV in the model effectively renders the LHC at $\sqrt{s} = 7$ TeV no more sensitive to the presence of anomalous couplings that the Tevatron at 1.96 TeV, since the form factor suppresses the higher energy contributions to which the LHC is more sensitive. We emphasize that the limits we measure assuming no form factor ($\Lambda = \infty$) are the more sensible limits, as well as the more model independent results.

2.6 Previous Measurements

2.6.1 Previous WZ Cross Section Measurements

The first WZ production cross section measurement was made by the CDF collaboration in 2007 [57] with 1.1 fb^{-1} at $\sqrt{s} = 1.96$ TeV, as mentioned previously. Only the LHC and the Tevatron have made direct measurements of the WZ production cross section. The most recent WZ cross section measurements from the Tevatron and from the LHC, not including the results of this analysis, are summarized in Table 2.2.

The most precise measurements of the WZ production cross section are made in the fully leptonic decay mode. At the Tevatron, the most precise measurements have an uncertainty of 15% (D0) and 20% (CDF). The ATLAS measurement performed

Table 2.2: Previous measurements of WZ production cross section. Results from the Tevatron are measured at $\sqrt{s} = 1.96$ TeV and from the LHC at $\sqrt{s} = 7$ TeV. Only published results are reported here.

Process	Channel	Experiment	Lumi [fb^{-1}]	Theory [pb]	Measurement [pb]	Ref.
$p\bar{p} \to WZ$	$\ell\nu\ell\ell$	CDF	7.1	3.5 ± 0.21	$3.93^{+0.60}_{-0.53}(_{\text{stat}})^{+0.59}_{-0.46}(_{\text{syst}})$	[3]
$p\bar{p} \to WZ$	$\ell\nu\ell\ell$	D0	8.6	3.21 ± 0.19	$4.50^{+0.63}_{-0.66}$	[70]
$pp \to WZ$	$\ell\nu\ell\ell$	ATLAS	1.02	$17.3^{+1.3}_{-0.8}$	$20.5^{+3.1}_{-2.8}(_{\text{stat}})^{+1.7}_{-1.5}(_{\text{syst}})$	[63]
$p\bar{p} \to WZ$	$\ell\nu qq$	D0	4.3	3.21 ± 0.19	$3.3^{+4.1}_{-3.3}$	[71]
$p\bar{p} \to WW + WZ$	$\ell\nu qq$	CDF	4.6	15.1 ± 0.8	17.4 ± 3.3	[67]
$pp \to WW + WZ$	$\ell\nu qq$	CMS	5.0	65.6 ± 2.2	$68.9 \pm 8.7 \pm 9.8$	[68]
$p\bar{p} \to WZ + ZZ$	$\ell\nu b\bar{b}, \ell\ell b\bar{b}, \nu\nu b\bar{b}$	CDF+D0	7.5-9.5	4.4 ± 0.2	$4.47 \pm 0.64^{+0.73}_{-0.72}$	[2]

with an integrated luminosity of 1.02 fb^{-1} has a total uncertainty of 17%.

2.6.2 Previous Limits on Δg_1^Z, $\Delta\kappa_Z$, and λ_Z from Diboson Production

The first direct study of the WWZ vertex was performed at LEP. Although WZ production was not accessible at LEP, information about the WWZ vertex can be obtained from the WW final state. The three WW production diagrams at LEP are shown in Figure 2.12, including a contribution from the WWZ triple gauge coupling vertex shown in Figure 2.12(b).

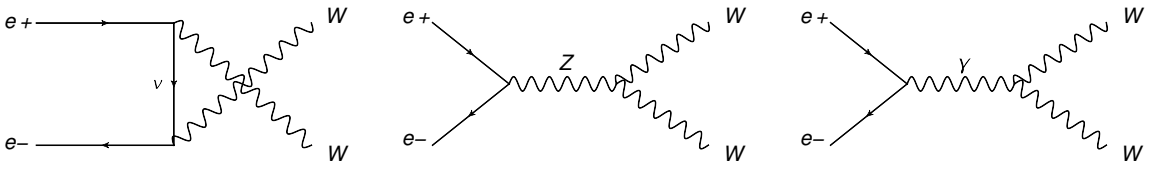

(a) (b) (c)

Figure 2.12: WW production diagrams at LEP. The diagram in (b) includes the WWZ triple gauge vertex.

If the neutrino-exchange diagram (Figure 2.12(a)) were the sole contribution to

WW production, the rate would grow with s and eventually diverge. Similarly, if only the diagrams in Figure 2.12(a) and 2.12(b) contributed, WW production would still diverge, though at a slower rate. It is only when contributions from all three diagrams in Figure 2.12 are considered that WW production respects unitarity at high center of mass energies. On account of this behavior, the presence of the WWZ vertex can be detected by measuring WW production. The LEP measurement of WW production, shown in Figure 2.13, confirms that that all three diagrams contribute.

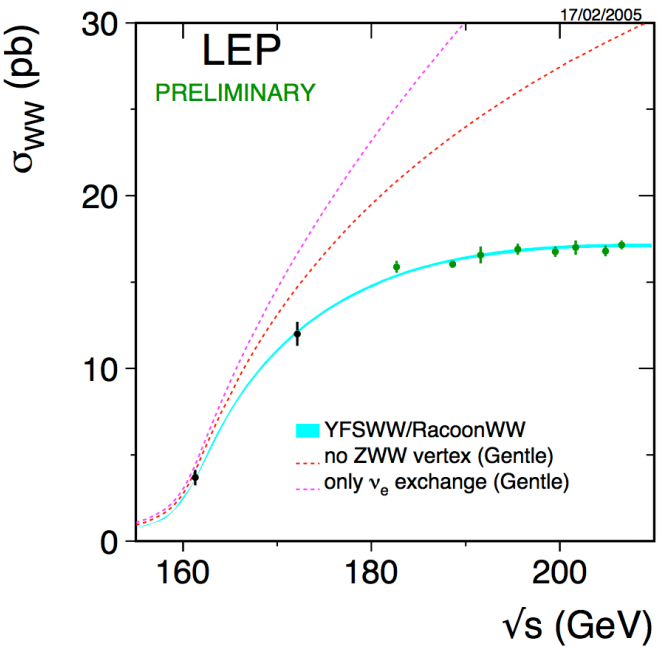

Figure 2.13: WW production measured at LEP [138]. The pink dotted line shows the WW production rate if the only contribution were from neutrino-exchange, as shown in Figure 2.12(a). If both the neutrino-exchange and $WW\gamma$ (Figure 2.12(c)) diagrams contribute, the rate would follow the red dotted line. The data in black and green points confirms that WW production is the sum of all three production diagrams, including the WWZ vertex, as predicted by the blue line.

All four LEP experiments measured the 95% Confidence Level (C.L.) values of the couplings at the $WW\gamma$ and WWZ vertex, with the assumption that $\kappa_\gamma = \kappa_Z$ and

$\lambda_\gamma = \lambda_Z$. The combined results from all four experiments are shown in Table 2.3.

Table 2.3: LEP triple gauge coupling measurements. These parameters were measured in $e^+e^- \to W^+W^-$ production in each of the four experiments and the combined results are shown. The κ_Z and λ_Z couplings are measured under the assumption that they are equal to the γ couplings. Note that the values of the couplings are directly reported, not the deviation from the Standard Model couplings, as is the case for the Tevatron and LHC experiments [7].

Parameter	95% C.L.
g_1^Z	[0.949, 1.034]
$\kappa_\gamma = \kappa_Z$	[0.895, 1.069]
$\lambda_\gamma = \lambda_Z$	[-0.059, 0.026]

At the Tevatron, both the CDF and D0 experiments put limits on deviations from the Standard Model values of the WWZ couplings by studying $WZ \to \ell\nu\ell\ell$ production and reporting the 95% Confidence Level for anomalous coupling values. The most recent results are reported in Table 2.4. For both the CDF and D0 measurements, the transverse momentum of the Z boson in the WZ final state was used to extract information about the anomalous couplings.

Table 2.4: Tevatron aTGC measurements of Δg_1^Z, $\Delta\kappa_Z$, and λ_Z. The results reported are measured in the process $p\bar{p} \to W^\pm Z \to \ell\nu\ell\ell$. The CDF results are measured with 7.1 fb^{-1} and the D0 results with 4.1 fb^{-1} and both results include a form factor with a cut-off scale of 2 TeV [3, 69].

Parameter	CDF 95% C.L.	D0 95% C.L.
Δg_1^Z	[-0.08, 0.20]	[-0.053, 0.156]
$\Delta\kappa_Z$	[-0.39, 0.90]	[-0.376, 0.686]
λ_Z	[-0.08, 0.10]	[-0.075, 0.093]

We performed an ATLAS measurement of the values of the anomalous couplings by extracting information from the production cross section measured with 1.1 fb^{-1}

at $\sqrt{s} = 7$ TeV. The limits on Δg_1^Z, $\Delta\kappa_Z$, and λ_Z from this measurement are shown in Table 2.5.

Table 2.5: Previous ATLAS aTGC measurements of Δg_1^Z, $\Delta\kappa_Z$, and λ_Z. The results reported are measured in the process $pp \to W^{\pm}Z \to \ell\nu\ell\ell$ with 1.02 fb^{-1} and no form factor [63].

Parameter	95% C.L.
Δg_1^Z	[-0.16, 0.24]
$\Delta\kappa_Z$	[-0.8, 1.0]
λ_Z	[-0.14, 0.14]

The analysis presented in this thesis uses the full 2011 dataset of 4.6 fb^{-1} and sets limits based on the transverse momentum of the Z boson. We expect a roughly 40% increase in sensitivity to the values of anomalous couplings from the increase in luminosity and an additional 40% increase in sensitivity from studying the differential distribution rather than the production rate alone.

2.6.3 Indirect Limits on Δg_1^Z, $\Delta\kappa_Z$, and λ_Z

The presence of anomalous couplings would affect certain low energy observables, including the electron dipole moment [107], the muon magnetic moment [83], the $b \to s\gamma$ decay rate [83], and parity violation in cesium decays [93]. For example, Figure 2.14 shows some of the Feynman diagrams that could contribute to a dipole moment for the electron with anomalous triple gauge couplings. In principle, a measurement of the electron's electric dipole moment could be sensitive to the presence of anomalous couplings, in particular couplings which introduce new sources of CP violation.

However, low energy limits on anomalous triple gauge couplings are limited by

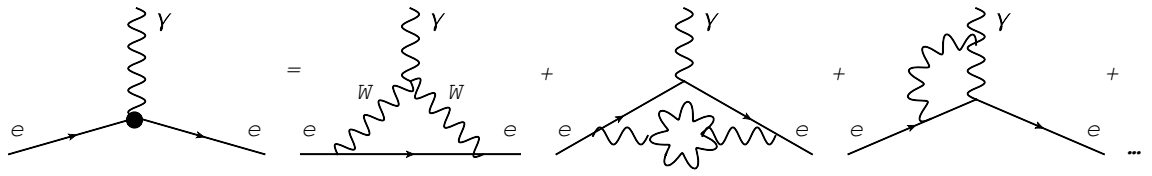

Figure 2.14: Some of the diagrams which could contribute to the electron electric dipole moment with anomalous triple gauge couplings.

the fact that complete cancellations between different terms are possible, and even likely given theoretical arguments [100]. This is particularly true for low energy measurements because the scale of the interactions with anomalous couplings is so large compared to the measurement scale. Therefore, it is necessary to make significant assumptions about the relationships between the anomalous couplings in order to derive limits on their values from measurements of low energy observables [100]. Such assumptions require developing a specific model to motivate the anomalous couplings, which negates the model independent approach of the effective Lagrangian parametrization. Therefore, it is not possible to extract significant model independent limits on anomalous triple gauge couplings from low energy precision measurements. For more information, see References [100, 83].

Chapter 3

The Large Hadron Collider

The Large Hadron Collider (LHC) is a proton-proton collider located at CERN in Geneva, Switzerland. At 26.7 km in circumference, it is the largest scientific instrument in the world. It is designed to collide protons at a center of mass energy, $\sqrt{s}$, of 14 TeV at an instantaneous luminosity of 1×10^{34} cm^{-2} s^{-1}, making it the world's highest energy and highest luminosity proton collider. It is also designed to accelerate lead ions to 2.76 TeV per nucleon and collide them at luminosities of 1×10^{27} cm^{-2} s^{-1}. The LHC turned on in 2010 and provided collisions at center of mass energies of 900 GeV, 2.36 TeV, and 7 TeV. The peak luminosity achieved in 2010 was about 2×10^{32} cm^{-2} s^{-1}, and the LHC provided an integrated luminosity of about 50 pb^{-1} to the ATLAS detector. In 2011, the LHC operated at $\sqrt{s} = 7$ TeV and the peak luminosity reached was about 4×10^{33} cm^{-2} s^{-1}. In 2011, the LHC provided over 5 fb^{-1} to the ATLAS detector. In 2012, the LHC operated at 8 TeV and delivered 23 fb^{-1} to ATLAS.

The Large Hadron Collider was built in the existing tunnel which housed the

Large Electron Positron (LEP) accelerator and makes use of existing accelerators at CERN to accelerate protons to 450 GeV for injection into the LHC. The injection chain is briefly summarized in Section 3.1. The design of the LHC is summarized in Section 3.2 and its performance and operation parameters are discussed in Section 3.3. Finally, in Section 3.4, the method of measuring the luminosity delivered to the ATLAS detector is presented. A useful summary of the LHC design is available in Reference [49] and an in-depth overview can be found in Reference [84]. Sections 3.1 and 3.2 summarize material from these references. Complete technical information can be found in References [51], [52], and [47].

3.1 Injection Chain

The injection chain for the LHC is shown in Figure 3.1. The first accelerator in the chain is Linac 2, which replaced Linac 1 in 1978 as the primary accelerator of protons at CERN. Protons that will eventually make their way into the LHC originate from a bottle of hydrogen gas at the starting point of Linac 2. The hydrogen atoms pass through an electric field which strips off their electrons, leaving protons. Linac 2 has a series of radio frequency cavities that accelerate the protons to 50 MeV, at which point they are transferred to the Proton Synchrotron Booster (PSB or The Booster.)

The Booster, which began operation in 1972, is composed of four stacked synchrotron rings which accelerate protons from 50 MeV to 1.4 GeV, after which they are injected into the Proton Synchrotron (PS.) The PS can accept protons of 50 MeV directly, but at a reduced intensity. The Booster increases the intensity of protons that the Proton Synchrotron can accept, which is necessary for the high instantaneous

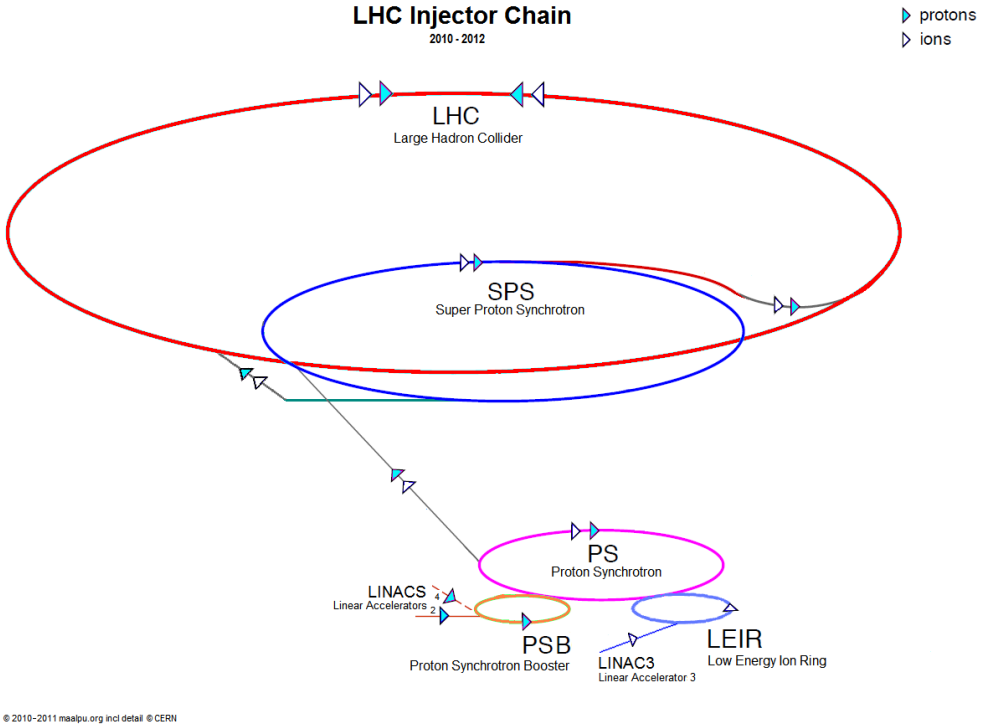

Figure 3.1: LHC injection chain [116].

luminosities demanded by the the LHC.

The Proton Synchrotron consists of 277 conventional iron electromagnets arranged along a circular beam path of circumference 628 meters. It accepts protons from the Booster, but it can also accelerate ions, electrons, positrons and antiprotons. Ions are first accelerated by the Linac 3, and then by the Low Energy Ion Ring (LEIR). The Proton Synchrotron accelerates protons up to 25 GeV. At the time of its construction in 1959, it was the world's highest energy particle accelerator.

The 25 GeV protons from the Proton Synchrotron are injected into the Super Proton Synchrotron (SPS), which began operation in 1976. The SPS measures almost 7 kilometers in circumference and has 1317 conventional iron electromagnets. It can accelerate protons as well as ions, electrons, positrons, and antiprotons. In 1983, running in proton-antiproton mode with a center-of-mass energy of 540 GeV, it produced the first observed W and Z bosons in the UA1 and UA2 experiments. Today, the SPS accelerates protons to 450 GeV for injection into the LHC, as well providing protons directly to several experiments including NA61 [125], NA62 [126], COMPASS [73], and CNGS [60].

3.2 The Large Hadron Collider Design

The Large Hadron Collider contains over 8000 superconducting magnets and is designed to accelerate two intense beams of protons to 7 TeV per particle or two beams of lead ions to 2.759 TeV per nucleon. The beams collide at four different locations around the ring, corresponding to the center of the ATLAS [61], CMS [59], ALICE [9], and LHCb [115] experiments.

The design energy of the LHC was limited by the size of the existing tunnel from the Large Electron Position (LEP) accelerator and the superconducting technology available at the time of its design. The radius of curvature of the LEP tunnel is 2804 m. Using the relation between particle momentum p, magnetic field B, and radius of curvature R:

$$p[GeV] = 0.3 \times B[T] \times R[m] \tag{3.1}$$

we find that for a beam energy of 7 TeV, the bending magnets of the LHC must be 8.33 T. This is higher than the saturation field of iron, and it would be very difficult to produce a uniform field in an iron electromagnet at this field value. Moreover, providing this field with iron magnets would require an enormous current, with large (and expensive) power consumption and problems in distributing the heat load. This motivates the use of superconducting magnets, which can maintain the 8.33 T field with less current, lower power consumption, and other associated benefits. At the time of the LHC design, the most common superconductors were made of Niobium and Titanium, which could carry magnetic fields of around 5 T at the normal boiling point of liquid helium, around 4.3 K. As the magnetic field increases, the NbTi alloy loses its ability to carry current. More exotic superconductors such as Nb_3Sn can carry currents in high magnetic fields at liquid helium temperatures; these superconductors, however, are brittle and it was difficult to use them for magnet windings. Moreover, they were very expensive and not fully developed at the time of the start of the LHC [49].

The solution adopted for the LHC is to use NbTi and to cool the superconductor to 1.9K. At this temperature, the superconductor stays superconducting in fields

up to about 10 T. Superfluid helium at 1.9 K is therefore used, which necessitates an extensive cryogenic system around the entire beam. There is about 120 tonnes of helium, mostly in the superfluid state, inside the LHC magnets during normal operation. Refrigeration is provided by eight large cryogenic helium refrigerators located around the ring. The longest distance between a refrigerator and a magnet is 3.3 km; over this distance, 0.1 K is gained in transport. Therefore, the refrigerators cool the helium to 1.8 K and this is sufficient to keep all magnets operating below 1.9 K.

The circumference of the LHC is composed of eight arcs, each 2987 meters long and connected by 528 meter-long straight sections. The tunnel slopes 1.4% down toward Lake Geneva. Of the 8000 superconducting magnets, 1232 are the main bending dipoles. The other 6800 magnets include quadrupole, sextapoles, octopoles, and single bore dipoles. These are used in focusing the beams, squeezing the beams before collisions, correcting trajectories, and damping oscillations in beam position. The tunnel has a diameter of 3.7 m, which makes it very difficult to install two separate proton rings. To save space, as well as money, the LHC magnets are *twin bore*, in which both proton beams are within the same cryostat, with separate magnetic fields and vacuum pipes for each beam.

The dipole magnets provide the main bending field for the beams. The cross section of an LHC dipole is shown in Figure 3.2. Each dipole magnet is 16.5 m long, has an outer diameter of 0.57 meters, and weighs about 28 tonnes. Inside of each magnet are two separate beam-pipes, each with a diameter of 5 cm. The beam-pipes are kept at 1.9 K and under vacuum to prevent interactions between the protons in

the beam and any gas atoms in the beam pipe. The 54 km of vacuum inside the LHC beam pipe is kept at 10^{-9} - 10^{-8} mbar without beam. Surrounding the beam pipe are the superconducting coils that produce the magnetic field. The superconducting NbTi cable is wound in two layers in each magnet; the cable in the inner layer has a diameter of 1.065 mm and a diameter of 0.825 mm in the outer layer. To produce a magnetic field of 8.33 T, the cables conduct 12 kA of current. Due to this current and the magnetic field, forces on the order of 10^5 N per meter are produced across the conductor. Significant structural elements, including stainless steel collars, are engineered to withstand these forces.

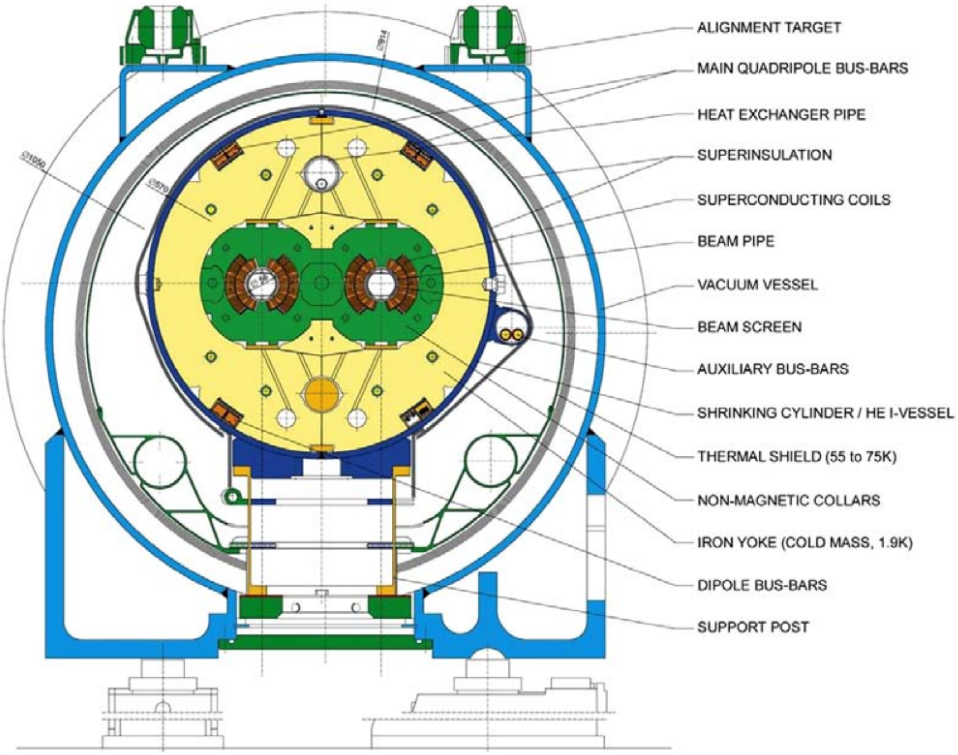

Figure 3.2: LHC dipole cross section [116]. The inner diameter of the beam-pipe is 5 cm and the outer diameter of the magnet is 0.57 meters.

The LHC is the first proton-proton collider in which synchrotron radiation is non-negligible. In the bending regions, 0.22 W/m is expected to be emitted at nominal energy, for a total of 3.9 kW per beam. This radiated energy could cause the temperature of the liquid helium to rise if absorbed by the magnets. If the temperature rises too far, superconductivity can be lost, causing a magnet *quench*. To prevent this, a copper *beam screen* is placed inside the vacuum tube, whose role is to absorb the ultraviolet light emitted by the accelerating protons. The copper screen is cooled to 5 - 20 K by circulation of superfluid helium.

Acceleration is performed by superconducting radio frequency (RF) cavities operating at 400 MHz. The acceleration gradient in the cavities is 5 MV/m. After accelerating the proton beams from the injection energy of 450 GeV to 7 TeV, the RF acceleration compensates for the 7 keV of energy lost due to synchrotron radiation per beam per revolution.

3.3 Accelerator Parameters and Performance

The instantaneous luminosity of the accelerator is a function of the beam parameters:

$$L = \frac{N_b^2 n_b f_{rev} \gamma}{4\pi \epsilon_n \beta^*} F \tag{3.2}$$

where N_b is the number of protons per bunch, n_b is number of bunches in the beam, f_{rev} is the revolution frequency of the accelerator, γ is the relativistic Lorentz factor, ϵ_n is the normalized emittance, β^* is the beta function at the collision point, and F is a geometric factor related to the crossing angle of the beams at the collision point.

β and ϵ are beam parameters related to the transverse beam size by:

$$\sigma = \sqrt{\epsilon\beta} \tag{3.3}$$

where σ is the width of a Gaussian describing the shape of the beam in the transverse direction. The beta function generally changes as a function of position along the beam, and β^* is the value at the collision point. The emittance ϵ is a measure of the average spread of particles in position and momentum phase space.

Maximizing the instantaneous luminosity of the accelerator involves a delicate balancing act of tuning the parameters in equation 3.2. The frequency of revolution is fixed by the size of the LHC tunnel and the velocity of the protons. The smaller the crossing angle, the higher the luminosity, and the crossing angle inside ATLAS is 285 μrad. The main parameter which can be controlled by the LHC operation is β^*, and the lower the value of β^*, the higher the luminosity. Increasing the number of bunches in the beam or the number of protons per bunch increases the luminosity, but it also increases the total stored energy in the beam. It is important to limit the stored energy for many reasons, including the possibility of damage to the detectors or accelerator if control of the beam is lost. For the nominal LHC conditions with 2808 bunches of 10^{11} protons per beam, at 7 TeV, the total stored energy in the two beams is 362 MJ, which is equivalent to 80 kg of TNT [49].

The LHC beam is divided into 3654 *bunches* of length 25 ns each. Each bunch holds roughly 10^{11} protons. At nominal operation, 2808 bunches would be filled; the remaining bunches are empty due to an injection gap, and a long train called the *abort gap* is left empty in case the beam needs to be dumped. In 2011, only 1404 bunches were filled with a spacing of 50 ns between filled bunches. The proton bunches are

arranged in bunch *trains* of 72 bunches, followed by an empty gap of 12 bunches. The bunch train structure is a remnant of the bunch structure of the injection chain. Within each bunch, the protons are placed in RF *buckets* which are 2.5 ns apart, due to the 400 MHz RF frequency.

The main parameters of the LHC beam and magnets are displayed in Table 3.1. The parameters are shown as designed for the injection energy at 450 GeV and the nominal operation energy at 7 TeV per beam. The value of certain parameters is also shown for data-taking during 2011 operation at 3.5 TeV per beam.

Table 3.1: LHC parameters. The designed parameters are shown at the injection energy (450 GeV) and nominal operating energy (7 TeV) per beam. The actual operating parameters in 2011, corresponding to a beam energy of 3.5 TeV, are shown in the last column [84, 81].

Parameter	Unit	Injection (Design)	Nominal (Design)	Operation 2011 (Data taking)
Beam Energy	TeV	0.450	7	3.5
Peak instantaneous luminosity	$s^{-1}cm^{-2}$	-	10^{34}	4×10^{33}
Average collisions per crossing		-	23	15
Bunch spacing	ns	25	25	50
Intensity per bunch	10^{11} p	1.15	1.15	1.2
Number of filled bunches		2808	2808	1404
Normalized rms transverse emittance	μm	3.75	3.75	2.5
β^*	m			1.5
Bunch area (2σ)	eVs	1.0	2.5	
Bunch length (4σ)	ns	1.71	1.06	
Energy spread (2σ)	10^{-3}	0.88	0.22	
Beam Current	A	0.582	0.582	
Synchrotron radiation loss/turn	keV	-	7	
Longitudinal damping time	h	-	13	
Frequency	MHz	400.789	400.790	
RF voltage/beam	MV	8	16	
Energy gain/turn (20 min. ramp)	keV	485	485	
RF power during acceleration/beam	kW	275	275	
Current in magnets	A	763	11850	
Stored energy	MJ		362	110
Magnetic Field	T	0.54	8.33	4.2
Operating Temperature	K	1.9	1.9	
Bending Radius	m	2803.98	2803.98	

The integrated luminosity of the 2011 run at $\sqrt{s} = 7$ TeV is shown in Figure 3.3 as a function of calendar date. The luminosity delivered by the LHC is shown in green. The luminosity that ATLAS recorded is shown in yellow. The difference between the delivered and recorded luminosity is due to the fact that ATLAS stays in *standby* mode while the LHC begins a fill. In standby mode, the high voltage on the Pixel, SCT, CSC, MDT, and TGC detectors is lowered to prevent damage to the detectors in case the beam is not fully controlled. Once the beam is injected, ramped to full energy, and declared *stable* by the LHC operation team, the ATLAS detector turns all high voltages to nominal and begins taking data. Additional requirements on the condition of each sub-detector during data taking further reduces the luminosity that is used for analysis, as discussed in Section 8.3.

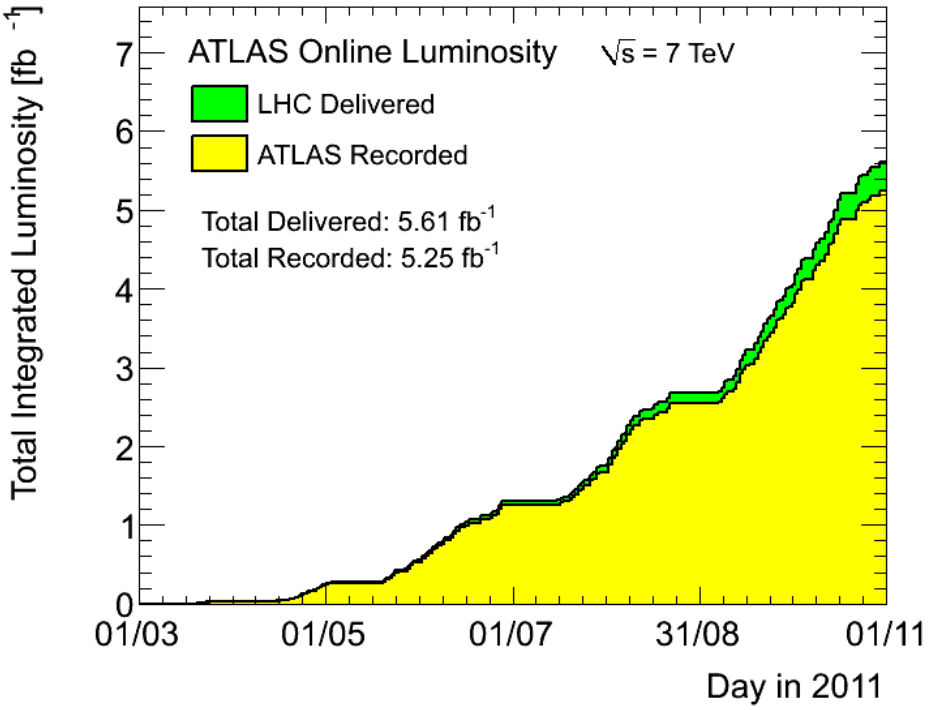

Figure 3.3: Luminosity per day in 2011 [18].

3.4 Luminosity Measurement

The instantaneous and integrated luminosity delivered to the ATLAS detector is measured in two steps. First, dedicated detectors on ATLAS record information related to the number of proton-proton inelastic collisions that occur while the LHC is running. This provides both an observed instantaneous rate as well as an integrated total number of observed inelastic proton-proton collisions. Second, beam scans performed in dedicated LHC runs are used to calibrate the absolute luminosity scale and to convert the observed rate of proton-proton inelastic collisions to a luminosity measurement. These dedicated scans are called van der Meer scans [142]. Detailed information on how the luminosity is measured for the ATLAS detector can be found in Reference [30] and specifics on the algorithms used for the 2011 data can be found in Reference [43]. The section closely follows these two references.

The luminosity of a proton-proton collider can be expressed in terms of the rate of inelastic proton-proton collisions, $R_{inelastic}$, and the inelastic cross section, $\sigma_{inelastic}$:

$$L = \frac{R_{inelastic}}{\sigma_{inelastic}} \tag{3.4}$$

The rate of inelastic collisions can be expressed in terms of the average number of collisions per bunch, μ, the frequency of the accelerator revolution f_r, and the number of bunches which cross at the collision point n_b:

$$R = \mu n_b f_r \tag{3.5}$$

If we knew $\sigma_{inelastic}$ and could measure μ at all times, we'd be all set. We measure μ using dedicated luminosity detectors on ATLAS. However, there is an efficiency for observing inelastic collisions, ϵ, so we do not directly measure μ but rather $\epsilon\mu$, which is

called the visible number of inelastic crossings per bunch, μ^{vis}. The efficiency ϵ is the detection efficiency corresponding to a single inelastic interaction in a bunch crossing. The efficiency is dependent on the η and particle type, and differs for each luminosity detector [30] and specific luminosity algorithm. We can rewrite equation 3.4 using μ^{vis} and equation 3.5:

$$L = \frac{\mu n_b f_r}{\sigma_{inelastic}} = \frac{\mu^{vis} n_b f_r}{\epsilon \sigma_{inelastic}} = \frac{\mu^{vis} n_b f_r}{\sigma^{vis}_{inelastic}} \tag{3.6}$$

where $\sigma^{vis}_{inelastic} \equiv \epsilon \sigma_{inelastic}$ is the visible cross section of inelastic collisions. The luminosity detectors described in the next section extract μ^{vis} from measurable quantities during data collection. The dedicated luminosity scans described in Section 3.4.2 are used to calibrate $\sigma^{vis}_{inelastic}$ for each detector.

3.4.1 Luminosity Detectors on ATLAS

There are four detectors on ATLAS for which luminosity measurement is a main goal: the Minimum Bias Trigger Scintillator (MBTS), the Beam Conditions Monitor (BCM), the Luminosity measurement using a Cherenkov Integrating Detector (LUCID), and the Zero Degree Calorimeter (ZDC). The properties of each of these detectors is summarized in Table 3.2 and described below.

Table 3.2: Luminosity detectors on ATLAS [30].

Detector	Pseudorapidity coverage	# Readout Channels	Type of Detector
MBTS	$2.09 < \|\eta\| < 3.84$	32	scintillator
BCM	$\|\eta\| = 4.2$	8	diamond
LUCID	$5.6 < \|\eta\| < 6.0$	32	gas Cherenkov
ZDC	$\|\eta\| > 8.3$	16	calorimeter

The MBTS is a wheel of scintillators at a distance of ±365 cm from the collision center. The detector's primary purpose is to provide triggers for minimal collision activity, particularly for low luminosity running. The wheel is segmented into 16 chambers on each side of the collision point, and the light from the scintillators is collected by wavelength-shifting optical fibers before being guided to photomultipler tubes for detection. A hit in the MBTS detector is defined as any signal above the discriminator threshold.

The BCM detector [141] is composed of two sets of diamond sensors located at 184 cm from the collision point along the beam line and at a distance of $r = 5.5$ cm in the transverse direction. Diamond is chosen as an active sensor for its ability to withstand the high particle flux - on the order of 10^{15} charged particles per square centimeter - near the beam pipe. The BCM provides continual feedback on the beam near ATLAS to the detector and to the LHC. The detector monitors the rate of charged particles, and with a precise timing of 1-2 ns, it can resolve the difference between charged particles from proton-proton interactions and particles from collisions between protons and gas in the beam-pipe, since the latter do not occur at the interaction point. If there is a large spike in the particle flux, the BCM detector can issue a direct abort signal to the LHC beam. This protects the detector in case control of the beam is lost. By monitoring the rate of charged particle interactions, the BCM detector can also provide information used for determining μ^{vis}.

The LUCID detector is composed of two sets of 200 tubes, one set on each side of the interaction point at a distance of 17 m along the beam-pipe [143]. The tubes are 1.5 m long and filled with C_4F_{10}, which produces Cherenkov radiation when charged

particles go through the detector at velocities greater than the velocity of light in the gas, which corresponds to a threshold of 2.7 GeV for pions and 9 MeV for electrons. The tubes have a diameter of 15 mm and are arranged conically, pointing toward the interaction point. The detector is able to withstand a high particle flux and provides pointing capability as well as good timing resolution. The primary purpose of LUCID is to measure μ^{vis}.

The Zero Degree Calorimeter is located at $z = \pm 140$ m from the interaction point and consists of one electromagnetic calorimeter 29 radiation lengths deep and three hadronic calorimeter modules, each 1.14 interaction lengths deep. The ZDC is placed right behind the point where the LHC beam pipe transitions from a single pipe for both beams (necessary for collisions) and separate pipes for each beam (necessary for bending the two beams). In this location, it is directly in-line with the collision point in z and therefore is actually located at zero degrees. As there is significant shielding between the interaction point and the ZDC, primary charged particles do not make it to the detector from the collision, and its primary purpose is to measure neutrons and photons.

All luminosity detectors discussed above have front-end electronics that allow fast processing of signals independently of the ATLAS global data acquisition system. For the BCM, this is necessary in order to provide prompt feedback to the LHC in case of beam losses. For all the detectors, this allows measurements of the luminosity even when ATLAS is not taking data.

The measurement of μ^{vis} relies on two separate types of algorithms. The first type, called *event counting*, counts the number of events that pass a minimum threshold for

an inelastic proton-proton collision. This threshold varies among the detectors and there are several variations for each detector. For example, in the LUCID detector, one algorithm requires at least one hit in one tube on either side of the detector to pass the event threshold. Another algorithm requires a hit on the A-side of the detector in coincidence with a hit on the C-side. For details on the event counting algorithms, see Reference [30]. If $\mu << 1$, the number of events passing the event counting threshold can be taken as μ^{vis}, as the chance of two collisions per crossing is quite low. However, if the probability of multiple collisions in the same crossing is non-negligible, as it was for most of the 2011 data, this equality does not hold.

Crucially, the detectors also count the number of colliding bunches in which no inelastic collision is observed. The distribution of the number of collisions per crossing is assumed to follow the Poisson distribution. With this assumption, μ^{vis} can be extracted from the measured probability of detecting at least one collision in a crossing, $P_{\geq 1 \text{ collision}}$:

$$P_{\geq 1 \text{ collision}} = 1 - e^{-\mu^{vis}} \tag{3.7}$$

This method also assumes that the efficiency to detect a single inelastic proton-proton interaction is constant and does not depend on the number of collisions in the crossing.

As μ increases, the precision of the event counting method decreases because $P_{\geq 1 \text{ collision}}$ approaches 1. The μ value at which the event counting method no longer works depends on the efficiency of the detector; the lower the efficiency, the lower the value of $P_{\geq 1 \text{ collision}}$, and the larger the range of validity. For the BCM detector, event counting worked for the full 2011 run. For the LUCID detector, the method was not viable for much of the data-collecting period.

To address the saturation of the event counting method, a second set of algorithms employing *hit counting* is used. These algorithms count the number of hits in a detector in each bunch crossing. Assuming that the number of hits follows a Binomial distribution and that the probability of a single hit is independent of the number of collisions per crossing, μ^{vis} can be extracted from a measurement of the number of hits per crossing. For details, see Reference [43]. The hit counting algorithm was used for measurements by the LUCID detector in 2011.

3.4.2 Absolute Luminosity Determination

Equation 3.2 can be written for a more general beam profile as:

$$L = \frac{n_b f_r n_1 n_2}{2\pi \Sigma_x \Sigma_y} \tag{3.8}$$

where n_1 and n_2 are the number of protons in each of the two colliding bunches, and Σ_x is a measure of the beam size in the x direction:

$$\Sigma_x = \frac{1}{\sqrt{2\pi}} \frac{\int R_x(\delta) d\delta}{R_x(0)} \tag{3.9}$$

where δ is the distance between the center of the two beams and $R_x(\delta)$ is is the luminosity or number of collisions in arbitrary units. $R(0)$ is the luminosity when the beams are centered on each other. If the beam profile follows a Gaussian distribution, Σ_x is its standard deviation.

The number of protons in each beam is measured using Bunch Current Transformers, as described in detail in Reference [13]. These measurements take advantage of the fact that the beam, as a moving set of charges, produces a magnetic field in proportion to its current. The beam acts as the primary winding for two DC current

transformers and two fast beam current transformers which are installed on each ring. Coils in the secondary winding of the transformers produce a current in response to the changing magnetic field produced by the beam. This allows continual measurement of the number of protons in each beam. The DC current transformers have high accuracy for the total beam population but can not measure individual bunch current. The fast beam current transformers produce measurements for the number of protons in each individual bunch, normalized by the higher accuracy DC measurements.

Measurements of Σ_x and Σ_y are performed for specific calibration runs with dedicated van der Meer scans. In these scans, the two beams are first centered on each other, and the hit rate in each detector, as well as the event rate for each type of counting algorithm, is recorded. One beam is then moved a distance δ in the x direction, and the rates are recorded. The beams are separated in discrete steps until the event counting rate approaches zero, and then the beams are stepped back together and moved in the $-x$ direction. From these measurements, Σ_x can be extracted using equation 3.9. The procedure is repeated in the y direction for Σ_y. The results of one van deer Meer scan in 2011 are shown in Figure 3.4 for data from a single BCID from one algorithm in the BCM detector.

Using equation 3.8 and the measured values of of n_1, n_2, Σ_x and Σ_y, the absolute luminosity can be calculated for the runs in which the van der Meer scans were performed. During these runs, each luminosity detector measures μ^{vis} using several counting algorithms. With the absolute luminosity calibration provided by the van der Meer scans, equation 3.6, and the measurement of μ^{vis}, a value of $\sigma^{vis}_{inelastic}$ is extracted for each algorithm and each detector. While the visible inelastic cross

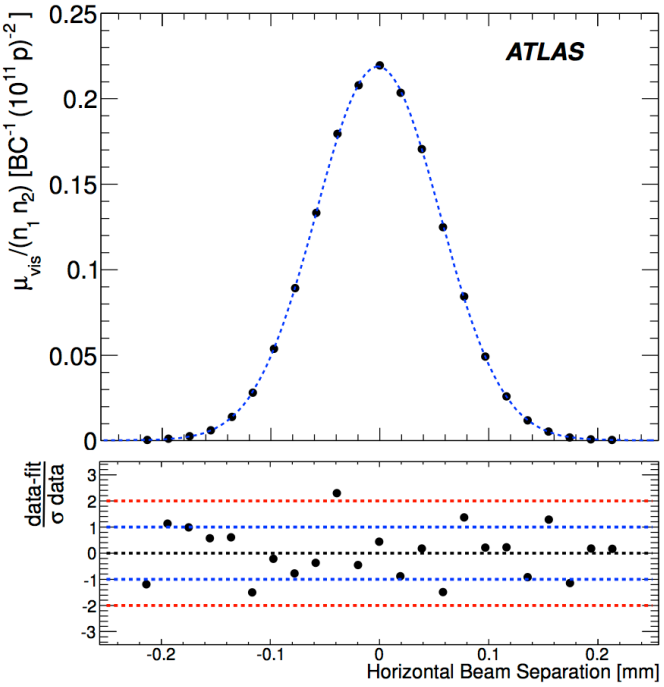

Figure 3.4: LHC beam profile during one van der Meer scan. The visible interaction rate, μ^{vis}, is shown for one event counting algorithm in the BCM detector as a function of the horizontal separation of the beams during a van der Meer scan in 2011. The data is shown for a single BCID and is fit with a single Gaussian plus a constant [43].

section varies from detector to detector, it is independent of the luminosity at which it is measured. Therefore, once the luminosity is calibrated for each detector, it is not necessary to remeasure Σ_x and Σ_y for each run, even if the beam parameters change.

The luminosity is individually calculated for each BCID. The central value is taken from the measurements by the LUCID detector. Systematic uncertainties on the luminosity measurement are estimated in part by comparing the luminosity measurements from all algorithms and all detectors. Multiple van der Meer scans are used to estimate the systematic uncertainty on Σ_x and Σ_y. One of the largest uncertainties on the absolute luminosity normalization comes from the measurement of the beam current. Other systematic uncertainties arise from uncertainties on backgrounds to the event counting and hit counting algorithms from non proton-proton collisions, including beam-gas events or hits from long lived photons and neutrons.

For the 2011 data set, the total luminosity delivered to ATLAS is measured to be 5.61 fb^{-1} with an uncertainty of 1.8% [43]. ATLAS recorded 5.25 fb^{-1} of these collisions with the nominal detector conditions.

Chapter 4

The ATLAS Detector

A Toroidal LHC Apparatus (ATLAS) is a particle detector designed to study proton-proton collisions at energies up to $\sqrt{s} = 14$ TeV in order both to precisely measure Standard Model physics processes and to search for evidence of physics beyond the Standard Model. ATLAS is located at one of the four collision points along the LHC ring, and proton-proton collisions occur at the heart of its concentric cylinder design, which follows the 4π detector layout first employed by the Mark I detector in 1973 [118].

The design of the detector is motivated by the requirements of a range of physics studies, from the search for the Higgs boson to searches for new, heavy resonances to high energy QCD measurements. To meet these physics goals, the detector is designed to provide precise measurements of electrons, muons, photons, taus, b-jets, and hadronic jets, with momenta from 1 GeV to several TeV, over a large solid angle, while withstanding a harsh radiation environment close to the interaction point and along the beampipe. The main performance goals for the ATLAS detector are

summarized in Table 4.1.

Table 4.1: The main performance goals of the ATLAS detector. Energy and momentum are listed in GeV and $\oplus$ indicates a sum in quadrature [28].

Detector	Resolution	Measurement Coverage	Trigger Coverage
Tracking	$\sigma_{p_T}/p_T = 0.05\% p_T \oplus 1\%$	$\|\eta\| < 2.5$	
Electromagnetic Calorimeter	$\sigma_E/E = 10\%/\sqrt{E} \oplus 0.7\%$	$\|\eta\| < 3.2$	$\|\eta\| < 2.5$
Hadronic Calorimeter			
Barrel / End-Cap	$\sigma_E/E = 50\%/\sqrt{E} \oplus 3\%$	$\|\eta\| < 3.2$	$\|\eta\| < 3.2$
Forward	$\sigma_E/E = 100\%/\sqrt{E} \oplus 10\%$	$3.1 < \|\eta\| < 4.9$	$3.1 < \|\eta\| < 4.9$
Muon Spectrometer	$\sigma_{p_T}/p_T = 10\%$ at 1 TeV	$\|\eta\| < 2.7$	$\|\eta\| < 2.4$

The main components of the ATLAS detector are shown in Figure 4.1. The detector is composed of several main subsystems. Two magnet systems provide a strong magnetic field to the inner detector and muon spectrometer, respectively, for measuring the momenta of charged particles. The inner detector provides precision tracking and vertex reconstruction for all charged particles with pseudorapidity $|\eta| < 2.5$. The calorimeters provide precise measurements of the energy of electrons, photons, hadrons, and hadronic jets within a central region of roughly $|\eta| < 2.5$, and provides coarser hadronic energy measurements up to $|\eta| < 4.9$. The large solid angle coverage of the calorimeter is essential for identifying missing transverse energy from particles that do not interact with the detector, including Standard Model neutrinos and more exotic neutral, long-lived particles predicted by models of Dark Matter or Supersymmetry. The muon spectrometer identifies muons as well as providing an independent, precision measurement of their position and momentum. The ATLAS detector has a diameter of 22 meters and is 46 meters long. It weighs 7,000 tons and cost roughly 550 million Swiss francs to build [89].

Extensive information is available about the ATLAS detector in References [61]

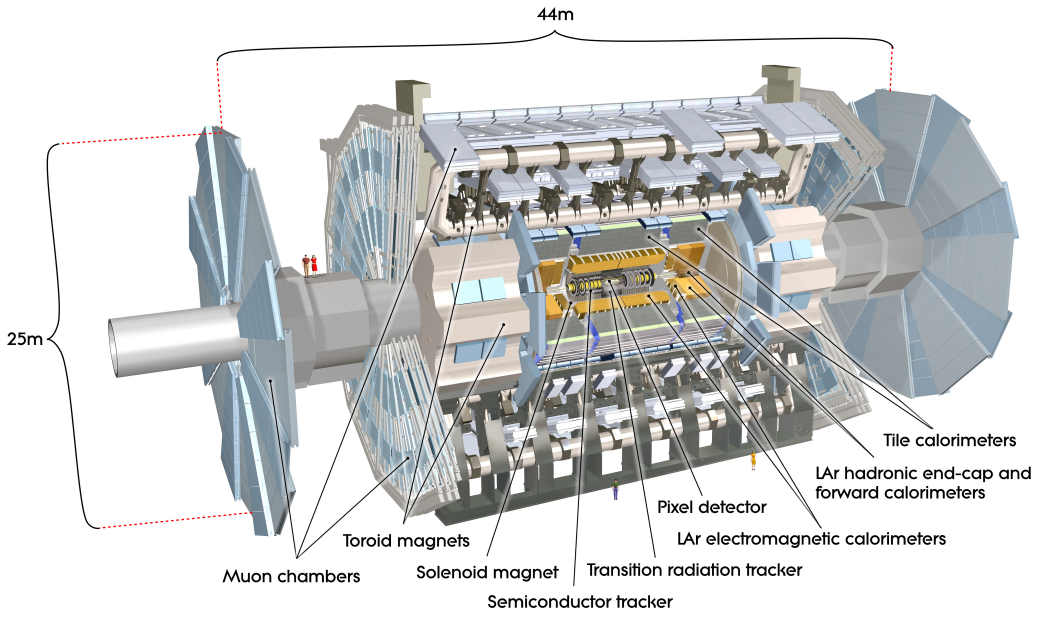

Figure 4.1: A schematic of the ATLAS detector [28].

and [62]. For a clear discussion motivating the detector design, see Reference [49]. To see a comparison between the ATLAS and CMS detectors, Reference [89] is useful. For an introduction to the physics and designs of detectors, see Reference [99].

The measurements of the $WZ \to \ell\nu\ell\ell$ final state presented in this thesis, where ℓ includes both electrons and muons, require information from nearly the entire ATLAS detector. Measurements of muon momenta and position are made using the inner detector and the muon spectrometer. The inner detector and electromagnetic calorimeters are used to measure the position and energy of electrons. The inner detector, electromagnetic, and hadronic calorimeters are used to measure the missing transverse energy that is the signature of the neutrino.

4.1 Coordinate System

The coordinate system of the ATLAS detector is oriented by the beam line, which defines the z-direction. The x-direction points toward the center of the LHC ring, and y-direction points upward from the origin. The positive z side of the detector is referred to as the A-side (it points toward the airport), and the negative z side of the detector is called the C-side (it points toward Charly's, the pub in St. Genis-Pouilly.) The azimuthal angle ϕ runs around the z axis with $\phi = 0$ coinciding with the x-axis, and θ is the angle from the z-axis. As the initial z momentum of the partons is not known, it is useful to use the rapidity of the produced particles, as rapidity differences are invariant to boosts along the beam-axis. Rapidity y is defined as:

$$y = \frac{1}{2} \ln \frac{E + p_z}{E - p_z} \tag{4.1}$$

where E is the particle's energy and p_Z is the momentum in the z-direction. Under the approximation that a particle is massless, equation 4.1 can be rewritten:

$$\eta = -\ln \tan \frac{\theta}{2} \tag{4.2}$$

where η is called the pseudorapidity and $\eta = y$ for a massless particle. A particle travelling perpendicular to the beampipe has $\eta = 0$; a particle travelling parallel to the beampipe has $\eta = \infty$. Pseudorapidity is often used rather than rapidity because it is a geometrical variable and does not depend on any specific particle; therefore, it is a fixed, geometric coordinate system. Pseudorapidity is preferred over θ not only because rapidity differences are invariant to boost along the beam-axis, but also because particle production from inelastic collisions is roughly uniform in η up to a kinematic threshold, which corresponds to about $|\eta| = 5$ in ATLAS. [49]

To achieve detector coverage over a large range of η, most detector sub-systems are divided into three pieces: a central section called a *barrel* section, and two forward sections called *endcaps*. The location of the transition between barrel and endcap regions varies among the subdetectors.

The x-y plane is called the transverse plane. The energy and momentum of particles are frequently projected onto the transverse plane; the transverse energy and momentum are called E_T and p_T respectively. The transverse plane is preferred because the initial transverse energy and momentum of the partons is close to zero. In contrast, the initial energy and momentum in the z direction is unknown a priori for hadron colliders, including the LHC.

4.2 Magnetic Field

The magnetic field in ATLAS is produced by four separate magnets. A superconducting solenoid provides a magnetic field for particles traversing the inner detector. To measure the momentum of particles traversing the muon spectrometer, a toroidal magnetic field is produced by a barrel toroid and two endcap toroids. Information on each of the four magnets in ATLAS is summarized in Table 4.2.

The ATLAS magnetic system is designed to provide a field that allows for accurate stand-alone measurement of muon momentum up to several TeV and up to $|\eta| < 2.7$. This ensures that all benchmark physics processes involving leptons, including the Higgs decay to leptons, can be accurately measured independently of the performance of the other subdetectors. To achieve sufficient muon resolution, the magnet system must provide a strong field without introducing too much mate-

Table 4.2: ATLAS magnet parameters [89, 61].

Parameter	Solenoid	Barrel toroid	End-cap toroids
Inner diameter (m)	2.4	9.4	1.7
Outer diameter (m)	2.6	20.1	10.7
Axial length (m)	5.3	25.3	5.0
Number of coils	1	8	8
Number of turns per coil	1173	120	116
Conductor size (mm^2)	30×4.25	57×12	41×4.25
Bending power (T m)	2	3	6
Peak field (T)	2.6	3.9	4.1
Current (kA)	7.7	20.5	20.0
Stored Energy (MJ)	38	1080	206
Weight (tons)	5.7	830	239

rial that would induce additional multiple scattering. ATLAS adopted an "air-core toroid" approach, in which a toroidal magnetic field is provided by individual superconducting coils, separated by air, in the barrel region. The layout of the magnet system and the bending power of the toroidal field is shown in Figure 4.2. Each of barrel toroid coils is housed in a separate vacuum and cold chamber. On each side, the endcap toroid coils on are housed together in a single vacuum and cold chamber and are rotated by 22.5% relative to the barrel toroids to provide a more uniform field in the transition region. The original ATLAS design had 12 coils in the toroid; for budget reasons, this was later reduced to 8 coils.

The solenoid provides a magnetic field approximately along the z-direction in the inner detector, which bends charged particles primarily in the ϕ direction due to Lorentz forces. The toroid provides a field in the ϕ direction and bending in the muon spectrometer occurs primarily in the η direction.

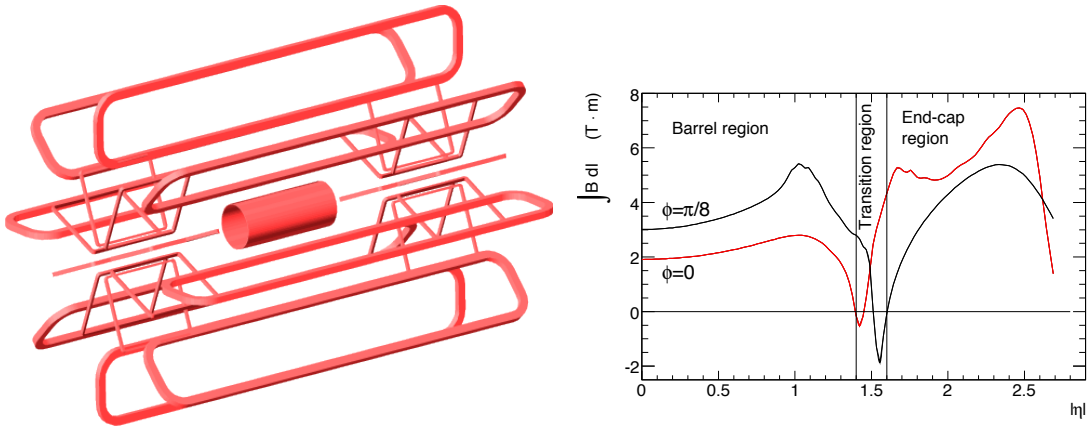

Figure 4.2: ATLAS magnet system. On the left, the elements of the ATLAS magnet system are shown with the solenoid in the center, and the separate barrel and endcap toroid coils outside. On the right, the bending power of the toroidal field is shown as a function of η [28].

4.3 Inner Detector

The inner detector provides precise and efficient tracking coverage out to $|\eta| < 2.5$ for charged particles with transverse momentum above 500 MeV. Inner detector tracks are used to identify electrons and measure their position, to identify photon conversions, to measure the momentum of muons (in combination with measurements from the muon spectrometer), to assign particles and jets to different primary vertices, and to correct the measurement of missing transverse energy for contributions from low-energy particles. With measurements from the inner detector, collision vertices and the transverse and longitudinal impact parameter of individual tracks are reconstructed with enough precision to separate tracks from 20 collisions or more in the same event (see Section 5.2). Vertex information is also used to distinguish and measure secondary vertices to identify tracks consistent with the decay of long-lived particles, including τ leptons, kaons, lambda baryons, and hadrons containing

b quarks.

The ATLAS inner detector consists of three separate subdetectors, as illustrated in Figure 4.3, which shows the trajectory of a charged particle passing through the inner detector barrel. The Pixel system is composed of 80 million individual silicon pixels, each with approximately 10 μm position resolution in the bending plane, and provides 3 layers of precise position measurements closest to the interaction point. The Pixel detector is encircled by the Semiconductor Tracker (SCT), a silicon strip detector that provides at least eight measurements for each charged particle traversing the detector. The final subdetector in the inner detector is the Transition Radiation Tracker (TRT). The TRT is composed of small gaseous drift tubes that provide 36 additional hits per particle, providing position information that further constrains the trajectory of particles passing through the inner detector. The parameters of the Pixel, SCT, and TRT detectors are summarized in Table 4.3.

Table 4.3: ATLAS inner detector parameters. In the table, X_0 is the radiation length of an electron in the material, and λ_0 is the nuclear interaction length. Resolution shown is expected performance [89, 61].

Parameter	Total ID	Pixels	SCT	TRT
η coverage		2.5	2.5	2.0
Material (X/X_0) at $\eta = 0$	0.3			
Material (X/X_0) at $\eta = 1.7$	1.2			
Material (X/X_0) at $\eta = 2.5$	0.5			
Material (λ/λ_0) at max	0.35			
Number of hits on track	47	3	8	≈ 36
Radius of innermost layer (cm)	5.0	5.0	30	56
Total number of channels	8.7×10^7	8×10^7	6.2×10^6	3.5×10^5
Cell size ($R\phi \times z/R$)		50μm $\times$400μm	80μm $\times$12 cm	
Cell size (mm in $R\phi\times$cm in z)				4×70
Total active silicon area (m^2)	62	1.7	60	
Sensor thickness (μm)		250	280	
Resolution in $R\phi$ (μm)		≈ 10	16	170
Resolution in z/R (μm)		≈ 80	580	

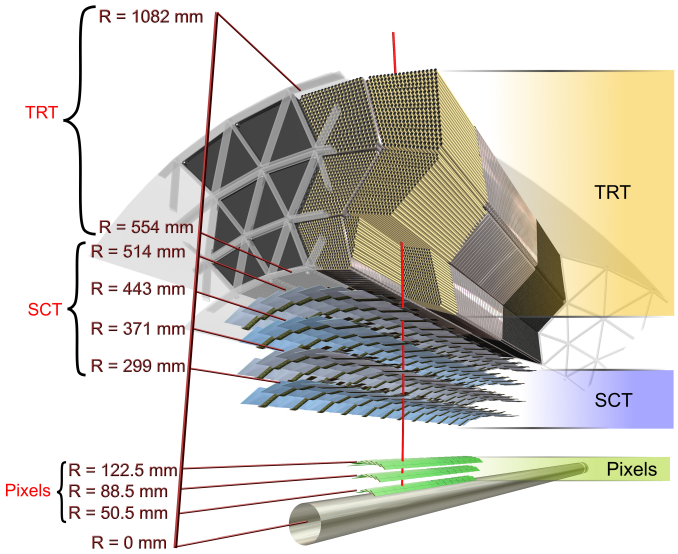

Figure 4.3: This schematic shows the trajectory (red line) of a high p_T charged particle passing through the layers of the ATLAS inner detector barrel [17].

The performance of the ATLAS inner detector tracking is summarized in Table 4.4. Examples are given for the expected reconstruction efficiencies, momentum resolution, and transverse and longitudinal impact parameter resolutions for particles with varying type, momenta, and η location. These values are reported from simulation and test-beam measurements. For a discussion of the detector's performance as measured with collision data, see Section 7.2.

To limit multiple scattering and energy loss by charged particles, and to limit the conversion of photons in the inner detector, it is important to keep the inactive material budget of the inner detector as small as possible. Significant effort has been made to design the readout, cooling, gas, and support structures of all three subdetectors with as little material as possible. Still, given the dense silicon sensors themselves and

Table 4.4: Expected ATLAS inner detector tracking performance. Reconstruction efficiencies, momentum resolution, and transverse and longitudinal impact parameter (i.p.) resolutions are given for various particle types, transverse momenta, and pseudorapidities [89].

Parameter	Example Particle	Value	
Reconstruction efficiency	muons, $p_T = 1$ GeV	96.8%	
	pions, $p_T = 1$ GeV	84.0%	
	electrons, $p_T = 5$ GeV	90.0%	
		$\eta \approx 0$	$\eta \approx 2.5$
Momentum resolution	$p_T = 1$ GeV	1.3%	2.0%
	$p_T = 100$ GeV	3.8%	11%
Transverse i.p. resolution (μm)	$p_T = 1$ GeV	75	200
	$p_T = 1000$ GeV	11	11
Longitudinal i.p. resolution (μm)	$p_T = 1$ GeV	150	900
	$p_T = 1000$ GeV	90	190

the size of the system, there is significant material in the inner detector, in particular around $|\eta| = 1.7$, which is the transition from the barrel to the endcap. The amount of material in the inner detector can be seen in Figure 4.4(a).

4.3.1 Pixel Detector

The Pixel detector provides the first three, high precision measurements of a particle's trajectory as it traverses the inner detector. It is composed of three layers of silicon pixel modules; each module is 20×60 mm^2 and 250 μm thick and contains 46,080 pixels channels. Each individual sensing silicon pixel is bump-bonded to a readout element. There are 1744 modules in the entire pixel system, which is divided into two endcap and one barrel sections.

The layers are arranged cylindrically in the barrel region at radii of 50.5 mm, 88.5 mm, and 122.5 mm from the interaction point. In the endcap, the layers are

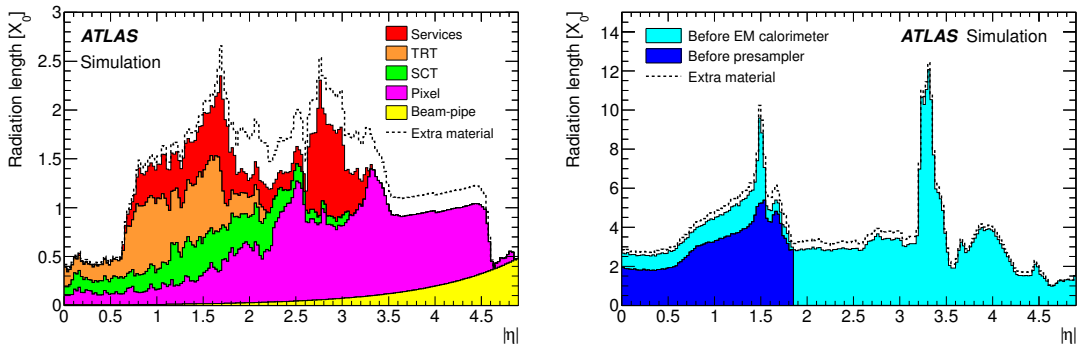

(a) (b)

Figure 4.4: The amount of material, in radiation lengths, as a function of η in different parts of the inner detector (left) and before the electromagnetic calorimeter (right). Extra material is used in simulation studies to estimate the systematic uncertainties associated to the knowledge of the material budget. A bulk of the material between the end of the inner detector and the beginning of the calorimeter is the solenoid and the liquid argon cryostat [35].

arranged as disks transverse to the beampipe are are located at $|z| = 495$ mm, 580 mm, and 650 mm. The innermost layer of the Pixel detector is called the B-layer and is particularly useful for reconstructing secondary vertices from long lived particles, including hadrons with b and c quarks. To minimize the effect of radiation damage, the Pixels are cooled to -7 degrees C, which reduces leakage current.

4.3.2 Semiconductor Tracker

The Semiconductor Tracker (SCT) is composed of strips of silicon detectors and is designed to provide eight precision measurements per track after a particle has passed through the Pixel detector. While additional layers of silicon pixels would provide higher accuracy measurements than the silicon strips, the cost and complexity of the electronic channels necessary to read out the Pixel detector would become

prohibitive. The strip sensors provide adequate resolution at a fraction of the expense and complexity.

Each individual silicon strip sensor has an area of 6.36×6.40 cm^2 and contains 768 readout strips with 80 μm pitch. Pairs of sensors are wire-bonded together end-to-end, to form individual strips with a length of 12.8 cm. Two such detector pairs are then placed back-to-back at a 40 mrad tilt with respect to each other. The small angle stereo separation of the strips is used to obtain the z measurement of a hit. There are four layers of these detector pairs, for a total of eight strip layers in total providing 8 precision measurements in $R\phi$ and 4 measurements in z.

The total SCT detector contains 6.2 million readout channels and has a 16 μm resolution in $R\phi$ and a 580 μm resolution in z, per module. Individual tracks can be cleanly separated if separated by more than 200 μm.

4.3.3 Transition Radiation Tracker

The Transition Radiation Tracker (TRT) provides 36 additional hits on a track traversing the inner detector, giving additional precision information in the ϕ (bending) direction, which contributes to the momentum measurement of charged particles.

This subdetector is composed of Kapton-aluminum straw tubes with a diameter of 4 mm and a gold-plated W-Re wire of 30 μm diameter. The gas inside the tubes is a 70% Xe, 27% CO_2, 3% O_2 mix. There are 350,000 tubes in total, split into a central barrel with tubes parallel to the beam-pipe and two end-caps with tubes arranged radially in disks. When charged particles pass through the tubes, the gas inside ionizes, and the electrons and ions move under an electric field applied between the

wire and tube wall. Avalanche multiplication occurs in the high electric field close to the wire, producing a current signal on the wire, which is read out by the electronics.

In addition to tracking, the detector provides some discrimination between electrons and heavier charged particles, mostly pions, with a measurement of transition radiation. The space between the tubes is filled with a mesh of polypropylene foil and flooded with CO_2 gas. When relativistic charged particles cross the boundary between these two media with different dielectric constants, they emit radiation in proportion to their Lorentz factor γ. For particles of a given energy, lighter particles radiate significantly more energy. The X-rays emitted from transition radiation are absorbed by the Xenon in the straw tubes, which kick out electrons that further ionize inside the tube. For a minimum ionizing particle traversing the TRT, the energy deposited inside a single tube is around 2 keV. A typical energy deposit from an electron producing transition radiation is 8-10 keV [124]. The TRT readout electronics have two thresholds, one which corresponds to the ionization signal from a minimum ionizing particle, and one which corresponds to the signal from an electron producing transition radiation in addition to ionization.

4.4 Calorimeters

The calorimeters measure the energy and position of electrons, photons, mesons, and hadronic jets from gluons, quarks, and hadrons. Their measurements are used to calculate the missing transverse energy in the event (see Section 5.5). The ATLAS calorimetry includes an electromagnetic calorimeter ($|\eta| < 3.2$), a barrel hadronic calorimeter ($|\eta| < 1.7$), two endcap hadronic calorimeters ($1.5 < |\eta| < 3.2$), and

forward calorimeters ($3.1 < |\eta| < 4.9$). An overview of the ATLAS calorimeter system is shown in Figure 4.5.

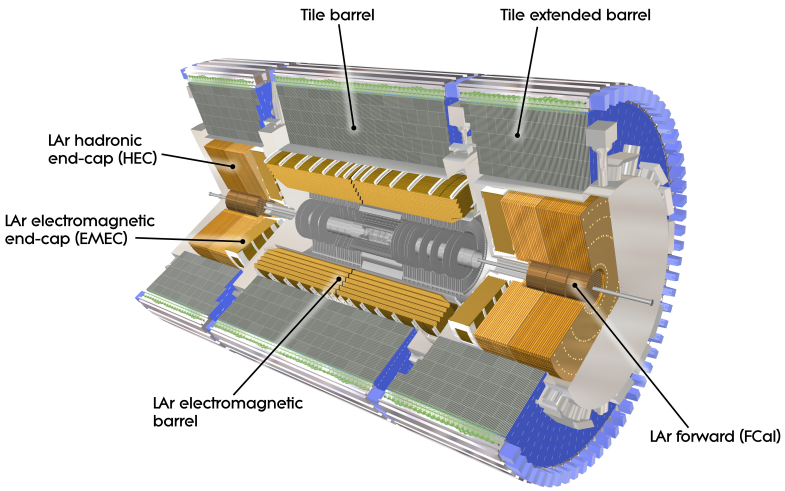

Figure 4.5: A schematic of the ATLAS calorimeters. [17].

The electromagnetic calorimeter is finely segmented for precision measurements of electrons and photons. The other calorimeters have a coarser granularity, which is sufficient for jet reconstruction and the calculation of missing transverse energy.

The depth of the electromagnetic calorimeter is greater than 22 radiation lengths in the barrel and 24 radiation lengths in the endcap. The hadronic calorimeter is 10 interaction lengths thick at $\eta = 0$. The thickness of the calorimeters ensures that both electromagnetic showers and hadronic jets are fully contained and well measured. Additionally, the depth of the calorimeters prevents particles from punching through to the muon system; the rate of hadronic punch-through is significantly below the rate of muons from decays in jets [62].

Table 4.5 summarizes the main parameters of the calorimeters in ATLAS.

Table 4.5: ATLAS Calorimeter parameters [62, 61, 108].

Component	Layers	Coverage	Granularity ($\Delta\eta \times \Delta\phi$)	Depth
EM Calorimeter				
Total	3 + presamp	$\|\eta\| < 3.2$	varies	22 X_0
Barrel				
Presampler	1	$\|\eta\| < 1.52$	0.025×0.1	10 mm
Layer 1 (strips)	1	$\|\eta\| < 1.475$	$\sim 0.003 \times 0.1$	4.3 X_0
Layer 2 (main)	1	$\|\eta\| < 1.475$	$\sim 0.025 \times 0.025$	16 X_0
Layer 3 (back)	1	$\|\eta\| < 1.475$	0.05×0.025	2 X_0
Endcap				
Presampler	1	$1.5 < \|\eta\| < 1.8$	0.025×0.1	4 mm
Layer 1 (strips)	1	$1.375 < \|\eta\| < 3.2$	$\sim 0.003 \times 0.1$	4.0 X_0
Layer 2 (main)	1	$1.375 < \|\eta\| < 3.2$	$\sim 0.025 \times 0.025$	20 X_0
Layer 3 (back)	1	$1.5 < \|\eta\| < 2.5$	0.05×0.025	2 X_0
Hadronic Tile Calorimeter				
Total	3	$\|\eta\| < 1.7$	varies	9.7-13.0 λ_0
Layer 1,2	2	$\|\eta\| < 1.7$	0.1×0.1	
Layer 3	1	$\|\eta\| < 1.7$	0.2×0.1	
LAr Hadronic End-Cap Calorimeter				
Low η Layers	4	$1.5 < \|\eta\| < 2.5$	0.1×0.1	9.7-12.5 λ_0
High η Layers	4	$2.5 < \|\eta\| < 3.2$	0.2×0.2	9.7-12.5 λ_0
Forward Calorimeter				
FCAL Layers	3	$3.1 < \|\eta\| < 4.9$	$\sim 0.2 \times 0.2$	9.5-10.5 λ_0

4.4.1 Electromagnetic Calorimeter

The electromagnetic calorimeters are built of an accordion-shaped sandwich with alternating layers of liquid argon and lead. Electrons and photons produce electromagnetic showers as they pass through the lead. The electrons and positrons in these showers ionize the liquid argon; kapton electrodes in the center of the liquid argon layer absorb the ionization electrons. The accordion shape of the layers forces electrons and photons to pass through many layers when traversing the detector, while allowing complete and uniform coverage in ϕ. A schematic of a portion of the barrel liquid argon electromagnetic calorimeter is shown in Figure 4.6.

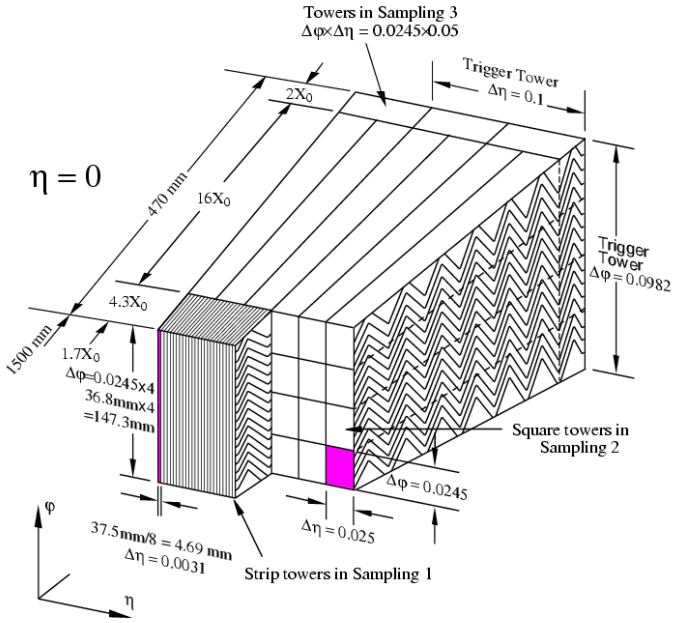

Figure 4.6: A schematic of the barrel ATLAS liquid argon electromagnetic calorimeter [17].

The liquid argon calorimeter has three sampling layers, along with a presampler. The amount of material which a particles passes through before reaching the

electromagnetic calorimeter is shown in Figure 4.4(b) as a function of η. The presampler detector consists of a thin layer of liquid argon and serves to correct the energy measurement for energy lost upstream of the calorimeter. The first layer of the electromagnetic calorimeter is finely segmented in η and is called the strip layer. The high position resolution enhances photon, electron, and neutral pion separation, as well as providing a precise position measurement in η for photons and for track matching for electrons. The second layer is 16 radiation lengths thick and designed to contain the electromagnetic shower. It provides the main energy measurement for photons and electrons. The third layer or back section aids in separating electromagnetic showers from hadronic showers and provides an estimate of energy leaked out of the electromagnetic calorimeter.

The energy resolution of the electromagnetic calorimeter is:

$$\frac{\sigma(E)}{E} = \frac{10\%}{\sqrt{E}} \oplus 0.7\% \tag{4.3}$$

where E is the energy of the cluster, $\sigma(E)$ is its resolution, and $\oplus$ represents a sum in quadrature. The constant noise is around 250 MeV per cluster. The signal from the electromagnetic calorimeter is read out in approximately 5 samples, each 25 ns long.

4.4.2 Hadronic Calorimeters

Hadronic calorimetry spans the range $|\eta| < 2.7$ using a variety of different technologies suited to the required resolution and radiation environment, both of which change as a function of η. In the range $\eta < 1.7$, the barrel hadronic calorimeter is composed of alternating tiles of iron and plastic scintillator. Hadronic showers are generated in the iron; the plastic scintillator produces a light signal proportional to

the number of minimum ionizing particles in the shower. The light from the shower is transmitted to photomultiplers via wavelength shifting optical fibers. The signal from the hadronic calorimeter has a time resolution of 50 ns.

Over the range $1.5 < |\eta| < 3.2$, the hadronic calorimeter is composed of alternating layers of liquid argon and copper. In the forward region, for $3.1 < |\eta| < 4.9$, the forward calorimeter provides a coarse energy measurement in a high radiation environment using a dense matrix of copper and tungsten filled with liquid argon.

The pion energy resolution of the hadronic calorimeter (including the electromagnetic contribution) in the barrel is:

$$\frac{\sigma(E)}{E} = \frac{55\%}{\sqrt{E}} \oplus 2.3\% \oplus \frac{3.2 \text{ GeV}}{E} \tag{4.4}$$

4.5 Muon Spectrometer

The muon spectrometer is the outermost layer of the ATLAS detector and it is designed to measure, with high precision, the momentum and position of charged particles up to $|\eta| < 2.7$ and to trigger on charged particles up to $|\eta| < 2.4$. All neutral hadrons, photons, and charged particles, except muons, which are produced in the proton-proton collision lose all their energy to electromagnetic or hadronic showers before reaching the muon spectrometer, leaving behind a bath of low energy neutrons and photons. The only high energy (> 1 GeV) particles that reach the muon spectrometer are neutrinos, which do not interact with the detector at all, and muons. Therefore, the muon spectrometer serves not only to measure the trajectory of muons but also to identify charged particles that make it to the spectrometer as muons.

The large-η precision coverage of the muon spectrometer is essential for efficiently reconstructing signals with multiple leptons, including $WZ \to \ell\nu\ell\ell$ events and the Higgs$\to$ $ZZ \to \ell\ell\ell\ell$ decay. For Higgs events, roughly two-thirds of leptonically decaying ZZ pairs include at least one lepton with $\eta > 1.4$ [89].

The ATLAS muon spectrometer is designed to provide a stand-alone measurement of muon momenta, which can be combined with an inner detector track to improve the resolution. The design goal of the muon spectrometer is to measure the momentum of a 1 TeV muon to within 10% accuracy. This would allow the identification of a narrow, heavy resonance that decays to muons with transverse momenta at the TeV scale, if such a particle exists. The expected muon momentum resolution, $\frac{\Delta p_T}{p_T}$, in ATLAS is shown in Table 4.6 for both standalone and combined muons. The measured muon momentum resolution is shown in Figure 4.7. The momentum is measured in a sample of $Z \to \mu\mu$ events [31]. Standalone muons are measured solely with the muon spectrometer; combined muons include information from the inner detector track. For muons with transverse momentum less than 50 GeV, the inner detector measurement dominates the measurement. For muons in the range $50 < p_T < 100$ GeV, both the muon spectrometer and the inner detector contribute significantly to the momentum measurement and uncertainty. For high p_T muons with transverse momentum above 100 GeV, the muon spectrometer measurement dominates.

The layout of the muon spectrometer is shown in Figures 4.8 through 4.12 . Monitored drift tubes (MDTs) provide precise measurements of the muon trajectory over most of the spectrometer coverage. In the inner layer of the endcap, the rate of interactions from neutrons and photons is too high for the MDTs, and the region between

Table 4.6: ATLAS muon momentum resolution. Expected muon momentum resolution, $\frac{\Delta p_T}{p_T}$, in ATLAS, for standalone (muon spectrometer only) and combined (muon spectrometer + inner detector track) muons. The expected momentum resolutions are shown for different momenta muons at example locations in the barrel ($\eta = 0$) and endcap ($\eta = 2$) [89].

	Resolution			
Muon momentum (GeV)	Standalone		Combined	
	$\eta = 0$	$\eta = 2$	$\eta = 0$	$\eta = 2$
$p = 10$	3.9%	6.4%	1.4%	2.4%
$p = 100$	3.1%	3.1%	2.6%	2.1%
$p = 1000$	10.5%	4.6%	10.4%	4.4%

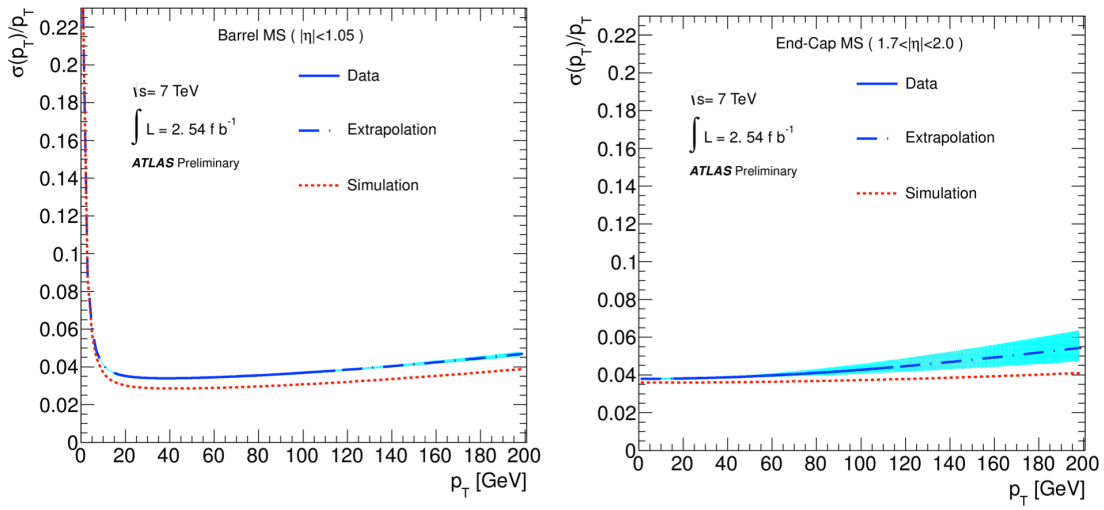

Figure 4.7: Measured muon momentum resolution, $\frac{\Delta p_T}{p_T}$, in ATLAS, for muons measured in the muon spectrometer [31].

$2.0 < |\eta| < 2.7$ is covered by Cathode Strip Chambers (CSCs) which provide precision tracking measurements. In the central region, the muon trigger is provided by Resistive Plate Chambers (RPCs). To handle the higher rate in the forward region, Thin Gap Chambers (TGCs) are used. There are three layers of precision (MDT or CSC) chambers over the full spectrometer, called the inner, middle, and outer *stations*, respectively. There are also three layers of trigger coverage. For the MDTs, RPCs, and CSCs, the azimuthal coverage is broken into 16 ϕ sectors. Eight *large* chambers span the area between the coils of the toroid and eight *small* chambers sit inside or on-top of toroid coils. The layout in ϕ is shown in Figure 4.12. The large and small chambers sit at different radi from the beam-line and overlap in ϕ to ensure complete coverage. The TGCs have a 12-fold ϕ symmetry. A summary of the parameters for each detector subsystem in the muon spectrometer is given in Table 4.7.

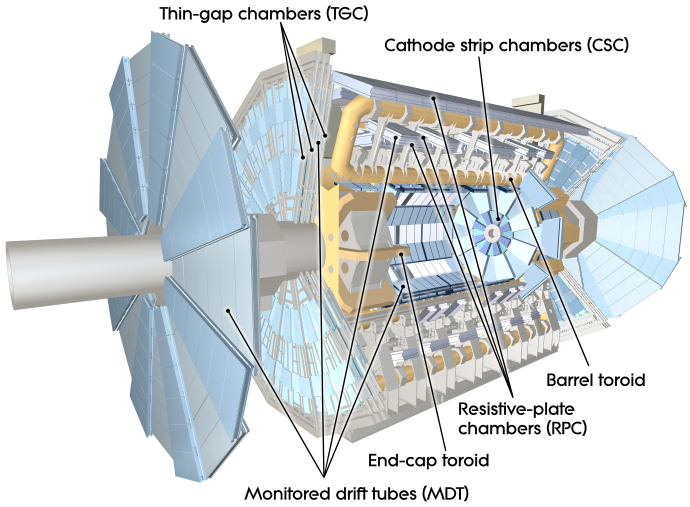

Figure 4.8: A schematic of the ATLAS muon system. [17].

Table 4.7: ATLAS muon spectrometer parameters [62, 61].

Parameter	MDT	CSC	RPC	TGC
η coverage	$\lvert\eta\rvert < 2.7$ (< 2.0 inner layer)	$2.0 < \lvert\eta\rvert < 2.7$ (inner layer)	$\lvert\eta\rvert < 1.05$	$1.05 < \lvert\eta\rvert < 2.7$ (< 2.4 trigger)
Primary function	tracking	tracking	trigger	trigger
Hits per track	20	4	6	9
Chambers	1150	32	606	3588
Channels	339,000	30,700	373,000	318,000
Resolution z/R (μm)	35 (z)	40 (R)	10,000 (z)	$\approx 3,000$ (R)
Resolution ϕ (mm)	-	5	10	≈ 5
Time resolution (ns)	-	7	2	4
Area (m^2)	5500	27	3650	2900

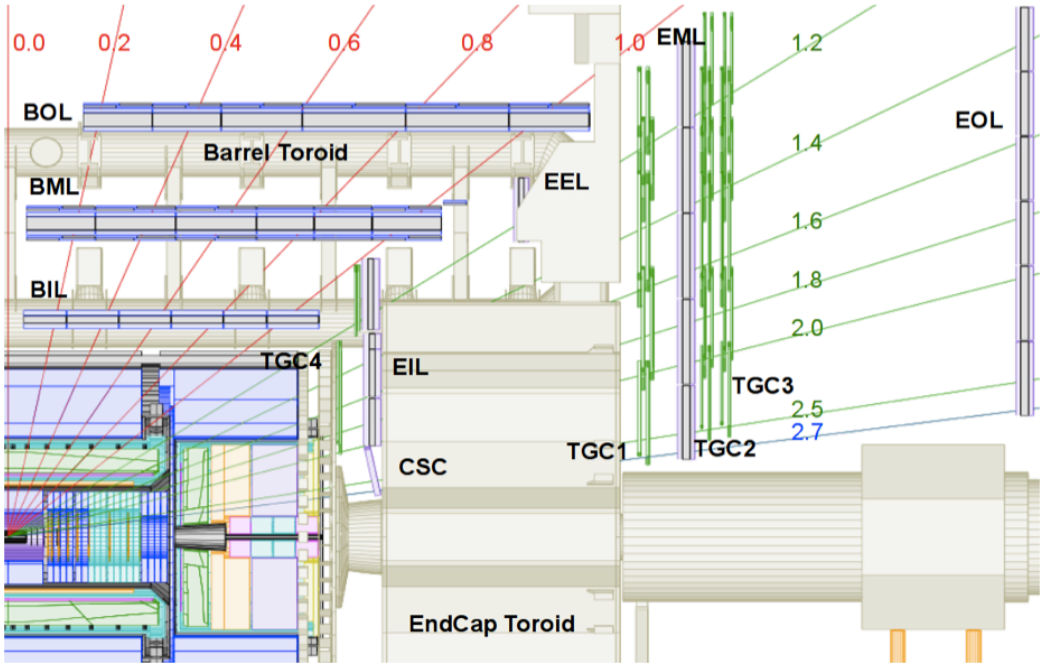

Figure 4.9: A schematic of the ATLAS muon system, showing where muons of a given η pass through the spectrometer for one quadrant of the detector where the beam-line is the x-axis. The MDT chambers are shown in light blue. In the barrel, the middle and outer layers include RPC chambers. The TGC chambers are shown in the endcap in green. The CSCs are shown in light blue in the inner endcap layer and are a slight angle to the interaction point. Only the large chambers are shown here.

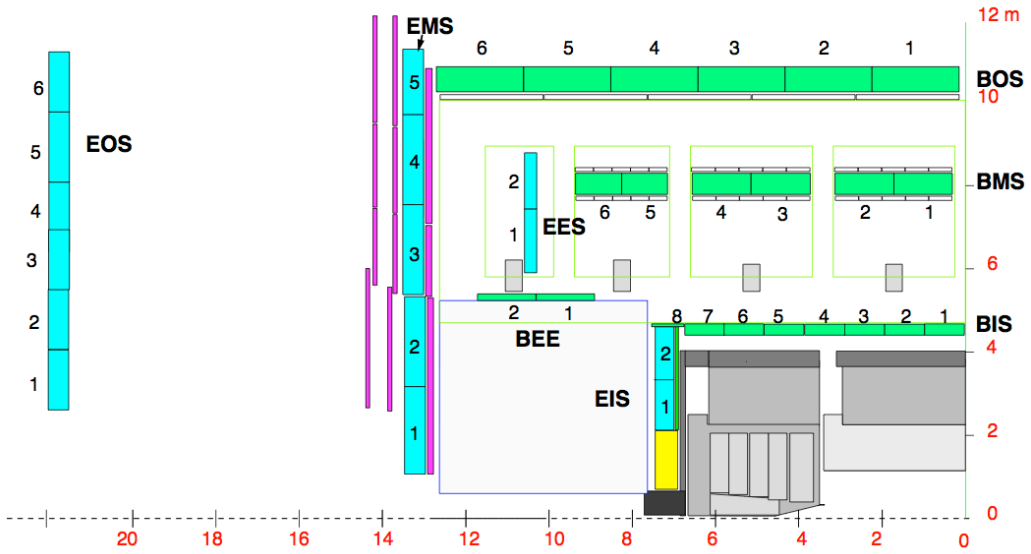

Figure 4.10: A schematic of the ATLAS muon system, for one quadrant of the ATLAS detector, which shows the location of small chambers in z and R. The beam-line runs along the x-axis. MDT chambers are shown in green in the barrel and in cyan in the endcap. The RPC chambers are shown in white and the TGC chambers are shown in magenta. The CSCs are shown in yellow.

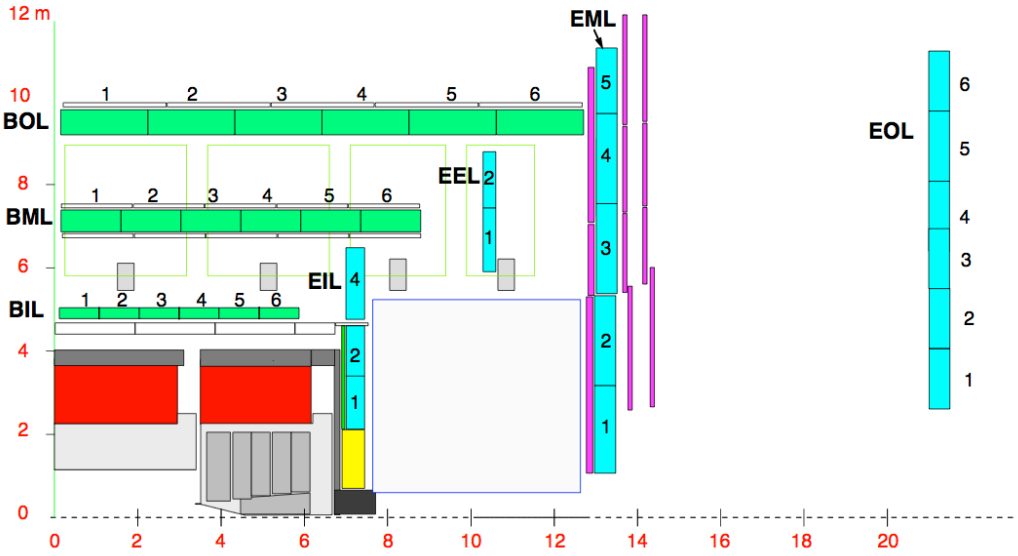

Figure 4.11: A schematic of the ATLAS muon system, for one quadrant of the ATLAS detector, which shows the location of large chambers in z and R. The legend is the same as Figure 4.10.

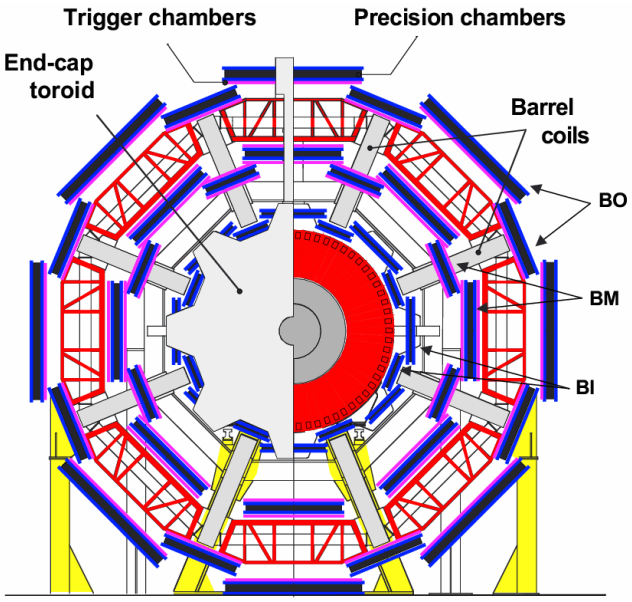

Figure 4.12: A schematic of the ATLAS muon system, looking in the x-y plane at the barrel MDT (blue) and RPC (pink) chambers. The chambers in between the toroid coils are called large chambers and the chambers centered on the coils are called small chambers.

4.5.1 Monitored Drift Tubes

To achieve the design goal of measuring the momentum of a 1 TeV muon with 10% resolution, the precision muon chambers must be able to measure a deviation from a straight path with a precision of 50 μm. Over most of the muon spectrometer coverage, the Monitored Drift Tubes (MDTs) provide this measurement.

The basic detection element of the MDTs are aluminum tubes with a diameter of 3 cm, with a 50 μm W-Re wire running down the center. The tubes are filled with a gas mixture of 93% Argon, 7% CO_2, and trace amounts of H_2O (300 parts per million). When a charged particle traverses an MDT tube, it ionizes the gas, and under an electric field provided by keeping the wire at 3,000 V and the wall of the tube at ground, the ionized electrons drift toward the central wire. Near the wire,

the electric field is strong enough to cause an electron avalanche, which produces a detectable current on the wire. Individual tubes have a maximum drift time around 750 ns and a resolution of around 80 μm.

Tracking a muon's trajectory through several layers of tubes in an MDT chamber improves the position resolution to 35 μm per chamber. The schematic of an MDT chamber is shown in Figure 4.13. MDT chambers are built of two *multi-layers* of 3-4 tubes each, with a gap between them. The inner stations have chambers with 8 total layers of tubes; the middle and outer stations have chambers with 6 layers of tubes.

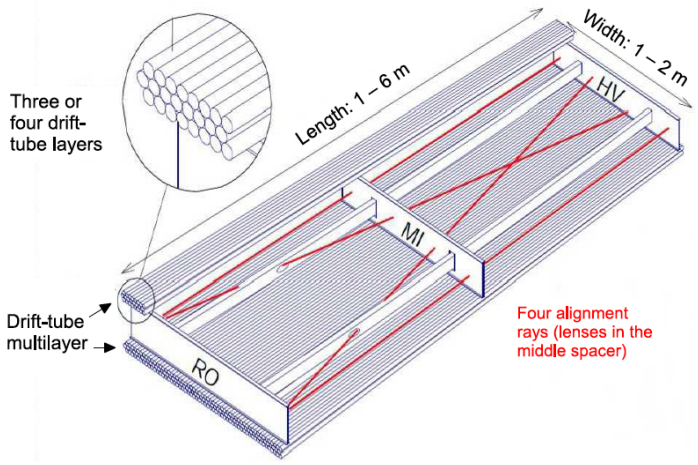

Figure 4.13: Layout of an MDT chamber [27]. The two multilayers containing three layers of tubes each are shown, along with the support structure and the optical alignment system (red lines) within the chamber.

In order to achieve 50 μm position resolution over the entire muon track, which passes through three muon chambers on average, the position of individual tubes, relative to each other, must be known to 30 μm accuracy over the whole spectrometer. This daunting alignment task is performed by an optical laser alignment system which continually monitors both the shape of an individual chamber to correct for deformations from temperature changes, gravitational sag, and the effect of the toroid

coils turning on and off, and the position of individual chambers with respect to fixed measurement points in the cavern.

The intrinsic resolution of the tubes and the knowledge of the alignment limit the momentum resolution for muons with momenta above several hundred GeV. The contributions to the muon momentum resolution are shown in Figure 4.14 for standalone muons, measured solely in the muon spectrometer. For muons with momentum between tens of GeV and several hundred GeV, multiple scattering dominates the resolution. For low p_T muons with transverse momentum below 20 GeV, fluctuations in energy loss before the muon enters the muon spectrometer are the dominant contribution.

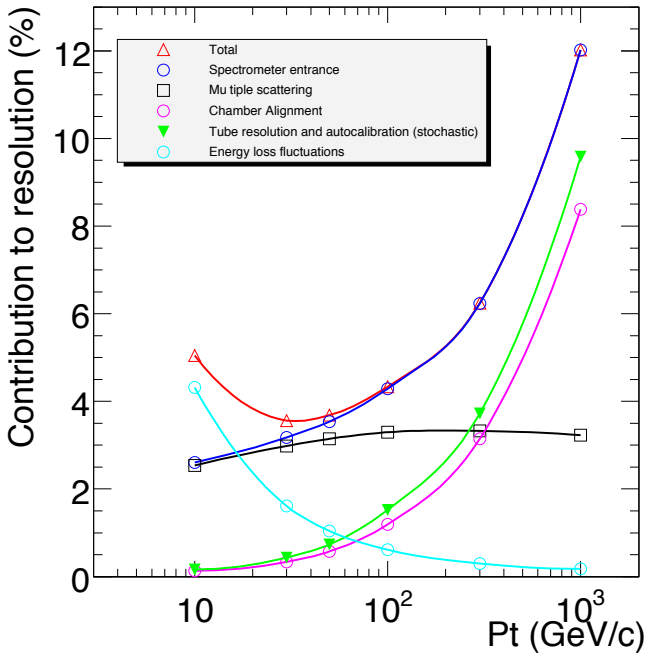

Figure 4.14: Contributions to muon momentum resolution for standalone muons measured solely with the muon spectrometer [21].

4.5.2 Cathode Strip Chambers

The maximum hit rate that individual MDT tubes can sustain is around 150 Hz/cm^2 due to limitations from the long drift-time and the readout electronics. At nominal luminosity, the rate of interactions from low-energy photons and neutrons was expected to reach this limit in the forward region of the inner endcap layer. Therefore, in the region of $2.0 < |\eta| < 2.7$ in the inner endcap layer, Cathode Strip Chambers (CSCs) are used instead of MDTs. The CSCs can be operated up to hit rates around 1000 Hz/cm^2, which is sufficient for the expected hit rates in this region.

The CSCs are multiwire proportional chambers whose wires are oriented in the radial direction. The chamber gas is 30% Ar, 50% CO_2, and 20% CF_4. The readout is provided by strips on both cathodes. One set of strips runs perpendicular to the wires and provides the precision η measurement; the other set of strips runs parallel to the wires and proves the ϕ coordinate. Each chamber therefore provides both an η and a ϕ measurement. There are four layers of CSC chambers on each side of the detector. The CSCs are installed in a tilted position so that tracks originating from the interaction point will be normal to the chambers.

4.5.3 Resistive Plate Chambers

The Resistive Plate Chambers (RPCs) provide muon triggers and a measurement of the ϕ position for muons passing through the barrel. Relative to the MDTs, they are fast (few ns time resolution) but spatially imprecise ($\approx$ 1 cm spatial resolution).

The basic unit is formed by two parallel resistive plates separated by 2 mm and filled with a gas mixture based on $C_2H_2F_4$. Electrons from primary ionization are

multiplied into an avalanche by an electric field of order 4-5 kV/mm. The signal is read out by metal strips on the outside of the chamber, which are capacitively coupled to signals inside the gas volume. One set of strips measures the ϕ coordinate and the other orthogonal set measures the η coordinate.

Each RPC chamber is made from two detector layers, providing two ϕ measurements and two η measurements per chamber. Two sets of RPC chambers sandwich the MDT chambers in the middle station of the spectrometer, and a third layer of RPC chambers rests against the inside of the MDT outer station chambers (see Figure 4.12).

4.5.4 Thin Gap Chambers

The Thin Gap Chambers (TGCs) provide the muon trigger and ϕ coordinate measurement for muons passing through the endcap. Compared to the RPCs, they have higher spatial resolution. This aids in separating hits from muons from neutron and photon background hits, which are significantly more numerous (a factor of 10 or more) in the endcap than in the barrel. The fine granularity is also important for ensuring accurate p_T thresholds for muon triggers, as muons which pass through the endcap have a much higher total momentum, p, than muons in the barrel for the same p_T. Finally, the three muon trigger stations are physically closer together in the endcap than in the barrel, and improved granularity is necessary to achieve the same level of p_T discrimination with a shorter lever arm [28].

The TGCs are a form of multiwire proportional chamber with an anode-wire pitch that is larger than the cathode-anode pitch. On the outside of the chambers,

there are readout strips perpendicular to the wires. Signals from both the wires and the strips are read out by the front-end electronics, providing a two-dimensional position measurement. The chamber is filled with a gas mixture of 55% CO_2 and 45% n-pentane. There are seven layers of TGC chambers in the middle station of the endcap, and two layers of chambers in the inner station. Only the middle station chambers provide information that is used by the Level 1 trigger.

Chapter 5

Reconstruction

This chapter summarizes the reconstruction of physics objects used in the WZ analysis, including inner detector tracks, vertices, muons, electrons, and missing transverse energy. Charged particles with $p_T > 400$ MeV produce inner detector tracks which are used in the reconstruction of electrons, muons, and vertices. Missing transverse energy is reconstructed from the calorimeters to identify particles which do not interact with the detector, including the neutrino from the W leptonic decay. The reconstruction of calorimeter-based missing transverse energy is modified with information from the muon spectrometer and with low p_T inner detector tracks. The detector performance in reconstructing muons and electrons is not covered in this chapter, but is discussed in Sections 7.2.2 and 7.2.3, respectively. The specific selections applied to muons and electrons in the WZ analysis are discussed in Sections 8.4 and 8.5.

5.1 Inner Detector Track Reconstruction

Inner detector tracks are reconstructed in ATLAS with several different algorithms, described in Reference [76]. The standard algorithm begins with hits in the silicon detectors and works from the center of the detector out to the TRT. This is called the *inside-out* algorithm. A second algorithm begins with hits in the TRT and works inward, looking for silicon hits that match the extrapolated TRT track. This is called the *outside-in* algorithm and is particularly useful for finding tracks that correspond to photon conversions and to secondary particles from the decay of primary particles [76]. As the WZ analysis requires only prompt electrons and muons, we will focus on the standard inside-out algorithm.

The first step in finding inner detector tracks is to construct three dimensional *space-points* for hits in the Pixel and SCT detectors. The pixel hits give three dimensional hit information automatically. Three dimensional information is obtained from SCT hits by combining information from hits in two orthogonal strips, as well as using the beam-spot as a constraint. These space-points are used to build track seeds. Pairs of space-points are matched to pre-built templates corresponding to tracks consistent with a given momentum and transverse impact range. Wide roads are built from the seeds and the templates; the roads define an η and ϕ range in which to look for additional hits to associate to the track-seed. The track-fitting procedure finds track candidates for about 10% of the track-seeds.

After the seeds and roads are formed, the space-points are no longer used; the track-fitting algorithm directly uses the raw hit information. Hits not associated to space-points can also be used in the track-fitting stage.

A track is built iteratively using the extended Kalman filter algorithm [90]. The Kalman filter algorithm works iteratively to fit the track and to identify which hits belong to the track. The algorithm fits the first set of hits to estimate track parameters and uncertainties. A prediction is then made about the location of the next hit. If a next hit is found whose χ^2 is consistent with the prediction, the hit is used to update the estimates of the track parameters, weighting the hit by its uncertainty. A prediction about the next hit is then made using the updated track parameters, and so forth until no more hits are found in the silicon detectors. Once a track candidate is formed, it is refit using a simulated detector geometry with detailed material description, necessary for simulating the effects of multiple scattering.

After track candidates have been formed from all possible seeds, ambiguities exist for hits which are associated to more than one track. To resolve these ambiguities, tracks are ranked according to the number of hits on each track, with different weights assigned to hits in different layers of the inner detector system. Tracks are penalized in the ranking if the track traverses an active sensor region where no hit is registered (called a track *hole*.) After all tracks have been scored, ambiguous hits are given to the track with the higher rank. All tracks are then refit, and tracks with too low a ranking are dropped.

The tracks are extrapolated to the TRT system, and a search is made for TRT hits within a road consistent with the extrapolated silicon track. The TRT hits do not change the silicon track parameters at this stage. If TRT hits are found, the entire track is refit with all associated hits; at this stage, silicon hits can be flagged as outliers. If the combined track has a higher rank than the silicon track alone, the

refit combined track is saved. If the silicon track has a higher rank than the refit track, the associated TRT hits are stored as outliers and the silicon track parameters are kept.

The *baseline* requirements in 2011 for a reconstructed inner detector track are:

- $p_T > 400$ MeV
- $|\eta| < 2.5$
- ≥ 7 hits in the silicon detectors
- ≤ 2 holes in the Pixels

The number of tracks reconstructed per event depends on the number of collisions per event, μ. The effect of pile-up on the reconstruction of inner detector tracks is discussed in Reference [41]. The number of baseline reconstructed tracks in an event is shown in Figure 5.1(a) separately for data with an average μ of 15, 29, and 32. For events with $\langle\mu\rangle = 15$, an average of 11.8 tracks per collision are reconstructed. For events with $\langle\mu\rangle = 32$, an average of 13.2 tracks per collision are reconstructed. Increasing the hit requirements on inner detector tracks to require ≥ 9 silicon hits and no holes in the pixel detector produces a track whose reconstruction rate is less sensitive to μ, called a *robust* track. The rate of reconstructed robust tracks is 10.3 tracks per collision and is independent of μ up to at least 32 collisions per crossing. The efficiency of reconstructing an inner detector track is defined as the fraction of of primary particles with $p_T > 400$ MeV and $|\eta| < 2.5$ which are matched to a reconstructed track in simulation. For the baseline tracks, this efficiency is between 70% and 90% as a function of η, as shown in Figure 5.1(b). The efficiency is comparable

for an event with 1 collision as for an event with 40 collisions. The efficiency for robust tracks is approximately 5% lower than the baseline track efficiency.

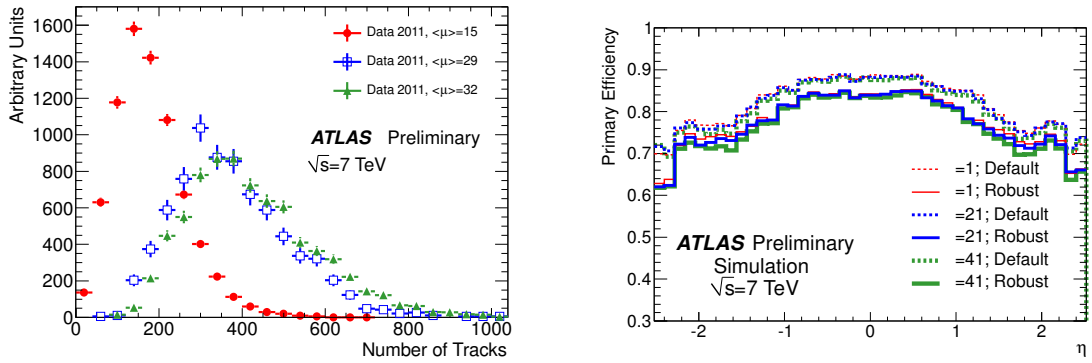

Figure 5.1: The number of inner detector tracks (left) in data and the inner detector track efficiency (right) from simulation. Both plots show distributions for datasets with different μ values. The number of inner detector tracks is shown for the baseline requirements on inner detector tracks. The efficiency is shown separately for baseline tracks (Default) and for more stringent hit requirements on the tracks (Robust.) [41]

In the WZ analysis, baseline inner detector tracks are used to reconstruct electrons and muons. Baseline tracks are also used in the calculation of missing transverse energy. Additional hit requirements are placed on the tracks associated with electrons (see Section 5.4) and to inner detector tracks used in muon reconstruction (see Section 8.4.)

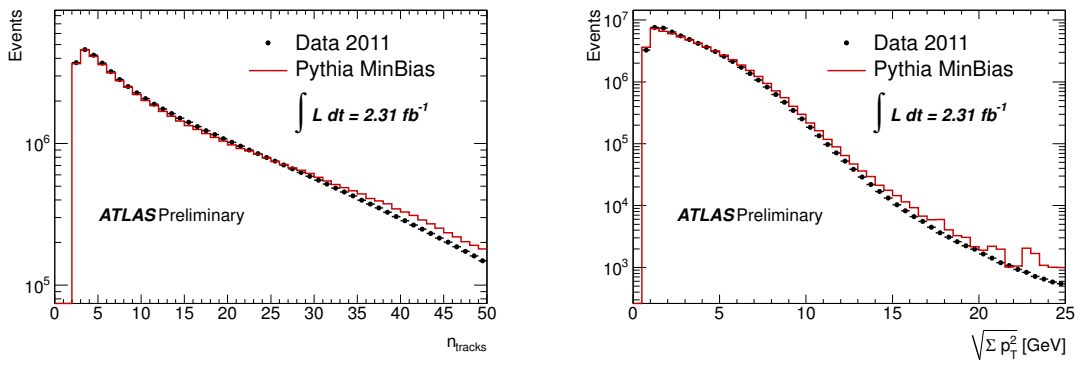

Figure 5.2: The distribution of the number of tracks (left) and the sum p_T of tracks (right) per reconstructed vertex in data and simulation. The simulation is a Pythia 6 minimum bias sample [122].

5.2 Vertex Reconstruction

The reconstruction of vertices in ATLAS is discussed in Reference [22]. Vertices are found using an iterative vertex finding approach. Seed vertex positions are obtained by looking for the global maximum in the distribution of z coordinates of tracks. Starting with the seed position, nearby tracks are combined to form a vertex, and an iterative χ^2 fit is made to the vertex as additional tracks are included. Outlying tracks are penalized with a low weight, and the vertex is refit. The down-weighting continues for a fixed number of iterations. If a track is incompatible with the vertex by more than 7σ, it is used to seed a new vertex. The procedure is performed until no new vertices can be found. All vertices with at least 2 associated tracks are stored. If there are multiple vertices in a single event, the vertex with the highest $\sum p_T^2$ calculated for all associated tracks is considered the primary vertex.

The resolution on the vertex position depends on the number of tracks associated to the vertex and on the $\sum p_T^2$ of the associated tracks. For an event with only a few

tracks with momentum just above the tracking threshold, the resolution on the x, y and z vertex position is on the order of 1 mm. For a vertex with $\sqrt{\sum p_T^2} > 8$ GeV, the resolution is around 30 μm for the x, y vertex position and around 50 μm for the z vertex position. The vertex resolution as a function of the $\sqrt{\sum p_T^2}$ of the associated tracks is shown in Figure 5.3 for both the x and z vertex positions. The y resolution looks very similar to the x resolution and is not shown.

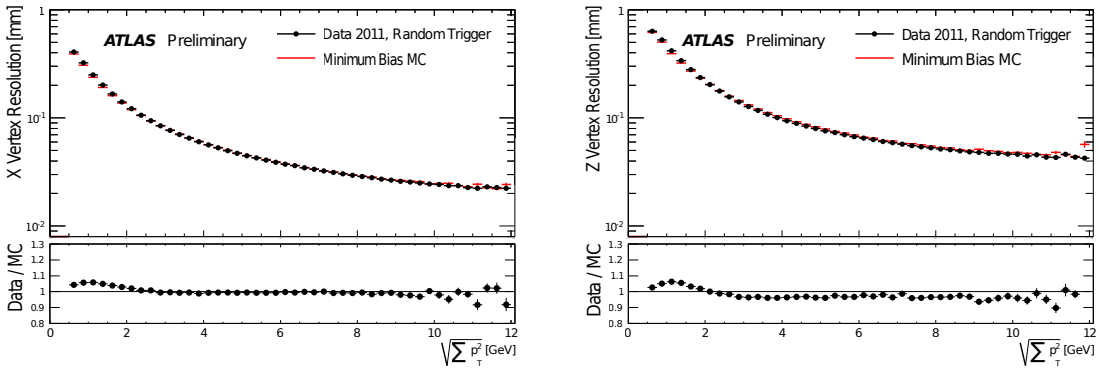

Figure 5.3: The vertex x (left) and z (right) resolution as a function of the $\sqrt{\sum p_T^2}$ of tracks fitted to the vertex. Each vertex has at least 3 associated tracks [122].

The scatter of vertex location is shown in Figure 5.4 for one particular run. The RMS of the vertex position gives an estimate of the size of the beam spot. For this run, the RMS is 15.7 μm in the x direction, 13.5 μm in the y direction, and 56 mm in the z direction.

For events with multiple collisions per crossing, the number of vertices should be a linear function of the number of collisions. For reconstructed vertices, this is true in data up to events with an average of 15 collisions. For events with more than 15 collisions, the vertex reconstruction efficiency suffers as tracks and vertices begin to overlap. This can be seen in Figure 5.5, which shows the number of reconstructed

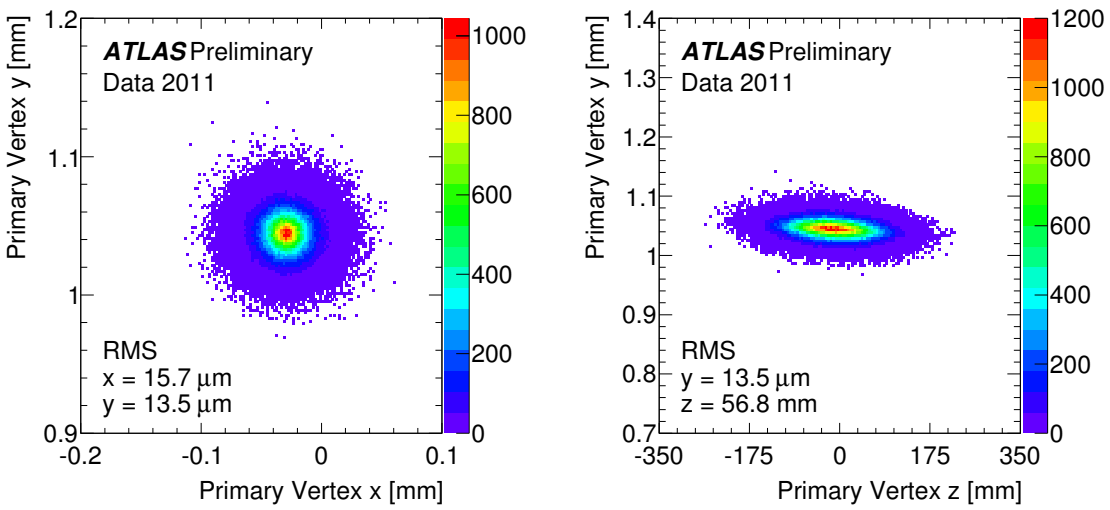

Figure 5.4: The two dimensional distribution of reconstructed primary vertices with at least 3 associated tracks in the transverse plane (left) and the y versus z plane (right) for one run in 2011. There is a 0.08 mrad tilt about the x-axis, shown here, whereas there is a 0.5 mrad tilt about the y-axis (not shown) [122].

vertices in data versus the average number of collisions per event. A linear fit is performed from $\mu = 1$ to $\mu = 11$ and extrapolated to higher values of μ. As is discussed in Section 7.2.1, only a few percent of the 2011 dataset has more than 15 average collisions per event. Therefore, the vertex reconstruction inefficiency at higher pileup is not a concern for this analysis.

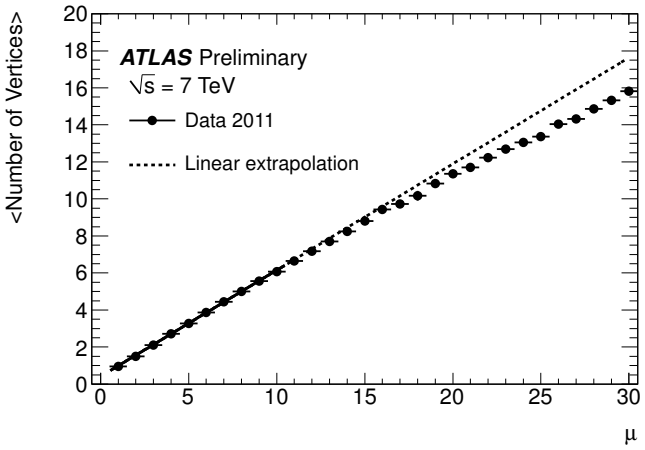

Figure 5.5: The distribution of the average number of reconstructed vertices as a function of the average number of interactions per bunch crossing [122].

5.3 Muon Reconstruction

5.3.1 Overview

The identification of muons and the measurement of their position, charge, and momentum is based on information from the inner detector and the muon spectrometer, with input from the calorimeters for certain cases. There are two separate classes of algorithms for reconstructing muon tracks in the ATLAS detector: STACO [130] and MUID [4]. Although the algorithms differ, the performances are quite similar, and the choice of which algorithm to use is fairly arbitrary. We use the STACO set of algorithms for the WZ analysis, which is discussed below. More details can be found in References [114], [112], and [82].

There are several challenges in reconstructing muon tracks in the ATLAS muon spectrometer. First, the toroidal magnetic field traversed by muons in the spectrometer is inhomogeneous, and analytical descriptions of the tracks cannot simply model

the trajectories. Second, the large separation between measurement stations results in extrapolation uncertainties. Finally, there is no true three dimensional hit information, as the precision MDT and CSC chambers are physically separated from the RPC and TGC trigger chambers which measure the phi coordinate.

Tracks in the muon spectrometer are reconstructed in several stages. First, hits in the MDT tubes are calibrated. For each individual tube, a timing constant, t_0, is subtracted from the recorded hit time. The t_0 is the timing offset for a hit from a prompt particle, relative to the crossing from which the particle came, for each individual tube due to signal delays on cables and the time of flight it takes for the particle to reach the tube from the interaction point. After subtraction of the t_0, the time of a hit is a function of the radius at which it traversed the tube. A radius-time relationship called the *r-t* function is used to convert the time measurement to a radius in the tube, known as a *drift circle*. The r-t function is a function of the tube's gas mixture, temperature, pressure, electric field, and magnetic field. Calibration constants for the r-t functions are calculated on a run-by-run basis for different regions in the MDTs. An example of the MDT r-t function is shown in Figure 5.6.

After converting hits to drift circles, sets of drift circles consistent with a straight line are identified in individual chambers. These short, straight tracks are called *segments*, and their reconstruction is discussed below. Next, several segments from different stations of the spectrometer are combined to form a track, and the track parameters are extracted from a fit to all hits on the track. The fit function is a helix modified by parameters that allow the muon to change its momentum and direction in areas of dense material. The five track parameters η, ϕ, transverse im-

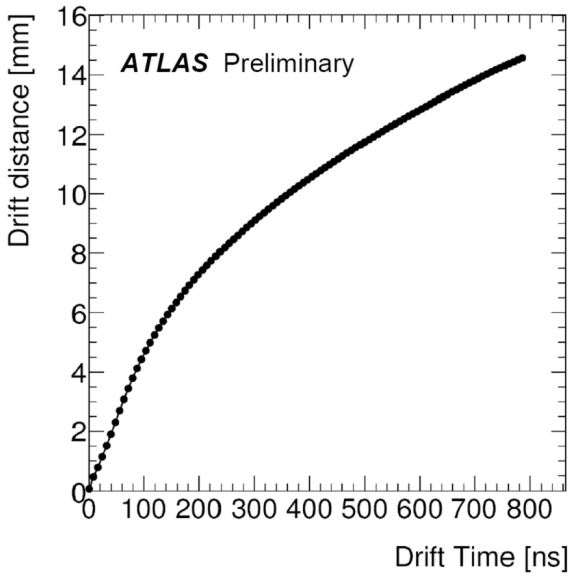

Figure 5.6: The MDT radius-time (rt) function.

pact parameter d_0, longitudinal impact parameter z_0, and track curvature q/p are all expressed in three locations: at the entrance to the muon spectrometer, at the origin of the detector, and at the primary vertex of the event. The extrapolation of the muon spectrometer track to the origin or primary vertex is calculated using a parametrization of energy loss in the calorimeters as a function of the muon's position and momentum. Multiple scattering is accounted for with a detailed simulation of the material in the detector.

If an inner detector track can be matched to the muon spectrometer track, a combined muon is formed from a combination of the respective track parameters. For muons with $p_T < 50$ GeV, the inner detector track dominates the measurement of momentum due to the strong solenoid magnetic field and the fact there is less material in and before the inner detector than in and before the entrance of the muon spectrometer, so energy loss fluctuations are smaller in the inner detector.

For muons with $p_T > 100$ GeV, the muon spectrometer track dominates a muon's momentum measurement, as the long lever arm of the spectrometer increases the small sagittas of high momenta muons. The resolution at high momenta is limited by the internal alignment of the muon spectrometer, knowledge of the magnetic field, and the intrinsic resolution of the MDT tubes, including calibrations. In the intermediate range $50 < p_T < 100$ GeV, both the muon spectrometer measurement and the inner detector measurement contribute roughly equally to the combined track's momentum, and the resolution is limited by multiple scattering.

5.3.2 STACO Muons

There are three types of reconstructed muons in the STACO class, differing in whether the main momentum measurement comes from the muon spectrometer, the inner detector, or from a combination of inputs from both detectors:

- *Standalone muons*: tracks are reconstructed by the *Muonboy* algorithm in the Muon Spectrometer. The track parameters are extrapolated to the beam line through the simulated detector geometry with average energy loss information.

- *Segment-tagged muons*: inner detector tracks are extrapolated to the muon spectrometer. The *MuTag* algorithm identifies a muon candidate if a segment in the muon spectrometer can be associated to the extrapolated track.

- *Combined muons*: If a match can be made between an inner detector track and a standalone muon reconstructed by Muonboy, the STACO algorithm makes a statistical combination of the two tracks and computes new track parameters.

The name STACO, which stands for STAtistical COmbination, is given to the algorithm which combines inner detector tracks and tracks in the muon spectrometers. However, STACO is also used to describe the set of reconstructed muons which are based on the Muonboy algorithm, including segment-tagged and standalone muons.

Segment Reconstruction

Segment reconstruction begins with pairs of MDT drift circles in regions of interest in the muon spectrometer in which a muon trigger fired. All four lines which are tangential to the two drift circles are formed. The lines are required to match roads which point back to the interaction point; if one line does not, it is dropped. The tangent lines are extrapolated through all other tube layers in the MDT station. If there is a hit in a tube through which the segment passes, it is preliminarily added to the segment. Segments can be formed with hits in multiple chambers in the same station. This happens, for example, at the overlap region between the small and large chambers, where a single muon could pass through 12 (in the middle and outer stations) or 18 (inner station) tubes.

After all possible MDT hits have been added, all segment candidates with fewer than 3 MDT hits are dropped. A straight line fit through all hits on the remaining segment candidates is performed. Rather than using a pure χ^2 to measure the quality of the fit, the Muonboy algorithm has a "penalty factor", χ^2_p, which takes into account the fact that a genuine muon hit might be masked by a hit from a delta ray which passes closer to the wire than the muon does. To account for this possibility, hits with drift radii that are smaller than the other tubes prefer are penalized less than

hits with larger drift radii. Hits which worsen the χ^2_p of the segment are dropped at this stage [114].

Next, trigger hits are added to the segment. If a trigger hit sits on a straight line with the track, it provides ϕ information. The ϕ information allows improved calibration of the drift-times because the position of a hit along the length of the tube changes the signal propagation time. The position of the hit along the tube can also change the Lorentz angle on account of the rapidly changing magnetic field. If a trigger hit is added to the segment, the MDT drift circles are recalculated and the segment is refit. If no trigger hits can be matched, 5 different ϕ positions are tested, and the result with the best χ^2_p is kept, taking advantage of the signal propagation time down the MDT wire.

Muonboy creates two classes of segments. *Strict* segments must have at least 3 MDT hits, two of which must be in different multilayers, and at least one trigger hit. An example of a *strict* segment is illustrated in Figure 5.7. After all *strict* segments are found, hits which are not associated to *strict* segments are used to build *loose* segments, which only require 3 MDT hits which can all be in one multilayer. Because the inner layer of the barrel spectrometer does not have trigger chambers, all segments in the inner layer are *loose*.

Track Reconstruction and Fit

Starting from strict segments in the middle and outer layers of the spectrometer, a rough estimate of the muon momentum can be made using the position and direction of the segment and the assumption that it came from the interaction point. Using

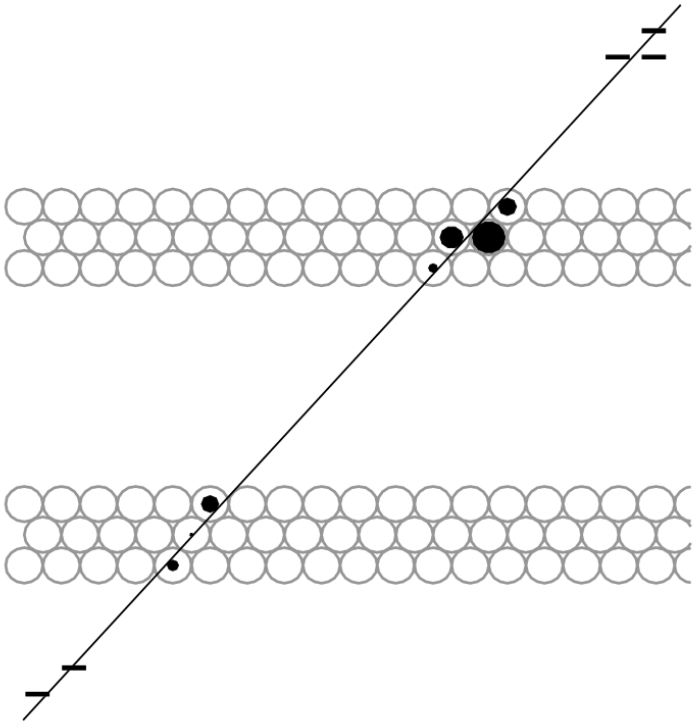

Figure 5.7: An example of a *strict* STACO muon segment with hits in both multi-layers of the MDTs and associated trigger hits [82].

this preliminary estimate, the track's trajectory through the magnetic field to the other layers of the spectrometer is extrapolated. If a matching segment is found in the next station, it is added to the original segment to make a track candidate. The momentum estimate is refined, and a new extrapolation is made to the third station, again checking for segments that can be added to the track candidate. At this stage, a track candidate is only kept if it contains at least two segments in different stations.

A fit is then performed using the hits from all segments associated to the track candidate. Hits which are inconsistent with the track, given their χ^2_p, are dropped. Finally, the track is adjusted to include corrections for energy the muon might lose in traversing the spectrometer. If the trajectory passes through a dense area, a *scattering center* is created in which the muon track is allowed to lose energy and change its direction. The scattering angle is a free parameter in the final fit, and the energy loss is parametrized. Between 3 and 5 scattering centers are allowed per track. A final fit is performed using full hit information as well as the scattering centers. Tracks with a poor χ^2_p are not kept.

Combined Muon Fit

If an extrapolated track from the muon spectrometer matches an inner detector track, a combined muon candidate is formed. Combined muons use information from both the inner detector and the muon spectrometer to improve the muon momentum resolution. Rather than performing a new fit with information from both detectors, the STACO statistical combination directly calculates combined track parameters from the inner detector and muon spectrometer track parameters. The combined

track parameters, P, with covariance matrix C, are derived from the track parameters of the inner detector track and the muon spectrometer track, P_{ID} and P_{MS}, as well as their respective covariances, C_{ID} and C_{MS}:

$$\begin{aligned} (C_{ID}^{-1} + C_{MS}^{-1}) \times P &= C_{ID}^{-1} \times P_{ID} + C_{MS}^{-1} \times P_{MS} \\ C &= (C_{ID}^{-1} + C_{MS}^{-1})^{-1} \end{aligned} \tag{5.1}$$

A χ^2 is also calculated from the track parameters, and tracks with a good χ^2 are kept as combined muons.

Segment-Tag Muons

After combined muons are formed, unused inner detector tracks and individual segments not used in a stand-alone track can be used to form *segment-tag* muons. To form a segment-tag muon, an inner detector track must match to one segment in the inner layer of the spectrometer. Around the transition region at $|\eta| = 1.2$, a muon could pass through the spectrometer without traversing any chambers in the inner layer. In this region, segment-tag muons can consist of an inner detector track paired with a segment in the middle or outer layer. For segment-tag muons, the track parameters are taken from the inner detector track. Segment-tag muons are useful for increasing the efficiency for selecting muons in the transition region and for low p_T muons which may not make it beyond the first layer of the spectrometer.

There are also *calo muons* built from inner detector tracks and calorimeter energy depositions consistent with a muon, but these are not used in the WZ analysis. Calo muons have a relatively high fake rate and are especially useful only for very low p_T muons which do not make it to the first layer of the spectrometer, and for muons at

$\eta = 0$ where there are no muon chambers.

5.4 Electron Reconstruction

The reconstruction of electrons in ATLAS is discussed in Reference [35] and summarized here. Electron reconstruction is factored into two pieces: cluster reconstruction and electron identification. In cluster reconstruction, calorimeter clusters and tracks are loosely matched to build objects that are consistent with electrons. In the identification process, more stringent selections are placed on the reconstructed objects to reject backgrounds from jets and photons.

The reconstruction of electrons in the central part of the detector, $|\eta| < 2.47$, uses the *sliding window* algorithm [110]. After pedestal subtraction, the total transverse energy deposited in all three layers of the calorimeter is summed longitudinally into calorimeter *towers*. The size of the tower is set by the 0.025×0.025 $\eta \times \phi$ granularity of the middle layer of the electromagnetic calorimeter. A *window*, or search area, is 3×5 $(\eta \times \phi)$ calorimeter towers. If the total transverse energy in a window, summed across all calorimeter towers, is a local maximum and is greater than 2.5 GeV, a seed calorimeter *cluster* is formed. The position of the seed cluster is computed as the energy-weighted η and ϕ center of the cluster's cells. For electrons with $p_T > 15$ GeV from W or Z decays, the efficiency of seed cluster formation is 100% in simulation.

Once a seed cluster is formed, the cluster is rebuilt using 3×7 towers in the barrel and 5×5 towers in the endcaps. The cluster energy is calculated by summing four contributions:

- Estimated energy deposit in material in front of the calorimeter

- Measured energy deposit in all towers in the cluster
- Estimated energy deposit outside the cluster (lateral leakage)
- Estimated energy deposit after the electromagnetic calorimeter (longitudinal leakage)

The estimated terms are parametrized as a function of the measured energy in the pre-sampler, the separate measured energy in all three layers of the electromagnetic calorimeter, and the number of collisions in the event. The estimation is based on detailed simulation of energy deposition in active and inactive regions of the detector.

To count the reconstructed cluster as an electron, an extrapolated inner detector track must be matched to the position of the cluster within $\Delta\eta < 0.05$. The *phi* matching conditions are asymmetric, relative to the bending direction of the electron, due to the fact that if the electron radiates a photon, its bending radius will only decrease. The track must align with the calorimeter cluster within $\Delta\phi < 0.1$ in the bending direction, and $\Delta\phi < 0.05$ on the other side. If there are multiple matched tracks, preference is first given to tracks with hits in the silicon detectors, and then to the track with the smallest $\Delta R = \sqrt{\Delta\phi^2 + \Delta\phi^2}$ distance to the seed cluster. The energy of the electron candidate is taken from the calorimeter cluster measurement corrected by estimations from simulation, and the η and the ϕ are taken from the matched track parameters. The transverse energy E_T is calculated as:

$$E_T = \frac{E_{cluster}}{\cosh(\eta_{track})} \tag{5.2}$$

Once electrons are reconstructed, further selection requirements are imposed to increase the purity of the sample and reject fake electrons from jets, pions, or photons.

This process is called electron *identification*. On ATLAS, these selection requirements are grouped into three distinct categories: *loose++*, *medium++*, and *tight++* electrons. The categories are designed to reject fake electrons with powers of roughly 500, 5000, and 50,000, respectively. The variables used in the identification requirements are shown in Table 5.1 for all three categories. The values corresponding to the calorimeter selection requirements are calculated in 10 bins of cluster η and 11 bins of cluster E_T. The selection values for an electron with $\eta \approx 0$ and with $40 < E_T < 50$ GeV are shown in Table 5.2.

The loose++ identification places requirements on the deposited energy and shower shape in the middle layer of the electromagnetic calorimeter to ensure that the cluster is consistent with an electron shower. Requirements on the energy leakage into the hadronic calorimeter reduce contamination from hadronic jets. Requirements on the shower energy and width in the strip layer of the electromagnetic calorimeter, as well as requirements on the track quality and the match between the track and the cluster position reduce the photon and π^0 contamination and ensure that the electron position is well measured.

For an electron to pass the medium++ identification, it must pass the full loose++ selection, and must pass many of the loose++ selection variables with tighter requirements. Additional shower shape and shower width variables in the strip layer of the electromagnetic calorimeter are used in the selection of medium++ electrons. To reduce the number of photon conversions in the sample, a hit is required on the first layer of the pixel detector (the B-layer.) Finally, to discriminate between charged pions and electrons, a requirement is placed on the ratio of the number of TRT hits

passing the high threshold to the total number of TRT hits.

For an electron to pass the tight++ identification, it must pass the full medium++ selection, and must pass many of the medium++ selections with tighter requirements. Additional requirements are placed on the match between the track and the cluster (including on the ratio of cluster energy to track momentum), the total number of TRT hits, and an explicit veto is placed on the electron if it is matched to a converted photon candidate.

Figures 5.8 through 5.13 show distributions of variables used in electron identification for electrons from $Z \to ee$ decays in both data and simulation. These plots are from the 2010 dataset and simulation, and the agreement between data and simulation is improved in the 2011 dataset due to improvements of the simulation material description, the alignment of the inner detector, and improvement in energy calibrations in data from increased $Z \to ee$ statistics in data.

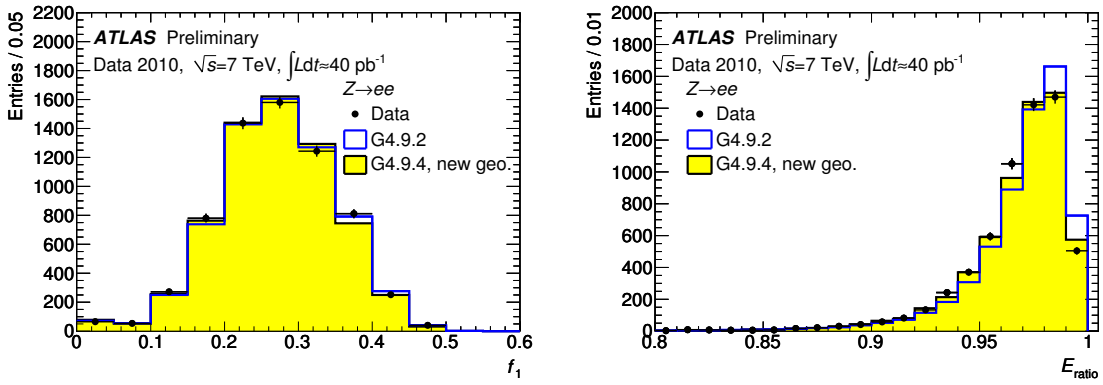

Figure 5.8: Calorimeter layer 1 energy variables used in electron reconstruction and identification, shown for electrons in $Z \to ee$ events. The left plot shows the fraction of cluster energy in layer 1. The right plot shows the distribution of energy difference between the strips of highest and second highest energy divided by the sum. G4 refers to GEANT4 simulation. The "new geo" was an improved geometry introduced in 2010 [20].

Table 5.1: Electron identification variables for each of the three categories: loose++, medium++, and tight++.

Category	Selection	Description	Name
Loose++	Acceptance	$\|\eta\| < 2.47$	η
	Hadronic Leakage	Ratio of E_T in the first layer of the hadronic calo to the E_T of the EM cluster	R_{had1}
		Ratio of E_T in hadronic calo to E_T of the EM cluster	R_{had}
	Middle layer of EM calo	Ratio of energy in 3×7 cell to the energy in 7×7 cells centered at cluster position	R_η
		Lateral shower width within 3×5 window of cells: $\sqrt{(\sum E_i\eta_i^2)/(\sum E_i) - ((\sum E_i\eta_i)/(\sum E_i))^2}$, where E_i is energy and η_i is η of cell i	$w_{\eta 2}$
		Energy deposited in middle layer	E_2
	Strip layer of EM calorimeter	Shower width: $\sqrt{(\sum E_i(i - i_{max})^2)(\sum E_i)}$, where i runs over strips in window of $\Delta\eta \times \Delta\phi = 0.0625 \times 0.2$, and i_{max} is index of highest-energy strip	w_{stot}
		Energy difference between max and 2nd max energy deposits	E_{ratio}
	Track-cluster matching	$\Delta\eta$ between cluster position in strip layer and track	$\Delta\eta$
	Track quality	Number of hits in the pixels	n_{pixel}
		Number of total hits in the pixels + SCT detectors	n_{si}
Medium++	Loose++	Tighter selections on loose++ variables	
	Strip layer of EM calorimeter	Fraction of EM calo energy in first strip layer	f_1
		Energy difference between strip energy of first minimum and second maximum of cluster	ΔE_s
		Shower shape in shower core in first sampling	f_m
		Shower width in strips, weighted by distance from shower max	$w_{\eta 1c}$
	Track quality	Distance of closest approach to primary vertex	A_0
	TRT	Ratio of high threshold to all TRT hits	f_{HT}
	Conversions	Require hits on the b-layer of the pixel	$n_{B-layer}$
Tight++	Medium++	Tighter selections on medium++ variables	
	Track-cluster matching	$\Delta\phi$ between cluster position in strip layer and the extrapolated track	$\Delta\phi$
		Ratio of energy of cluster over momentum of track	E/p
	TRT	Number of hits in the TRT	n_{TRT}
	Conversions	Veto if match to reconstructed photon conversions	

Table 5.2: Typical electron selection requirement values

Variable	Loose++ Selection	Tight++ Selection
R_{had}	< 0.011	< 0.008
R_{η}	> 0.920	> 0.930
w_{η^2}	< 0.011	< 0.011
w_{stot}	< 2.80	< 2.27
E_{ratio}	> 0.80	> 0.835
Δ_{η}	< 0.015	< 0.005
n_{pixel}	≥ 1	≥ 1
n_{si}	≥ 7	≥ 7
$\|d_0\|$	-	< 1
f_{HT}	-	> 0.08
$n_{B-layer}$	-	≥ 1
Δ_{ϕ}	-	$-0.03 < \Delta_{\phi} < 0.015$
E/p	-	$0.70 < E/p < 3.0$
n_{TRT}	-	≥ 18

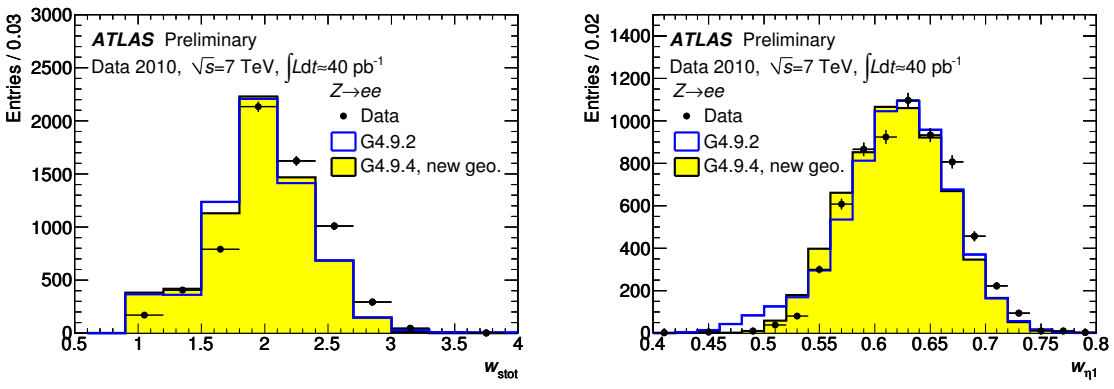

Figure 5.9: Calorimeter layer 1 shower width variables used in electron reconstruction and identification, shown for electrons in $Z \rightarrow ee$ events. The left plot shows the shower width determined in a window corresponding to the cluster size. The right plot shows the distribution of core shower width measured over ± 1 strip around the strip with maximum deposited energy [20].

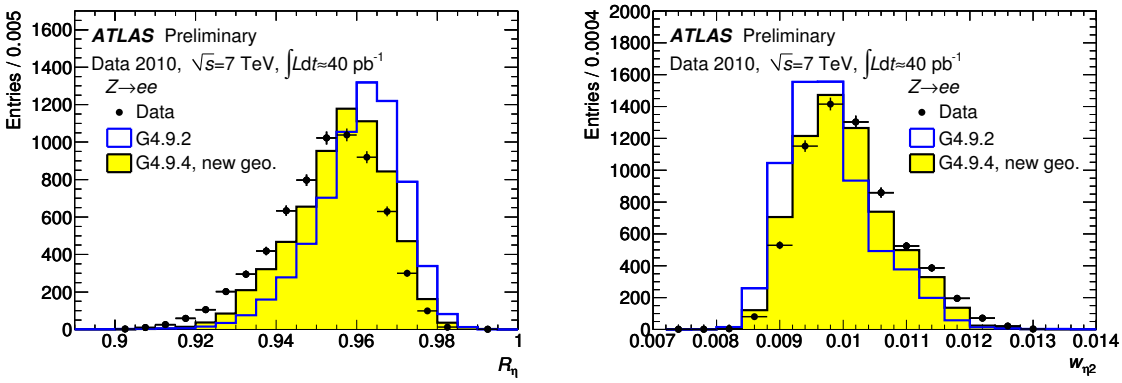

Figure 5.10: Calorimeter layer 2 variables used in electron reconstruction and identification, shown for electrons in $Z \rightarrow ee$ events. The left plot shows the ratio of energy in a cluster size corresponding to 3 eta cells by 7 phi cells with respect to the energy in a cluster size 7 by 7 cells. The right plot shows the distribution of shower width calculated with a window of 3 by 5 cells using the energy weighted sum over all cells [20].

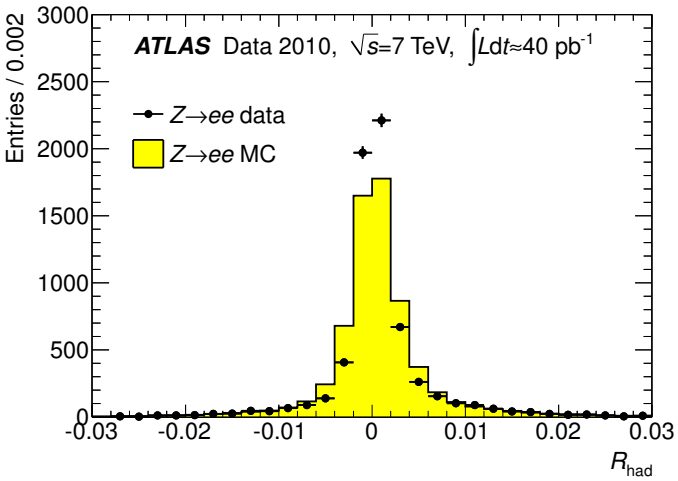

Figure 5.11: The distribution of the fraction of electron energy deposited in the hadronic calorimeter shown for electrons in $Z \rightarrow ee$ events [35].

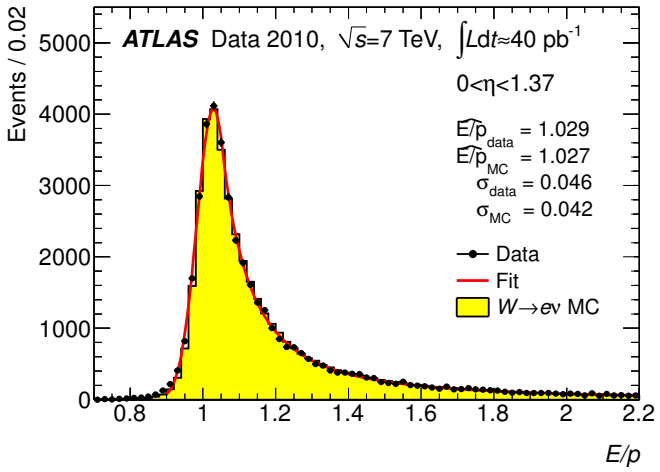

Figure 5.12: The ratio of calorimeter cluster energy to track momentum for a selection of barrel electrons in selected $W \to e\nu$ events. The most probable value and the Gaussian width of a fitted Crystal Ball function are given for both data and simulation [35].

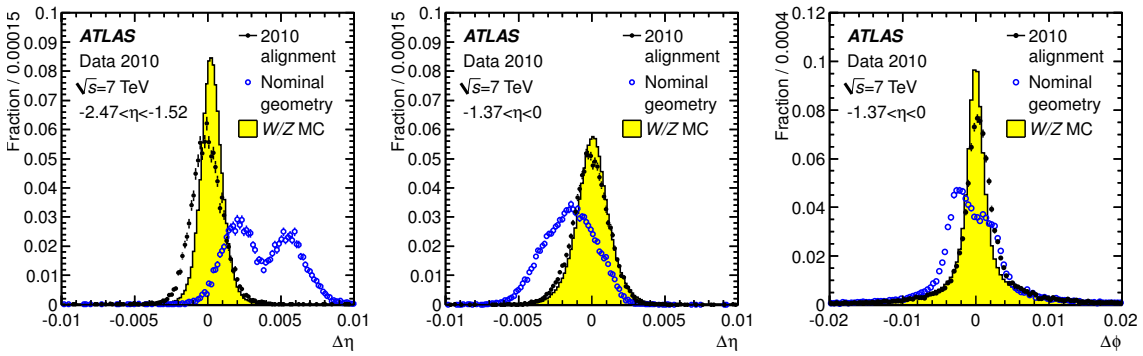

Figure 5.13: Track matching variables used in electron identification and reconstruction, shown for electrons in $Z \to ee$ and $W \to \mu\nu$ events. The $\Delta\eta$ distribution between the calorimeter cluster and the reconstructed track is shown for endcap electrons (left) and barrel electrons (center), and the $\Delta\phi$ distribution is shown for barrel electrons (right). The "nominal geometry" was the detector description in place at the start of LHC data-taking; the "2010 alignment" used data to improve knowledge of the alignment of the different inner detector sub-systems [35].

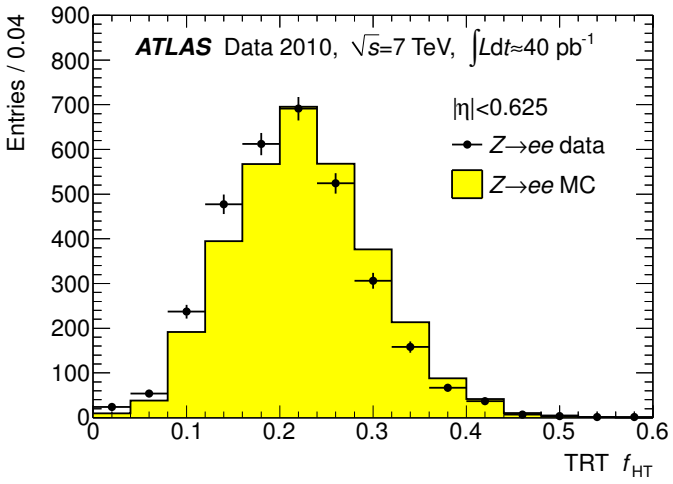

Figure 5.14: The distribution of the fraction of high-threshold hits in the TRT for electrons selected in $Z \to ee$ events [35].

The efficiency of the electron reconstruction and identification selections are discussed in Section 7.2.3. The reconstruction efficiency is close to 95% for $Z \to ee$ electrons with $15 < E_T < 50$ GeV within $|\eta| < 2.5$. The identification efficiency, given a reconstructed electron, varies from 75% for tight++ electrons to above 95% for loose++ electrons. The identification efficiency as a function of the number of reconstructed vertices in the event is shown in Figure 5.15 for the loose++, medium++, and tight++ identifications separately. The pileup dependence of the efficiency is discussed in Section 7.2.1.

5.4.1 Electron Scale Calibration

The energy scale calibration of electrons in the electromagnetic calorimeter is performed in several steps. These are described in detail in Reference [35], and the discussion is summarized here. The baseline electronic scale is determined with test-beam measurements, with an uncertainty around 3% due largely to uncertainties in

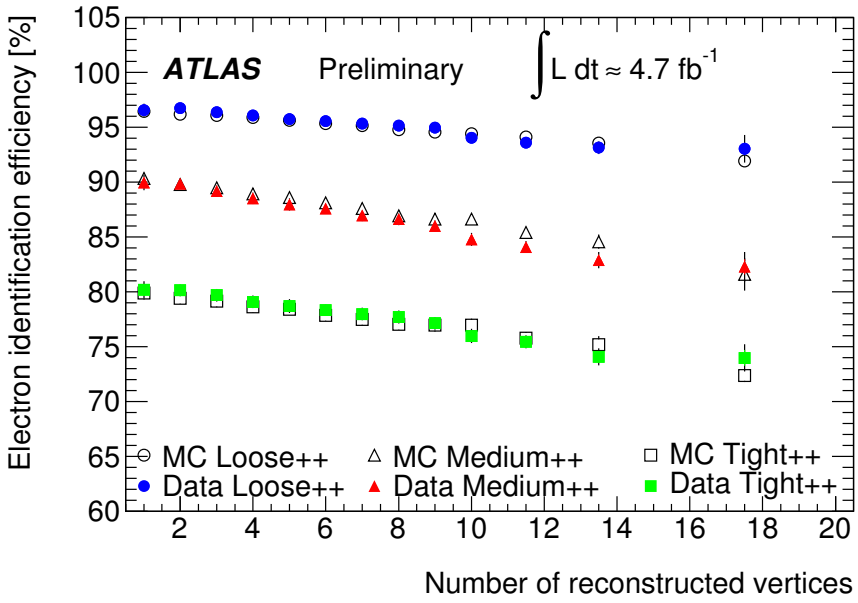

Figure 5.15: The efficiency of selecting an electron given a reconstructed calorimeter cluster and a good quality track pointing to it for electrons with $20 < E_T < 50$ GeV as a function of the number of reconstructed vertices per event. The identification efficiency is calculated using a $Z \to ee$ sample in data and simulation and is shown separately for loose, medium, and tight electron selection criteria [20].

transferring the team-beam results to the ATLAS detector. This calibration is used to convert the raw signal extracted from each cell in ADC counts into a measurement of deposited energy. Corrections based on simulation are applied to electromagnetic clusters to correct for energy loss due to absorption in passive detector material as well as lateral leakage out of the cluster. Finally, $Z \to ee$ decays are used in data to improve the calibration of the energy scale, and a data-derived correction is applied to electrons. This correction procedure is described below.

Corrections to the energy scale are derived in dielectron events with an invariant mass between 80 and 100 GeV. For these events, the known Z mass and shape is used to correct the measured energy scale. For each electron, the residual miscalibration is parametrized as a function of the electron η with 26 η bins:

$$E^{measured} = E^{true}(1 + \alpha_\eta) \tag{5.3}$$

where E^{true} is the true electron energy, $E^{measured}$ is the measured energy, and α_η are η-dependent correction factors. The α_η correction factors are determined from a fit to data across all $Z \to ee$ pairs that minimizes the log-likelihood:

$$-\ln L = \sum_{i,j} \sum_{k=1}^{N_{ij}^{events}} -\ln L_{ij}\left(\frac{m_k}{1 + (\alpha_i + \alpha_j)/2}\right) \tag{5.4}$$

where i and j are indices denoting the η regions under calibration (one for each electron in the $Z \to ee$ pair), N_{ij}^{events} is the total number of events in that region, m_k is the measured di-electron mass in a given decay, and $L_{ij}(m)$ is a probability distribution function which quantifies the compatibility of an event with the Z boson line-shape, obtained from simulation. The calibration constants are within 2% in the central region and within 5% in the forward region. These constants are used to

correct the measured energy of electrons in data.

Once the corrections have been applied to the measured electron energy, the ratio between measured and true electron energy is on the order of 1-2% for central electrons [35]. The $Z \to ee$ invariant mass distribution for calibrated electrons in data and electrons in simulation in Figure 7.9.

The energy-scale calibration is cross-checked with $J/\psi \to ee$ decays using the known J/ψ mass, as well as with $W \to e\nu$ decays by comparing the measured track momentum with the measured energy deposition in the calorimeter.

5.5 E_T^{miss} Reconstruction

The missing transverse energy, E_T^{miss}, used in this analysis is calculated from energy deposits in calorimeter cells which are calibrated with information from the reconstructed objects to which they are associated. Muons reconstructed in the muon spectrometer and inner detector tracks also enter into the missing transverse energy calculation. This calibrated missing transverse energy is called *Ref Final* and its reconstruction is detailed in Reference [24].

The reconstructed missing energy is calculated in the x and y directions in the calorimeter and in the muon spectrometer:

$$\vec{E}_{x(y)}^{\text{miss}} = \vec{E}_{x(y)}^{\text{miss, calo}} + \vec{E}_{x(y)}^{\text{miss},\mu} \tag{5.5}$$

The magnitude, E_T^{miss} and azimuthal angle, ϕ^{miss} of the missing transverse energy is

calculated as follows from the x and y components:

$$E_T^{\text{miss}} = \sqrt{(\vec{E_x}^{\text{miss}})^2 + (\vec{E_y}^{\text{miss}})^2}$$
$$\phi^{\text{miss}} = \arctan(E_y^{\text{miss}}/E_x^{\text{miss}}) \tag{5.6}$$

The calorimeter contribution to the missing energy is calculated over each cell of the calorimeter which is part of a topological cluster for cells within $|\eta| < 4.5$. Clusters are seeded by cells which have energy deposits greater than 4 times the width of the Gaussian noise term for that cell. Neighboring cells with energy greater than twice the noise threshold are added, and finally the neighboring cells of all accumulated cells are added. Only cells which are part of a cluster contribute to the missing energy calculation to suppress noise contributions. The calorimeter cell term is defined as:

$$\vec{E}_x^{\text{miss, calo}} = -\sum_{i=1}^{N_{cell}} E_i \sin\theta_i \cos\phi_i \hat{x} \quad \vec{E}_y^{\text{miss, calo}} = -\sum_{i=1}^{N_{cell}} E_i \sin\theta_i \sin\phi_i \hat{y} \tag{5.7}$$

The calibration of each cell is based on the association of reconstructed object to calorimeter cluster. Calorimeter cells are associated to a parent reconstructed object in the following order: electrons, photons, hadronically decaying tau leptons, jets, and muons. If a cluster is not associated to any of the preceding physics objects, it is considered in the *Cell Out* term. After calibrating the energy scale of the cluster based on its parent object, the calorimeter term of the missing energy is calculated as:

$$\vec{E}_{x(y)}^{\text{miss, calo}} = \vec{E}_{x(y)}^{\text{miss},e} + \vec{E}_{x(y)}^{\text{miss},\gamma} + \vec{E}_{x(y)}^{\text{miss},\tau} + \vec{E}_{x(y)}^{\text{miss, jets}} + \vec{E}_{x(y)}^{\text{miss, softjets}} + \vec{E}_{x(y)}^{\text{miss, calo},\mu} + \vec{E}_{x(y)}^{\text{miss, CellOut}} \tag{5.8}$$

where each term is calculated from the negative sum of its calibrated cell energies, as described in Equation 5.7 and E_i, θ_i, and ϕ_i are the energy, polar angle, and azimuthal angle of the calorimeter cells. The reconstructed objects are:

- $\vec{E}^{\text{miss},e}_{x(y)}$, $\vec{E}^{\text{miss},\gamma}_{x(y)}$, and $\vec{E}^{\text{miss},\tau}_{x(y)}$ are reconstructed from cells in electrons, photons, and taus with $p_T > 10$ GeV

- $\vec{E}^{\text{miss, jets}}_{x(y)}$ is calculated from cells in jets with $p_T > 20$ GeV reconstructed with the anti-k_T algorithm with a cone of $\Delta R = 0.6$ and calibrated with the jet energy scale calibrations

- $\vec{E}^{\text{miss, softjets}}_{x(y)}$ is reconstructed from cells in jets with $7 < p_T < 20$ GeV reconstructed with the anti-k_T algorithm with a cone of $\Delta R = 0.6$ and calibrated with the hadronic scale calibrations

- $\vec{E}^{\text{miss, calo},\mu}_{x(y)}$ is reconstructed from cells associated with energy loss by muons in the calorimeters

- $\vec{E}^{\text{miss, CellOut}}_{x(y)}$ is calculated from cells in clusters and inner detector tracks not associated to any other reconstructed object. If one or more reconstructed tracks with $p_T > 400$ MeV are associated to the cluster, the (sum of) track momentum is used instead of the cluster energy.

The muon contribution to the missing energy is taken from muons with both an inner detector and muon spectrometer track within $|\eta| < 2.5$, and from muons with a stand-alone muon spectrometer track for muons with $2.5 < |\eta| < 2.7$. The muon contribution is:

$$\vec{E}^{\text{miss},\mu}_{x(y)} = -\sum_{\text{selected muons}} \vec{p^{\mu}}_{x(y)} \tag{5.9}$$

and it is calculated slightly different for isolated muons and non-isolated muons, where a non-isolated muon is one that is within $\Delta R = \sqrt{\Delta\eta^2 + \Delta\phi^2} < 0.3$ from a reconstructed jet. For isolated muons, the p_T is determined from the combined track

parameters of the inner detector and muon spectrometer track. For isolated muons, the $\vec{E}_{x(y)}^{\text{miss, calo},\mu}$ term is not added to the calorimeter missing energy to avoid double counting. For non-isolated muons, the muon-spectrometer measurement is taken as the muon p_T.

The resolution of missing transverse energy is studied in $Z \to \mu\mu$ and $Z \to ee$ events in which there is no true missing transverse energy, except in rare events (1%) in which a b or c quark decay in a jet produces an energetic neutrino. In Figure 5.16, the reconstructed missing transverse energy in $Z \to \mu\mu$ events in shown. As seen in Figure 5.16, the distribution between data and simulation matches well. The amount of missing transverse energy is dependent on the number of collisions in the event, as discussed in Section 7.2.1.

The resolution of the missing transverse energy can be quantified as a function of the total transverse energy in the event, $\sum E_T$, which is the scalar sum of the energy of all calorimeter cells associated to clusters within $|\eta| < 4.5$. In $Z \to \ell\ell$ events, the resolution of the x and y missing energy components is estimated from the width of the distributions in bins of $\sum E_T$, assuming that the true value is zero. The E_x^{miss} and E_y^{miss} resolutions are shown in Figure 5.17 for $Z \to ee$ and $Z \to \mu\mu$ events separately. The resolution is fit with the function: $k\sqrt{\sum E_T}$, and k is found to be 0.66 in electron events and 0.67 in muon events. In a typical WZ event, the missing transverse energy resolution is around 15 GeV. This is large, but it is not problematic for our analysis because we do not make any measurements based on distributions of the W boson. Rather, we extract information about the anomalous triple gauge couplings from the transverse momentum of the Z boson in the event.

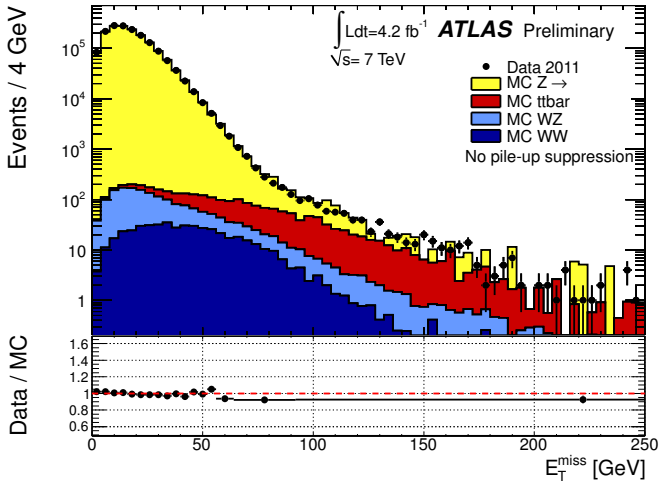

Figure 5.16: The distribution of E_T^{miss} in selected $Z \to \mu\mu$ events [39].

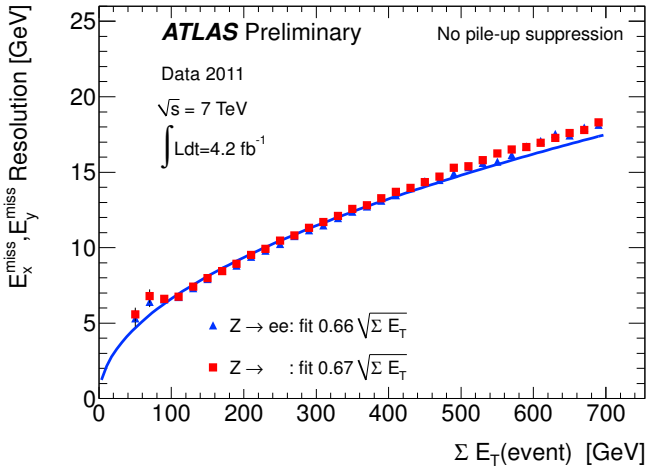

Figure 5.17: The x and y resolution of E_T^{miss} in selected $Z \to ee$ events (blue dots) and $Z \to \mu\mu$ (red dots) events. The resolution of the two E_T^{miss} components is fit with a $k\sqrt{\sum E_T}$ function and the fitted curve is drawn for the $Z \to ee$ resolution (blue line). The values for k are also shown on the figure [39].

Chapter 6

Trigger

The ATLAS trigger operates during data-taking to keep the data stream written to disk a manageable size and to preferentially record interesting events. On average, only one out of every million collisions is recorded, and the trigger system is responsible for determining which collisions are saved for further analysis offline. The ATLAS trigger scheme is summarized in Section 6.1. We look for $WZ \to \ell\nu\ell\ell$ events in the data sample in which a single muon or electron passed the trigger selection. The muon trigger is described in Section 6.2 and the electron trigger in Section 6.3. Details on the trigger selection of WZ events, including the trigger efficiency and corrections to the efficiency calculated in simulation, are presented in Section 6.5.

6.1 ATLAS Trigger Scheme

The nominal luminosity of the LHC is 10^{34} cm^{-2} s^{-1}, which corresponds to a spacing between proton bunches of 25 ns and an average of about 20 collisions per

crossing. In 2011, the highest luminosity that the LHC achieved in normal data taking was about 4×10^{33} cm^{-2} s^{-1} and the bunch spacing was fixed at 50 ns. This corresponds to a 20 MHz event rate and a 400 MHz collision rate. The event rate is the rate at which the LHC bunches cross inside the ATLAS detector. The detector triggers and records information per event. In each event, there may be multiple collisions, and the collision rate is the total rate of inelastic proton-proton collisions. The final data written to disk is limited by offline storage capacity and offline computing power [61], and is restricted in practice to between 200 and 400 Hz (exceeding the original design goal of 100 Hz.) The trigger system is responsible for selecting, within a few seconds, the one out of every million collisions, on average, that is recorded.

The ATLAS trigger system is broken into three stages: *Level 1* (LV1), *Level 2* (LV2), and *Event Filter* (EF). At each stage, the selection of events is refined and the output rate is reduced. The trigger decision chain is summarized in Figure 6.1.

The Level 1 trigger has 2 μs, including delays due to signal transmission, to make a trigger decision and must reduce the collision rate of 400 MHz to an output rate of 75 kHz. The longest time-of-flight and cable delays are in the TGC system and leave under 0.5 μs to make a decision. The extremely short decision time limits the data that can be used in making the trigger decision as well as the technology that can be used to process the decision. In the MDTs, for example, a full 2.5 μs of data is read out for a single event – this information can not be included in the Level 1 trigger decision. Likewise, although the inner detector is read out quickly, track finding is a relatively slow process and is not a part of the first level trigger decision. Moreover, the time it would take to move all the relevant data to a computer, process the event,

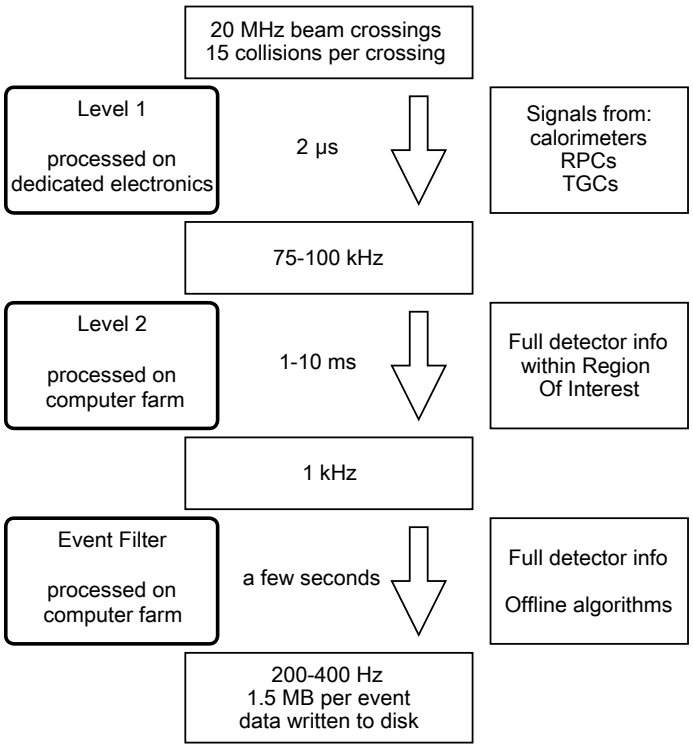

Figure 6.1: ATLAS trigger scheme. The three levels of the trigger system – Level 1, Level 2, and Event Filter – are shown along with the latency of the trigger step and the input and output data rate.

and return a decision is longer than a few microseconds. Therefore, dedicated custom electronics processes the Level 1 trigger information as close as possible to the relevant sub-detectors.

The sub-detectors capable of triggering at Level 1 are: the RPCs, TGCs, electromagnetic calorimeter, and hadronic calorimeter. The Level 1 trigger decision is made locally by each triggering sub-detector system – in the same event, the muon system and the calorimeters could each flag a Level 1 trigger, without knowing about the other. The Level 1 trigger objects are: muons, electromagnetic clusters, hadronic tau decays, jets, missing transverse energy, and total scalar energy. The granularity of the trigger objects is larger at Level 1 than at further trigger stages.

While the Level 1 decision is being processed, data is read out from all sub-detectors and stored in 2.5 μs buffers. If the trigger decision is to keep the event, a Level 1 trigger accept is issued to all sub-detectors, and the data from the full detector is read out. Data from the detector is divided into η and ϕ sections called *Regions of Interest* (ROIs) and in general only the data from the Region of Interest associated to a Level 1 trigger item is examined at Level 2. This allows for faster processing, as the Level 2 trigger has about 10 ms to make a decision and must reduce the event rate to a few kHz. For triggers involving missing transverse energy or the total energy in an event, data from the full calorimeter region must be used. At the Level 2 decision stage, information from the inner detector is added to muon, electron, or tau candidates found by the RPCs, TGCS, or calorimeters.

After an affirmative Level 2 trigger decision, data from the full event is transferred to the Event Filter. The Level 2 and Event Filter trigger decisions are made in

the same computing cluster located in the ATLAS counting room. Within a few seconds, on average, the Event Filter decides whether or not to keep an event based on information from the full detector and reconstruction algorithms based on the full offline reconstruction. The Event Filter reduces the event rate to the final 200-400 Hz rate.

6.2 Muon Triggers

6.2.1 Muon Level 1 Trigger

Level 1 triggers are found in the RPCs and TGCs by matching hits to pre-defined roads. Several roads with different widths are used, and the width of the road determines the minimum p_T threshold of muons whose hits are contained within the road. The hits from both a low p_T and a high p_T muon would be matched to a wide road. Only the hits from a high p_T muon would be fully contained by a narrow road.

In the barrel, the RPC station closest to the interaction point, in the middle barrel station, is called the *pivot plane*. In the endcap, the TGC station farthest from the interaction point, in the outer endcap, is designated the pivot plane. If trigger hits are found in the pivot plane, a straight line is drawn through the hit, the nominal interaction point, and the other trigger stations. Around this line, a window is defined in which to look for coincidence hits in the two other trigger stations, called *confirm* planes. The wider the window, the lower the p_T threshold. Depending on the trigger item, there must be a coincidence of hits in two stations (the pivot plane plus one confirm plane) or in all three stations to fire a Level 1 trigger.

The two Level 1 muon trigger items used in this analysis are described below:

- *L1_mu10* A level 1 trigger item with a p_T threshold corresponding to 10 GeV or higher. In the barrel, the trigger requires a 2-station coincidence and in the endcap, a 3-station coincidence is required. This was the lowest un-prescaled Level 1 single muon trigger for the first part of 2011.

- *L1_mu11* A level 1 trigger item with a p_T threshold corresponding to 10 GeV or higher. Unlike the L1_mu10 trigger, a 3-station coincidence is required in both the barrel and endcap.

6.2.2 Event Filter Muon Algorithm

The Muon Girl (MuGirl) algorithm was used as the primary event filter algorithm in data taking in 2011. MuGirl is also available as an offline muon reconstruction algorithm.

The main feature of MuGirl that distinguishes it from the Muonboy and Moore algorithms used primarily in offline reconstruction is that it begins with tracks in the inner detector and works "inside-out." [114] Inner detector tracks are extrapolated to the entrance of the muon spectrometer, and a road in η and ϕ is created around the extrapolated track. In the inner layer of the spectrometer, the algorithm searches for MDT hits within the road, and if it finds them, a segment is fit. TGC hits are included in the endcap inner layer. The segment is used to refine the track parameters, and the road is extrapolated to the middle layer of the spectrometer, where the process is repeated, including RPC hits in the barrel. The road is extrapolated to the outer layer, where segments are again built from hits within the road.

After segment-fitting and hit association is finished, a set of pre-calibrated neural network functions are applied to see if the pattern of segments and hits is consistent with a muon. If the candidate passes this test, a global fit of the complete track is performed, in which information from both the inner detector and muon spectrometer is used.

6.2.3 Muon Triggers

The Event Filter level muon triggers used in this analysis are described below:

- *EF_mu18_MG*: A single muon trigger based on the Muon Girl Algorithm which selects muons with $p_T > 18$ GeV. This trigger is seeded by the L1_mu10 trigger at Level 1.

- *EF_mu18_MG_medium*: A single muon trigger based on the Muon Girl Algorithm which selects muons with $p_T > 18$ GeV. This trigger is seeded by the L1_mu11 trigger at Level 1.

6.2.4 Single Muon Trigger Efficiency

The trigger efficiency for a single lepton trigger is defined as:

$$\epsilon_{trigger} = \frac{N_{\text{leptons firing trigger}}}{N_{\text{reconstructed leptons from Z bosons}}} \tag{6.1}$$

and is measured for muons in the region $|\eta| < 2.4$ and for electrons with $|\eta| < 2.5$. The trigger efficiency is measured with the Z tag-and-probe method. A sample of $Z \to \mu\mu$ events is identified using offline, reconstructed muons. If one muon from the Z decay fired the trigger, it is considered a *tag* muon. The other muon is called the

probe muon. Probe muons are tested to see if they fired the trigger and enter into equation 6.1. If both muons associated to the Z boson fired the trigger, they can both be used as tag muons.

The efficiency of the EF_mu18_MG_medium trigger is shown in Figure 6.2 for the barrel and endcap separately. The trigger efficiency for muons increases quickly with muon momentum in the range $15 < p_T < 20$ GeV and is flat by 20 GeV. For muons with $p_T > 20$ GeV, the triggering efficiency is 0.89 in the endcap region and 0.69 in the barrel region [42]. The difference in the trigger efficiency in the barrel and the endcap is due to the geometric coverage of the RPC and TGC chambers. In the barrel, the RPC chambers do not fully cover the geometric acceptance that is covered by the MDT chambers, so it is possible to reconstruct offline muons with MDT hits that do not pass through trigger chambers. Since the trigger efficiency is measured with respect to reconstructed offline muons, the fact that the RPC chambers do not fully cover the area covered by the MDT chambers reduces the trigger efficiency for muons with $|\eta| < 1.05$. If geometric acceptance is factored out, the efficiency of the RPC chambers for triggering on a muon traversing a chamber is 95% [15]. In the endcap, the trigger TGC chambers cover a similar fiducial volume to the MDT and CSC chambers within $|\eta| < 2.4$, so reconstructed offline muons mostly pass through trigger chambers.

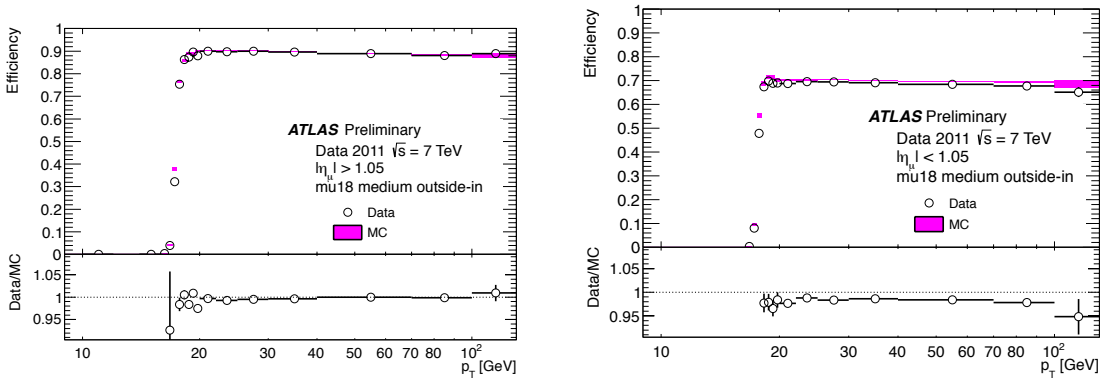

Figure 6.2: Single muon trigger efficiencies in the endcap (left) and barrel (right) for the Event Filter trigger EF_mu18_medium. The trigger efficiency is defined in equation 6.1 [42].

6.3 Electron Triggers

6.3.1 Electron Level 1 Trigger

The Level 1 electron trigger is based on *trigger towers* in both the electromagnetic and hadronic calorimeters within $|\eta| < 2.5$ [53]. A trigger tower is an analog sum of calorimeter cells within a 0.1×0.1 window in $\Delta\eta \times \Delta\phi$ space. As no track information is used at Level 1, electron and photon candidates can not be distinguished. The triggers are therefore called *egamma*.

The transverse energy of the trigger candidate is estimated using look-up tables. Within a central window of 2×2 trigger towers, the energy in each of the four 1×2 or 2×1 electromagnetic tower configurations is summed. At least one of the pairs of trigger towers must pass a predetermined energy threshold. The 12 towers in the electromagnetic calorimeters surrounding the 2×2 central window, as well as the hadronic towers behind the central electromagnetic tower, are used to estimate the

isolation. The local energy maximum within the 2×2 central window is used as the position of the trigger candidate, and the region of interest is defined by the 2×2 trigger tower. The relevant trigger towers for an electron candidate are illustrated in Figure 6.3.

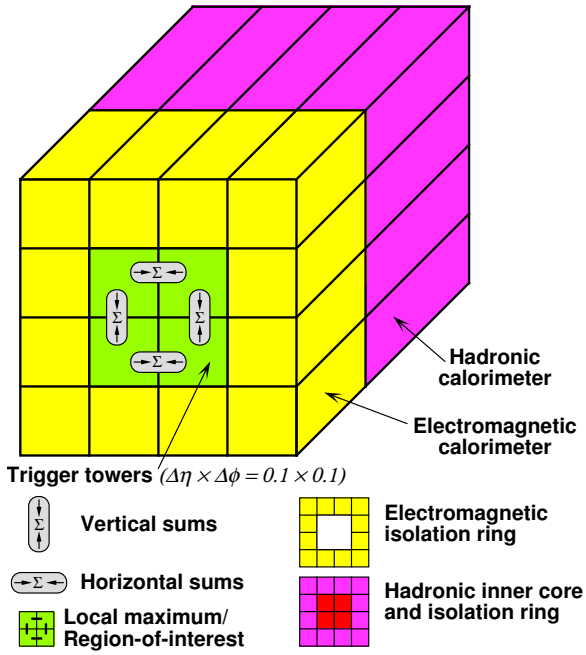

Figure 6.3: Electron level 1 trigger logic [28].

The Level 1 egamma trigger items used in this analysis are:

- *L1_EM14* A level 1 trigger item with an E_T threshold corresponding to 14 GeV.
- *L1_EM16* A level 1 trigger item with E_T threshold 16 GeV.
- *L1_EM16vh* A level 1 trigger item whose E_T threshold is a function of ϕ. In the regions of the electromagnetic calorimeter with the lowest trigger efficiency, mostly due to additional inactive material, the E_T threshold is 16 GeV. In areas with higher efficiency, the threshold is slightly higher. This "variable" threshold

is the "v" in the trigger name. The "h" stands for "hadronic veto"; the trigger requires less than 1 GeV of energy deposited in the hadronic calorimeter towers behind the central electromagnetic cluster. Both the L1_EM16 and L1_EM16vh triggers are nearly fully efficient for electrons with an $E_T > 25$ GeV.

- *L1_EM30* A level 1 trigger item with E_T threshold set to 30 GeV.

6.3.2 Electron Triggers

The electron event filter triggers used in the WZ analysis are described below:

- *EF_e20_medium*: A single electron trigger which selects electrons with $E_T > 20$ GeV. The trigger is seeded by the L1_EM14 trigger.

- *EF_e22_medium*: A single electron trigger which selects electrons with $E_T > 22$ GeV. Seeded by the L1_EM16 trigger.

- *EF_e22vh_medium1*: A single electron trigger which selects electrons with $E_T >$ 22 GeV. Relative to the EF_e22_medium trigger, a veto is placed on electron candidates with hadronic activity greater than 1 GeV. It is seeded by the L1_EM16vh trigger. To recover inefficiencies at high E_T due to increased leakage to the hadronic calorimeter, the trigger is used in an OR with the EF_e45_medium1 trigger.

- *EF_e45_medium1*: A single electron trigger which selects electrons with $E_T > 45$ GeV. The Level 1 seed is L1_EM30.

6.3.3 Single Electron Trigger Efficiency

The single electron trigger efficiency is defined in equation 6.1 and is measured in an analogous way to the measurement of the muon trigger efficiency, using a sample of $Z \to ee$ events. The efficiency of the EF_e20_medium trigger as a function of offline electron transverse energy is shown in Figure 6.4. The triggering efficiency is a steep function of transverse energy until 25 GeV, above which the efficiency is almost 100%.

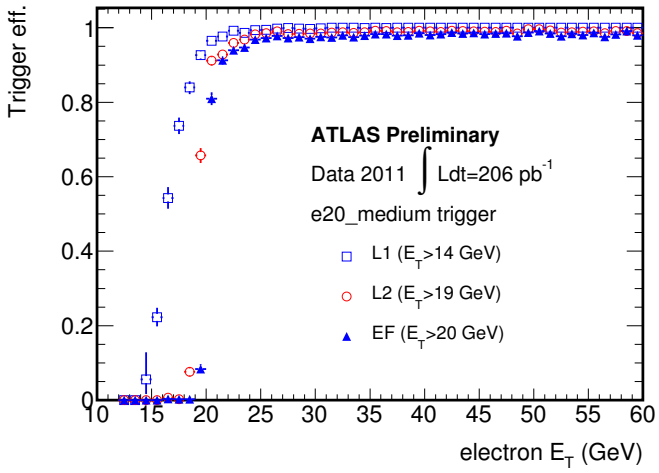

Figure 6.4: Single electron trigger efficiencies. The efficiency of the e20_medium single electron trigger at each trigger level as a function of the offline electron E_T is shown [23].

6.4 Trigger Streams and Overlap Removal

Events which fire one of the electron triggers are put into the *physics_Egamma* data stream and events which fire one of the muon triggers are put in the *physics_Muons* data stream. This analysis uses events from both trigger streams. As a single WZ event could fire both an electron and a muon trigger, the same event could end up in

both trigger streams. In a typical run, there is about 1% of overlap in total events between the physics_Egamma and physics_Muons stream. To avoid selecting the same event from both streams, the following event overlap removal procedure is observed: 1) all events firing one of the selected muon triggers in the physics_Muons data stream are kept, regardless of the electron trigger status, and 2) events are selected from the physics_Egamma trigger stream only if they do not fire any of the selected muon triggers. This event overlap removal is applied at the trigger selection stage.

6.5 WZ Trigger

6.5.1 WZ Trigger Selection

$WZ \to \ell\nu\ell\ell$ events have three high p_T, isolated leptons, and the probability that at least one of them fired a single muon or single electron trigger is high, above 98%. We use the lowest p_T un-prescaled single muon and electron triggers available. The momentum and selection requirements of the lowest un-prescaled triggers change as a function of when the data was collected, as the LHC instantaneous luminosity increased. The LHC dataset is broken down into several *data periods*, each of which contains data taken within a few days or weeks in which the accelerator conditions were relatively constant. The summary of the triggers used in the WZ analysis in 2011 are shown in Table 6.1.

In Table 6.2, the Level 1 and Event Filter muon and egamma trigger rates are shown for one run at a luminosity of 3.5×10^{33} cm^{-2}s^{-1}.

Table 6.1: WZ trigger selection. Events are required to pass the lowest available un-prescaled single muon or single electron trigger. The trigger at the Event Filter (EF) level is shown along with the Level 2 (L2) and Level 1 (L1) triggers that seed it. The specific lepton triggers vary as a function of data-taking period.

EF Trigger Item	L2 seed	L1 seed	Data Period	Data %
Muons				
EF_mu18_MG	L2_mu18_MG	L1_mu10	periods D-I	39%
EF_mu18_MG_medium	L2_mu18_MG_medium	L1_mu11	periods J-M	61%
Electrons				
EF_e20_medium	L2_e20_medium	L1_EM14	periods D-J	44%
EF_e22_medium	L2_e22_medium	L1_EM16	period K	12%
EF_e22vh_medium1	L2_e22vh_medium1	L1_EM16vh		
or			periods L-M	44%
EF_e45_medium1	L2_e45_medium1	L1_EM30		

Table 6.2: Example trigger rates for the lowest un-prescaled EF and L1 muon and electrons triggers used in data taking period M. These rates are taken from Run 191920 in the luminosity block corresponding to the peak luminosity at 3.5×10^{33} cm^{-2}s^{-1}, and are approximate.

Trigger Item	Rate at 3.5×10^{33} cm^{-2}s^{-1}
L1_mu11	10 kHz
EF_mu18_MG_medium	150 Hz
L1_EM16vh	12 kHz
EF_e22vh_medium1	100 Hz

6.5.2 WZ Trigger Efficiency

The efficiency of triggering a $WZ \to \ell\nu\ell\ell$ event is higher than the single electron or muon trigger efficiency, as there are three chances to fire the trigger. The event level trigger efficiency is defined as:

$$\epsilon_{trigger}^{WZ} = \frac{N_{\text{triggered WZ events}}}{N_{\text{selected WZ events}}} \tag{6.2}$$

and is calculated after all WZ event selection requirements have been applied (see Table 8.5), except the trigger requirement. The WZ event level trigger efficiency is shown in Table 6.5.2, calculated separately for simulated WZ events in all four channels. The efficiency is highest for the *eee* channel because the electron trigger is more efficient than the muon trigger, but for all channels the probability of passing the trigger is above 98%. The statistical uncertainty on this efficiency is $\sim 1\%$ and the systematic uncertainty due to applying scale factors, discussed in Section 6.5.4, is less than 1%.

Table 6.3: WZ event trigger efficiencies by channel. The first column shows the trigger efficiency defined in equation 6.5.2. The second column shows the systematic uncertainty due to applying scale factors to correct the efficiency in simulation to that measured in data.

Channel	Trigger Efficiency [%]	Systematic Uncertainty [%]
eee	99.7	$\pm < 0.05$
$ee\mu$	99.5	$\pm$ 0.08
$e\mu\mu$	98.9	$\pm$ 0.16
$\mu\mu\mu$	98.4	$\pm$ 0.29

6.5.3 Trigger Matching

After reconstructing a W and Z boson candidate, we require that one of the leptons from either the Z or W boson is matched to the lepton that fired the trigger. To pass the trigger matching requirement, at least one of the three final state muons (electrons) associated to the Z or W boson must be matched to a trigger muon or electron within $\Delta R = \sqrt{\phi^2 + \eta^2} < 0.1(0.15)$. To avoid differences in the measured efficiency between data and simulation in the p_T range in which the trigger efficiency is rapidly changing, the lepton that is trigger-matched is required to have $p_T > 20$ GeV for muons and $E_T > 25$ GeV for electrons.

6.5.4 Trigger corrections

The efficiency of triggering a WZ event is one input to the overall efficiency of selecting the events. Since we extrapolate the observed number of events in data to a measured cross section using the efficiency calculated in simulation, it is important that the simulation has the same trigger efficiency as the data. We ensure this by weighting simulated events with a scale factor, $SF_{trigger}$, which corrects the efficiency measured in simulation to the efficiency measured in data. The single muon scale factor is shown in the lower portion of Figure 6.2. The scale factor differs from 1 slightly in the barrel region because the RPCs had occasional chambers that were not working or were not properly timed in; these problems were fixed within a few runs but were not modeled in the simulation. As the WZ event can be triggered by multiple leptons, the scale factor for the whole event is calculated as a function of all

reconstructed leptons which are matched to a trigger object:

$$SF_{trigger} = \frac{1 - \prod_{n=1}^{N}[1 - \epsilon_{data}(l_n)]}{1 - \prod_{n=1}^{N}[1 - \epsilon_{MC}(l_n)]} \tag{6.3}$$

where N is the number of trigger matched leptons passing the p_T requirement and $\epsilon_{MC}(l_n)$ and $\epsilon_{data}(l_n)$ are the single lepton trigger efficiencies for lepton l_n in simulation and data respectively. The event level scale factor can be computed directly from the scale factors measured for single leptons, $SF^{single}_{trigger}(l_n)$, by recognizing that

$$\epsilon_{data}(l_n) = \epsilon_{MC}(l_n) \times SF^{single}_{trigger}(l_n) \tag{6.4}$$

The single lepton scale factors are measured for muons as a function of η and ϕ and for electrons they are measured as a function of η and E_T.

Chapter 7

Monte Carlo Simulation and WZ Signal

This chapter discusses the simulation of the WZ signal in the ATLAS detector. The generation of Monte Carlo WZ signal events is covered in Section 7.1. To ensure that the simulated events match the actual data as much as possible, several data-derived corrections are applied to simulated objects and events. These corrections, discussed in Section 7.2, are applied to simulated events for both signal and background processes. The simulation may not reproduce the data exactly due to the inexact knowledge of the material description of the detector, as well as uncertainty on the alignment of all detector components. Additionally, occasional detector problems, such as high voltage trips in a single chamber, affect the efficiency of the detector but are not in general reproduced in simulation. Distributions of kinematic variables are shown for the simulated WZ events in Section 7.3 at both the truth and reconstructed level. Truth level distributions are taken directly after event gen-

eration; reconstructed distributions are reconstructed offline after full simulation of the response of the ATLAS detector and include detector response and experimental resolutions.

7.1 Generation of WZ Signal Events

We model the $WZ \to \ell\nu\ell\ell$ signal production with the MC@NLO 4.0 generator [88]. MC@NLO generates fully exclusive events with rates and distributions of observables accurate to the next-to-leading order (NLO) in α_s.

The hard scatter producing the $WZ \to \ell\nu\ell\ell$ final state is calculated to next-to-leading order with a matrix element calculation in MC@NLO. This includes one-loop virtual WZ production and WZ production with an extra gluon or quark in the final state. The Feynman diagrams for the next-to-leading order contributions to WZ production are shown in Figure 2.5. To model the fragmentation of quarks and gluons and the hadronization of the event, the matrix element calculation is incorporated into HERWIG [74], which performs parton shower simulation.

Both the parton shower simulation and the matrix-element calculation produce events with $WZ + 1$ quark or 1 gluon in the final state, such as the diagram shown in Figure 2.5(d). To avoid double counting of events, a matching procedure is performed, in which hard (high p_T) emissions are kept from the matrix element calculation and soft (low p_T) and collinear emissions are kept from the parton shower simulation. This matching is achieved by calculating analytically how a first branching in a shower in the $2 \to 2$ body process would populate the $2 \to 3$ body phase space. This analytic expression is subtracted from the matrix element calculation. The showering

simulation re-populates the subtracted phase space. With the subtraction technique, the matching is "smooth" – that is, there is no double counting of events, and the rate of produced events is accurate to the next-to-leading order cross section. On account of the subtraction and the fact that the matrix element calculation does not necessarily produce a larger cross section than the showering in all regions of phase space, a small fraction of simulated events have negative weights.

We chose MC@NLO to model the WZ signal for two reasons. First, it is one of the few generators able to produce fully simulated events at NLO in α_s. This is important because the next-to-leading order terms are almost as large as the leading-order terms for WZ production at the LHC. Moreover, the kinematics of events produced to next-to-leading order differ significantly from events produced at leading order, in particular in the high mass or high p_T tails of distributions that are sensitive to anomalous couplings. Second, MC@NLO 4.0 has the capability to simulate events with anomalous triple gauge couplings and records event-by-event weights associated to the anomalous triple gauge coupling terms. The event-by-event weights allow us to re-weigh events simulated with a particular set of anomalous couplings to any other value of anomalous couplings. This event reweighting, described in detail in Section 11.1, allows us to simulate only one set of WZ events with anomalous couplings, and to use those events to scan the full range of coupling values when searching for anomalous couplings in the data.

The simulated WZ standard model and anomalous coupling events are produced with the parton density function (PDF) set CT10 [109]. Events are simulated with all permutations of electron, muon, and tau decays of the W and Z bosons, and

the gauge boson decays are simulated at the matrix element calculation stage. The TAULO [79] program simulates the decay of the tau leptons to all known final states. Full spin correlations between the leptons of the Z and W boson are simulated and the widths of the W and Z bosons are included in the generation. However, Z/γ interference is not included, and the effect of this omission is taken into account by normalizing the simulated events to the cross-section calculated by the next-to-leading order calculator MCFM [55], which does include Z/γ interference. For details on the calculation of the theoretical signal cross section, see Section 10.5.

The full list of simulated WZ events is shown in Table 7.1. We simulate one set of WZ events consistent with the Standard Model predictions, and one set of WZ events with anomalous couplings. The set with anomalous couplings is simulated with a form factor of 100 TeV (see equation 2.12 for a definition of the form factor). The values of the anomalous couplings in the simulated sample are set to: $\Delta g_1^Z = 0$, $\Delta\kappa_Z = 0$, and $\lambda_Z = 0.13$. After generation, we can reweight the simulation to any value of anomalous coupling (see Section 11.1). The values of the anomalous couplings with which we generate the sample are arbitrary, but chosen to ensure sufficient statistics after reweighting to any value of anomalous coupling not excluded by our previous analysis with 1 fb^{-1}.

After simulation of the hard scattering process and the fragmentation and hadronization of quarks and gluons, the events are interfaced to a GEANT4 [5] simulation of the ATLAS detector to simulate the interaction of all final state particles with the detector. The simulated detector signals are digitized and reconstructed using the ATLAS reconstruction software framework, Athena [16], in release 17.0. The Pythia

Table 7.1: WZ signal simulation. The $W^{\pm}Z$ signal production processes, generator, number of simulated events, and cross-sections are shown for fully simulated MC events. Also included is the ATLAS MC ID run number identifying the simulated process. The MC simulation "filter efficiency," ϵ_{filter}, is the efficiency of selecting events at the generator level. The k-factor corrects to the next-to-leading order production cross section and is 1.0 for the WZ events because MC@NLO simulates at NLO. The listed cross sections do not include k-factors or filter efficiencies. ℓ denotes e, μ and τ. Samples 126089-126106 are produced at anomalous coupling values $\Delta g_1^Z = 0$, $\Delta\kappa_Z = 0$, and $\lambda_Z = 0.13$ with a form factor scale $\Lambda = 100$ TeV.

MCID	Process	Generator	Events	k-factor	ϵ_{filter}	Cross-section [pb]
126053	$W^+Z \to e\nu ee$	MC@NLO	49999	1.0	1.0	0.04114
126054	$W^-Z \to e\nu ee$	MC@NLO	50000	1.0	1.0	0.02243
126055	$W^+Z \to e\nu\mu\mu$	MC@NLO	49999	1.0	1.0	0.04114
126056	$W^-Z \to e\nu\mu\mu$	MC@NLO	49900	1.0	1.0	0.02243
126057	$W^+Z \to e\nu\tau\tau$	MC@NLO	50000	1.0	1.0	0.04114
126058	$W^-Z \to e\nu\tau\tau$	MC@NLO	49950	1.0	1.0	0.02243
126059	$W^+Z \to \mu\nu ee$	MC@NLO	49999	1.0	1.0	0.04114
126060	$W^-Z \to \mu\nu ee$	MC@NLO	50000	1.0	1.0	0.02243
126061	$W^+Z \to \mu\nu\mu\mu$	MC@NLO	49950	1.0	1.0	0.04114
126062	$W^-Z \to \mu\nu\mu\mu$	MC@NLO	50000	1.0	1.0	0.02243
126063	$W^+Z \to \mu\nu\tau\tau$	MC@NLO	49950	1.0	1.0	0.04114
126064	$W^-Z \to \mu\nu\tau\tau$	MC@NLO	50000	1.0	1.0	0.02243
126065	$W^+Z \to \tau\nu ee$	MC@NLO	49999	1.0	1.0	0.04114
126066	$W^-Z \to \tau\nu ee$	MC@NLO	49949	1.0	1.0	0.02243
126067	$W^+Z \to \tau\nu\mu\mu$	MC@NLO	50000	1.0	1.0	0.04114
126068	$W^-Z \to \tau\nu\mu\mu$	MC@NLO	50000	1.0	1.0	0.02243
126069	$W^+Z \to \tau\nu\tau\tau$	MC@NLO	49950	1.0	1.0	0.04114
126070	$W^-Z \to \tau\nu\tau\tau$	MC@NLO	50000	1.0	1.0	0.02243
126089-97	$W^+Z \to \ell\nu\ell\ell$	MC@NLO	$\approx$ 49995	1.0	1.0	0.05516
126098-106	$W^-Z \to \ell\nu\ell\ell$	MC@NLO	$\approx$ 49995	1.0	1.0	0.02849

6 [139] generator is used to model the contribution from other proton collisions in the same event.

7.2 Corrections Applied to Simulation

7.2.1 Pileup Corrections

Data in our sample was taken during the full running period of 2011, during which the data-taking conditions varied significantly as the accelerator increased instantaneous luminosity. The peak luminosity and the peak number of interactions per crossing, averaged across all bunches, as a function of day, is shown in Figure 7.1. The average number of proton-proton interactions per crossing, averaged across all bunches, varied from 3 to 17 in the course of the data taking.

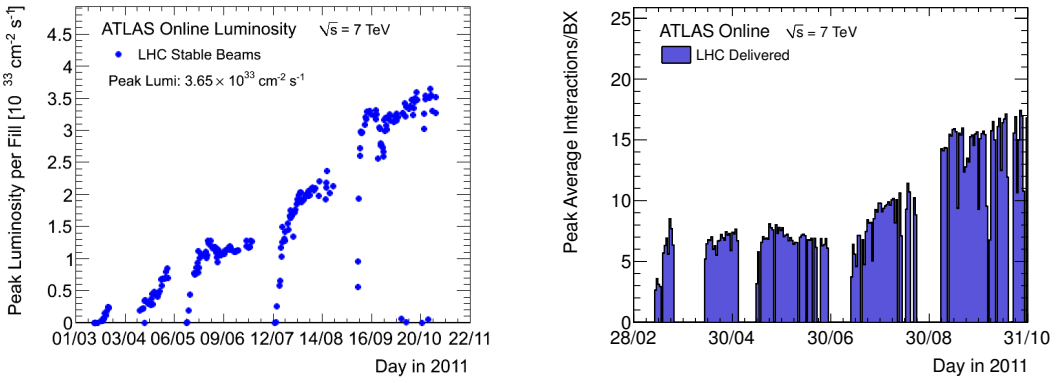

Figure 7.1: Peak Luminosity (right) versus day and peak average number of collisions per event (left) versus day for data collected in 2011. The peak average number of collisions is the maximum of the mean number of interactions per beam crossing per day. The mean number of interactions is averaged across all bunches and is calculated per luminosity block [18].

Each proton-proton interaction contributes particles to the event, and those par-

ticles in turn contribute hits, tracks, and energy deposits in the detector. The collective contribution to the detected event from collisions other than the one of interest is called *pileup*. For sub-detectors with timing resolution less than 50 ns, such as the inner detector, only contributions from collisions in the same crossing are relevant. This is called *in-time pileup*. For the calorimeters, which integrate signals over time periods greater than 50 ns, energy deposits from collisions before the current crossing can also be important. This contribution is called *out-of-time pileup*.

The selection of WZ events is affected by pileup in two main ways: 1) the efficiency of selecting electrons from gauge boson decays changes as a function of the pileup, and 2) the reconstruction of missing transverse energy is sensitive to the pileup, for events with and without high p_T neutrinos. The loss of efficiency for selecting electrons from Z decays as the number of reconstructed vertices in the event increases can be seen in Figure 5.15. For tight++ electrons, the efficiency drops from 80% for events with 2 reconstructed vertices to 73% for events with 17 reconstructed vertices. The loss of efficiency in selecting electrons is mainly due to enhanced hadronic activity overlaying the electron shower in the calorimeter. The reconstruction of missing transverse energy is also affected by pileup. The amount of reconstructed missing transverse energy in Z+jets events in data, which should have no "true" missing transverse energy from high p_T neutrinos, can be seen in Figure 7.2 for two subsets of the dataset with different pileup conditions. The average number of collisions per crossing was 6 for the first part of the dataset and 12 for the rest of the data. The fraction of Z+jets events which pass the missing transverse energy requirement of 25 GeV increases by 50% for events with 12 interactions per crossing relative to events

with 6 average interactions.

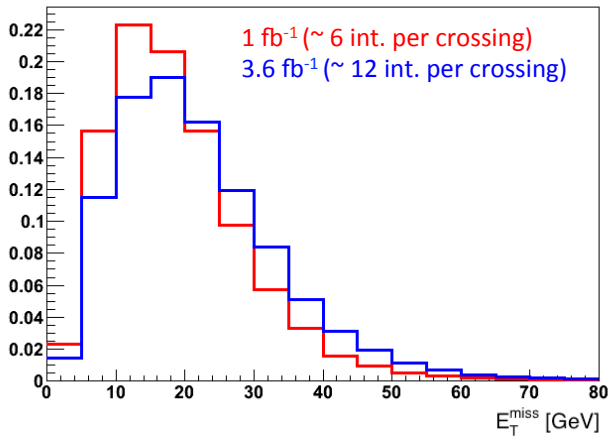

Figure 7.2: E_T^{miss} in Z+jets events with two different pileup conditions. The distribution of missing transverse energy in Z+jets events in a control region in data shown separately for events with 6 average collisions per crossing (red) and events with 12 average collisions per crossing (blue).

The simulation takes account of pileup by overlaying additional simulated events on top of the hard scatter collision of interest. The Monte Carlo is divided into four different periods to closely reflect the actual data-taking conditions. Each Monte Carlo period is simulated with a different distribution of μ, which is the average number of collisions per event, averaged over all bunches, calculated per luminosity block. A luminosity block is a discrete period of data taking in which accelerator and detector conditions are stable and generally lasts about two minutes. The average number of collisions per crossing is shown for our data sample in Figure 7.3, along with the distribution of μ for the four different simulation periods.

As both the electron and missing transverse energy reconstruction are sensitive to pileup, it is important for the simulation of signal and background events that the pileup conditions in the data are well reproduced by simulation. To ensure the

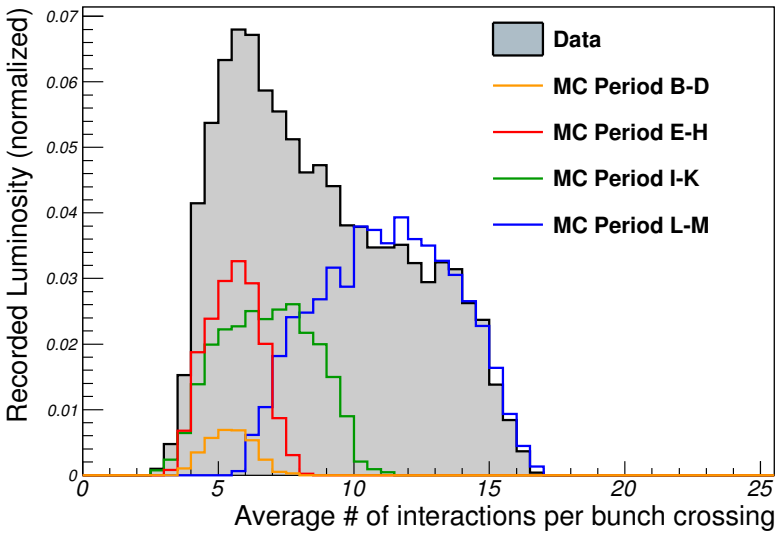

Figure 7.3: The distribution of μ values per event in data and MC (before reweighting), whereμ is the average number of interactions per bunch crossing, averaged over all bunches, calculated per luminosity block. The Monte Carlo is produced with 4 different distributions of μ corresponding to different run periods. Events in Monte Carlo are reweighted to match the distribution in data.

same distribution of pileup, the events in simulation are reweighted to have the same μ distribution as events in data. Specifically, each event in simulation, belonging to a Monte Carlo sample and having a specific μ and MC period, is reweighted with a weight calculated as:

$$\text{weight} = \text{weight}_{\text{period}} * \text{weight}_{\text{pileup}} = \frac{L_A/L}{N_A/N} \times \frac{L_i/L_A}{N_i/N_A} \tag{7.1}$$

where L_A is the luminosity associated to the Monte Carlo period in which the event falls, L is the total luminosity of the Monte Carlo sample, L_i is the fraction of luminosity in data that has the same μ as the simulation event, N_A is the number of events assigned to the MC period, N_i is the number of events in the MC sample with the same value of μ and the same MC period, and N is the total number of Monte Carlo events in the sample.

7.2.2 Muon corrections

To improve the agreement between the reconstruction and performance of muons in simulation and data, several data-based corrections are made to muons and events with muons in simulation. These include corrections for the muon reconstruction efficiency and the muon resolution.

Muon Reconstruction Efficiency

The efficiency of reconstructing and selecting a muon differs slightly between data and simulation. The muon efficiency in simulation is used to calculate the efficiency of selecting WZ events, which is a direct input to the calculation of the WZ cross

section. Therefore, it is important to correct the simulation to have the same muon reconstruction efficiency as the data.

The muon reconstruction efficiency is measured in both data and simulation using the Z tag-and-probe method. In this method, $Z \to \mu^+\mu^-$ decays are selected by requiring two oppositely charged isolated tracks with an invariant mass consistent with a Z boson. One of the tracks must be a combined muon and is called the *tag muon*. The second track, called the *probe muon*, has a looser selection criterion and is used to test the reconstruction efficiency. If measuring the inner detector efficiency, the probe is required to be a stand-alone muon. If measuring the stand-alone, segment-tagged muon, or combined muon efficiency, the probe is required to be an inner detector track. The reconstruction efficiency is the fraction of probes which are reconstructed as either inner detector tracks (if measuring inner detector efficiency) or as combined muons (if measuring combined muon efficiency). The matching is done using a requirement on the angular distance between the reconstructed muon and the probe. For this analysis, the important efficiencies are the inner detector muon reconstruction efficiency ϵ_{ID}, the efficiency of reconstructing combined muons, ϵ_{CB}, and the efficiency of reconstructing segment-tagged muons, ϵ_{ST}. The efficiency is defined by the number of probe muons, N, passing different selection requirements:

$$\epsilon_{ID} = \frac{N_{ID}}{N_{standalone}}, \quad \epsilon_{CB} = \frac{N_{CB}}{N_{ID}}, \quad \epsilon_{ST} = \frac{N_{ST}}{N_{ID}} \tag{7.2}$$

The detailed selection requirements of the muons used to measure the muon reconstruction efficiencies can be found in Reference [33]. Both tag and probe muons are required to have $p_T > 20$ GeV and to be isolated. The measured inner detector reconstruction efficiency is shown in Figure 7.4 as a function of the muon η. The inner

detector muon efficiency is between 97% and 100% across the full η range. There are dips at $\eta = 0$ and $|\eta| = 1.2$ due to hit requirements on the reconstructed inner detector track.

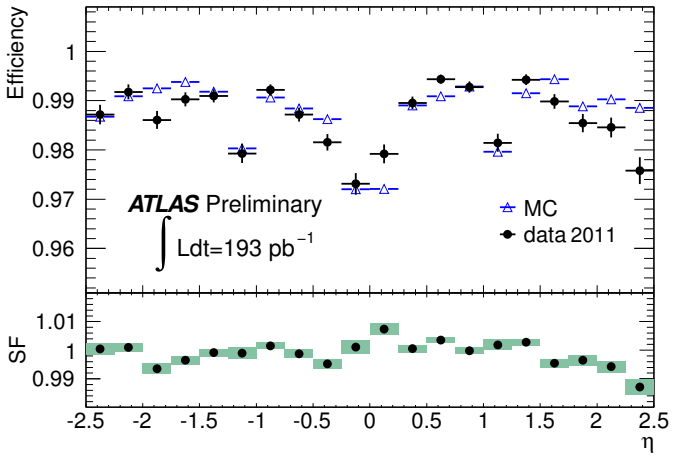

Figure 7.4: Inner detector muon reconstruction efficiency. The reconstruction efficiency of muons in the inner detector with respect to stand-alone muons as a function of η for muons with $p_T > 20$ GeV. The Scale Factors, SF, are the ratios between the data and MC efficiency and are used to correct the efficiency of reconstructing muons in simulation to match that of the data [33].

The measured efficiencies of reconstructing combined and segment-tagged muons are shown in Figure 7.5 as a function of the muon η. For combined muons, the reconstruction efficiency is close to 96% for most regions of the detector. At $\eta = 0$ and $|\eta| = 1.2$, the combined muon efficiency drops to 80%. At $\eta = 0$, there is a gap in the muon chamber coverage to allow services from the inner detector to pass through. $|\eta| = 1.2$ is the transition region between the barrel and the endcap muon chambers. In this region, muons will not necessarily pass through three or even two muon chamber stations. Some of these lost muons can be recovered by looking for segment-tagged muons, which are required to have an inner detector track matched

with a segment in one or more muon chambers. The efficiency of selecting muons which are either combined or segment-tagged is close to 100% for the full range, although the drop at $\eta = 0$ is still present because there are no muon chambers there. The combined + segment-tagged muon efficiency also drops to 96% for muons with $2.5 < |\eta| < 2.0$, which is the region covered by the CSCs.

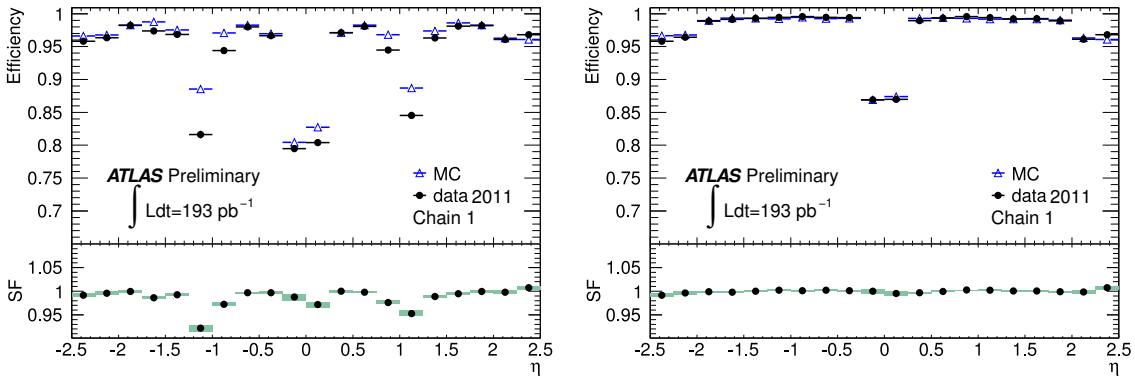

Figure 7.5: Combined muon and segment-tagged muon reconstruction efficiency. The muon reconstruction efficiency with respect to inner tracking efficiency as a function of η for muons with $p_T > 20$ GeV for combined muons (left) and combined muons + segment tagged muons (right). The Scale Factors, SF, are the ratios between the data and MC efficiency and are used to correct the efficiency of reconstructing muons in simulation to match that of the data [33].

To correct for the difference between the measured muon reconstruction efficiencies in data and simulation, a weight called a scale factor, SF, is applied to events in simulation with a reconstructed muon. The scale factors are calculated as a function of muon p_T, η, and data-taking period. The RPCs had timing problems in some data-taking periods that affected the hit efficiency in RPC chambers, so a data-period dependent scale factor is necessary. The simulated events are assigned to Monte Carlo data periods with fractions consistent with the luminosity of data taken in different data periods.

For an event with a single combined muon, the muon reconstruction efficiency scale factor, $SF_{\text{muon reco}}$, is calculated as:

$$SF_{\text{muon reco}} = SF_{\text{ID reco}} \times SF_{\text{CB reco}} = \frac{\epsilon_{ID}^{data}}{\epsilon_{ID}^{MC}} \times \frac{\epsilon_{CB}^{data}}{\epsilon_{CB}^{MC}} \tag{7.3}$$

and similarly for segment-tagged muons. For events with multiple muons, the muon reconstruction efficiency scale factor for the event is the product of the scale factors for each muon. The scale factors for the inner detector, combined muon, and segment-tagged reconstruction efficiencies are shown in the lower portion of Figures 7.4 and 7.5 and are close to 1.0 for all muons, with the exception of combined muons near $|\eta| = 1.2$.

Muon Momentum Resolution and Scale

The muon momentum resolution is measured from the width of the dimuon mass distribution in $Z \to \mu^+\mu^-$ decays. The measurement is described in detail in Reference [32]. Differences in the material distribution of the detector (including inactive parts, like shielding), as well as differences in the magnetic field description between the detector in simulation and the real detector result in a different muon resolution in simulation than in data for low momentum muons. For high momenta muons, an inaccurate description of the detector alignment, or inaccurate timing and gas calibration constants, produce differences in resolution between simulation and data. To account for differences in momentum resolution, the momentum of muons in simulation is convoluted with an additional Gaussian (a process called *smearing*) to have the same resolution of muons in data.

The width of the dimuon mass distribution for $Z \to \mu^+\mu^-$ decays is shown in

Figure 7.6 for muons in simulation and in data. The selected muons must have $p_T > 20$ GeV, be within $|\eta| < 2.5$, and have no nearby calorimeter activity. Data is collected with the 20 GeV muon trigger and simulation is generated using Pythia $Z \to \mu\mu$ events. The simulation has a narrower Z peak, and a smaller muon momentum resolution, than is observed in data.

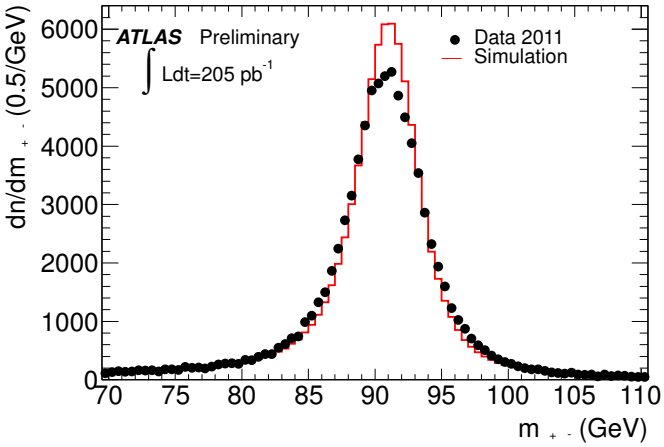

Figure 7.6: $Z \to \mu\mu$ mass for combined muons in data and simulation.

To measure the muon resolution, the dimuon invariant mass distribution is fit using a convolution of the Z line-shape and two Gaussians modeling the detector resolution effects. The Z line-shape includes the Z boson natural width, a term including photon radiation, and a photon interference term, and is parametrized as:

$$f(x) = A\left(\frac{1}{x^2}\right) + B\left(\frac{x^2 - \bar{x}^2}{(x^2 - \bar{x}^2)^2 + \sigma_x^2 \bar{x}^2}\right) + C\left(\frac{x^2}{(x^2 - \bar{x}^2)^2 + \sigma_x^2 \bar{x}^2}\right) \tag{7.4}$$

where x is the reconstructed dimuon invariant mass, A, B, C, and σ_x are fixed parameters determined from the muon pair invariant mass at particle level, and $\bar{x}$ is a free parameter in the fit. The Z boson distribution is fit from 60 to 120 GeV, and the

narrower Gaussian is constrained to contain at least 85% of the dimuon pairs [32]. The muon resolution is taken as the standard deviation of the core Gaussian in the fit. The dimuon distribution is fit separately in different η regions in the detector in both simulation and data. The fit resolution is shown in Figure 7.7 for muons reconstructed with the inner detector track, stand-alone muons, and combined muons. For all three track types, the resolution is larger in data than in simulation in all regions of the detector, due to miscalibration and misalignment of the real detector which is not captured by the simulation, and differences in the material distribution and magnetic field modeling between the real and simulated detector. For combined muons, the detector resolution contributes between 2 and 3 GeV to the invariant mass distribution of dimuon pairs.

To correct the resolution in simulation to that measured in data, the momentum of simulated muons is smeared and scaled. Both the inner detector track and the muon spectrometer track are smeared separately, and the combined muon track is re-fit using the smeared values. For the muon spectrometer track, the smeared muon $p'_T(MS)$ is calculated as a function of the original simulated muon $p_T(MS)$:

$$p'_T(MS) = p_T(MS)(1 + \Delta(MS)) \tag{7.5}$$

where

$$\Delta(MS) = f(0,1)\Delta p_1^{MS} + f(0,1)\Delta p_2^{MS} p_T \tag{7.6}$$

Δp_1^{MS} and Δp_2^{MS} are the correction terms to the simulated muon resolution and $f(0,1)$ is a random number from a Gaussian distribution with mean 0 and width 1. The correction terms to the resolution are obtained by producing a series of simulations with various values of the smearing parameters, and performing a χ^2 minimization fit

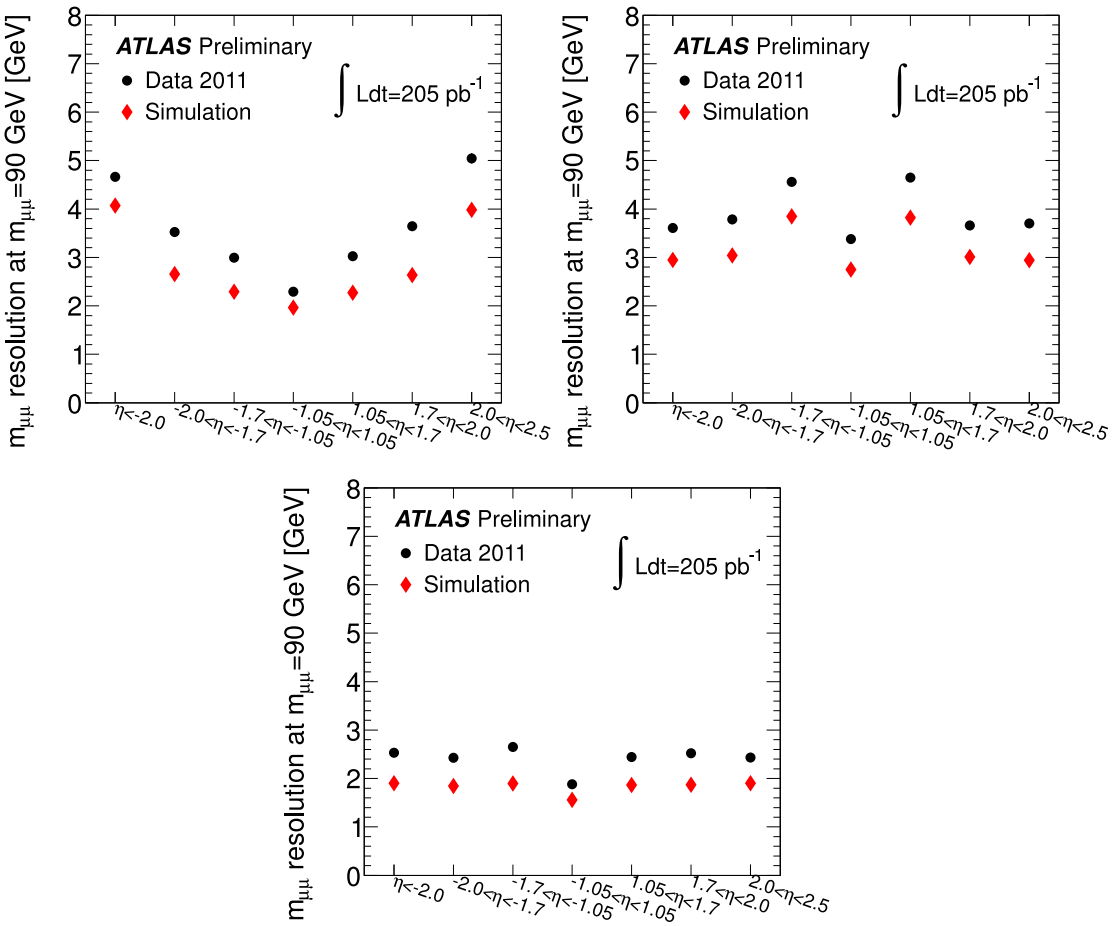

Figure 7.7: Mass resolution for muons in data and simulation, for muons in the inner detector (top left), muons reconstructed in the muon spectrometer (top right), and for combined muons (bottom). The resolution is shown in red for muons in simulation and in black for muons in data [33].

to select the simulated sample which best matches the resolution observed in data. For the smearing of the inner detector track, a similar procedure is followed, with the smeared muon $p'_T(ID)$ expressed as:

$$p'_T(ID) = p_T(ID)(1 + \Delta(ID)) \tag{7.7}$$

where

$$\begin{aligned} \Delta(ID) &= f(0,1)\Delta p_1^{ID} \quad (|\eta| < 1.9) \\ \Delta(ID) &= f(0,1)\Delta p_2^{ID} p_T / \tan\theta \quad (|\eta| > 1.9) \end{aligned} \tag{7.8}$$

and θ is the muon polar angle. For both the ID and MS tracks, Δp_1 describes the correction to the multiple scattering term of the resolution. Δp_2 describes the correction due to misalignment and miscalibration. In order to obtain the correction terms to the simulated muon resolution, constraints are placed based on the knowledge of the amount of possible misalignment and the uncertainty on the material budget.

For combined muons, the smeared muon momentum is calculated from the smearing on the inner detector and muon spectrometer tracks, weighted by the original contribution of the ID or MS momentum measurement to the track fit. The two measurements are treated as uncorrelated due to the large amount of calorimeter material between the inner detector and the muon spectrometer. A scale correction S is also applied to shift the entire distribution to match the location of the peak measured in data. Using the overall correction to the simulated p_T, $\Delta(MS)$ and $\Delta(ID)$, and the values for the resolution fit from the χ^2 minimization to data, $\sigma(MS)$ and $\sigma(ID)$, the new measurement of the smeared combined muon p'_T is calculated as:

$$p'_T(CB) = S \times p_T(CB) \times [1 + \frac{\Delta(MS)/\sigma^2(MS) + \Delta(ID)/\sigma^2(ID)}{1/\sigma^2(MS) + 1/\sigma^2(ID)}] \tag{7.9}$$

The values of the correction terms for our data sample are shown in Table 7.2.

Table 7.2: Muon momentum resolution and scale correction terms [33].

Correction Term	$\lvert\eta\rvert < 1.05$	$1.05 < \lvert\eta\rvert < 1.7$	$1.7 < \lvert\eta\rvert < 2.0$	$2.0 < \lvert\eta\rvert < 2.7$
S	0.999223	0.998684	0.998207	0.997724
Δp_1^{ID}	0.01607	0.02588	0.03389	0.05116
Δp_2^{ID}	0.000307	0.000331	0.000436	0
Δp_1^{MS}	0.02676	0.0452	0.03121	0.02635
Δp_2^{MS}	0.000103	0.000192	0.00008	0.000051

7.2.3 Electron corrections

As for muons, corrections are applied to the resolution and efficiency of reconstructed electrons in simulation to improve the agreement between simulation and data. These include corrections for the electron reconstruction efficiency, the electron identification efficiency, and the electron energy resolution.

Electron Reconstruction and Identification Efficiency

The efficiency of reconstructing and selecting an electron differs slightly between data and simulation. We used the WZ simulation to calculate the efficiency of selecting WZ events, and therefore it is important to correct the simulation to have the same electron efficiency as the data.

The electron efficiency in simulation is used to calculate the efficiency of selecting WZ events, which is a direct input to the calculation of the WZ cross section. Therefore, it is important to rescale the simulation to have the same electron efficiency as the data.

The efficiency of selecting electrons in ATLAS is factorized into two separate

pieces: ϵ_{reco}, the efficiency of reconstructing a cluster and matched-track consistent with an electron, given a cluster in the calorimeter, and $\epsilon_{identification}$, the efficiency of an electron passing the identification requirements (loose++,medium++, or tight++, see Section 5.4) given a reconstructed cluster and matched track. The total electron efficiency, in data or in simulation, is the product of these two efficiencies:

$$\epsilon_{electron} = \epsilon_{reco} \times \epsilon_{identification} \tag{7.10}$$

The electron reconstruction efficiency is measured in data and simulation using the $Z \to ee$ tag-and-probe method, which is described in Section 7.2.2 for $Z \to \mu\mu$ events. Tag electrons are required to be isolated, to pass the tight++ requirement and to have $20 < E_T < 50$ GeV. All calorimeter clusters are tested for probes. If the invariant mass of the tag electron and the calorimeter cluster is within $80 < m_{ee} < 100$ GeV, the probe is selected. The reconstruction efficiency is defined as the fraction of probe clusters which have a matched track that passes the basic track requirements defined in Section 5.4:

$$\epsilon_{reco} = \frac{N_{\text{clusters with matched tracks}}}{N_{\text{probe clusters}}} \tag{7.11}$$

The reconstruction efficiency is close to 95% for all electrons with $15 < E_T < 50$ GeV [20].

The identification efficiency is measured in data and simulation using the tag-and-probe method in $Z \to ee$ events. The identification efficiency is also measured using the tag-and-probe method in $J/\psi \to ee$ events, where one electron is the tag, and in $W \to e\nu$ events, where the missing transverse energy from the neutrino serves as the tag. The details of the measurement of the identification efficiency are described in Reference [35]. The probe electron is required to have a reconstructed cluster with a

matching track, and the identification efficiency is the ratio of the number of probes that pass the selection under study (loose++, medium++, or tight++) to the number of probes:

$$\epsilon_{identification} = \frac{N_{\text{loose++}}}{N_{\text{clusters with matched tracks}}} \tag{7.12}$$

and similarly for measuring the medium++ and tight++ identification efficiencies. The J/ψ data is used for electrons with $E_T < 15$ GeV; a weighted average of the efficiency measured in J/ψ, Z, and W data is used for electrons with $15 < E_T < 20$ GeV, and a weighted average of the Z and W data is used for electrons with $E_T > 20$ GeV. The loose++ identification efficiency, measured in data and in simulation, is shown in Figure 7.8.

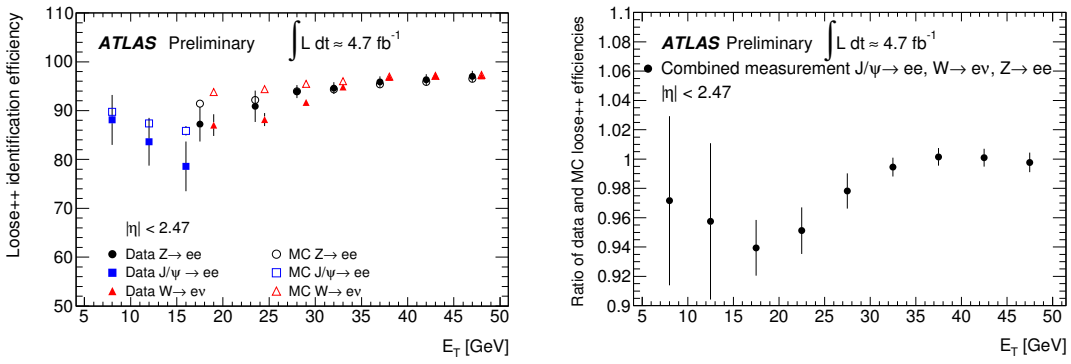

Figure 7.8: Electron identification efficiency (left) and simulation corrections (right), as a function of electron E_T. The identification efficiency shown here is the efficiency of an electron passing the loose++ selection criteria, given a reconstructed calorimeter cluster and a matched track. The simulation correction is a scale factor calculated from the ratio of the efficiency measured in data to the efficiency measured in simulation [20].

To correct the simulation for the difference between the reconstruction and identification efficiencies measured in simulation and data, a scale factor, SF, is a weight applied to events in simulation with a reconstructed electron. The scale factor is the

ratio of the measured efficiency in data to that in simulation. The total scale factor for each electron is a product of the reconstruction scale factor and the identification scale factor:

$$SF_{electron} = SF_{reco} \times SF_{identification} = \frac{\epsilon_{reco}^{data}}{\epsilon_{reco}^{MC}} \times \frac{\epsilon_{identification}^{data}}{\epsilon_{identification}^{MC}} \tag{7.13}$$

For events with multiple electrons, the total event scale factor due to electron selection is a product of the total scale factor for each electron. The reconstruction and identification scale factors are calculated in 11 bins of electron η, and the values are shown in Table 7.3.

Table 7.3: Electron efficiency corrections to simulation. The scale factors for the reconstruction efficiency are shown. Identification efficiency scale factors are shown separately for loose++, medium++, and tight++ electron requirements [20].

	Scale Factor			
Eta Range	Reconstruction	loose++	medium++	tight++
$-2.47 < \eta < -2.01$	1.0201	0.978162	0.956077	0.970385
$-2.01 < \eta < -1.52$	1.0067	0.989691	0.984517	1.00039
$-1.52 < \eta < -1.37$	1.0097	0.9892	0.9933	1.0294
$-1.37 < \eta < -0.8$	1.0017	1.00281	0.998451	1.02121
$-0.8 < \eta < -0.1$	0.9940	0.993113	0.998374	1.00159
$-0.1 < \eta < 0.1$	0.9916	0.994409	1.01566	1.01284
$0.1 < \eta < 0.8$	0.9925	0.995224	0.999115	1.00105
$0.8 < \eta < 1.37$	1.0013	1.00113	0.995048	1.01674
$1.37 < \eta < 1.52$	1.0073	0.9927	0.9972	1.0349
$1.52 < \eta < 2.01$	1.0057	0.990337	0.98697	1.00659
$2.01 < \eta < 2.47$	1.0230	0.98053	0.957895	0.971479

Electron Energy Resolution and Scale

The electron energy resolution and scale is determined in data and simulation using dielectron pairs consistent with the decay of a Z boson. Electrons are required to have transverse energy greater than 25 GeV, $|\eta| < 2.47$, and must pass the medium identification selection. The dielectron invariant mass distribution is fit by a convolution of the Z line-shape, described by a Breit-Wigner distribution, and a Crystal Ball function [147] which describes the detector resolution contribution. For all electron pairs, the obtained resolution, which is taken as the σ-parameter, or width, of the fit Crystal Ball, is 1.76 GeV in data, and 1.59 GeV in simulation [20]. Scale calibrations are applied to data (see Section 5.4.1) to correct the reconstructed energy of electrons for energy loss in the detector. The $Z \to ee$ invariant mass distribution for calibrated electrons in data and electrons in simulation in shown in Figure 7.9.

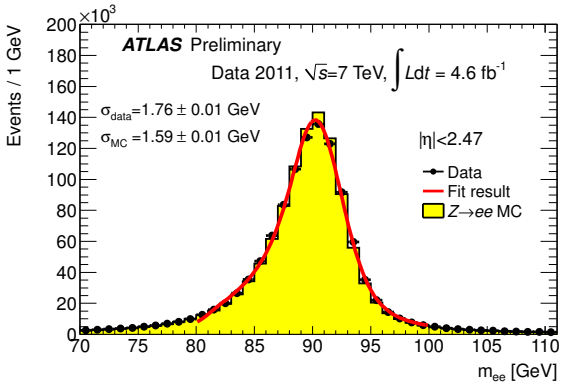

Figure 7.9: $Z \to ee$ mass for electrons in data and simulation, after calibrations have been applied to the electron energy scale in data [20].

To correct the mass resolution in simulation to match the resolution measured in data, the energy of the electromagnetic cluster associated to the electron, $E_{cluster}$, is

smeared according to the formula:

$$E'_{cluster} = E_{cluster}(1 + f(0, \sigma)) \tag{7.14}$$

where $f(0, \sigma)$ is randomly sampled from a Gaussian distribution with mean 0 and width σ, and σ is the fractional quadratic difference between the total energy resolution measured in simulation and the total energy resolution measured in data. The smearing term, $\sigma(\eta, E)$, is calculated as a function of the electron cluster η and energy.

The electron transverse energy, E_T, is recalculated after smearing using the track η:

$$E'_T = \frac{E'_{cluster}}{\cosh(\eta_{track})} \tag{7.15}$$

7.2.4 Trigger Corrections

A scale factor weight is applied to simulated events to match the trigger efficiency measured in data. This scale factor is discussed in Section 6.5.4.

7.3 WZ Signal Distributions in Simulation

This section contains several kinematic distributions of the simulated WZ signal events, whose generation is described in Section 7.1. For each kinematic variable, three different distributions are shown. The *truth* distribution contains all simulated WZ events at truth level, where truth level means that interaction between the particles and the detector is not included. The *truth, passed selection* distribution includes WZ events at truth level, only for events whose reconstructed objects pass all event

selections. Finally, the *reco, passed selection* distribution includes simulated WZ events after the detector response and reconstruction has been simulated, including the applications of the Monte Carlo corrections discussed above. The *reco, passed selection* distribution only includes events which pass all event selections. The Monte Carlo corrections are described in the previous section, and the event selections are summarized in Table 8.5. These distributions do not include events with selected electrons or muons from tau decays. All distributions are normalized to unit area.

Figure 7.10 shows the W lepton p_T and the missing transverse energy in the event. For the truth distributions, the missing transverse energy shown is simply the neutrino p_T. Both the lepton p_T and neutrino p_T distributions at truth level have a maximum in their distributions at around 30 GeV. The mean of the transverse momentum distribution is 43 GeV for the W lepton and 47 GeV for the W neutrino. If the W boson were produced at rest, both the neutrino and lepton p_T distributions should exhibit a Jacobian peak at half the W mass and fall off rapidly after 40 GeV. However, the average W boson in a WZ event has $p_T = 56$ GeV, and this momentum significantly smears out the distribution. The reconstructed W lepton p_T distribution after all selections shows the effect of the $p_T > 20$ GeV selection requirement, and similarly the reconstructed missing transverse energy distribution shows the effect of the selection of $E_T^{miss} > 25$ GeV. The lepton p_T resolution is better than the missing transverse energy resolution, which is evident in the comparison of the true and reconstructed distributions after selection.

The Z lepton p_T distributions are shown in Figure 7.11, separately for the Z lepton with the higher p_T (leading) and the Z lepton with the lower p_T (lagging) per event.

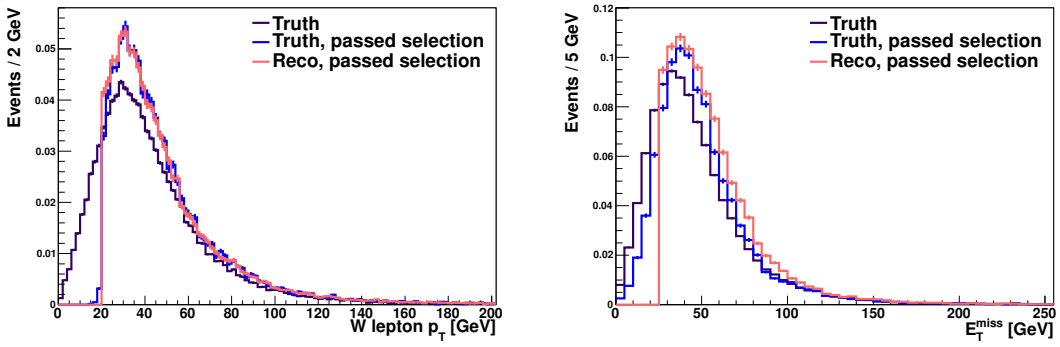

Figure 7.10: WZ signal distributions in simulation: W lepton p_T (left) and E_T^{miss} (right).

The highest point of the leading p_T distribution, before reconstruction, is around 50 GeV and the mean of the distribution is 65 GeV. The highest point of the lagging p_T distribution is around 30-40 GeV with a mean of 31 GeV. Both reconstructed leptons are required to have $p_T > 15$ GeV, but only the lagging lepton distribution shows the effect of this, as there are no leading leptons with $p_T < 15$ GeV after the lepton η requirements are imposed. The tail of the lepton p_T distribution goes to 200 GeV, and above. As shown in Figure 4.7, the muon momentum resolution for muons with transverse momentum of 200 GeV is around 4%.

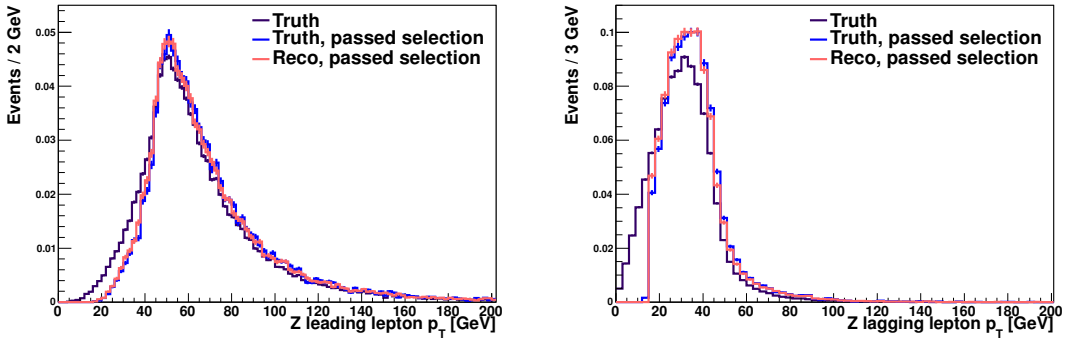

Figure 7.11: WZ signal distributions in simulation: lepton p_T distributions for the leading (left) and lagging (right) Z lepton.

The η distributions for both W and Z leptons are shown in Figure 7.12. Before selection, the η distributions have a maximum at 0 and fall off smoothly to $|\eta| < 4$. In event selection, we require W and Z leptons to be within $|\eta| < 2.5$, which is clear for the events which have passed selection. W muons are required to be combined muons, which require at least 2 stations of muon chamber coverage. There is a gap in muon chambers at $\eta = 0$ to allow inner detector services to exit the detector; the loss of efficiency in this region is clearly seen in the selected W leptons. Additionally, there is a loss of muon efficiency around $|\eta| = 1.5$ in the transition between the barrel and endcap chambers. This is also the transition between the barrel and endcap calorimeters, and there is a loss of electron efficiency there as well. Z muons have a looser selection (combined muons or segment-tagged), and segment-tagged muons can have an inner detector track and a segment in only one muon chamber. As a result, the gaps in the η distribution around 0 and 1.5 are partially filled in for Z leptons relative to W leptons.

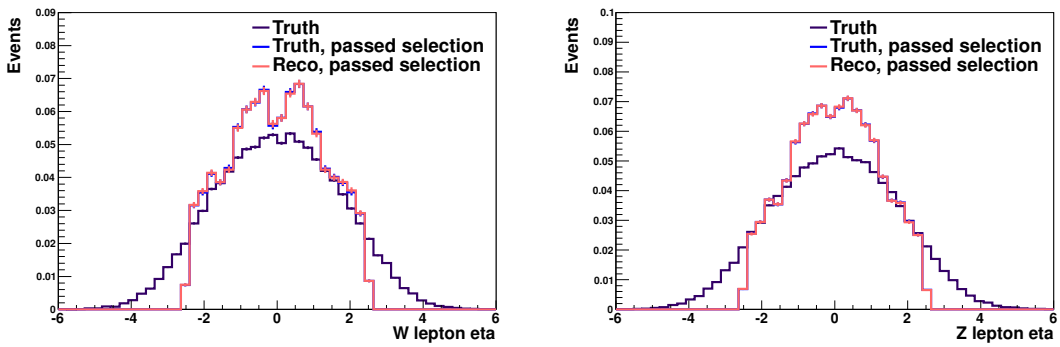

Figure 7.12: WZ signal distributions in simulation: W lepton (left) and Z lepton (right) η.

Once leptons and missing transverse energy are selected, we can reconstruct the

Z and W bosons. The invariant dilepton mass of the Z boson is shown in Figure 7.13 The Z boson mass shows the selection requirement $81 < m_{ll} < 101$ GeV at the reconstruction level. Although the lepton p_T and η resolutions are very good, the detector resolution effects are apparent for a narrow resonance like the Z boson in which the reconstructed invariant mass is significantly wider than the true mass with a natural width of 2.5 GeV. As discussed in Section 7.2.2, the muon detector resolution contributes between 2 and 3 GeV to the width of the reconstructed Z boson, and the electron detector resolution, discussed in Section 7.2.3, contributes between 1 and 2 GeV. The detector resolution effects can be modeled as a Gaussian distribution convoluted with the true Z boson Breit-Wigner distribution. The reconstructed dilepton invariant mass distribution has an asymmetric tail at lower values of Z mass, due to the contribution from events in which a lepton radiates a photon whose energy is not accounted for in the calculation of the dilepton invariant mass.

The W transverse mass distribution is also shown in Figure 7.13. We calculate the W transverse mass, M_T^W, from the missing transverse energy magnitude, E_T^{miss}, the azimuthal direction of the missing transverse energy, ϕ^{miss}, and the transverse momentum and azimuthal angle of the W lepton, respectively p_T^l and ϕ^l:

$$M_T^W = \sqrt{2 \times p_T^l \times E_T^{miss} \times (1 - cos(\phi^l - \phi^{miss}))} \tag{7.16}$$

For the truth distributions, the M_T^W is built from the true charged lepton and true neutrino p_T and ϕ. The reconstructed distribution shows the effect of the selection requirement $M_T^W > 20$ GeV. There is a significant difference in the shape between the reconstructed and truth distributions passing all selections. This is largely due to the missing transverse energy resolution in the detector, although the lepton p_T resolution

contributes to a lesser degree. At truth level, the distribution has a Jacobian peak at the W mass. The missing transverse energy resolution smears out the Jacobian peak.

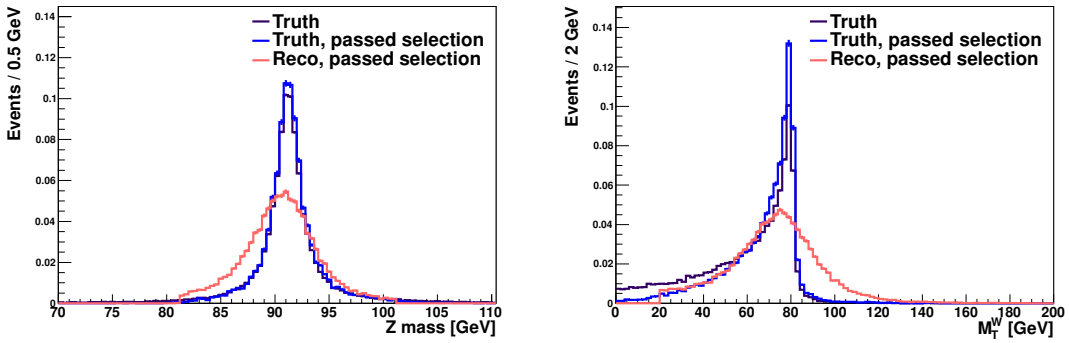

Figure 7.13: WZ signal distributions in simulation: Z mass (left) and W_{m_T} (right).

The distribution of Z boson p_T is shown in Figure 7.14. The truth distribution reaches a maximum at 30 GeV and has a mean of 56 GeV (same for the W boson, whose p_T can not be easily reconstructed.) For comparison, single Z boson production at the LHC produces Z bosons with a mode of $p_T = 5$ GeV. Although the truth and reconstructed level distributions do not agree exactly at the peak, the tail of the truth distribution is well modeled after reconstruction. This is important because p_T^Z is one of the kinematic variables most sensitive to WZ production with anomalous triple gauge couplings, and the sensitivity is highest at large p_T^Z.

Figure 7.15 shows the Z boson rapidity and η distributions. The rapidity distribution at truth level reaches a maximum at 0 and falls off completely by 4. The selection requirements select for centrally produced bosons, and after selection the highest rapidity Z bosons are at 2.5. The pseudo-rapidity η is an approximation to the rapidity for massless particles; because the Z is massive, the approximation is not

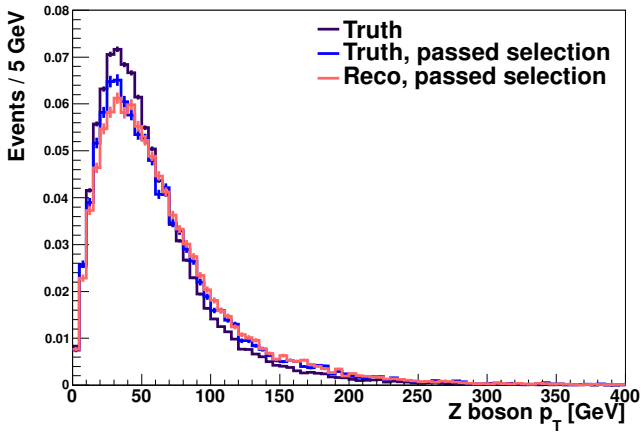

Figure 7.14: WZ signal distributions in simulation: Z p_T.

very good and produces the dip at $\eta = 0$.

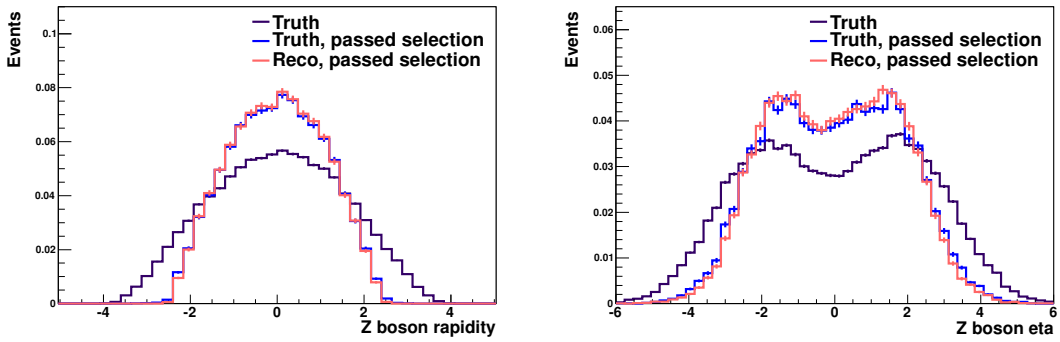

Figure 7.15: WZ signal distributions in simulation: Z rapidity (left) and $Z\eta$ (right).

Finally, we can use the selected Z and W bosons to probe the WZ system. In Figure 7.16, the invariant mass and the rapidity of the WZ system is shown. To reconstruct the WZ system, the W mass is used as a constraint to solve for the W four-vector.[1] This algorithm does a reasonable job of reconstructing the WZ mass, as shown in Figure 7.16. The mode of the WZ invariant mass distribution at truth

[1]In the case of two real solutions, the solution yielding the lower neutrino $|p_Z|$ is selected.

level is 220 GeV, with a mean of 306 GeV and a tail going up to 1000 GeV - WZ events are often produced highly energetic collisions. The WZ rapidity distribution shows that WZ pairs are produced centrally, with a central distribution that falls off to zero by a rapidity of 3. Due to the lepton η and p_T requirements, the WZ selection preferentially selects for centrally produced WZ pairs. Moreover, selecting the smaller value of neutrino longitudinal momentum in reconstructing the W boson, when there are two solutions, biases the reconstructed WZ rapidity toward a central rapidity.

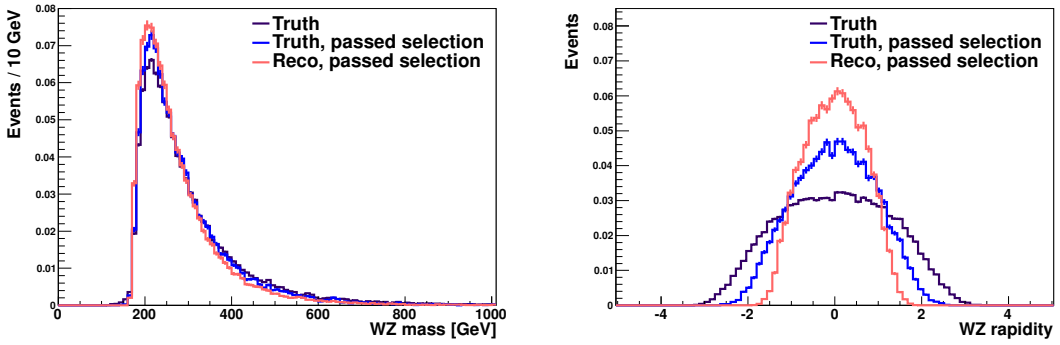

Figure 7.16: WZ signal distributions in simulation: WZ mass (left) and rapidity (right).

Chapter 8

Event Selection

In selecting WZ events, we aim to separate a very small signal from processes with production cross-sections many orders of magnitude larger. For every trillion collisions, we expect to reconstruct and identify about one $W^{\pm}Z \to \ell\nu\ell'\ell'$ event. However, $W^{\pm}Z \to \ell\nu\ell'\ell'$ events have two distinctive features that allow us to effectively select signal events while strongly rejecting background processes: three high p_T, isolated leptons from the Z and W decays and missing transverse energy from the neutrino from the W boson.

The selection requirements outlined in this chapter are designed to discriminate against background events while efficiently selecting WZ signal events. Selection requirements are imposed on the leptons to ensure that they are in a fiducial region of the detector in which their momentum can be well measured. After selecting three high p_T, isolated leptons and missing transverse energy, we require that one pair of oppositely charged leptons has a mass consistent with a Z boson, and that the missing transverse energy and third lepton pass a selection on W transverse

mass. Finally, event level selections reject a small percentage of events in which the missing transverse energy cannot be well reconstructed due to electronic noise in the calorimeters.

8.1 Data Sample

This analysis uses a data sample of proton-proton collisions collected between April 2011 and October 2011 at $\sqrt{s} = 7$ TeV at the LHC. This dataset corresponds to data periods D through M of the 2011 data and has an integrated luminosity of 4.64 fb^{-1}. The luminosity uncertainty for 2011 data is 1.8% [43]. Data is taken from both the *physics_Muons* and *physics_Egamma* trigger streams (see Section 6.4).

The data has been reconstructed offline with Athena release 17.0 [16]. The data is processed by the Standard Model W and Z physics group into the D3PD format, which is an ATLAS ROOT-based ntuple. The first selection step is performed to reduce the dataset size by selecting a dilepton sample: events from the muon and electron trigger streams are kept only if the event contains at least two leptons with $p_T > 13$ GeV. To further reduce the size of the dilepton dataset, at least one of the leptons must have $p_T > 15$ GeV and must be a combined muon or an electron passing the loose++ criteria. This dataset has the NTUP_SMDILEP tag and is the starting point for the WZ event selection outlined below.

8.2 Overview of selection

We select $W^{\pm}Z \to \ell\nu\ell'\ell'$ events by requiring two leptons that are consistent with a Z boson decay and a third lepton and missing transverse energy that are consistent with a W boson decay. The leptons can be either electrons or muons. The Z and W boson can each decay to muons or electrons, and there are four combinations of lepton flavors which we call channels: $eee\nu$, $ee\mu\nu$, $\mu\mu e\nu$, and $\mu\mu\mu\nu$.

The WZ event selection is broken down into several stages. First, in the event pre-selection, trigger requirements are imposed and event level selections ensure that the detector was functioning well at the time the data was collected.

Next, we identify well reconstructed, isolated electrons and muons in our sample. The leptons must be within $|\eta| < 2.5$ and have $p_T > 15$ GeV.

Finally, we use the leptons and missing transverse energy to reconstruct and select Z and W bosons in the sample. Additional selection requirements are imposed on the lepton from the W boson to further reject background events.

8.3 Event Pre-selection

The first step in selecting WZ events is to look for events that fired either a single muon or a single electron trigger. The signal events have three high p_T, isolated leptons, and the probability that at least one of them fired a single lepton trigger is above 98%. We use the lowest p_T un-prescaled single muon and electron triggers available. The triggers used for the WZ analysis are summarized in Table 6.1 and details on the trigger selection are provided in Section 6.5.

There are several event level selections imposed to ensure that the events in our sample are well measured by the detector. First, we require that the event be taken during a period when all sub-detectors necessary for the analysis – the inner detector, calorimeters, muon spectrometer, magnets, luminosity detectors, and trigger and data acquisition systems – were functioning properly. The data quality is stored in a *Good Run List (GRL)* as a function of luminosity block (two minute interval), which is produced by the data quality group. We require our events to be on a GRL tailored for analyses which use W bosons.[1] The calculated luminosity of our data sample correctly accounts for events which are vetoed by the GRL.

To reject events that are not consistent with a proton-proton collision, we require that each event have a reconstructed primary vertex with at least 3 associated tracks. For each vertex with at least 3 tracks in the event, the sum of the momentum of the tracks associated to the vertex is calculated:

$$\sum_{i=1}^{n \text{ tracks}} p_{T \text{ tracks}}^2 \tag{8.1}$$

The primary vertex is defined as the vertex in the event for which this quantity is the largest.

It is essential that the missing transverse energy is well reconstructed in each event in order to reconstruct the W boson in our events. The Liquid Argon calorimeter occasionally has large, coherent electronic noise spikes that interfere with the measurement of energy deposition in the calorimeter cells. Events in which a part of the LAr Calorimeter has been identified as having a noise spike are rejected. This

[1] data11_7TeV.periodAllYear_DetStatus-v36-pro10_CoolRunQuery-00-04-08_WZjets_allchannels_DtoM.xml

requirement rejects about 0.3% of events. Additionally, events are rejected if they contain a jet with $p_T > 20$ GeV, that does not overlap ($\Delta R > 0.3$) with a selected lepton, whose electromagnetic calorimeter signal is out of time with the collision or consistent with electronic noise in the Liquid Argon Calorimeter. This selection drops 0.1% of events.

8.4 Muon Selection

The muons used in this analysis are reconstructed offline using the STACO algorithm described in Section 5.3. Muons from the decay of the Z boson can be either combined or segment-tagged muons. Including segment-tagged muons, which are inner detector tracks with one or two matched segments in the muon spectrometer, increases the efficiency for identifying muons in the transition region of the spectrometer.

Muons are required to fall inside the coverage of the inner detector, $|\eta| < 2.5$, and the transverse momentum of the muons must be larger than 15 GeV.

After selecting STACO combined or segment-tagged muons, we impose additional selection requirements on the inner detector track associated to the muon. The inner detector track determines the reconstructed momenta for segment-tagged muons, dominates the momentum resolution for combined muons up to 50 GeV, and contributes roughly equally with the muon spectrometer measurement to the resolution for muons in the range $50 < p_T < 100$ GeV [29]. Therefore, it is important that the inner detector track have enough hits to be accurately constrained. Hit requirements on the inner detector track for muons also help reject decay-in-flight backgrounds.

The summary of hit requirements on the inner detector track for muons is listed in Table 8.1, and details are provided below:

- *B-layer*: At least 1 hit in the Pixel B-layer if the track crosses an active B-layer sensor.
- *Pixels*: At least 2 hits in the Pixels. If the track crosses a known dead channel, it is counted as a hit.
- *SCT*: At least 6 hits in the silicon strip tracker, where dead sensors crossed are counted as hits.
- *Pixel or SCT Holes*: No more than 2 holes on the combined Pixel+SCT track. If the track crosses a working sensor but does not register a hit, it counts as a hole.
- *TRT Hits*: If the track has $|\eta| < 1.9$, within the full coverage of the TRT detector, the track must have at least 6 TRT hits, including outliers.
- *TRT Outlier Threshold*: If the track is within $|\eta| < 1.9$, the ratio of TRT Outlier hits to all TRT hits must be less than 0.9. The outlier requirement must be also met by tracks with $|\eta| > 1.9$ if they have at least 6 TRT hits.

Collectively, the requirements on the inner detector track remove about 2% of muons with $p_T > 15$ GeV. The distribution of track variables before the selections have been applied, for W muon candidates in Z + lepton events, can be seen in Figure 8.1 for the silicon track variables and in Figure 8.2 for the TRT track variables.

To ensure that all muons used to build the W and Z candidates come from the primary vertex in the event, requirements are placed on the muon longitudinal impact parameter, z_0, and on the muon transverse impact parameter, d_0. The distance between the muon z_0 and the z position of the primary vertex, z^{vertex}, must meet the requirement:

$$\left|z_0 - z^{vertex}\right| < 1 \text{ mm} \tag{8.2}$$

Rather than imposing selection requirements directly on the muon d_0, selection is based on the d_0 significance, which is defined as the transverse impact parameter d_0 over its uncertainty. The d_0 significance for each muon must meet the following requirement:

$$|d_0 \text{ significance}| < 3\sigma \tag{8.3}$$

Together, these requirements reject cosmic muons, muons from b or c quark decay in Z + jet and $t\bar{t}$ events, and muons from other vertices in the same event. The W candidate muon d_0 and d_0 significance distributions before this selection have been applied can be seen in Figure 8.3.

The largest source of events containing a Z boson and an additional muon are Z + jet events in which a jet produces a muon from b quark, c quark, or meson decay. To reject muons from hadronic jets, we look for muons that are spatially separated from jets by imposing an isolation criteria based on the sum p_T of inner detector tracks near the muon candidate. The specific requirement for muon isolation is:

$$\frac{\sum_{i=1}^{n \text{ tracks within } \Delta R<0.3} p_T^{\text{tracks}}}{p_T^{\text{muon}}} < 0.15 \tag{8.4}$$

The numerator of the right hand of equation 8.4, which is the sum of the p_T of inner detector tracks in a cone of $\Delta R < 0.3$ around the muon, is called *ptCone30*. All inner

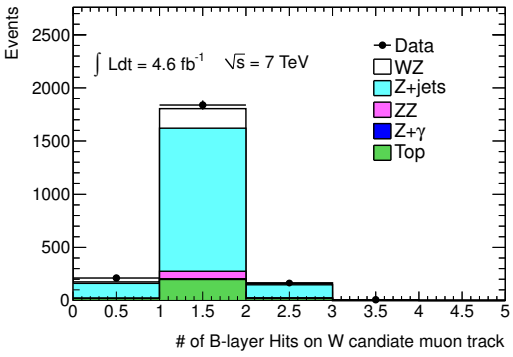

(a) We require at least 1 B-layer hit

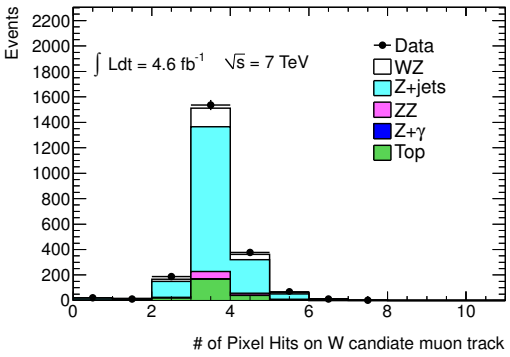

(b) We require at least 2 Pixel hits

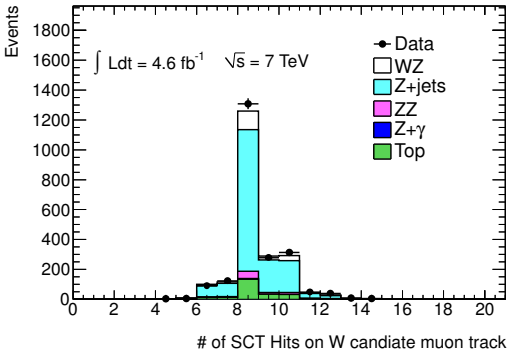

(c) We require at least 6 SCT hits

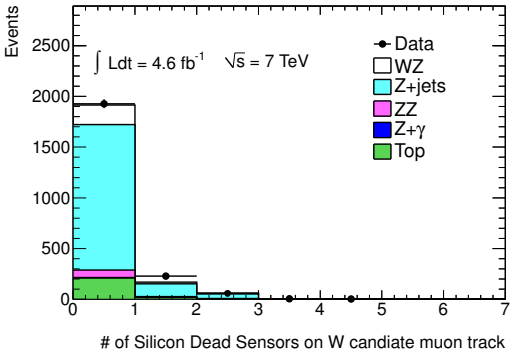

(d) Dead sensors count as hits on track

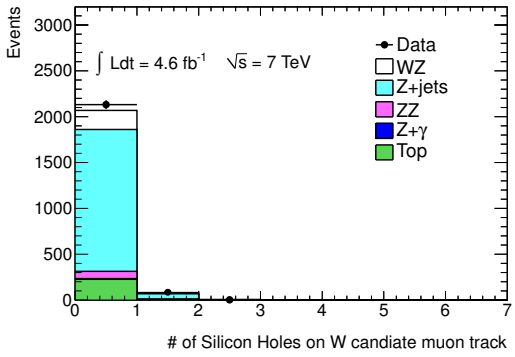

(e) We require fewer than 3 holes

Figure 8.1: The distribution of ID silicon track variables for W candidate muons in Z + muon events, before the selections on these variables have been applied. The Z+jets and $t\bar{t}$ backgrounds are MC normalized by data-driven estimates; all other processes are taken from MC. The requirements we place on these variables reject only a small number of tracks (2% in total).

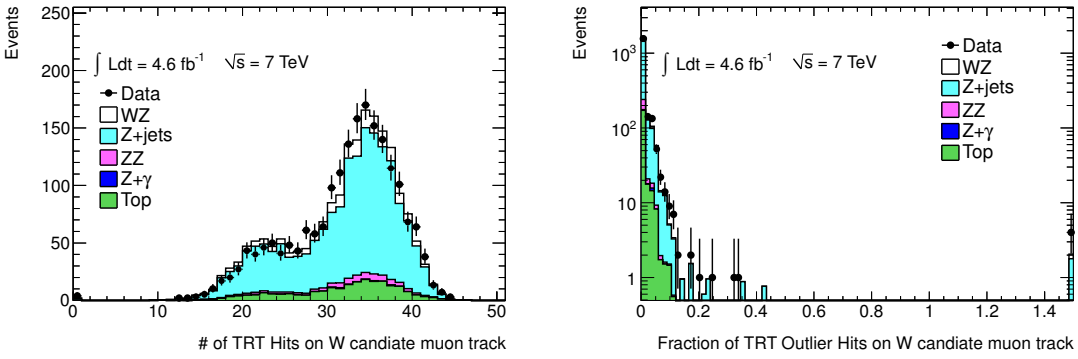

(a) We require at least 6 TRT hits

(b) We require TRT outlier fraction < 0.9

Figure 8.2: The distribution of TRT ID track variables for W candidate muons in Z + third muon events, before the selections on these variables have been applied. The Z+jets and $t\bar{t}$ backgrounds are MC normalized by data-driven estimates; all other processes are taken from MC. The requirements we place on these variables reject only a small number of tracks.

detector tracks used in the calculation of *ptCone30* are required to originate from the primary vertex, which significantly reduces the contribution from other collisions within the same event. This isolation requirement, which is imposed on all muons in the event, can be seen in Figure 8.4 for the third muon in Z + muon events.

The number of muons that pass each selection requirement in data is reported in Table 8.2.

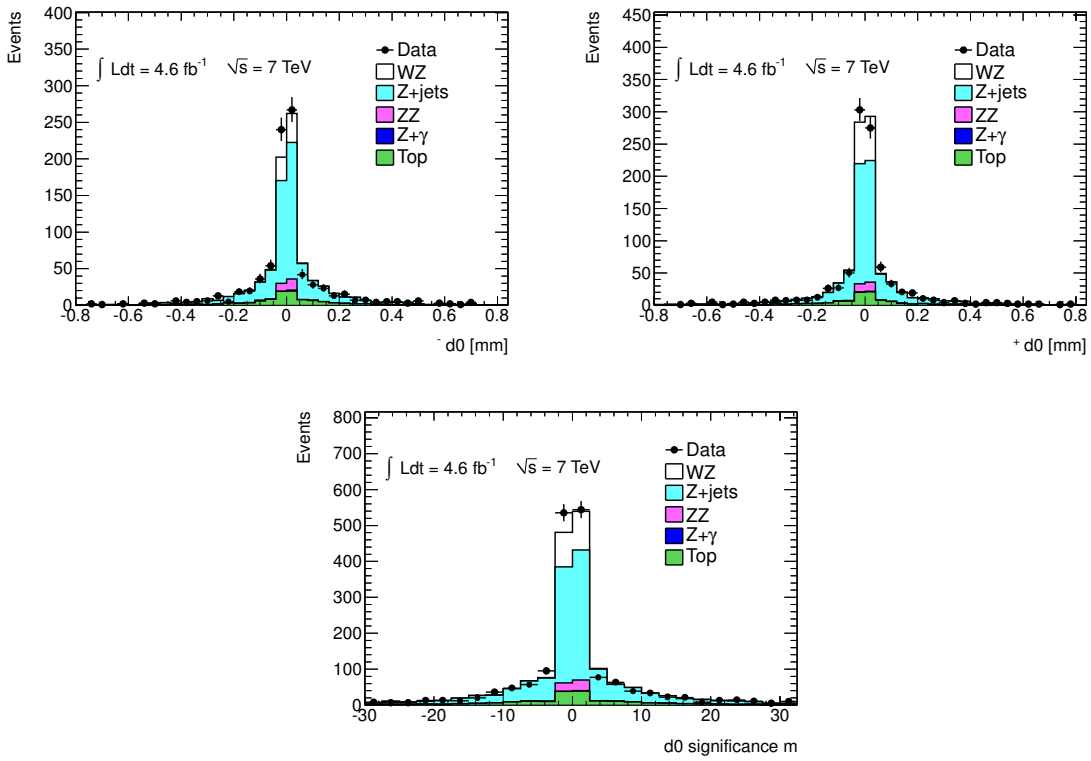

Figure 8.3: Muon transverse impact parameter significance. The d_0 distribution for negatively charged muons (top left), positively charged muons (top right), and d_0 significance (bottom) distributions for the third muon in Z + muon events. A requirement of d_0 significance < 3 is applied to reject muons that do not originate from the primary vertex in the event, including muons from the decay of b and c quarks. The Z+jets and $t\bar{t}$ backgrounds are MC normalized by data-driven estimates; all other processes are taken from MC.

Table 8.1: Selection requirements for muons.

Selection	Details
Algorithm	Combined or Segment-Tagged STACO muons
p_T	$p_T > 15$ GeV
η	$\lvert\eta\rvert < 2.5$
z_0	$\lvert z_0\rvert < 1$ mm
d_0	$\lvert d_0$ significance$\rvert < 3\sigma$
Isolation	$\frac{ptCone30}{p_T} < 0.15$
ID Track	≥ 1 B-layer hit (if expected)
	≥ 2 Pixel Hits
	≥ 6 SCT Hits
	≤ 3 Pixel+SCT Holes
	If $\lvert\eta\rvert < 1.9$: ≥ 6 TRT Hits
	If $\lvert\eta\rvert < 1.9$: $\frac{\#TRTOutliers}{\#TRTOutliers+\#TRTHits} < 0.9$
	If $\lvert\eta\rvert > 1.9$ and ≥ 6 TRT hits: $\frac{\#TRTOutliers}{\#TRTOutliers+\#TRTHits} < 0.9$

Table 8.2: The number of reconstructed muons in our sample that pass each selection requirement. Muon selection is performed after the event primary vertex selection. No events are rejected during muon selection and there may be more than one selected muon per event. The tighter selection requirements applied to the W muon are not included at this stage.

Selection	Number of Muons Passing
Algorithm	217,503,359
p_T	178,349,198
ID Track Hit Requirements	175,185,104
η	175,149,715
z_0	172,826,936
Isolation	70,576,489

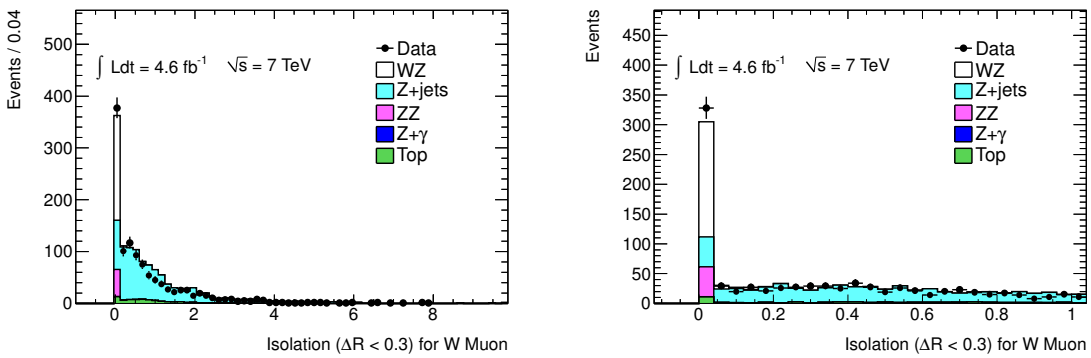

Figure 8.4: Muon isolation. The sum of the p_T of all inner detector tracks in a cone of $\Delta R < 0.3$ around the muon, divided by the muon p_T, for W candidate muons in Z + muon events. The right plot is a zoom of the left distribution. Selecting muons with $\frac{ptCone30}{p_T} < 0.15$ rejects secondary muons from hadronic jets in both Z + jet and $t\bar{t}$ events. The Z+jets and $t\bar{t}$ backgrounds are MC normalized by data-driven estimates; all other processes are taken from MC.

8.5 Electron Selection

We select well-measured electrons by requiring that the electrons are within the coverage of the inner detector tracking; the electrons must be reconstructed using a cluster with $|\eta| < 2.47$. To avoid the transition region between the barrel and endcap calorimeters where energy is not well measured, electrons with clusters with $1.37 < |\eta| < 1.52$ are not accepted.

The energy of the electron candidates is taken from the calorimeter measurement, while the η and ϕ measurements are taken from the track. Using transverse energy defined with the cluster energy and track η, we require that electrons have $E_T > 15$ GeV.

Electrons are reconstructed from a cluster in the electromagnetic calorimeter and a matched track from the inner detector (see Section 5.4). Reconstructed electrons in ATLAS are classified into six different qualities: loose, loose++, medium, medium++,

tight, and tight++, with increased electron purity and decreased selection efficiency moving from loose to tight++. The full list of selection variables on which the quality classification is based is shown in Table 5.1. To select the quality requirements for the W and Z electrons, we compare the significance of the selected sample for each combination of W electron quality and Z electron quality, where significance is defined by:

$$\frac{S}{\sqrt{S+B}} \tag{8.5}$$

where S is the number of simulated signal events passing all selection and B is the number of expected background events. The number of expected signal and background events for 4.7 fb^{-1}, along with the significance, is shown in Figure 8.5 for all combinations of Z and W electron quality requirements. Requiring the Z electrons to pass the loose++ requirements and the W electrons to pass the tight++ requirements maximizes our expected significance. Qualitatively, this makes sense because it is harder for two jets to fake a $Z \to ee$ candidate than for one jet to fake a W candidate, so imposing tight requirements on the W electron reduces background while keeping the Z electron selection less restrictive increases the signal acceptance.

Some of the readout electronics of the Liquid Argon calorimeter did not function correctly during data-taking, and some cells were dead or masked as a result of electronics problems. To ensure that the the energy of the electrons used in our analysis was measured accurately, the electron candidates are required to pass an object quality check that removes electrons if the cluster is affected by at least one of these conditions:

1. The presence of a dead front-end board in the first or second sampling layer,

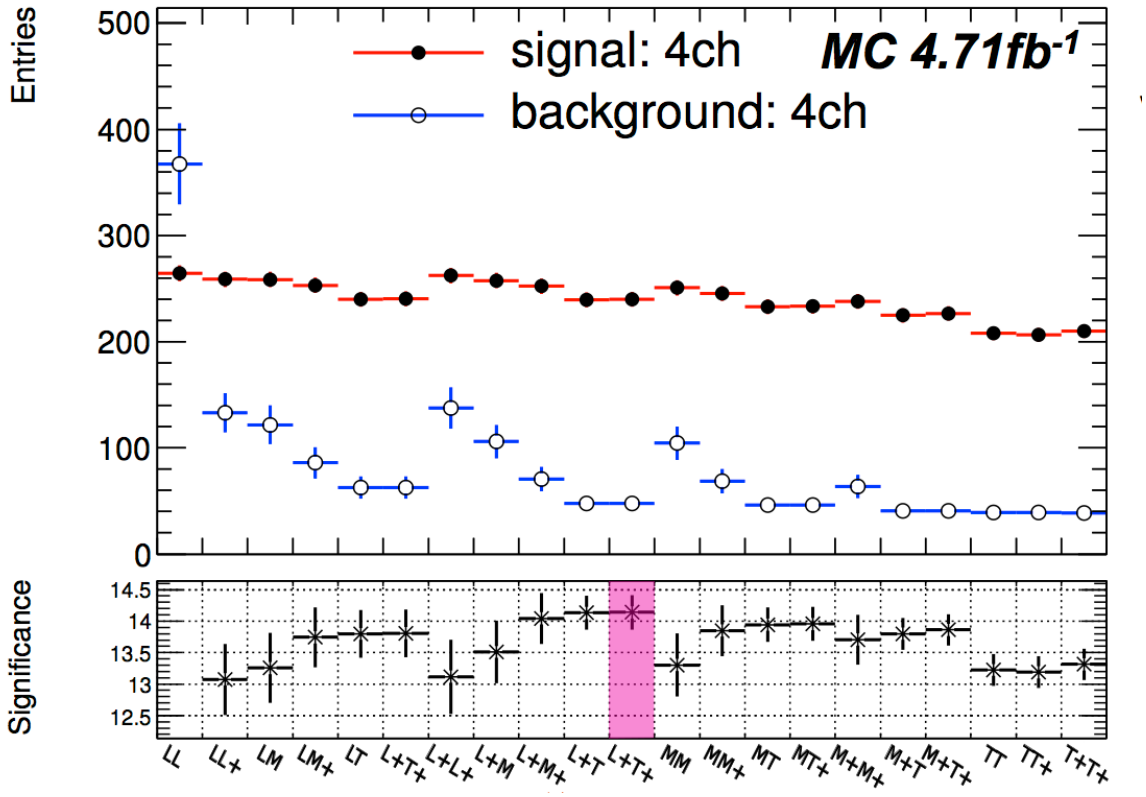

Figure 8.5: The number of expected WZ signal and background (Z+jets, $Z+\gamma$, $t\bar{t}$, and ZZ) events and expected significance of selected sample as a function of the quality requirement for Z and W electrons, from simulation. The number of expected events and significance is shown for all four channels combined. The electron qualities are listed as Z electron quality followed by W electron quality, and the abbreviations are: L = loose, M = medium, T = tight, and + stands for ++. The highest significance, which is highlighted in pink, is obtained by selecting loose++ Z electrons and tight++ W electrons.

2. A dead region affecting the three samplings,

3. A masked cell in the core.

Altogether, these requirements on the electron data-quality remove fewer than 1% of all electrons.

As with muon candidates, electrons are selected to be consistent with coming from the primary vertex by requiring that the electron z_0, with respect to the primary vertex, meet the condition:

$$|z_0| < 1 \text{ mm} \tag{8.6}$$

and the d_0 significance, with respect to the primary vertex, must pass:

$$|d_0 \text{ significance}| < 10\sigma \tag{8.7}$$

The d_0 significance requirement is looser for electrons than for muons because Bremsstrahlung radiation causes a broader smearing of the d_0 significance distribution for electrons than for muons. This can be seen in Figure 8.6, which shows the d_0 distribution separately for positive and negative electrons. The energy loss due to Bremsstrahlung causes positive and negative electrons to curve in opposite directions, producing complementary asymmetric tails in the d_0 distributions.

Hadronic jets can leave energy depositions in the calorimeters that are reconstructed as electrons; jets can also contain real electrons from decays within the jet. As W and Z decays produce isolated electrons, we select against hadronic backgrounds by requiring that electron candidates are spatially separated from jets. We impose two isolation criteria. The first uses the *ptCone30* isolation variable also used

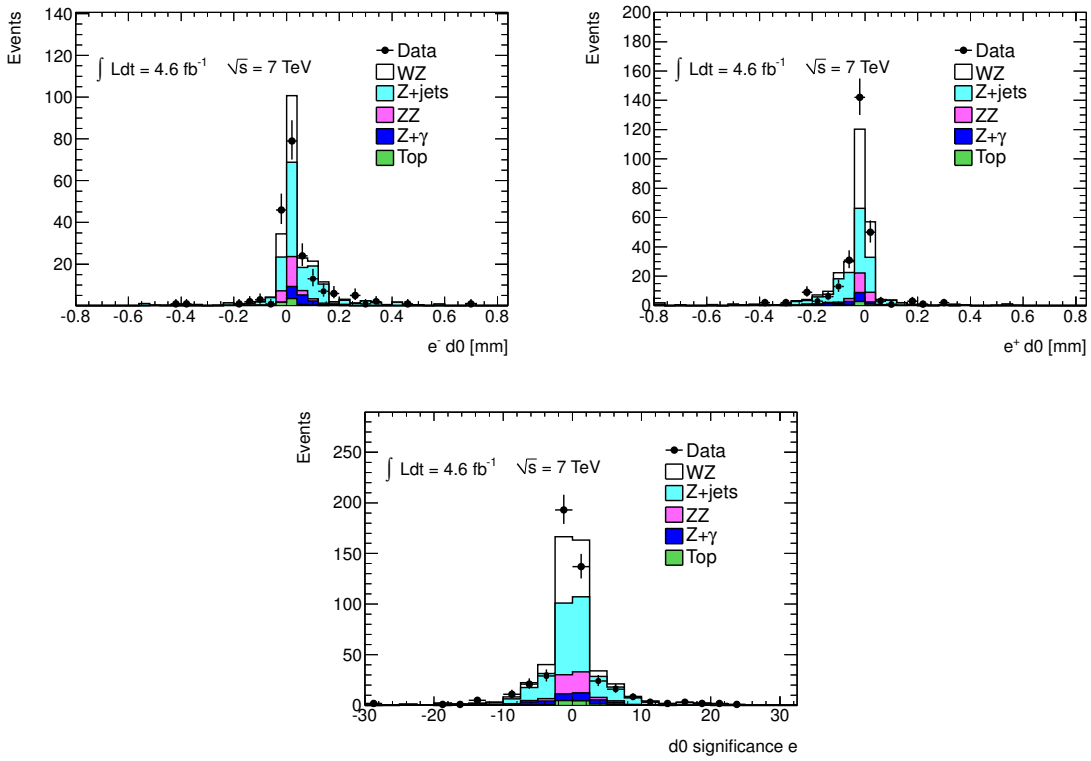

Figure 8.6: Electron transverse impact parameter significance. The d_0 distribution for negatively charged electrons (top left), positively charged electrons (top right), and d_0 significance (bottom) distributions for the third electron in Z + electron events. A requirement of d_0 significance < 10 is applied to reject electrons that do not originate from the primary vertex in the event. The Z+jets and $t\bar{t}$ backgrounds are MC normalized by data-driven estimates; all other processes are taken from MC.

for imposing muon isolation:

$$\frac{\sum_{i=1}^{n \text{ tracks within } \Delta R<0.3} p_T^{\text{tracks}}}{p_T^{\text{electron}}} < 0.13 \tag{8.8}$$

All inner detector tracks used in the calculation of *ptCone30* are required to originate from the primary vertex, which significantly reduces the contribution from other collisions within the same event. The second criteria uses the sum of the calorimeter E_T in a cone of $\Delta R < 0.3$ around the electron, the *EtCone30* isolation variable:

$$\frac{\sum_{i=1}^{n \text{ calo cells within } \Delta R<0.3} E_T^{\text{cells}}}{E_T^{\text{electron}}} < 0.14 \tag{8.9}$$

The calculation of *EtCone30* includes cells from the electromagnetic and hadronic calorimeters, and excludes a 5×7 $\eta \times \phi$ grid of cells at the center of the cone where the electron energy is deposited. The calculation of *EtCone30* includes a correction for energy depositions from other collisions in the same event [19]. The calorimeter-based isolation distribution can be seen in Figure 8.7 for the third electron in Z + electron events.

In rare cases, a muon passing through the calorimeter can radiate an energetic photon, which converts to an electron-positron pair, one of which may pass our E_T threshold. To ensure that muons are not also reconstructed as electrons in this case, reconstructed electrons are thrown away if they are within $\Delta R < 0.1$ of any selected muon. Similarly, an energetic electron could emit Bremsstrahlung that produces a nearby electron or positron of sizable energy. If two electrons overlap within $\Delta < 0.1$, the lower-p_T electron is not counted or selected. The overlap removal affects less than 0.01% of selected electrons.

The electron selection requirements are summarized in Table 8.3 and the number of electron candidates found in the data sample is shown in Table 8.4.

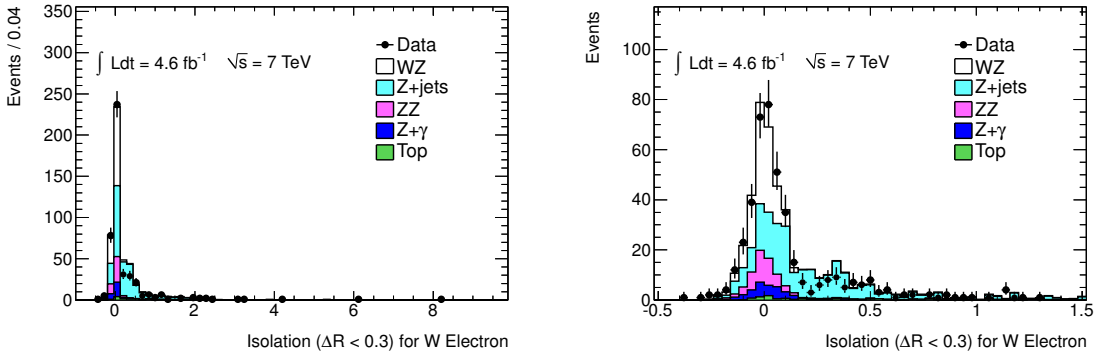

Figure 8.7: Electron isolation, where isolation is the distribution of the sum of the calorimeter E_T in a cone of $\Delta R < 0.3$ around the electron, divided by the electron E_T, for W candidate electrons in Z + electron events. The right plot is a zoom of the left distribution. Selecting electrons with $\frac{EtCone30}{E_T} < 0.13$ rejects secondary electrons and jets that mimic electrons from hadronic jets in both Z + jet and $t\bar{t}$ events. The Z+jets and $t\bar{t}$ backgrounds are MC normalized by data-driven estimates; all other processes are taken from MC.

Table 8.3: Selection requirements for electrons.

Selection	Details
Algorithm	Central calo + ID track
E_T	$E_T > 15$ GeV
η	$\lvert\eta\rvert < 1.37$ or $1.52 < \lvert\eta\rvert < 2.47$
Quality	loose++
OQ: LAr Quality	OQ &&1446 == 0
z_0	$\lvert z_0\rvert < 1$ mm
d_0	$\lvert d_0$ significance$\rvert < 10\sigma$
Isolation	$\frac{EtCone30}{E_T} < 0.14$ and $\frac{ptCone30}{p_T} < 0.13$

Table 8.4: The number of reconstructed electrons in our sample that pass each selection requirement. Electron selection is performed after the event primary vertex selection. No events are rejected during electron selection and there may be more than one selected electron per event. The requirements do not include the tighter selections applied to the W lepton at this stage.

Selection	Number of Electrons Passing
Algorithm	751,729,311
OQ	746,556,814
E_T	238,396,088
η	212,194,201
loose++ quality	140,912,755
z_0	135,258,392
Isolation	86,573,810
Overlap with electrons	86,573,714
Overlap with muons	86,555,518

8.6 WZ Event Selection

A summary of the WZ event selection is shown in Table 8.5.

After the event pre-selection and lepton selection, Z candidates are selected by requiring two leptons with the same flavor and opposite charge with an invariant mass consistent with the Z mass:

$$|M_{ll} - 91.1876| < 10 \text{ GeV} \tag{8.10}$$

If more than one pair of leptons form a Z candidate, the candidate with the invariant mass closest 91.1876 is selected.

The invariant mass of Z candidates before the mass requirement is imposed is shown in Figure 8.8. Additionally, the number of leptons and reconstructed vertices in the selected Z sample are shown in Figure 8.9, the missing transverse energy distribution is shown in Figure 8.10, the rapidity of the selected Z bosons is shown in Figure 8.11, and the η, p_T, and ϕ distributions of the leading Z lepton are shown

Table 8.5: WZ event selection in data and simulation. For requirements on selected muons and electrons, see Tables 8.1 and 8.3 respectively. For details on the trigger selection, see Table 6.1.

Selection	Details
Good Runs List	Event on Good Runs Lists (data only)
Trigger	Single muon or electron trigger
Primary Vertex	Primary vertex must have at least 3 tracks
E_T^{miss} Cleaning	No out of time jets with $p_T > 20$
E_T^{miss}Cleaning	Veto data events w/ LAr Calo noise error flag
Z candidate	$\lvert M_{ll} - 91.1876\rvert < 10$ GeV
3 Leptons	≥ 3 electrons and/or muons
W muon requirements	Combined muon, $p_T > 20$ GeV
W electron requirements	Tight++ quality, $p_T > 20$ GeV
E_T^{miss}selection	$E_T^{miss} > 25$ GeV
W transverse mass	$M_T^W > 20$ GeV
Trigger Matching	One of Z or W leptons must match trigger lepton
Trigger Matched muon	$p_T > 20$ GeV
Trigger Matched electron	$p_T > 25$ GeV

in Figures 8.12, 8.13, and 8.14. The normalization for the processes shown is taken from their theoretical cross section and the $Z \to \ell\ell$ Monte Carlo is simulated by ALPGEN. There are more Z candidates observed in data than predicted by the simulation; moreover, the Z rapidity and lepton η distributions do not agree between data and simulation in the central region of the detector. This was traced to the fact that this particular ALPGEN simulation was produced with leading-order parton distribution functions (CTEQ6L1) that do not seem to reproduce the data well. When the ALPGEN sample is reweighted to have next-to-leading order parton distribution functions, the agreement improves [26]. However, as we use data-driven techniques to estimate the Z+jets background to WZ events (see Section 9.1), the discrepancies between data and simulation in the Z sample are not a concern for this analysis.

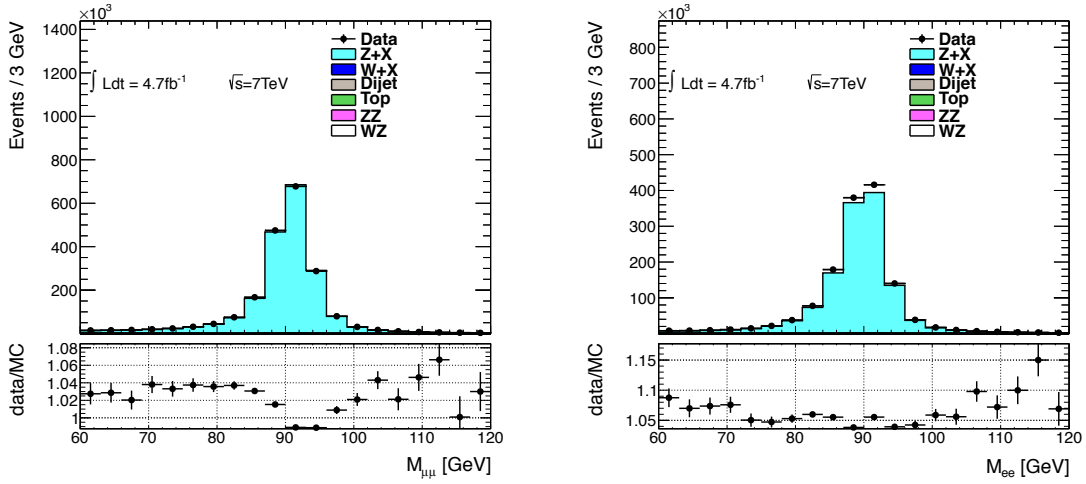

Figure 8.8: The invariant mass distribution of $Z \to \mu\mu$ (left) and $Z \to ee$ (right) candidates before the Z mass requirement is imposed.

After the Z boson is selected, we require that the event must have a third lepton. The W candidate lepton must meet stricter criteria than the Z leptons in order to reduce background from Z+jets events. The additional requirements on the W lepton

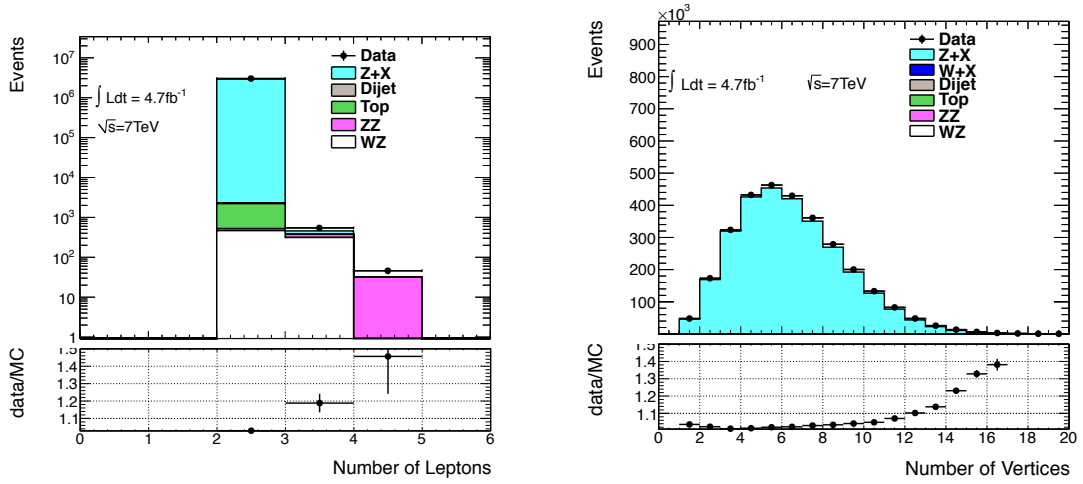

Figure 8.9: The number of selected leptons (left) and reconstructed vertices (right) in selected Z events.

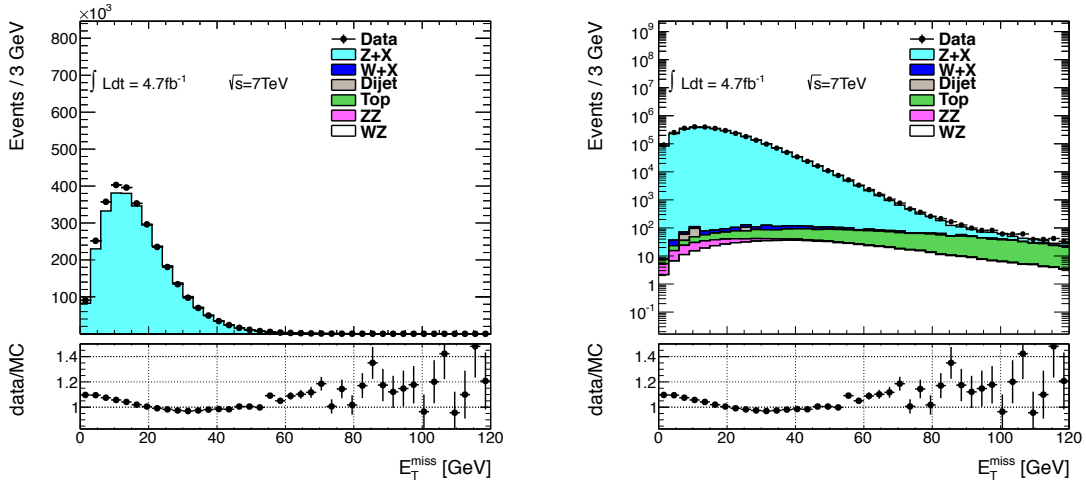

Figure 8.10: The missing transverse energy distribution in selected Z events in linear (left) and log (right) scales.

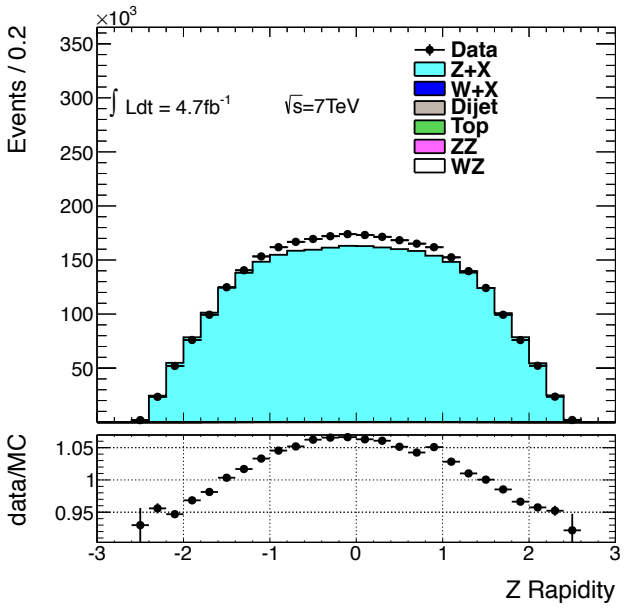

Figure 8.11: The Z boson rapidity for selected Z events.

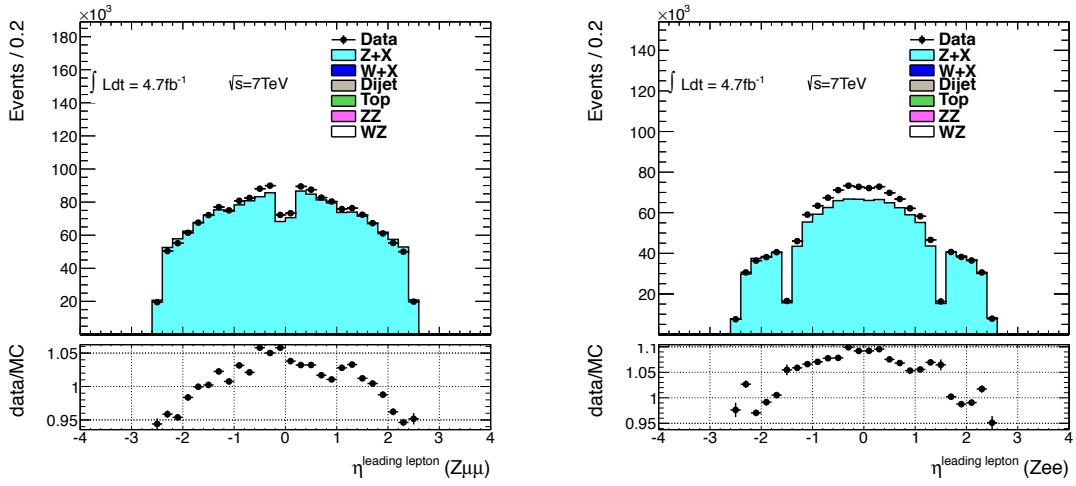

Figure 8.12: The η distributions for the leading muons (left) and electrons (right) in selected Z events. The muons already have a requirement of $\eta < 2.5$ applied; the dip in the distribution at $\eta = 0$ is due to holes in the muon chamber coverage to allow cables to pass out of the detector. Electrons are excluded from the crack between the endcap and barrel calorimeter around $\eta = 1.5$.

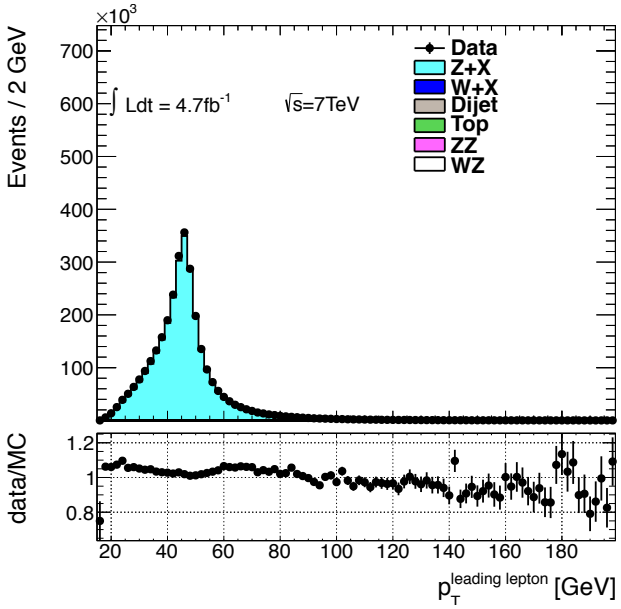

Figure 8.13: The p_T distributions for leading leptons in selected Z events. The requirement of $p_T > 15$ GeV has already been applied.

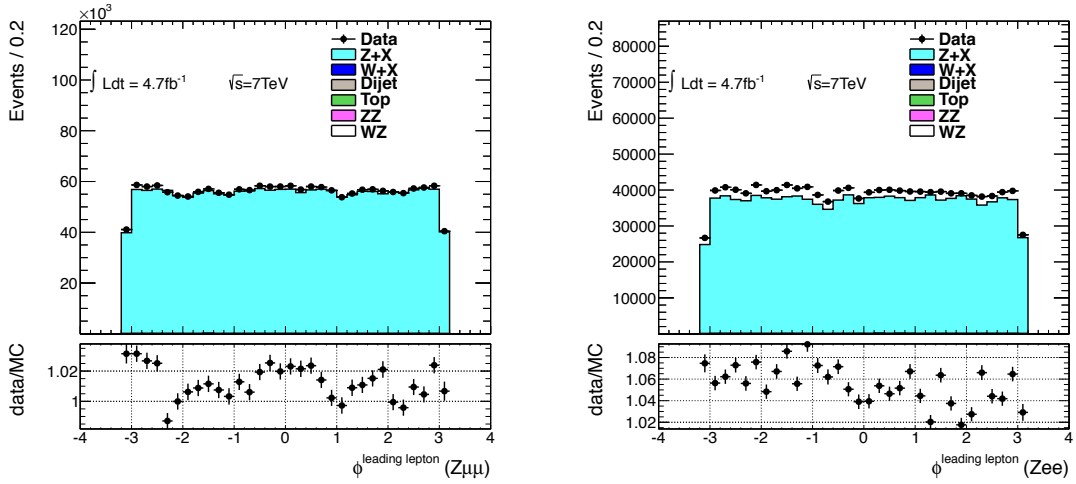

Figure 8.14: The ϕ distributions for the leading muons (left) and electrons (right) in selected Z events.

are:

1. W candidate lepton $p_T > 20$ GeV.

2. W electrons must pass the tight++ quality.

3. W muons must be combined muons.

The transverse momenta distribution of W candidate leptons is shown in Figure 8.15.

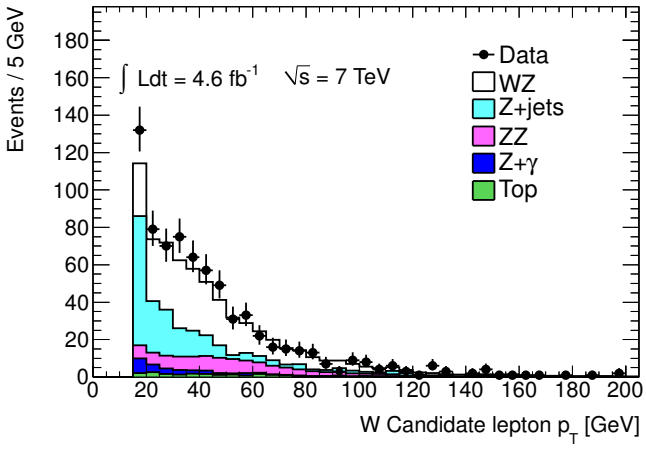

Figure 8.15: Lepton transverse momentum distribution in Z + lepton events. The p_T distribution of the third lepton in Z + lepton events after requiring a third selected lepton. We require the W candidate lepton to have $p_T > 20$ GeV, which removes significant background from Z + jet events. The Z+jets and $t\bar{t}$ backgrounds are MC normalized by data-driven estimates; all other processes are taken from MC.

To reject Z+jets, ZZ and $Z + \gamma$ backgrounds remaining after requiring three leptons in the event, we require the event to have missing transverse energy greater than 25 GeV. The missing transverse energy distribution of events with three selected leptons, including two which form a Z candidate, is shown in Figure 8.16. A W candidate is formed with the third lepton and the missing transverse energy. We require that the transverse mass of the W candidate (see equation 7.16), shown in

Figure 8.17, be greater than 20 GeV to remove Z+jets and ZZ events. In data, there are more W candidates with a transverse mass between 60 and 80 GeV than predicted by the simulation. The significance of the excess is between four and five sigma, depending on the binning of the distribution. The Kolmogorov-Smirnov test gives a 0.03 probability that the data and simulation describe the same distribution. After much study of this excess, we could not find any systematic explanation for its source. Moreover, the excess is narrower than the missing transverse energy resolution of our detector, so it is not consistent with a resonance.

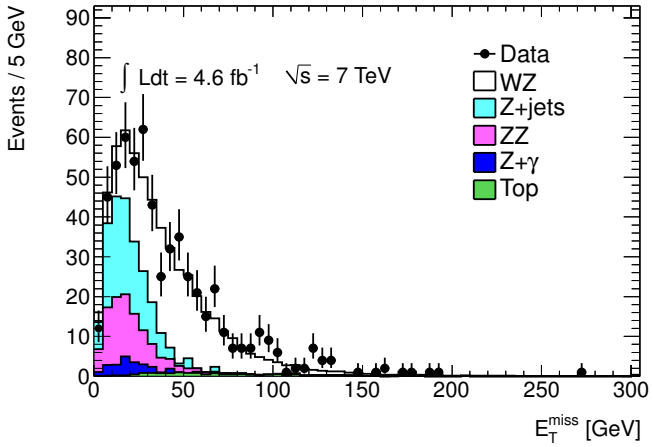

Figure 8.16: The missing transverse energy distribution for Z + lepton events, after all selections have been applied to the third lepton. We require $E_T^{miss} > 25$ GeV to reject Z + jets and ZZ backgrounds. The Z+jets and $t\bar{t}$ backgrounds are MC normalized by data-driven estimates; all other processes are taken from MC.

Table 8.6 shows the expected number of $W^{\pm}Z \to \ell\nu\ell'\ell'$ signal events passing each selection requirement for a luminosity of 4.64 fb^{-1}, and Table 8.7 shows the relative acceptance for each selection, as calculated in Monte Carlo. The relative acceptance is defined as the acceptance of each selection step i relative to the previous requirement:

$$\text{relative acceptance} = \frac{N_{\text{WZ events passing selection } i}}{N_{\text{WZ events passing selection } i-1}} \tag{8.11}$$

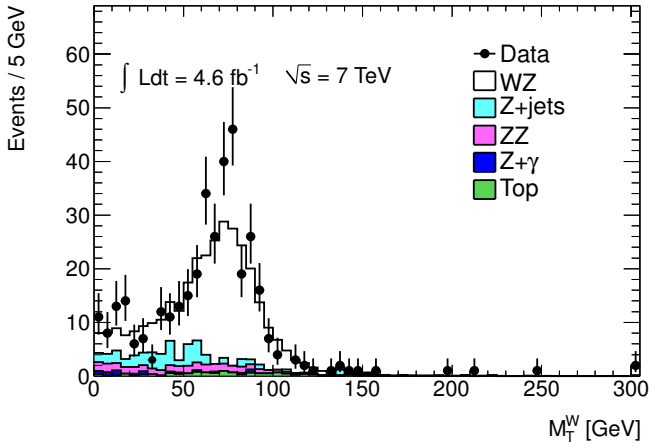

Figure 8.17: The transverse mass distribution of W candidates after the missing transverse energy selection. The Z+jets and $t\bar{t}$ backgrounds are MC normalized by data-driven estimates; all other processes are taken from MC. See text for a discussion of the discrepancy between data and simulation at the peak.

Finally, because tau decays can produce electrons and muons, we show the expected number of selected $W^{\pm}Z \to \tau + X$ events in Table 8.8.

Distributions of kinematic variables for the selected sample can be found in Section 10.2.

Table 8.6: Expected number of $WZ \to \ell\nu\ell\ell$ events, calculated from simulation, after each selection requirement for $\mathcal{L} = 4.64$ fb^{-1}.

Selection Requirements	Events			
	eee	$ee\mu$	$\mu\mu e$	$\mu\mu\mu$
$WZ \to \ell\nu\ell\ell$ simulated events	1202.26			
Muon or electron trigger	1120.78			
Primary vertex	1117.91			
E_T^{miss} cleaning	1116.16			
Z candidate	218.88		317.37	
Three leptons	51.22	70.55	74.82	106.55
E_T^{miss} selection	40.50	57.00	59.17	86.44
M_W^T requirement	38.07	54.05	55.67	81.85
Trigger match	38.04	53.99	55.29	81.67
Scale factors	37.24	51.77	54.20	78.32

Table 8.7: Relative acceptance of $W^{\pm}Z \to \ell\nu\ell'\ell'$ events for each selection requirement, as calculated in simulation. The relative acceptance is defined in equation 8.11. The Z and third lepton selection include the acceptance and efficiency of selecting 2 and 3 leptons respectively.

Selection Requirements	Acceptance (%)			
	eee	$ee\mu$	$\mu\mu e$	$\mu\mu\mu$
$WZ \to \ell\nu\ell\ell$ simulated events	100			
Muon or electron trigger	93.22			
Primary vertex	99.74			
E_T^{miss} cleaning	99.84			
Z candidate	19.61		28.43	
Three leptons	23.40	32.23	23.57	33.57
E_T^{miss} selection	79.07	80.80	79.09	81.12
M_W^T requirement	93.99	94.82	94.08	94.70
Trigger match	99.93	99.90	99.31	99.78
Scale factors	97.89	95.89	98.04	95.89

Table 8.8: Expected number of $W^{\pm}Z \to \tau + X$ events, calculated from simulation, after each selection requirement for $\mathcal{L} = 4.64$ fb^{-1}.

Selection Requirements	Events			
	eee	$ee\mu$	$\mu\mu e$	$\mu\mu\mu$
$WZ \to \tau + X$ simulated events	1502.83			
Muon or electron trigger	950.01			
Primary vertex	947.66			
E_T^{miss} cleaning	942.34			
Z candidate	107.07		152.36	
Three leptons	2.98	4.02	4.39	5.62
E_T^{miss} selection	2.42	3.12	3.44	4.44
M_W^T requirement	1.77	2.38	2.46	3.49
Trigger match	1.76	2.38	2.44	3.50
Scale factors	1.71	2.28	2.37	3.35

Table 8.9: The number of data events in our sample that pass each selection requirement.

Selection Requirements	Number of Events in Data
All muon + egamma triggered data	806,692,544
Good Runs List	754,558,976
Muon or electron trigger	362,649,408
Primary vertex	362,252,960
E_T^{miss} cleaning	361,827,264
LAr noise	360,761,792
Z candidate	3,122,786
Three leptons	591
E_T^{miss} selection	367
M_W^T requirement	321
Trigger match	317

Chapter 9

Backgrounds to WZ production

The largest backgrounds to the $WZ \to \ell\nu\ell\ell$ signal after selection requirements are imposed are, in order of size: Z + jets, ZZ, $t\bar{t}$, and $Z + \gamma$ events.

For Z+jets events to pass the full selection, a jet must produce a lepton through the decay of a pion, kaon, b or c quark, or by depositing energy in the calorimeter that is reconstructed as an electron. We call leptons produced by jets *fake* leptons, even though they may be real electrons or muons if the product of a heavy flavor decay. There must also be reconstructed missing transverse energy in the event, which can come from mismeasurement of jets or from event pileup. We estimate the Z+jets background from data, and it is predicted to contribute 11% of selected events.

ZZ events in which both Z bosons decay leptonically can pass the WZ selection if there is a source of missing transverse energy in the event. Missing transverse energy in ZZ events can arise from pileup from other collisions, mismeasurement of jets, or if one of the four leptons is not reconstructed by the detector. The ZZ background contributes 7% of the total expected events. The ZZ background shape and accep-

tance are determined from simulation, after the simulation has been corrected to look like the data (see Section 7.2), and the normalization is taken from the theoretical cross section.

Top quark pair production can produce background to WZ events in two ways. If both top quarks decay leptonically, the event has 2 isolated, high p_T leptons, 2 neutrinos, and 2 b quarks. If one of the b jets produces an isolated lepton with $p_T > 15$ GeV, the event has 3 leptons and missing transverse energy and can be reconstructed as a WZ event. The background from $t\bar{t}$ events in which a b jet produces the third lepton is estimated from data, and contributes 2% of all events after the full selection. Alternatively, one of the top quarks can radiate a Z boson before decaying. $t\bar{t} + Z$ events contain two W bosons and a Z boson. We treat this WZ production as background and estimate it from simulation. It contributes 2% to the expected event count.

$Z + \gamma$ events in which the photon converts to an electron/positron pair can be reconstructed as an $WZ \to \mu\mu e$ or $WZ \to eee$ event if one of the converted electrons passes the p_T selection and if there is a source of missing transverse energy in the event. Missing transverse energy can arise from pileup from other collisions in the same event, mismeasurement of jets, or mismeasurement of the converted photon energy. The background from $Z + \gamma$ events is determined from simulation. This background contributes about 1% of all expected events.

Other background processes involve one or more fake leptons, including WW production, W+jet events, single top and multijet production. The WW production cross section is 3 orders of magnitude smaller than the Z production cross section,

so while both processes can produce tri-lepton events with one fake lepton, the WW background contribution is negligible compared to that from Z+jets. The probability of a jet faking a lepton is on the order of 1 in 10^4; processes with two fake leptons are negligibly small. To confirm this estimate, the background from these processes is estimated from simulation. WW, single-top, QCD, and W+ jets production each contribute less than 0.1% of estimated events after all selections, and these backgrounds are neglected.

9.1 Z + jets background

The Z + jets background contains two prompt leptons from the Z decay and a third *fake* lepton from a mis-identified jet, heavy quark decay, or pion and kaon decay in-flight. A lepton from semi-leptonic decay in jets is also considered a fake lepton. The source of missing transverse energy in the event can be the mismeasurement of one or more jets in the event, a contribution from other collisions in the same event, or a neutrino from b or c quark decay. The probability of reconstructing a lepton from a jet is small and depends on the type and kinematics of the jet as well as the selection requirements for the lepton. For our lepton selection, the probability of reconstructing a third lepton in a Z+jets event is about 1 in 10,000. The Z+jets cross section is 3 orders of magnitude larger than the WZ production cross section, so the background due to Z+jets is significant.

We estimate the Z+jets background from data. First, we measure the ratio between isolated leptons and lepton-like jets, known as the *fake factor*. Second, we count the number of Z+lepton-like jet events that pass all other selection require-

ments. The product of these two numbers gives us an estimate of how many Z+jets events are in our signal region.

We define a lepton-like jet or *loose lepton* as an object that passes a specific subset of the lepton selections but fails at least one selection. The loose lepton requirements differ for electrons and muons. A *tight lepton* is a lepton that passes all selection requirements. The fake factor, f, is defined as a ratio between the number of tight and loose leptons:

$$f = \frac{N_{\text{tight}}}{N_{\text{loose}}} \tag{9.1}$$

and f is defined and calculated separately for electron and muons.

To avoid signal contamination in the control regions, the selection requirements separating loose and tight leptons should cleanly separate leptons from W decays from leptons from jets. For muons, reversing the isolation requirement yields a loose lepton control region dominated by Z+jets events. Loose electrons must fail either the isolation selection or one of the shower shape, width, or track matching selections described in the Tight++ electron quality requirements in Section 5.4. Therefore, equation 9.1 can be rewritten:

$$f_{\text{electron}} = \frac{N_{\text{tight++, isolated}}}{N_{\text{reconstructed electrons which fail tight++ or are non-iso}}} \qquad f_{\text{muon}} = \frac{N_{\text{isolated}}}{N_{\text{non-isolated}}} \tag{9.2}$$

The rate of reconstructing an isolated lepton from a jet depends on the jet η, p_T, and the original parton from which the jet emerged. Jets with b and c quarks produce leptons through semi-leptonic W decay, whereas jets produced by light quarks or gluons produce fake leptons through decay-in-flight of pions, kaons, or by depositing energy in the calorimeters that mimics the energy deposition mimics of an electron. Instead of parameterizing the fake factor as a function of several jet parameters, we

choose to measure it in a sample as close as possible to our background. Specifically, we measure the fake factor in a Z + jets control region obtained by reversing the missing transverse energy requirement on our data sample.

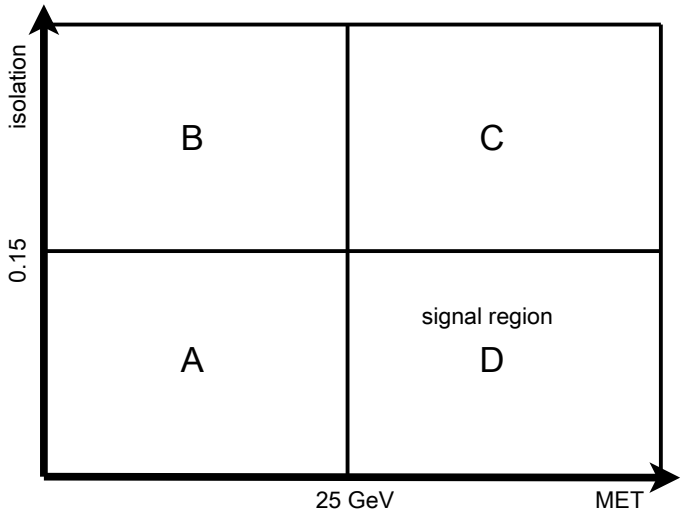

Figure 9.1: Illustration of Z+jets data-driven background estimation technique. The x-axis is the E_T^{miss} in events with a reconstructed Z boson and a muon. The y-axis is the isolation of the muon in these events. A and B are control regions in which the fake factor is measured. The fake factor times the number of events in control region C is an estimate of the number of Z+jets events in signal region D.

The three control regions used in the background estimate are shown in Figure 9.1 for events with fake muons. The fake factor f is the ratio of the number of isolated to non-isolated muons for events with a reconstructed Z boson and $E_T^{miss} < 25$ GeV. In the diagram, this is the ratio of events in control region A to control region B. Multiplying the fake factor by the number of events with a Z + non-isolated muon with $E_T^{miss} > 25$ GeV yields the final background estimate:

$$\text{Z+jets estimate in signal region } D = \frac{A}{B} \times C \tag{9.3}$$

We calculate the fake factor f using an inclusive sample of $Z \to \mu\mu + \ell$ and $Z \to$

$ee + \ell$ events. The probability that the W candidate muon is isolated is independent of the flavor of the Z leptons. The same logic applies for electrons. Therefore, we use the same muon fake factor for the $\mu\mu\mu$ and $ee\mu$ channels. The electron fake factor is the same for the eee and $\mu\mu e$ channels. To estimate the background in each of the four channels, we count the events in control region C in each channel.

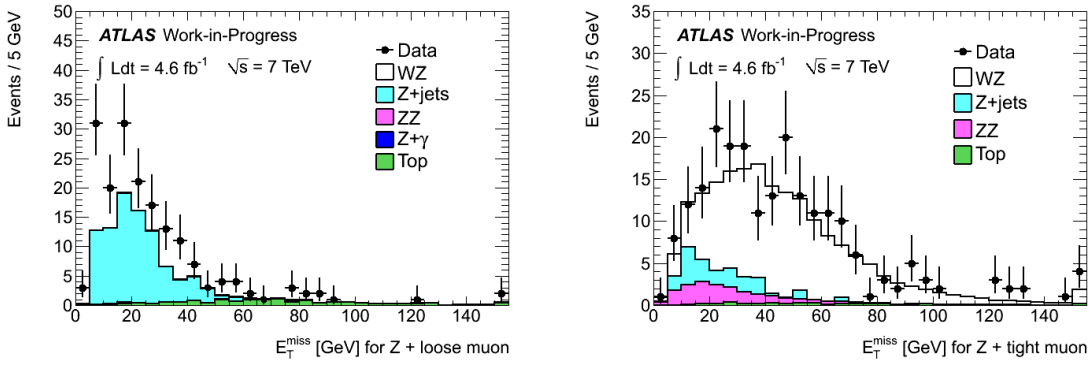

Figure 9.2: E_T^{miss} distribution for Z + muon events, shown for non-isolated muons (left) and isolated muons (right). The Z+jets contribution shown is taken from simulation and does not necessarily reproduce the data in the control regions very well.

Figure 9.2 shows the missing transverse energy distribution separately for isolated (*tight*) and non-isolated (*loose*) muons. In Figure 9.3, the missing transverse energy distribution for electrons which fail one of the selection criteria (*loose* electrons) is shown alongside the distribution for electrons passing all selection requirements, including isolation (*tight* electrons). The events in these distributions are used directly in the calculation of the background estimate.

In Figures 9.2 and 9.3, the Z+jets distribution shown is taken from simulation and normalized by the *NLO* Z+jets cross section and the integrated luminosity. The events are simulated with the ALPGEN [117] generator with the CTEQ6L1 PDF

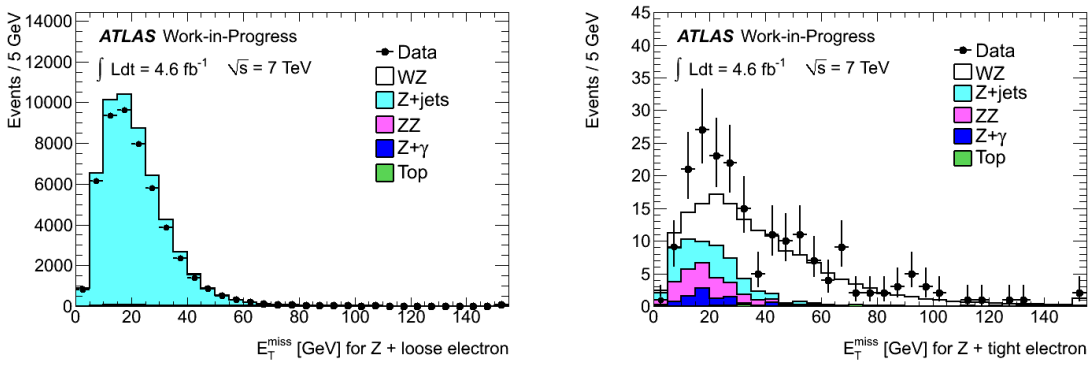

Figure 9.3: E_T^{miss} distribution for Z + electron events, shown for electrons that fail the isolation selection or fail one of the shower width, shape, or track matching requirements (left) and electrons that pass all selections (right). The Z+jets contribution shown is taken from simulation and does not necessarily reproduce the data in the control regions very well.

set. The generated events are interfaced with JIMMY [75] to model multi-parton interaction and HERWIG [74] to simulate hadronization, initial state radiation, and final-state QCD radiation. The normalization of the Z+jets events with a third lepton does not match the data well in the control regions. Simulating the rate of lepton production and the isolation of the leptons in jets requires precise modeling of the tails of jet fragmentation, hadronization, and the p_T and kinematics of heavy quarks in jets, as well as accurate simulation of the interaction between all particles in the jet and the detector. It is difficult to accurately simulate the tails of jet distributions, and it is not surprising that the simulation does not reproduce the data exactly. Since we take the background estimate directly from data, this is not a problem for this analysis.

When calculating the estimated background, contributions from other processes are subtracted from the control regions using estimates from simulation. In the loose lepton control regions B and C, this subtraction involves less than 1% of events. How-

ever, in the tight lepton control region A, both the WZ and ZZ processes contribute significant events and the subtraction is a significant source of systematic uncertainty, as will be discussed shortly.

For the $ee\mu$ and $\mu\mu e$ channels, there is no ambiguity between W and Z leptons. However, for the $\mu\mu\mu$ and eee channels, it is possible that one of the leptons in the reconstructed Z boson was not from the Z decay. This is possible for WZ events as well, but simulation predicts an incorrect lepton assignment of less than 1%. The simulation predicts a higher rate of incorrect assignment for Z+jets events which pass all WZ selection requirements, including all lepton selections. Events in which a fake lepton pairs with a real lepton to make a Z with an invariant mass closer to the Z mass also contribute to the total background. There is a small probability of the wrong pair having an invariant mass closer to the Z mass than the true pair, but in those rare events, the Z lepton which is incorrectly excluded from the Z boson often makes a good W candidate lepton because it is usually high p_T and isolated. Moreover, our WZ selection has tighter p_T and selection requirements on the W lepton than on the Z leptons. It is easier for a jet to fake a 15 GeV loose++ electron or segment-tagged muon than a 20 GeV tight++ electron or combined muon. The jet p_T distribution falls steeply between 15 and 20 GeV, so there are also more jets available to fake a 15 GeV lepton. Therefore, it is easier to fake a Z lepton than a W lepton.

To measure the contribution to the Z+jets background from events in which one of the Z leptons is from a jet, we define a separate control region in which one of the Z leptons is a loose lepton, and the other Z lepton and the W lepton pass the

tight lepton selections. In the *eee* channel, this control region is dominated by Z+jets events. In the $\mu\mu\mu$ channel, this region is dominated by $t\bar{t}$ events, so we can not use the data to measure this in the $\mu\mu\mu$ channel.

In the *eee* events, we estimate the fake-factor for the Z electron requirements in data, and estimate the background from events where the Z lepton is the fake, not the W lepton. These events contribute an additional 8% to the Z+jets data-driven estimate in the *eee* channel. The simulation predicts 10%. Since there is good agreement between the simulation prediction and the data measurement in the *eee* channel, and we can't measure the contribution in the $\mu\mu\mu$ channel directly, we apply a correction to the $\mu\mu\mu$ data estimate based on the simulation prediction of the ratio of background events with a fake W muon to background events with a fake Z muon.

There are several sources of uncertainty on the background prediction for Z+jets. The three largest sources of uncertainty are:

- *statistical uncertainty*: Due to limited data in the control regions, in particular in control region A, there is a significant statistical uncertainty on the calculated fake-factor, which propagates to a significant uncertainty on the final background estimate. The statistical uncertainty due to limited data is about 25% on the final background estimate in the *eee* and $\mu\mu e$ channels and 40% in the $\mu\mu\mu$ and $ee\mu$ channels.

- E_T^{miss} *scaling of fake-factor*: We measure the ratio of loose to tight leptons in Z+jets events with $E_T^{miss} < 25$ GeV, and apply it in Z+loose lepton events with $E_T^{miss} > 25$ GeV. If there is a correlation between the isolation of muons in jets and the E_T^{miss} in the event (similar for electrons), it is ignored by the

background estimation technique. We treat a possible correlation as a systematic uncertainty, and estimate the size by looking in simulation. The systematic uncertainty is taken as the deviation from unity in the ratio between the fake-factor in the high E_T^{miss} region to the low E_T^{miss} region in Z+jets simulation, or the statistical uncertainty on the ratio in MC, whichever is larger. For events with a W muon, this uncertainty is 35%. For events with a W electron, it is 20%.

- *Background subtraction*: There is significant WZ, ZZ, and $t\bar{t}$ contamination in control region A. We subtract the estimated contributions from these processes from the control region, but there is an uncertainty on how well we know the subtracted background normalizations. To estimate the uncertainty that this subtraction has on the final Z+jets estimate, the normalization of the WZ and ZZ samples are varied by the uncertainty of the measured cross-sections in the most recent ATLAS results. This is 20% for WZ and 15% for ZZ. The $t\bar{t}$ contribution is varied by 100%, since the $t\bar{t}$ contribution to the three lepton sample requires a third lepton and is not necessarily well modeled by the simulation. The uncertainty on the final Z+jets estimate is taken as half of the difference between the data-driven estimate with the varied MC sample normalization and the data-driven estimate with the nominal MC cross sections.

All statistical and systematic uncertainties are added in quadrature within each channel. When combining channels or calculating the cross section, the fact that the measured fake factor is the same for the $\mu\mu\mu$ and the $ee\mu$ channels, and separately the same for the eee and $\mu\mu e$ channels, is taken into account as a full correlation in

uncertainties resulting from the fake factor.

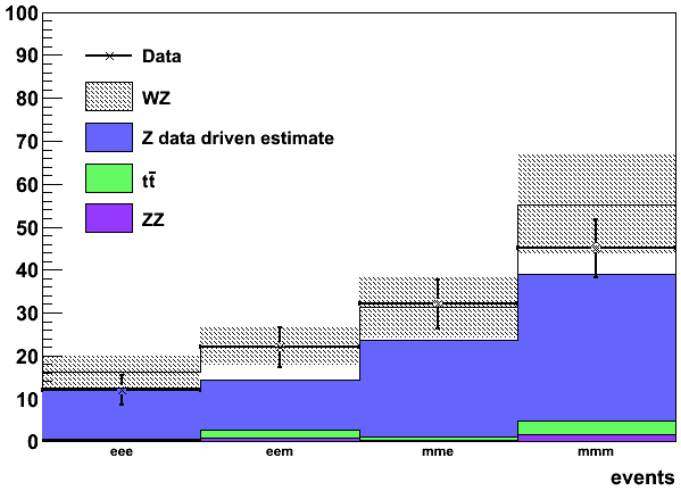

Figure 9.4: Z+jets background estimation in control region. Events in the control region have a Z boson and a W candidate lepton with $10 < p_T < 20$ GeV and are dominated by Z+jets events. Shown here is the number of events in each of the four lepton channels, as predicted by the Z+jets data-driven method, and the number of events observed in data. The prediction for other processes are taken from simulation. There is good agreement between the number of predicted and observed events.

In events with a Z boson and a W candidate lepton with $10 < p_T < 20$ GeV, the Z+jets background dominates over WZ signal events (see Figure 8.15.) This provides a good control region to test the Z+jets background estimation technique. The data-driven background estimation method described above is performed, in each of the four lepton channels, for the exclusive sample of events with a Z boson and a W lepton with $10 < p_T < 20$ GeV. The estimated number of events agrees well with the observed number of events in data, as shown in Figure 9.4.

The measurement of limits on anomalous triple gauge couplings is performed using the Z boson transverse momentum distribution. For this measurement, it is important to have an accurate estimation of the background as a function of p_T^Z. To provide this, we estimate the background independently in bins of p_T^Z using the

Table 9.1: Z+jets background estimates, as estimated from data, per channel. The first uncertainty is statistical in nature; the second is systematic.

Channel	Expected Z+jets Events
eee	$8.8 \pm 2.1 \pm 1.9$
$ee\mu$	$3.7 \pm 1.7 \pm 1.6$
$\mu\mu e$	$10.2 \pm 2.4 \pm 2.2$
$\mu\mu\mu$	$9.1 \pm 3.9 \pm 3.9$

same fake-factor method. All control regions are counted independently in each bin, and the fake-factor is derived as a function of Z transverse momentum. Figures 9.5 and 9.6 show the fake factor as a function of p_T^Z for electrons and muons respectively. As there are limited statistics for events with high Z transverse momentum, the fake factor is calculated in the last three bins inclusively. Both simulation and data show that the fake factors are not flat as a function of p_T^Z.

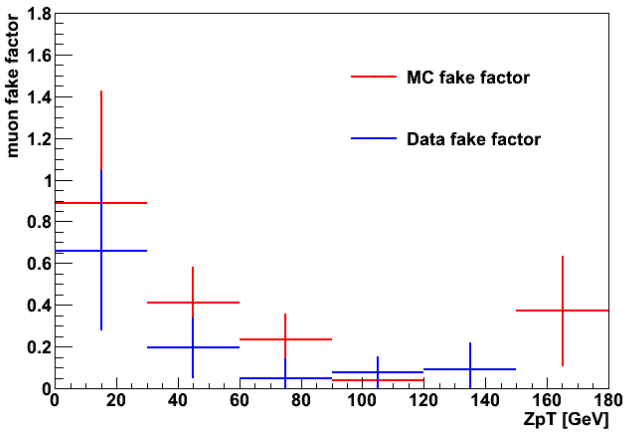

Figure 9.5: Muon fake factor as a function of p_Z^T. The fake factor is the ratio of isolated to non-isolated muons, for muons in Z+jets events which pass all other muon selection requirements.

The final Z+jets background estimates are shown in Table 9.1 for each of the four decay channels.

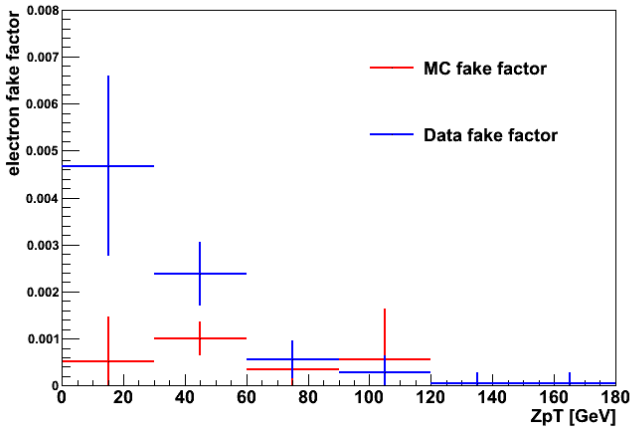

Figure 9.6: Electron fake factor as a function of p_Z^T. The fake factor is the ratio of the number of electrons which pass all selection requirements to the number of electrons which fail at least one isolation, shower shape, width, or track matching selection requirement, for electrons in Z+jets events.

9.2 ZZ background

The shape of the ZZ background is estimated from simulation by applying the full WZ selection and applying the corrections, including re-weighting and smearing, described in Section 7.2. The total number of expected events is determined by scaling the ZZ sample according to the theoretical cross section and the measured luminosity.

The ZZ background is simulated using Pythia [139]. Pythia simulates the hard scatter as well as the hadronization. The simulation includes the full $(Z\gamma^*)(Z\gamma^*)$ structure; that is, either or both of the Z bosons is allowed to be off-shell, and $Z-\gamma$ interference is correctly treated. Full angular correlations are included in the leptonic decays of the Z bosons. The leading-order cross section provided by Pythia is normalized to next-to-leading order cross section calculated by MCFM [55].

$ZZ \to \ell\ell\ell\ell$ events can have reconstructed missing transverse energy from several

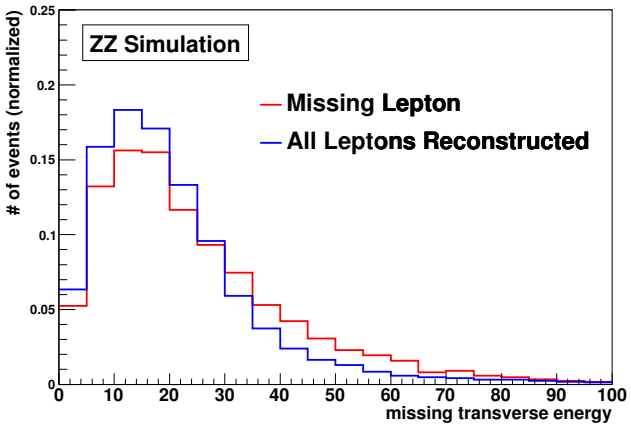

Figure 9.7: E_T^{miss} of ZZ events in simulation. Event with all leptons reconstructed have all four truth leptons from the Z bosons matched to a reconstructed lepton within $\Delta R < 0.1$. Events with a missing lepton are events in which one or more truth leptons is not matched to a reconstructed lepton.

sources. If one of the leptons is not reconstructed by the detector, it carries away momentum that shows up in the calculation of missing transverse energy. In Figure 9.7, the missing transverse energy distribution of ZZ events is shown for events in simulation. If all four truth leptons are matched within $\Delta R < 0.1$ to a reconstructed lepton, the event is considered to have all leptons reconstructed. If one or more of the truth leptons from a Z boson decay is not matched with a reconstructed lepton, the event is called a *missing lepton* event. Events with a missing lepton have on average 3 GeV more missing transverse energy than events in which all leptons are reconstructed. Truth leptons which are not matched with a reconstructed lepton are largely located in regions of the detector with reduced detector coverage. In Figure 9.8, the η distribution of missing leptons is shown separately for missing electrons and muons in ZZ simulated events which pass the full WZ selection requirements. The distribution of missing electrons peaks around $|\eta| = 1.4$, which is the transition

between the barrel and endcap electromagnetic calorimeters, where there are gaps in calorimeter coverage. Missing muons are predominately around $\eta = 0$, where there is a gap in muon spectrometer coverage to allow cables from the inner detector to pass out of the detector, and above $|\eta| = 2.7$, where the muon spectrometer coverage ends.

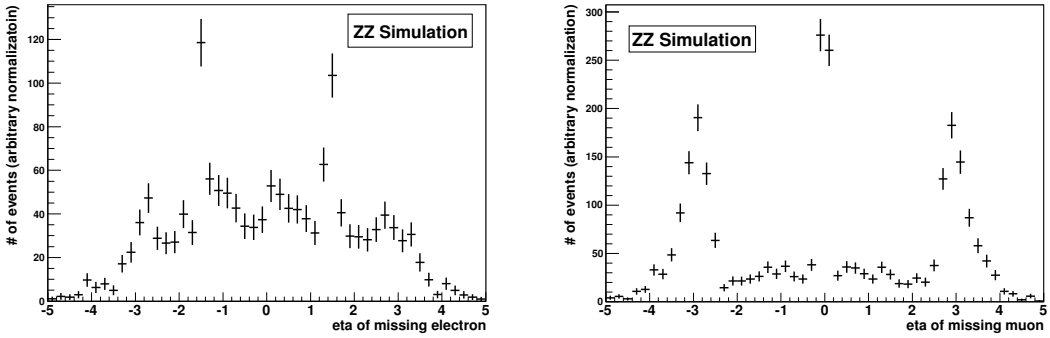

Figure 9.8: η distribution of leptons not reconstructed in ZZ events, for electrons (left) and muons (right.) Missing leptons, which are truth leptons not matched with a reconstructed lepton within $\Delta R < 0.1$, peak in regions of the detector with limited coverage and contribute to the E_T^{miss} in ZZ events.

Missing transverse energy in ZZ events can also be contributed from other collisions in the same event. This can be seen in Figure 9.9, which shows the mean missing transverse energy in a ZZ event as a function of the number of reconstructed vertices. The average amount of missing transverse energy is 16 GeV for ZZ events with 1 reconstructed vertex and 27 GeV for ZZ events with 15 reconstructed vertices.

The shape and normalization of simulated ZZ events is checked in data in events with four reconstructed leptons before the missing transverse energy selection requirement. The four lepton sample is dominated by ZZ events, and the prediction matches the data well within the statistics of the sample. Figure 9.10 shows the distribution of missing transverse energy and the number of jets in the four lepton sample before

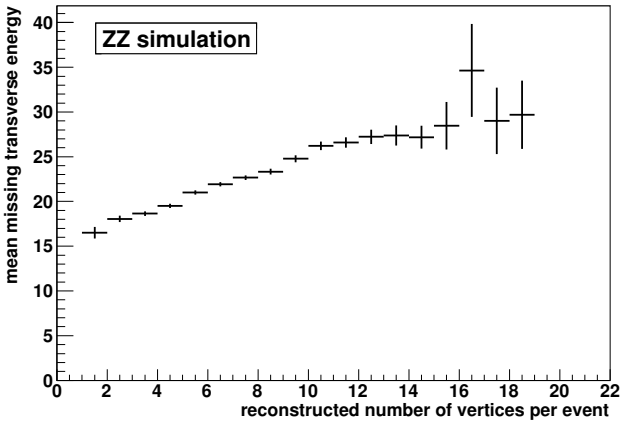

Figure 9.9: Average E_T^{miss} versus number of of reconstructed vertices in ZZ events, for simulated ZZ events.

the missing transverse energy selection.

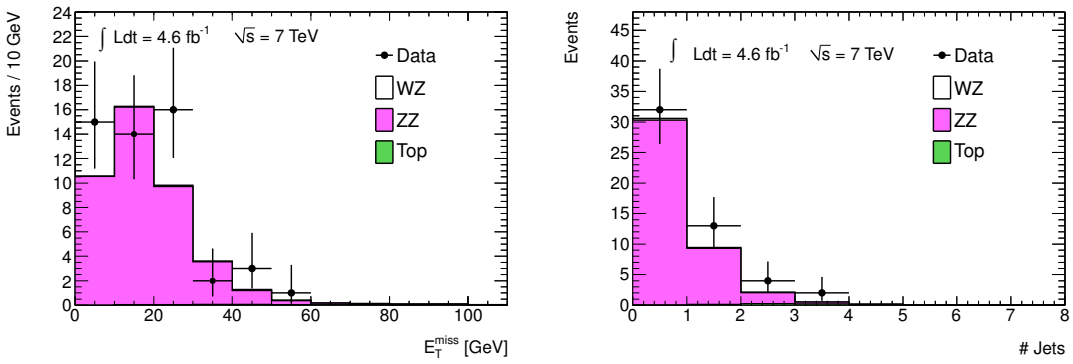

Figure 9.10: Four lepton events in data before E_T^{miss} selection. The E_T^{miss} distribution (left) and the number of jets (right) in events with a reconstructed Z boson and two additional leptons passing all lepton selections, before the E_T^{miss} selection requirement. This control region confirms that the ZZ simulation models the data.

Systematic uncertainties on the normalization of the ZZ background are discussed in Section 10.4. The expected number of ZZ events in the final data sample is shown in Table 9.2.

Table 9.2: ZZ and $Z+\gamma$ background estimates from Monte Carlo. Expected number of events passing all selection cuts for background MC samples, normalized to an integrated luminosity of $\mathcal{L} = 4.64$ pb^{-1}. The first error is statistical while the second is systematic.

Sample	Events			
	eee	$ee\mu$	$e\mu\mu$	$\mu\mu\mu$
$Z+\gamma$	1.4±0.7±0.1	–	2.3±0.9±0.1	–
ZZ	3.2±0.1±0.2	4.9±0.1±0.2	5.0±0.1±0.1	7.9±0.1±0.2

9.3 $t\bar{t}$ background

Events with top quark pair production can pass the WZ event selection if both W bosons decay leptonically and if a lepton is reconstructed from a b-quark jet. In a study of simulated $t\bar{t}$ events, more than 99% of events passing the full WZ selection had two leptons matched to W truth leptons and one lepton from a b jet (where matched leptons must have $\Delta R < 0.05$ from the truth object.) Fewer than 1% of events had 2 leptons matched to b jets and one lepton from a W decay.

The next-to-leading order (NLO) in QCD generator MC@NLO is used to model the shape of $t\bar{t}$ events and single top events. However, the normalization of the expected $t\bar{t}$ contribution is taken from data.

Events with top quarks are the only significant background to WZ events which do not contain a true Z boson. If we select WZ events with the full selection requirements but require that the reconstructed Z boson has leptons of the same charge rather than the opposite charge, we obtain a sample dominated by top quark events with 3 reconstructed leptons. The kinematic distributions of the $t\bar{t}$ sample which pass the nominal WZ selection are similar to the $t\bar{t}$ sample which pass the WZ selection with the same-sign Z boson. This can be seen in Figure 9.11, which shows both the

invariant mass of the reconstructed Z boson and the missing transverse energy distribution separately for $t\bar{t}$ events with opposite-charge and same-charge reconstructed Z candidates.

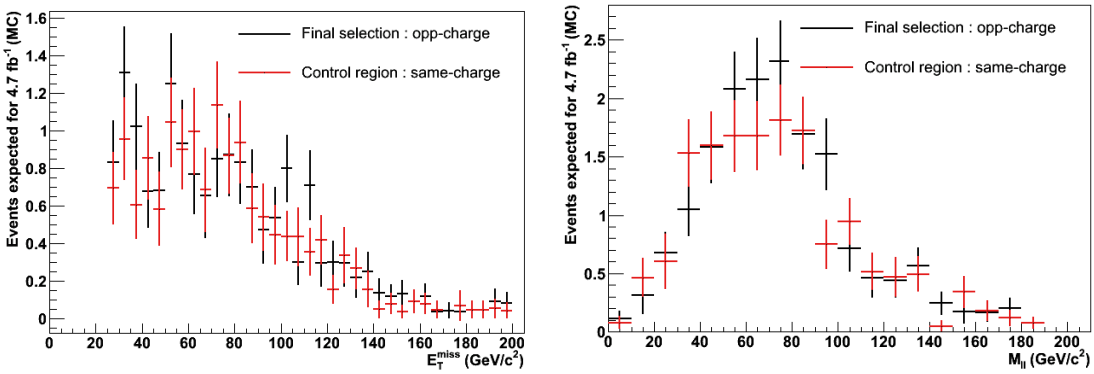

Figure 9.11: $t\bar{t}$ events with same-sign Z candidate. The missing transverse energy distribution (left) and invariant mass of the Z candidate (right) is shown for simulated $t\bar{t}$ events. Distributions are shown for events which pass the nominal WZ selection (opp-charge, in black) and for events in which the Z candidate has leptons with the same charge (same-charge, in red). The two sets of events have similar kinematics.

Events with a same-sign Z candidate are used as a control region for the $t\bar{t}$ background. The missing transverse energy distribution for this control region is shown in Figure 9.12 for the $ee\mu$ and $\mu\mu e$ channels in both data and simulation. The ratio of the total number of data events to the number of top events predicted by simulation, after subtracting the number of expected events from other processes as predicted by simulation, is taken as a data-derived scale factor. This scale factor is used to normalize the $t\bar{t}$ contribution predicted by simulation in the signal region, resulting in a final $t\bar{t}$ background estimate.

The normalization scale factor has a value of 2.2 with a statistical uncertainty of 1.0. The statistical uncertainty on the scale factor results in a systematic uncertainty on the total $t\bar{t}$ background. The $t\bar{t}$ simulation prediction in the signal region also con-

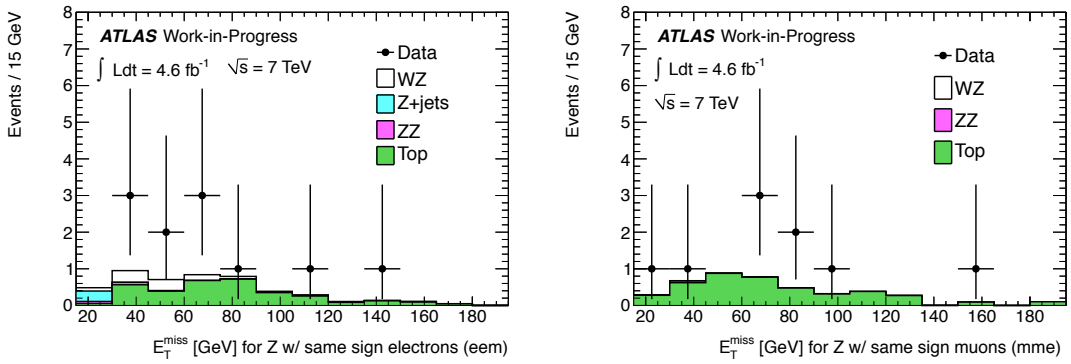

Figure 9.12: $t\bar{t}$ control region in data for the $ee\mu$ (left) and $\mu\mu e$ (right) channels. The control region is composed of events which pass the full WZ selection, except the reconstructed Z boson must have leptons with the same charge. This region is used to obtain a normalization scaling for the $t\bar{t}$ simulation.

tributes significant statistical uncertainty to the final background estimate, as there are very few events that pass the full WZ selection in simulation. Other systematic uncertainties are studied, including differences in kinematics between $t\bar{t}$ events with a same sign Z and $t\bar{t}$ events with an opposite sign Z, but all other systematics are small compared to the 50% uncertainty due to the limited statistics in the control region in data, and are neglected. The final $t\bar{t}$ background estimates are shown in Table 9.3.

There is one additional way in which top quark pair production can contribute to the WZ background. Before decay, an off-shell top quark can radiate a Z boson; though the cross section for this process is only 90 fb, the events contain two W bosons and a Z boson and have a high efficiency to pass the full WZ selection. A similar process can occur in which a $t\bar{t}$ event is produced with an additional W boson. This process does not contain a Z, but if the three W bosons all decay leptonically, the event has three isolated, high p_T leptons.

Table 9.3: $t\bar{t}$ and $t\bar{t}$+X background predictions per decay channel. $t\bar{t}$ numbers are obtained from Monte Carlo estimates which are rescaled to data by a factor 2.2. The first uncertainty is from the statistics of the MC estimation; the second uncertainty is from the rescaling, and is due to limited data statistics in the region in which the scale factor is calculated. $t\bar{t} + W^{\pm}$ and $t\bar{t} + Z$ estimations come directly from simulation, and are shown with statistical uncertainties.

Channel	Expected Events		
	$t\bar{t}$	$t\bar{t} + W^{\pm}$	$t\bar{t} + Z$
eee	0.4±0.3±0.2	0.1±0.02	0.6±0.1
$ee\mu$	1.7±0.5±0.8	0.1±0.02	1.1±0.1
$\mu\mu e$	2.3±0.5±1.0	0.1±0.03	1.2±0.1
$\mu\mu\mu$	2.4±0.5±1.1	0.1±0.03	1.5±0.1

The $t\bar{t}+Z$ and $t\bar{t}+W$ background contributions are estimated from simulation. As the events contain three leptons from vector boson decay, the efficiency and acceptance for identifying three leptons in the event should be well modeled in Monte Carlo. We generate these events with MadGraph [11], interfaced with Pythia to model the hadronization and initial and final state QCD radiation.

In the calculation of the $t\bar{t}$ data-derived normalization in the same-sign Z control region, expected contributions from $t\bar{t} + W/Z$ events are subtracted from the data. In this way, the two top quark background estimates do not overlap. The predicted background from $t\bar{t} + W/Z$ events is shown in Table 9.3. Systematic uncertainties on the normalization of the $t\bar{t} + W/Z$ background are discussed in Section 10.4.

9.4 Z + γ background

Leptonic decays of Z bosons produced in association with a photon can mimic the tri-lepton signature of WZ events when a photon undergoes conversion into an

electron-positron pair upon interaction with the material of the detector. These events differ from the $Z\gamma^*$ events simulated in the ZZ background because the photon is a real photon, not virtual.

This process is simulated using the matrix element calculation of the MadGraph generator, interfaced with Pythia to simulate the event hadronization and Photos and GEANT4 to simulate photon conversions in the detector.

Systematic uncertainties on the normalization of the $Z + \gamma$ background are discussed in Section 10.4. The expected number of $Z+\gamma$ events in the final data sample is shown in Table 9.2. This background only contributes to channels with a W electron candidate.

9.5 Specifics on Background MC Samples

Details on the simulated samples used are shown in this section. The Z+jets background, detailed in Table 9.4, is used only for illustration purposes: the actual background is estimated from data for both the cross-section and anomalous triple gauge coupling limits.

The ZZ and $Z + \gamma$ backgrounds are estimated from simulation. Details on the MC samples used to estimate these backgrounds are shown in Table 9.7.

The $t\bar{t}$ simulation is used to derive the shape of the background, including the distribution as a function of p_T^Z. The normalization for this background process is taken from data. The expected background from $t\bar{t} + W/Z$ events is taken directly from simulation. The details on the simulation of events with top quarks is shown in Table 9.6.

Also included are the simulation details for WW, dijet, and W+jet events in Tables 9.7, 9.6, and 9.5, respectively. As noted earlier, the MC predicts that each of these processes contributes less than 0.1% of all expected events, and these sources are not included in background estimates.

Table 9.4: MC samples/processes used to model Z+X, including Z+jets, Zbb+jets and Drell-Yan samples. The corresponding cross-sections, generator names, generator level filter efficiencies and total numbers of events are shown. The listed cross sections do not include k-factors or filter efficiencies. NpX (X = 0...5) in the process name refers to the number of additional partons in the final state.

MCID	Process	Generator	Events	k-factor	ϵ_{filter}	σ [pb]
107650	ZeeNp0	Alpgen	6618284	1.25	1.0	668.32
107651	ZeeNp1	Alpgen	1334897	1.25	1.0	134.36
107652	ZeeNp2	Alpgen	2004195	1.25	1.0	40.54
107653	ZeeNp3	Alpgen	549949	1.25	1.0	11.16
107654	ZeeNp4	Alpgen	149948	1.25	1.0	2.88
107655	ZeeNp5	Alpgen	50000	1.25	1.0	0.83
107660	Z$\mu\mu$Np0	Alpgen	6615230	1.25	1.0	668.68
107661	Z$\mu\mu$Np1	Alpgen	1334296	1.25	1.0	134.14
107662	Z$\mu\mu$Np2	Alpgen	1999941	1.25	1.0	40.33
107663	Z$\mu\mu$Np3	Alpgen	549896	1.25	1.0	11.19
107664	Z$\mu\mu$Np4	Alpgen	150000	1.25	1.0	2.75
107665	Z$\mu\mu$Np5	Alpgen	50000	1.25	1.0	0.77
107670	Z$\tau\tau$Np0	Alpgen	10613179	1.25	1.0	668.40
107671	Z$\tau\tau$Np1	Alpgen	3334137	1.25	1.0	134.81
107672	Z$\tau\tau$Np2	Alpgen	1004847	1.25	1.0	40.36
107673	Z$\tau\tau$Np3	Alpgen	509847	1.25	1.0	11.25
107674	Z$\tau\tau$Np4	Alpgen	144999	1.25	1.0	2.79
107675	Z$\tau\tau$Np5	Alpgen	45000	1.25	1.0	0.77
109300	ZeebbNp0_nofilter	Alpgen	409999	1.25	1.0	6.57
109301	ZeebbNp1_nofilter	Alpgen	160000	1.25	1.0	2.48
109302	ZeebbNp2_nofilter	Alpgen	60000	1.25	1.0	0.89
109303	ZeebbNp3_nofilter	Alpgen	30000	1.25	1.0	0.39
109305	Z$\mu\mu$bbNp0_nofilter	Alpgen	409949	1.25	1.0	6.56
109306	Z$\mu\mu$bbNp1_nofilter	Alpgen	155000	1.25	1.0	2.47
109307	Z$\mu\mu$bbNp2_nofilter	Alpgen	60000	1.25	1.0	0.89
109308	Z$\mu\mu$bbNp3_nofilter	Alpgen	29999	1.25	1.0	0.39
116250	ZeeNp0 M10to40 pt20	Alpgen	994949	1.22	1.0	3051.62
116251	ZeeNp1 M10to40 pt20	Alpgen	299998	1.22	1.0	87.87
116252	ZeeNp2 M10to40 pt20	Alpgen	999946	1.22	1.0	41.10
116253	ZeeNp3 M10to40 pt20	Alpgen	149998	1.22	1.0	8.38
116254	ZeeNp4 M10to40 pt20	Alpgen	40000	1.22	1.0	1.85
116255	ZeeNp5 M10to40 pt20	Alpgen	10000	1.22	1.0	0.46
116260	Z$\mu\mu$Np0 M10to40 pt20	Alpgen	999849	1.22	1.0	3051.62
116261	Z$\mu\mu$Np1 M10to40 pt20	Alpgen	300000	1.22	1.0	87.87
116262	Z$\mu\mu$Np2 M10to40 pt20	Alpgen	999995	1.22	1.0	41.45
116263	Z$\mu\mu$Np3 M10to40 pt20	Alpgen	150000	1.22	1.0	8.38
116264	Z$\mu\mu$Np4 M10to40 pt20	Alpgen	39999	1.22	1.0	1.85
116265	Z$\mu\mu$Np5 M10to40 pt20	Alpgen	10000	1.22	1.0	0.46

Table 9.5: MC samples/processes used to model W+jets. The corresponding cross-sections, generator names, generator level filter efficiencies and total numbers of events are shown. The listed cross sections do not include k-factors or filter efficiencies. NpX (X = 0...5) in the process name refers to the number of additional partons in the final state.

MCID	Process	Generator	Events	k-factor	ϵ_{filter}	σ [pb]
107680	W$e\nu$Np0	ALPGEN	6952874	1.2	1.0	6921.60
107681	W$e\nu$Np1	ALPGEN	4998487	1.2	1.0	1304.30
107682	W$e\nu$Np2	ALPGEN	3768632	1.2	1.0	378.29
107683	W$e\nu$Np3	ALPGEN	1008947	1.2	1.0	101.43
107684	W$e\nu$Np4	ALPGEN	250000	1.2	1.0	25.87
107685	W$e\nu$Np5	ALPGEN	69999	1.2	1.0	7.0
107690	W$\mu\nu$Np0	ALPGEN	3462942	1.2	1.0	6919.60
107691	W$\mu\nu$Np1	ALPGEN	4998236	1.2	1.0	1304.20
107692	W$\mu\nu$Np2	ALPGEN	3768737	1.2	1.0	377.83
107693	W$\mu\nu$Np3	ALPGEN	1008446	1.2	1.0	101.88
107694	W$\mu\nu$Np4	ALPGEN	254950	1.2	1.0	25.75
107695	W$\mu\nu$Np5	ALPGEN	70000	1.2	1.0	6.92
107700	W$\tau\nu$Np0	ALPGEN	3418296	1.2	1.0	6918.60
107701	W$\tau\nu$Np1	ALPGEN	2499194	1.2	1.0	1303.20
107702	W$\tau\nu$Np2	ALPGEN	3750986	1.2	1.0	378.18
107703	W$\tau\nu$Np3	ALPGEN	1009946	1.2	1.0	101.51
107704	W$\tau\nu$Np4	ALPGEN	249998	1.2	1.0	25.64
107705	W$\tau\nu$Np5	ALPGEN	65000	1.2	1.0	7.04

Table 9.6: MC samples/processes used to model top (including $t\bar{t}$ and single top) and dijet backgrounds. The corresponding cross-sections, generator names, generator level filter efficiencies and total numbers of events are shown. The listed cross sections do not include k-factors or filter efficiencies.

MCID	Process	Generator	events	k-factor	ϵ_{filter}	σ [pb]
105200	$t\bar{t}$	MC@NLO	14983835	1.0	0.55551	166.8
119353	$t\bar{t} + W^{\pm}$	MADGRAPH	100000	1.3	1.0	0.12444
119355	$t\bar{t} + Z$	MADGRAPH	99997	1.3	1.0	0.095581
108340	t-channel→e	MC@NLO	299998	1.0	1.0	7.1522
108341	t-channel→ μ	MC@NLO	299999	1.0	1.0	7.1767
108342	t-channel→ τ	MC@NLO	299999	1.0	1.0	7.1277
108343	s-channel→e	MC@NLO	299948	1.0	1.0	0.46856
108344	s-channel→ μ	MC@NLO	299998	1.0	1.0	0.46837
108345	s-channel→ τ	MC@NLO	299899	1.0	1.0	0.46978
108346	Wt	MC@NLO	899694	1.0	1.0	13.102
105757	bbcc mu10mu10X	PYTHIAB	296599	1.0	1.0	2830.3
105758	bbcc mu10e10X	PYTHIAB	795695	1.0	1.0	4017.1
105759	bbcc e10e10X	PYTHIAB	290995	1.0	1.0	1693.0

Table 9.7: MC samples/processes used to model diboson backgrounds, including WW, ZZ, and $Z\gamma$. The corresponding cross-sections, generator names, generator level filter efficiencies and total numbers of events are shown. The listed cross sections do not include k-factors or filter efficiencies.

MCID	Process	Generator	Events	k-factor	ϵ_{filter}	σ [pb]
105985	WW	Herwig	2489244	1.52	0.38863	29.592
109292	ZZ	Pythia	149999	1.40	0.6235	0.07494
108290	$W^-(\tau)\ \gamma$	Pythia,MadGraph	50000	1.83	1.0	16.8
126015	$Zee\gamma$_1jet	Sherpa	199899	1.0	1.0	14.7
126016	$Z\mu\mu\gamma$_1jet	Sherpa	199950	1.0	1.0	14.7
108325	$Z(\tau\tau)\ \gamma$	Pythia,MadGraph	49949	1.41	0.15	9.41

Chapter 10

Measurement of the WZ Cross Section

This chapter describes the measurement of the WZ cross section at $\sqrt{s} = 7$ TeV through the process

$$pp \to W^{\pm}Z \to \ell^{\pm}\nu\ell'^{+}\ell'^{-} \tag{10.1}$$

where $\ell = e, \mu$. WZ events are identified by selecting events with three leptons and missing energy in the final state, as described in Chapter 8. The backgrounds processes and estimation methods are discussed in Chapter 9.

The measured cross section is extracted using a maximum likelihood fit to the observed number of events in each of the four decay channels in data. We measure two cross sections: a fiducial cross section within the phase space in which we observe WZ events, and a total cross section which extrapolates from the observed events to the total WZ production phase space. The total cross section is the more fundamental theoretical quantity and more useful for comparisons with theoretical calculations;

however, the extrapolation is done assuming Standard Model production of signal events. The fiducial cross section is what we actually measure; it has a lower theoretical uncertainty than the total cross section, largely due to smaller uncertainties from PDFs, and suffers a smaller theoretical bias.

The selection acceptance and efficiency are modeled using Monte Carlo simulations of the WZ signal. Corrections are applied to the MC to account for several observed differences between simulation and data; these corrections are described in Chapter 7. Uncertainties on the corrections lead to systematic uncertainties on the signal acceptance and efficiency. This chapter covers these systematic uncertainties, as well as additional systematic uncertainties on the measured cross section.

10.1 Theoretical Cross Section

The theoretical prediction of the WZ production cross section is calculated using Monte Carlo For FeMtobarn processes (MCFM) [55]. MCFM calculates cross sections at the parton-level to next-to-leading order (NLO) in α_S for a range of processes at hadron colliders. We use MCFM, rather than MC@NLO, to calculate the theoretical cross section because the former includes $Z-\gamma$ interference, while the latter does not. We calculate both the total and fiducial cross section using MCFM; the definition of the fiducial cross section is given in Section 10.3.1.

For the nominal PDF, we use CT10 [109], a set of PDFs extracted in 2010 which includes recent collider data from deep-inelastic scattering, vector boson production, and single-inclusive jet production, with the exception of the the D∅ Run-II W lepton asymmetry data, which is excluded due to disagreement with other data. The QCD

renormalization and factorization scales are set in MCFM to $\frac{1}{2}(m_W + m_Z) = 85.7863$ GeV.

Due to the $Z - \gamma$ interference, there is not a clear separation between the $W\gamma$ and WZ processes. Indeed, MCFM computes the following process:

$$\sigma(pp \to W(Z \text{ or } \gamma) \to l\nu ll) \tag{10.2}$$

The minimum of the process in equation 10.2 occurs around $m_{ll} = 50$ GeV. For our total cross section measurement, we choose to define the Z boson, consistent with the ATLAS single Z measurements and with earlier LEP measurements, as:

$$66 < m_{ll} < 116 \text{ GeV} \tag{10.3}$$

This choice is arbitrary but significant. Figure 10.1 shows the WZ production cross section as a function of the minimum Z mass for both MCFM and MC@NLO and for a selection of different PDF sets. Depending on the choice of PDF and minimum Z mass, the WZ cross section can vary from around 17 to above 22 pb. Limiting the upper Z mass has a non-negligible effect; with the lower bound set at 66 GeV, restricting the upper bound of the Z boson to 116 GeV omits about 2.5% of the otherwise total cross section.

The calculated cross sections for $pp \to WZ$ with $66 < m_{ll} < 116$ GeV, calculated with MCFM and MC@NLO, for a variety of input PDF sets, are shown in Table 10.1.

Uncertainties on the theoretical cross section calculation come from several sources. The sources of systematic uncertainty which we consider are:

- *PDFs*: The uncertainty due to the choice of PDF is calculate by adding the difference between the nominal PDF and the 52 eigenvectors of the CT10 PDF

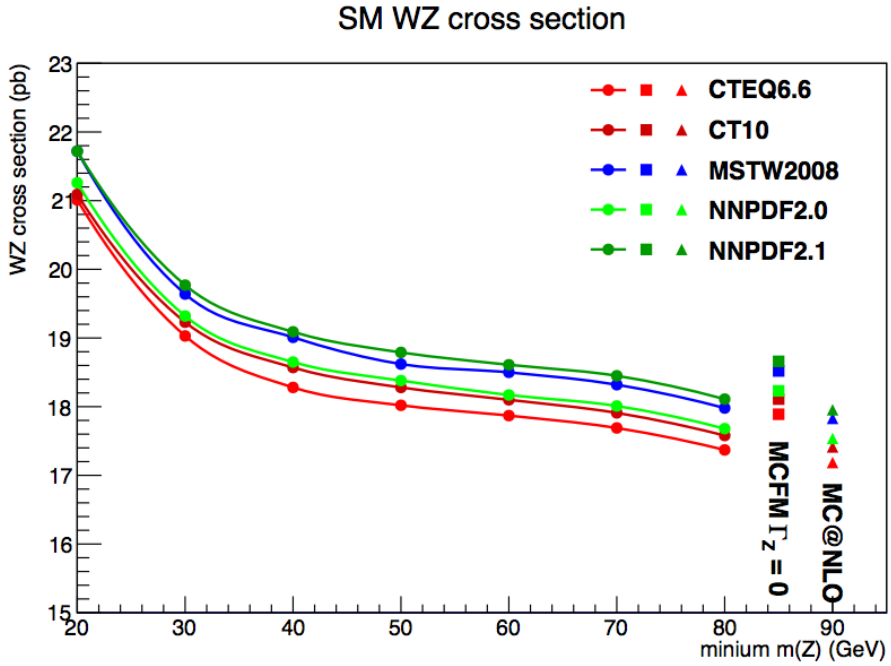

Figure 10.1: The theoretical WZ cross section as a function of the choice of minimum Z boson mass as calculated by MCFM (circles) for several different PDF sets. There is no upper bound on the Z mass for these calculations. The cross section is also shown with no $Z-\gamma$ interference as calculated by MCFM (squares) and MC@NLO (triangles).

Table 10.1: WZ theoretical cross section with different PDF sets. The Standard Model cross sections (pb) for $pp \to WZ$ at $\sqrt{s} = 7\,\text{TeV}$ computed with MCFM and MC@NLO.

	MCFM		MC@NLO	
PDF	total	fiducial	total	fiducial
CTEQ6.6	17.39±0.03	6.10±0.03	17.07	6.02
CT10	17.61±0.03	6.18±0.03	17.28	6.14
MSTW 2008	17.98±0.03	6.39±0.04	17.69	6.31
NNPDF2.0	17.67±0.03	6.22±0.02	17.42	6.18
NNPDF2.1	18.11±0.03	5.34±0.03	17.82	0.32

set in quadrature. The uncertainties are calculated separately for positive and negative errors using the equations:

$$\begin{aligned} \sigma_+ &= \sum_{i=1}^{52} \max(\sigma_{WZ}^i - \sigma_{WZ}^{\text{default}}, 0)^2 \\ \sigma_- &= \sum_{i=1}^{52} \min(\sigma_{WZ}^i - \sigma_{WZ}^{\text{default}}, 0)^2 \end{aligned} \tag{10.4}$$

The resulting uncertainties are +3.1%, -3.9% for the total cross section and +0.13, -0.40% for the fiducial cross section. The PDF uncertainty is significantly larger for the total cross section than for the fiducial cross section.

Comparisons are made with other PDF sets, included NNPDF2.1 and CTEQ 6.6. However, the differences between CT10 and the other PDF sets tested are smaller than the uncertainties calculated from the CT10 eigenvectors, so we do not include them separately.

- *QCD renormalization and factorization scale*: We vary the QCD renormalization scale and the factorization scale in the MCFM calculation simultaneously by $\times 2$ and $\times 0.5$. The resulting differences, which we take as a systematic uncertainty, are +5.4%, -4.0% for the total cross section and +4.7%, -4.3% for the fiducial cross section.

- α_S: We vary the strong coupling constant α_S by ± 0.001, which is consistent with its measured uncertainty at the Z mass. The change is taken as an uncertainty of +0.2%, -0.5% for the total cross section and +0.6%, -0.8% for the fiducial cross section.

All systematic uncertainties are combined in quadrature. In summary, the theoretical WZ cross section is calculated using MCFM and the CT10 PDF set in the Z

mass window $66 < m_{ll} < 116$ GeV, resulting in a total cross section of:

$$\sigma_{WZ}^{tot} = 17.6^{+1.1}_{-1.0} \text{ pb} \tag{10.5}$$

The MC@NLO samples are scaled to the total cross section when calculating the expected number of signal events.

10.2 Selected Events

We observe 317 WZ candidates in data with 231.2 signal and 68.1 background events expected. The breakdown of observed and expected events by channel and process is shown in Table 10.2, including statistical and systematic uncertainties. The Z+jets background is estimated using data-driven methods; top quark production is estimated with simulation and rescaled to match data control regions. All other predictions are from simulation, and the systematic uncertainty on MC estimates are discussed in Section 10.4. All numbers are calculated with 3, but rounded up to 2 decimal places. The systematic uncertainties listed in Table 10.2 are not used directly in the cross section extraction; the fit procedure accounts for the full granularity and correlation of systematic sources across different channels.

Kinematic distributions of the selected sample are shown in Figure 10.2. Distributions of the selected Z and W boson are show in Figure 10.3, including the WZ invariant mass. However, since we only measure the transverse component of the neutrino's momentum, there is ambiguity about the full W boson 4-vector. We solve the equation $E^2 = P^2 + M^2$ using the x and y components of E_T^{miss} and the full 4-vector of the electron or muon assigned to the W boson to estimate the p_Z of the

Table 10.2: Summary of observed events and expected signal and background contributions in the four tri-lepton channels and combined. The first error is statistical while the second is systematic. The systematics for the Z+jets estimates with a $Z \to \mu\mu$ are summed linearly since the uncertainties for the muon fakes are correlated in both channels. The same applies to the estimates in the channels with a $Z \to ee$. The two sets of Z+jets systematic uncertainties are then summed in quadrature, since the uncertainties associated with fake electrons and fake muons are uncorrelated. The systematics for the MC estimates are added linearly since they are correlated across channels. These are summed in quadrature with the systematics from the Z+jets background.

Final State	eee	$ee\mu$	$e\mu\mu$	$\mu\mu\mu$	Combined
Observed	56	75	78	108	317
ZZ	$3.2\pm0.1\pm0.2$	$4.9\pm0.1\pm0.2$	$5.0\pm0.1\pm0.1$	$7.9\pm0.1\pm0.2$	$21.0\pm0.2\pm0.7$
Z+jets	$8.8\pm2.1^{+1.9}_{-1.9}$	$3.7\pm1.7^{+1.6}_{-1.6}$	$10.2\pm2.4^{+2.2}_{-2.2}$	$9.1\pm3.9^{+3.9}_{-3.9}$	$31.9\pm5.3^{+7.5}_{-7.5}$
Top	$1.1\pm0.3\pm0.2$	$2.9\pm0.5\pm0.8$	$3.5\pm0.5\pm1.0$	$4.0\pm0.5\pm1.1$	$11.5\pm0.9\pm3.4$
$W/Z+\gamma$	$1.4\pm0.7\pm0.1$	–	$2.3\pm0.9\pm0.1$	–	$3.7\pm1.1\pm0.1$
Bkg (total)	$14.5\pm2.2^{+1.9}_{-1.9}$	$11.5\pm1.8^{+1.8}_{-1.8}$	$21.0\pm2.6^{+2.4}_{-2.4}$	$21.0\pm3.9^{+4.0}_{-4.0}$	$68.1\pm5.5^{+8.2}_{-8.2}$
Expected signal	$38.9\pm0.5\pm2.0$	$54.0\pm0.5\pm2.1$	$56.6\pm0.6\pm1.6$	$81.7\pm0.7\pm2.0$	$231.2\pm1.1\pm7.8$
Expected S/B	2.7	4.7	2.7	3.9	3.4

neutrino, using the W mass as a constraint. There are two possible solutions for p_Z. If there are two real solutions, we choose the one with the smaller magnitude. If there is no real solution, we select the real part of the solution with the smaller magnitude. In a MC study, choosing the smaller of the two solutions was found to reproduce the true WZ mass better than choosing the larger solution.

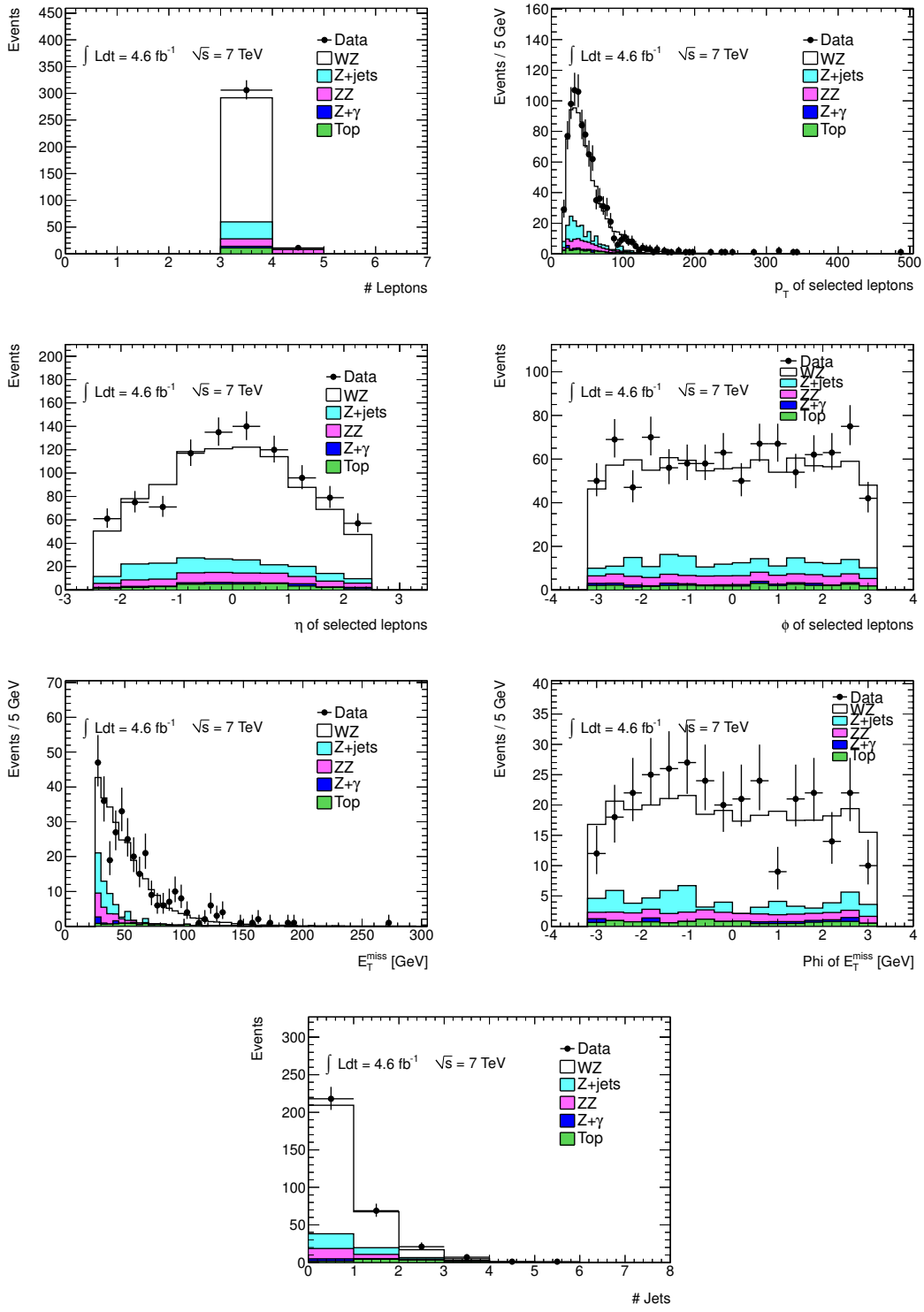

Figure 10.2: Selected kinematic distributions for events in the selected WZ sample. The Z+jets and $t\bar{t}$ backgrounds are MC normalized by data-driven estimates.

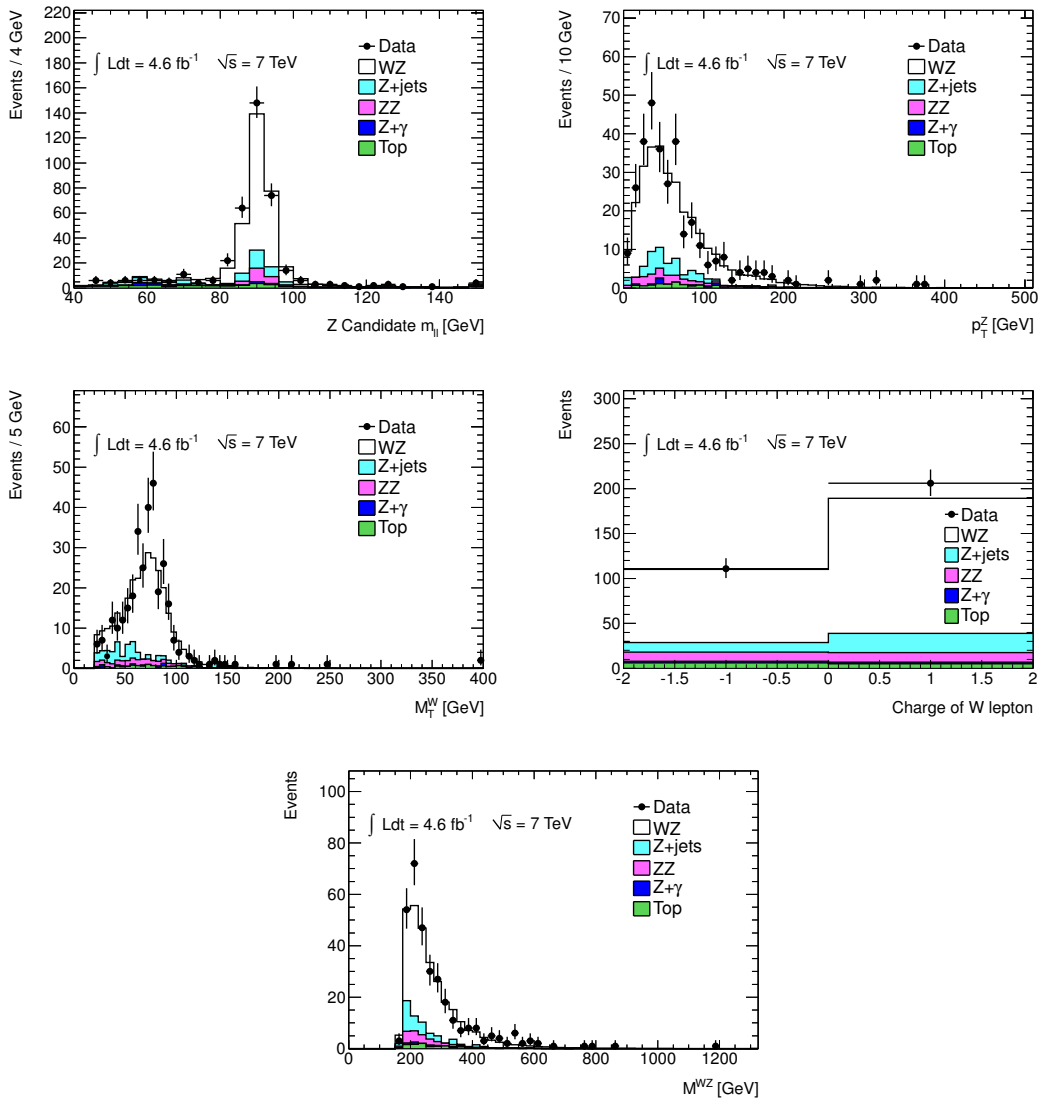

Figure 10.3: Distributions of selected W and Z bosons. Distributions are shown after all selections, except for the Z invariant mass distribution, which is shown with the Z mass requirement lifted. The Z+jets and $t\bar{t}$ backgrounds are MC normalized by data-driven estimates; all other processes are taken from MC.

10.3 Acceptance and Efficiency

To convert the number of observed WZ events to a measured cross section, we need to know the probability with which a collision containing a WZ final state was counted in our selected events. We calculate the fiducial cross section by correcting the number of observed events for the efficiency of reconstructing a WZ event, if that event is within the detector volume. The efficiency correction, called the *fiducial efficiency*, C_{WZ}, corrects the number of observed events to the number of produced events, for events within the fiducial volume (see next section.)

The total cross section is then calculated by extrapolating to the full phase space of WZ events, which includes events with leptons which fall outside the detector and selection volume. The correction from events produced within the fiducial volume to the full WZ phase space is called the *acceptance correction*, A_{WZ}.

10.3.1 Fiducial Volume

The fiducial volume is a phase space designed to be as close as possible to that in which we select WZ events with the ATLAS detector and with our selection cuts. Measuring a cross section within the fiducial volume minimizes theoretical extrapolation.

We define the fiducial volume with the same requirements on truth level objects in all four channels. It is defined as:

- $p_T^\ell > 15\,\text{GeV}$ for the two charged leptons from the Z decay
- $p_T^\ell > 20\,\text{GeV}$ for the charged lepton from the W decay

- $|\eta^{\ell}| < 2.5$ for the three charged leptons
- $p_T^{\nu} > 25\,\text{GeV}$ for the neutrino
- $|m_{\ell\ell} - m_Z| < 10\,\text{GeV}$ for the Z candidate
- $m_T^W > 20\,\text{GeV}$ for the W candidate
- $dR(l, l) > 0.3$ for all leptons

Since our WZ selection requirements on electrons and muons are slightly different, there is some extrapolation needed to move from the observed events to the fiducial volume. The extrapolation is minimal and having a common volume defined for all combinations of leptons allows us to compute a cross section that is easily comparable and combined across all the four channels.

The truth leptons used in calculating the fiducial volume and efficiency in simulation are final state electrons and muons including all photons within $\Delta R < 0.1$ of the lepton. The photons are added so that the final state leptons are physically well defined and to minimize the measured cross section's dependence on the modeling of soft and collinear photon radiation from the leptons.

10.3.2 Fiducial Efficiency

The fiducial efficiency C_{WZ} corrects from the truth objects in the fiducial volume to the reconstructed level. This correction gives us the probability of reconstructing an event, given that all objects in the event would have been in the detector and passed our selection requirements at truth level in simulation.

The fiducial efficiency is the product of the trigger efficiency, the efficiency of event level selections like identifying a primary vertex and reconstructing the E_T^{miss} and the individual efficiencies of all three charged leptons to pass the lepton selection requirements.

We calculate C_{WZ} by finding the ratio of the number of events which pass the reconstruction level selections to the number of events which are inside the fiducial volume at the generator level. Corrections are applied to the signal simulation to reproduce the resolutions measured in the data, including smearing and scaling of the lepton momentum and pileup reweighting (see Section 7.2). The fiducial efficiency is defined as:

$$C_{WZ\to l\nu l'l'} = \frac{N^{\text{MC Pass All Cuts}}_{\text{Reconstructed } WZ\to l\nu l'l'} \times \text{SF}}{N^{\text{MC Fiducial Volume}}_{\text{Generated } WZ\to l\nu l'l'}} \tag{10.6}$$

where the Scale Factor (SF) is an event level correction to account for the differences in reconstruction and trigger efficiencies between simulation and data. Specifically, the scale factor is calculated as:

$$SF = \frac{\epsilon^{data}_{trig}}{\epsilon^{MC}_{trig}} \cdot \frac{\epsilon^{data}_{lep\,reco}}{\epsilon^{MC}_{lep\,reco}} \cdot \frac{\epsilon^{data}_{event\,reco}}{\epsilon^{MC}_{event\,reco}} \tag{10.7}$$

where ϵ_{trig} is the event level trigger efficiency, $\epsilon_{lep\,reco}$ is the efficiency of reconstructing all three leptons, and $\epsilon_{event\,reco}$ is the efficiency of the event passing event level selections including the primary vertex identification and missing transverse energy reconstruction.

10.3.3 Total Acceptance

The acceptance correction A_{WZ} extrapolates from the truth level fiducial volume to the full phase space in which WZ events are produced. The acceptance correction

is calculated separately in each channel with events from the MC@NLO WZ signal simulation, and is defined as:

$$A_{WZ\to l\nu l'l'} = \frac{N^{\text{MC Fiducial Volume}}_{\text{Generated } WZ\to l\nu l'l'}}{N^{\text{MC All}}_{\text{Generated } WZ\to l\nu l'l'}} \tag{10.8}$$

To correct for the missing $Z-\gamma$ interference in the MC@NLO simulation, we apply a correction factor of 1.018 taken from a comparison of the acceptance correction calculated by MC@NLO before showering and MCFM. We can not compute A_{WZ} directly from MCFM because MCFM simulates event at the parton level, without showering or photon final state radiation. However, comparing the parton-level acceptances between MCFM and MC@NLO allows us to correct the MC@NLO acceptance to the MCFM total cross section, which includes $Z-\gamma$ interference.

The complete correction from reconstruction level to the total phase space is given by the product $C_{WZ\to l\nu l'l'} \times A_{WZ\to l\nu l'l'}$. The fiducial efficiency, acceptance correction, and total correction $C_{WZ} \times A_{WZ}$ are given in Table 10.3 for each of the four lepton channels. The efficiency of reconstructing the three muon channel is 78%, while the efficiency of reconstructing the three electron channel is 38%. The single electron reconstruction efficiency is lower than the single muon reconstruction efficiency, and requiring three electrons costs us three times.

Table 10.3: Fiducial and total acceptance corrections per channel.

	$\mu\mu\mu$	$e\mu\mu$	$ee\mu$	eee
A_{WZ}(pre-showering)	0.352	0.352	0.352	0.352
A_{WZ}(post-showering)	0.338	0.333	0.332	0.330
C_{WZ}	0.780	0.548	0.525	0.380
$A_{WZ} \times C_{WZ}$	0.263	0.182	0.174	0.125

Table 10.4: Uncertainties on theoretical cross sections for MC samples used in the analysis.

Sample	Uncertainty (%)
WZ	$^{+7.5}_{-4.6}$
ZZ	$^{+5.0}_{-4.1}$
$Z+\gamma$	± 5.0
$t\bar{t}$	$^{+7.0}_{-9.6}$

10.4 Systematic Uncertainties

The systematic uncertainties covered in this section are uncertainties reflecting how well we know the fiducial efficiency and acceptance correction used in calculating the measured cross sections, as well as uncertainties on the normalization of backgrounds estimated from simulation. The uncertainties are also used in extracting limits on anomalous triple gauge couplings, although additional systematic uncertainties, discussed in Section 11.5, are included for calculating the limits.

The uncertainties on the theoretical cross-sections used to normalize signal and background MC are shown in Table 10.4. The uncertainties on the ZZ, $Z+\gamma$, and $t\bar{t}$ cross section are described in detail in References [25, 1, 105, 98], and include uncertainties on PDF modeling, the renormalization and factorization scales, and experimental measurements. The uncertainty on the theoretical WZ cross section does not affect the measured cross section; it is considered, however, when extracting aTGC limits.

The uncertainty on the luminosity measurement is 1.8%, as discussed in Section 3.4.

Systematic uncertainties on the fiducial efficiency C_{WZ} are due to uncertainties on

muon, electron, and E_T^{miss} resolutions and efficiencies, on trigger efficiencies, and from PDFs. To estimate the size of the uncertainty from a particular systematic source on the signal efficiency, we vary the underlying systematic source in signal simulation and compare the event yield to the nominal selection. The uncertainty is taken as the fractional difference between the nominal predicted number of events and the number of events predicted with the varied systematic. The fractional uncertainty calculated from the signal simulation is also applied to the ZZ and $Z+\gamma$ backgrounds, as there are not enough MC statistics to calculate the uncertainties directly in the background simulation.

The systematic uncertainties on the acceptance A_{WZ} arise from PDF uncertainties, the choice of generator, and the renormalization and factorization scale used in the simulation.

10.4.1 Muons

We consider three sources of systematic uncertainty on the reconstruction and selection of muons in this analysis.

Details on the systematic uncertainties on muon acceptance and efficiency are listed below:

- *Reconstruction efficiency*

  The efficiency of reconstructing a muon in data and simulation differs slightly, and this difference is taken into account by weighing simulated events by a scale factor for each selected muon. The scale factor is calculated as a function of muon η and p_T, as described in Section 7.2.2, and scale factors are multiplica-

tive for events with multiple muons. There are several sources of uncertainty on the correction factor. There are statistical uncertainties from the tag-and-probe measurements of muon efficiency in data. There are systematic uncertainties due to background subtraction, on the order of 0.2%. Finally, there is an uncertainty on the efficiency for reconstructing high momenta muons, which requires extrapolating the scale factor and relies on the simulation of muon energy loss at high energies. For high p_T muons, the extrapolation uncertainty on the correction factor is around 1%.

- *Resolution*

  As discussed in Section 7.2.2, the muon momentum resolution is determined from studies of data taken with the toroid off and from studies on the dimuon mass resolution at the Z pole. The momentum of muons in simulation is smeared to reproduce the resolution measured in data. Uncertainties on the smearing function arise from statistical uncertainties on the measured resolution, uncertainties on background subtraction, the knowledge of the ATLAS material budget and muon spectrometer alignment, and uncertainties on p_T extrapolation. The degree of smearing is varied within its 1σ uncertainties on the Inner Detector track and the Muon Spectrometer Track separately, and the full difference in fractional event yield, as compared to the nominal smearing, is taken as the systematic uncertainty.

- *Isolation and impact parameter* A p_T and η based event weight, or scale factor, is applied to simulated events with muons to correct for very small differences in the measured efficiencies of the muon isolation, d_0, and z_o selection requirements

Table 10.5: Detailed list of systematic uncertainties on the expected event yields for muon objects in MC signal samples, tau channels included.

Uncertainty per channel (%)		μee	$\mu\mu e$	$\mu\mu\mu$
Rec. efficiency		$^{+0.27}_{-0.27}$	$^{+0.53}_{-0.53}$	$^{+0.79}_{-0.8}$
p_{T} smearing	ID	0.03	0.01	0.04
	MS	0.02	0.05	0.04
	combination	0.04	0.05	0.06
Isolation & Impact Parameter Efficiency		$^{+0.2}_{-0.2}$	$^{+0.43}_{-0.43}$	$^{+0.61}_{-0.62}$
Total		0.34	0.68	1.01

between data and MC (see Section 7.2.2.) Uncertainties in the correction factor due to background modeling and statistical uncertainties in the data used to measure the correction result in an overall uncertainty on the event yield.

For each systematic considered, the fractional difference in event yield is calculated for all three channels that contain at least one muon. The uncertainties scale linearly with the number of muons in the final state. The correlations in systematic uncertainties due to the same source in different channels are calculated and input to the cross section fit. The size of each muon systematic uncertainty, per channel, is shown in Table 10.5. The total is shown for illustration only; each systematic uncertainty is input independently to the cross section fit.

10.4.2 Electrons

We consider four sources of systematic uncertainty on the reconstruction and selection of electrons in this analysis.

Details on the systematic uncertainties on electron acceptance and efficiency are listed below:

- *Reconstruction and identification efficiency*

  The efficiency of reconstructing and selecting an electron in data and simulation differs slightly, and this difference is taken into account by weighing simulated events by a scale factor for each selected electron. The scale factor is calculated as a function of electron η and E_T, as described in Section 7.2.3, and scale factors are multiplicative for events with multiple electrons. The dominant uncertainty on the electron reconstruction scale factor arise from background subtraction in the tag-and-probe measurements of electron efficiency in W, Z, and J/Ψ data samples. There are also statistical uncertainties in the data samples. The uncertainties are calculated separately for the reconstruction efficiency – the probability that an electron traversing the detector produces a calorimeter cluster and a track – and the identification efficiency – the probability that, given a cluster and a track, an electron is selected.

- *Energy Scale* The electron energy scale is calibrated in both data and simulation using a sample of $Z \to ee$ events. Uncertainties on the modeling of material in the detector and the calibration of the EM calorimeter pre-sampler energy scale dominate the uncertainty on the energy scale correction applied to both MC and data. The calibration of the electron energy scale is varied in simulated signal events within its uncertainties; the fractional change in the event yield compared to nominal calibrations is taken as the systematic uncertainty.

- *Resolution*

  As for muons, and as discussed in Section 7.2.3, the electron energy resolution

Table 10.6: Summary of electron systematic uncertainties on the expected event yields in MC signal samples.(%).

Source	eee	$ee\mu$	$e\mu\mu$
Energy scale	0.5	0.3	0.3
Energy smearing	0.1	0.1	0.0
Reconstruction Efficiency	2.5	1.7	0.8
Identification Efficiency	3.5	2.3	1.2
Isolation & Impact Parameter Efficiency	1.5	1.1	0.4
Total	4.5	3.1	1.5

is corrected in simulation to match observed data by applying an E_T and η dependent smearing to simulated electron E_T. The largest systematic uncertainty on the energy smearing of the electrons results from the background estimation and modeling in the $Z \to ee$ data sample used to measure resolution in data.

- *Isolation and impact parameter* A p_T and η based event weight, or scale factor, is applied to simulated events with electrons, as for muons, to correct for very small differences in the measured efficiencies of the electron isolation, d_0, and z_o selection requirements between data and MC (see Section 7.2.3.) Uncertainties in the correction factor due to background modeling and statistical uncertainties in the data used to measure the correction result in an overall uncertainty on the event yield.

For each systematic considered, the fractional difference in event yield is calculated for all three channels that contain at least one electron. The uncertainties scale linearly with the number of electrons in the final state. The correlations in systematic uncertainties due to the same source in different channels are calculated and input to the cross section fit. The size of each electron systematic uncertainty, per channel, is shown in Table 10.6. The total is shown for illustration only; each systematic

uncertainty is input independently to the cross section fit.

10.4.3 E_T^{miss}

The E_T^{miss} used in this analysis is built from reconstructed electrons, muons, taus, jets, photons, soft jets, and from cells in the calorimeter not included in any physics objects, as described in Section 5.5. The uncertainties on the efficiency of WZ events passing our E_T^{miss} and W transverse mass requirements can be determined by propagating the uncertainty on the constitute objects through the E_T^{miss} calculation. For example, the uncertainty on the E_T^{miss} due to the jet energy scale calibration can be calculated by varying the energy scale of the jets directly, since they are an input to the E_T^{miss} calculation. Details on the calculation of E_T^{miss} systematics can be found in Reference [24].

Since electrons and muons are inputs to the E_T^{miss} calculation, the uncertainties on the muon and electron momentum and resolutions affect the E_T^{miss} uncertainty. However, these uncertainties are already accounted for in calculating the muon and electron systematics, since the variations applied to muons and electrons in calculating those systematics are propagated through the E_T^{miss} calculation, and because the uncertainties are determined from final event yields.

Aside from the uncertainties on muon and electron momentum and resolution, the main sources of uncertainty which affect the efficiency of the E_T^{miss} and M_T^W selections are:

- uncertainty on the cluster energy scale
- uncertainty on the jet energy scale

- uncertainty on the jet energy resolution
- the description of pileup by the simulation

The uncertainty on the cluster energy scale affects the cells in the calorimeter which are not associated to any physics object. The uncertainty on the topocluster energy scale is studied in comparisons between data and simulation for the $\frac{E}{p}$ response for single tracks, and this uncertainty is propagated to an uncertainty on the E_T^{miss} in $W \to e\nu$ samples by varying the energy scale of topoclusters in simulation as a function of the cluster E_T and η.

Differences in the material description between the simulation and the detector, the choice of shower model, and the choice of model for the underlying event in the simulation also affect the knowledge of the cluster energy scale. The uncertainties due to these sources is studied in dedicated simulations in which these models are changed. For example, five MC samples are generated to study the effect of the dead material description on the E_T^{miss} uncertainty, with the following changes: 1) 5% increase in the inner detector material, 2) 0.1 X_0 additional in front of the EM barrel calorimeter, 3) 0.05 X_0 added between he pre-sampler and the EM barrel calorimeter, 4) 0.1 X_0 added in the cryostat after the EM calorimeter, and 5) extra material in the barrel-endcap transition of the EM calorimeter. Similarly, different choices of the GEANT4 physics list for modeling calorimeter showers are used in a dedicated MC study, and different tunes of Pythia parameters with increased final state radiation and more soft particles are tested.

The contribution of the cell term to the total E_T^{miss} uncertainty is calculated in WZ signal events by varying the cell term within the uncertainties derived in the

dedicated studies discussed above and comparing the event yields to the nominal E_T^{miss} values. The total uncertainty on the cell term is around 13%, but it is a small contribution to the total E_T^{miss} in events with three charged leptons.

The uncertainties on the jet energy scale and resolutions are found by studies on dijet, Z+ jet, and γ+ jet balance in data and simulation, and the jets contributing to the E_T^{miss} calculation are varied within their uncertainties to find the effect on the E_T^{miss}.

Each additional collision within a single event (in-time pileup) contributes to the energy in the calorimeter, smearing the E_T^{miss} resolution. Additionally, since the calorimeter integrates over several 25-ns samplings, collisions in the few events previous to the event of interest can leave energy depositions that get included in the current event (out-of-time pileup.) If the pileup from additional collisions is not well modeled by the simulation, differences in the selection efficiency of the E_T^{miss} may occur between data and simulation. The modeling of the in-time pileup is studied by comparing E_T^{miss} distributions in Z events in data and simulation as a function of the number of reconstructed vertices in the event. In-time pileup contributes most to the jet, cell, and tau terms in the E_T^{miss} calculation, and these terms are varied up and down by 3% to cover the uncertainty due to in-time pileup.

For out-of-time pileup, the simulation is not found to reproduce the contributions to E_T^{miss} exactly for the first third of each bunch train; a 5 GeV smearing applied to 33% of the MC events covers the difference and an uncertainty corresponding to this variation is applied.

Following the procedure in [40], the uncertainties due to each of the sources

Table 10.7: Summary of systematic uncertainties on the expected event yields (%) for E_T^{miss}in MC signal samples.

Source	eee	$ee\mu$	$e\mu\mu$	$\mu\mu\mu$
Topo cluster energy scale	0.40	0.17	0.57	0.18
Jet energy scale	0.11	0.08	0.10	0.08
Jet energy resolution	0.28	0.30	0.39	0.25
Pileup	0.32	0.11	0.32	0.13

discussed above are propagated through the E_T^{miss} in WZ signal events to obtain the uncertainties detailed in Table 10.7. As WZ events have three high p_T charged leptons, the E_T^{miss} measurement is dominated by the lepton's momentum and the uncertainty is relatively small – less than 1% on event yield, per source, across all channels.

10.4.4 PDF, Scale and Generator

The uncertainty on the underlying PDF translates into an uncertainty on the lepton kinematic distributions in WZ simulated events; in turn, this uncertainty affects our acceptance calculation. The uncertainty on A_{WZ} from PDFs is evaluated by varying the eigenvalues of the CT10 PDF set in MC@NLO and comparing the acceptance in the varied sample to the nominal set, and by comparing the acceptance calculated with the MSTW2008 NLO PDF set with that from the CT10 PDF set.

The uncertainty within the CT10 PDF set is evaluated by averaging the positive and negative uncertainty for all 52 error eigenvectors i:

$$\sigma^+ = \sigma^- = \frac{\sqrt{\sum_{i=1}^{n}[max(A_i - A_{WZ}, 0)]^2} + \sqrt{\sum_{i=1}^{n}[max(A_{WZ} - A_i, 0)]^2}}{2A_{WZ}}, \qquad (10.9)$$

where A_{WZ} is the acceptance evaluated at the central value of CT10. The uncertainty

from the 52 CT10 error eigenvectors is 0.8%, and there is a 0.3% statistical uncertainty on the central A_{WZ}.

The acceptance is also calculated with the MSTW2008 NL0 68% CL PDF set [119] by reweighting, on an event-by-event level, the WZ MC@NLO signal sample. The difference in acceptance between the nominal CT10 set and the MSTW2008 set is 0.8%. The total PDF uncertainty on A_{WZ}, which is the quadratic sum of the CT10 variations, the difference between the two PDF sets, and the statistical uncertainty, is 1.2%.

The nominal renormalization and factorization scale in the WZ MC@NLO signal samples is a dynamic average of the transverse mass squared of the W and Z boson. To determine the uncertainty on A_{WZ} due to this choice of scale, privately produced MC@NLO samples are made after parton showering but before ATLAS GEANT4 simulation and reconstruction in which the normalization and factorization scales are varied by a factor of 2 and 0.5. The difference between the acceptance of the nominal simulation and the varied samples is taken as an uncertainty and is 0.4% per channel.

Finally, the choice of MC@NLO as generator is checked by calculating the acceptance with fully simulated POWHEG BOX [87, 121] WZ events. The difference in A_{WZ} between MC@NLO and the POWHEG BOX is 0.4%, which is taken as a generator systematic.

A summary of all systematic uncertainties affecting the expected number of signal events is found in Table 10.8.

Table 10.8: Summary of all systematic uncertainties (%) on expected WZ event yield, used in the cross section calculation.

Source	$\mu\mu\mu$	$e\mu\mu$	$ee\mu$	eee
μ reconstruction efficiency	0.8	0.53	0.27	-
μ p_{T} scale & resolution	0.06	0.05	0.04	-
μ isolation & impact parameter efficiency	0.62	0.43	0.2	-
e reconstruction efficiency	-	0.8	1.7	2.5
e identification efficiency	-	1.2	2.3	3.5
e isolation & impact parameter efficiency	-	0.4	1.1	1.5
e energy scale	-	0.3	0.3	0.5
e energy resolution	-	0.0	0.1	0.1
E_T^{miss} cluster energy scale	0.18	0.57	0.17	0.40
E_T^{miss} jet energy scale	0.08	0.10	0.08	0.11
E_T^{miss} jet energy resolution	0.25	0.39	0.30	0.28
E_T^{miss} pileup	0.13	0.32	0.11	0.32
Trigger - μ	0.29	0.15	0.07	-
Trigger - e	-	<0.05	<0.05	<0.05
Generator	0.4	0.4	0.4	0.4
PDF	1.2	1.2	1.2	1.2
Scale	0.4	0.4	0.4	0.4
Luminosity	1.8	1.8	1.8	1.8

10.5 Cross Section Calculation

We calculate the WZ cross section by building a likelihood function based on the number of expected and observed events, and finding the cross section which minimizes the negative log-likelihood of the likelihood function. The cross section is measured in each of the four channels. To combine channels, a total likelihood is built from the product of each the individual channel probabilities; one advantage of the likelihood method is that it ensures that the calculated cross section is the best value that is consistent across all channels. Another advantage is that the $WZ \to \tau + X$ contribution can be easily included.

The number of expected events can be expressed as the sum of expected signal events in channel i after all full selection, N_s^i, and the number of predicted background events, N_b^i:

$$N_{exp}^i = N_s^i + N_b^i \tag{10.10}$$

Using the observed number of events, N_{obs}^i, we construct a likelihood L based on the Poisson probability that the expected number of signal and background events produces the observed number in channel i:

$$L(N_{obs}^i; N_s^i + N_b^i) = \frac{e^{-(N_s^i+N_b^i)} \times (N_s^i + N_b^i)^{N_{obs}^i}}{(N_{obs}^i)!} \tag{10.11}$$

The introduction of systematic uncertainties on the acceptance and efficiency of the signal and background selections results in a change in the number of expected events. Rather than using the uncertainties on A_{WZ} and C_{WZ} directly, we introduce nuisance parameters that modify the number of expected events. Each systematic uncertainty in channel i, is assumed to follow a normal distribution with mean zero

and a variance of one. The correlations between uncertainties across the four channels are treated by using a single nuisance parameter for each systematic across all correlated channels. Uncertainties are treated either as fully correlated or uncorrelated. We rewrite the number of expected events to include systematic uncertainties:

$$\begin{aligned} N_s^i(\{x_k\}) &= N_s^i(1+\sum_{k=1}^{n} x_k S_k^i) \\ N_b^i(\{x_k\}) &= N_b^i(1+\sum_{k=1}^{n} x_k B_k^i) \end{aligned} \tag{10.12}$$

where the parameters S_k^i and B_k^i are the standard deviation representing the the k^{th} fractional systematic uncertainty in channel i on the signal and background respectively. The nuisance parameters x_k are the same across all channels, except they may be zero if a particular systematic does not affect one or more channels.

The number of signal events can be expressed either as a function of the fiducial cross section, $\sigma \equiv \sigma^{fid}_{WZ\to l\nu l'l'}$:

$$\begin{aligned} N_s^i(\sigma^{fid}_{WZ\to l\nu l'l'}, \{x_k\}) = & \frac{\sigma^{fid}_{WZ\to l\nu l'l'}}{\sigma^{tot}_{MC,\ WZ\to l\nu l'l'} \times A_{WZ\to l\nu l'l'}} \\ & \times \left(N^{MC}_{WZ\to l\nu l'l'} + N^{MC}_{WZ\to \tau+X} \right) \times (1+\sum_{k=1}^{n} x_k S_k^i) \end{aligned} \tag{10.13}$$

or as a function of the total cross section measurement $\sigma \equiv \sigma^{tot}_{WZ}$

$$N_s^i(\sigma^{tot}_{WZ}, \{x_k\}) = \frac{\sigma^{tot}_{WZ}}{\sigma^{tot}_{MC,\ WZ}} \times \left(N^{MC}_{WZ\to l\nu l'l'} + N^{MC}_{WZ\to \tau+X} \right) \times (1+\sum_{k=1}^{n} x_k S_k^i) \tag{10.14}$$

Using equation 10.11 and either equation 10.13 or 10.14, we rewrite the negative log-likelihood as a function of the calculated cross section σ and the nuisance

parameters x_k:

$$-\ln L(\sigma, \{x_k\}) = \sum_{i=1}^{4} -\ln\left(\frac{e^{-(N_s^i(\sigma,\{x_k\})+N_b^i(\{x_k\}))} \times (N_s^i(\sigma,\{x_k\}) + N_b^i(\{x_k\}))^{N_{obs}^i}}{(N_{obs}^i)!}\right) + \sum_{k=1}^{n} \frac{x_k^2}{2} \tag{10.15}$$

The final term in the likelihood equation is the product of the Gaussian constraints on the nuisance parameters x_k.

To find the most probable value of σ, equation 10.15 is minimized simultaneously over σ and all nuisance parameters. The value of σ at the log-likelihood minimum is used as the measurement of σ. The minimization and error calculation is performed with the Minuit package [106] in ROOT.

In equations 10.13 and 10.14, the simulation is used to determine the total number of expected events. This expectation is then scaled by the ratio of the measured cross section to the theoretical cross section. Minimizing the negative log-likelihood function in equation 10.15 allows the data to find the rescaling of the expected signal contribution that best matches the data, resulting in a measured cross section.

The errors on σ are estimated by taking the difference of the cross-section at the minimum to the cross-section where the log-likelihood is 0.5 units above the minimum along the direction of the parameter σ. This calculation is performed both in the positive and negative directions separately, and thus may yield different positive and negative errors. As the nuisance parameters account for the systematic errors on our measurement, the error is the combined statistical and systematic uncertainty on our measurement.

The full likelihood function with nuisance parameters will automatically take into

account all the systematic errors, and propagate them to the final uncertainty. To understand the contribution from each systematic error separately, we can propagate by hand each systematic uncertainties on our acceptance to the final cross-section. We do this by adjusting the acceptance of our signal and background in the likelihood function up and down by one sigma of that parameter, and re-minimizing the likelihood function (without nuisance parameters) to find a new cross-section value.

The systematic uncertainties on the fiducial and total cross-section are summarized in Tables 10.9 and 10.10. All systematic uncertainties are added in quadrature to yield the total uncertainty, excluding the uncertainty in luminosity.

Table 10.9: Relative systematic uncertainties (%) on the fiducial cross section for each channel.

Source	$\mu\mu\mu$	$e\mu\mu$	$ee\mu$	eee	Combined
μ - Rec. efficiency	$^{+0.88}_{-0.87}$	$^{+0.57}_{-0.56}$	$^{+0.32}_{-0.32}$	$^{+0.00}_{-0.00}$	$^{+0.52}_{-0.53}$
μ -p_T smearing	$^{+0.11}_{-0.11}$	$^{+0.11}_{-0.11}$	$^{+0.00}_{-0.00}$	$^{+0.00}_{-0.00}$	$^{+0.07}_{-0.07}$
μ - isolation & IP efficiency	$^{+0.66}_{-0.65}$	$^{+0.45}_{-0.45}$	$^{+0.22}_{-0.22}$	$^{+0.00}_{-0.00}$	$^{+0.39}_{-0.40}$
e - Rec. Efficiency	$^{+0.00}_{-0.00}$	$^{+0.91}_{-0.90}$	$^{+1.86}_{-1.80}$	$^{+2.84}_{-2.71}$	$^{+1.12}_{-1.11}$
e - Id. Efficiency	$^{+0.00}_{-0.00}$	$^{+1.37}_{-1.34}$	$^{+2.53}_{-2.42}$	$^{+4.02}_{-3.76}$	$^{+1.61}_{-1.57}$
e - Energy Smearing	$^{+0.00}_{-0.00}$	$^{+0.00}_{-0.00}$	$^{+0.11}_{-0.11}$	$^{+0.11}_{-0.11}$	$^{+0.04}_{-0.04}$
e - Energy Scale	$^{+0.00}_{-0.00}$	$^{+0.34}_{-0.34}$	$^{+0.32}_{-0.32}$	$^{+0.56}_{-0.55}$	$^{+0.25}_{-0.25}$
e - iso IP	$^{+0.00}_{-0.00}$	$^{+0.34}_{-0.34}$	$^{+1.20}_{-1.17}$	$^{+1.58}_{-1.53}$	$^{+0.62}_{-0.63}$
E_T^{miss} - jes	$^{+0.11}_{-0.11}$	$^{+0.11}_{-0.11}$	$^{+0.11}_{-0.11}$	$^{+0.11}_{-0.11}$	$^{+0.11}_{-0.11}$
E_T^{miss} - jer	$^{+0.22}_{-0.22}$	$^{+0.45}_{-0.45}$	$^{+0.32}_{-0.32}$	$^{+0.33}_{-0.33}$	$^{+0.32}_{-0.32}$
E_T^{miss} - cluster	$^{+0.22}_{-0.22}$	$^{+0.68}_{-0.67}$	$^{+0.22}_{-0.22}$	$^{+0.45}_{-0.44}$	$^{+0.36}_{-0.37}$
E_T^{miss} - pileUp	$^{+0.11}_{-0.11}$	$^{+0.34}_{-0.34}$	$^{+0.11}_{-0.11}$	$^{+0.33}_{-0.33}$	$^{+0.20}_{-0.20}$
μ - Trigger	$^{+0.33}_{-0.33}$	$^{+0.23}_{-0.23}$	$^{+0.11}_{-0.11}$	$^{+0.00}_{-0.00}$	$^{+0.20}_{-0.20}$
Signal stat. (MC)	$^{+0.86}_{-0.85}$	$^{+1.07}_{-1.05}$	$^{+0.93}_{-0.92}$	$^{+1.30}_{-1.27}$	$^{+0.50}_{-0.51}$
Bkg stat. (MC)	$^{+0.11}_{-0.11}$	$^{+1.59}_{-1.59}$	$^{+0.16}_{-0.16}$	$^{+1.70}_{-1.70}$	$^{+0.43}_{-0.42}$
Bkg stat. (Data Driven)	$^{+4.52}_{-4.52}$	$^{+4.30}_{-4.30}$	$^{+2.79}_{-2.79}$	$^{+5.12}_{-5.12}$	$^{+2.30}_{-2.23}$
Data Driven method - Z+jets	$^{+4.43}_{-4.44}$	$^{+3.85}_{-3.86}$	$^{+2.46}_{-2.47}$	$^{+4.59}_{-4.57}$	$^{+3.05}_{-3.04}$
Data Driven method - top	$^{+1.26}_{-1.26}$	$^{+1.75}_{-1.75}$	$^{+1.26}_{-1.26}$	$^{+0.48}_{-0.48}$	$^{+1.26}_{-1.26}$
Total (no lumi)	$^{+6.63}_{-6.64}$	$^{+6.68}_{-6.67}$	$^{+5.31}_{-5.24}$	$^{+8.93}_{-8.75}$	$^{+4.67}_{-4.62}$

Table 10.10: Relative systematic uncertainties (%) on the total cross section for each channel.

Source	$\mu\mu\mu$	$e\mu\mu$	$ee\mu$	eee	Combined
μ - Rec. efficiency	$^{+0.88}_{-0.88}$	$^{+0.57}_{-0.56}$	$^{+0.32}_{-0.32}$	$^{+0.00}_{-0.00}$	$^{+0.53}_{-0.53}$
μ -p_T smearing	$^{+0.10}_{-0.12}$	$^{+0.11}_{-0.11}$	$^{+0.00}_{-0.00}$	$^{+0.00}_{-0.00}$	$^{+0.07}_{-0.07}$
μ - isolation & IP efficiency	$^{+0.65}_{-0.66}$	$^{+0.45}_{-0.45}$	$^{+0.22}_{-0.21}$	$^{+0.00}_{-0.00}$	$^{+0.40}_{-0.40}$
e - Rec. Efficiency	$^{+0.00}_{-0.00}$	$^{+0.91}_{-0.89}$	$^{+1.86}_{-1.79}$	$^{+2.87}_{-2.72}$	$^{+1.10}_{-1.09}$
e - Id. Efficiency	$^{+0.00}_{-0.00}$	$^{+1.37}_{-1.34}$	$^{+2.53}_{-2.41}$	$^{+4.06}_{-3.77}$	$^{+1.57}_{-1.55}$
e - Energy Smearing	$^{+0.00}_{-0.00}$	$^{+0.00}_{-0.00}$	$^{+0.11}_{-0.11}$	$^{+0.11}_{-0.12}$	$^{+0.04}_{-0.04}$
e - Energy Scale	$^{+0.00}_{-0.00}$	$^{+0.34}_{-0.34}$	$^{+0.32}_{-0.32}$	$^{+0.56}_{-0.56}$	$^{+0.24}_{-0.24}$
e - iso IP	$^{+0.00}_{-0.00}$	$^{+0.34}_{-0.34}$	$^{+1.19}_{-1.17}$	$^{+1.58}_{-1.54}$	$^{+0.61}_{-0.60}$
E_T^{miss} - jes	$^{+0.10}_{-0.12}$	$^{+0.11}_{-0.11}$	$^{+0.11}_{-0.11}$	$^{+0.11}_{-0.12}$	$^{+0.11}_{-0.11}$
E_T^{miss} - jer	$^{+0.21}_{-0.23}$	$^{+0.45}_{-0.45}$	$^{+0.32}_{-0.32}$	$^{+0.33}_{-0.34}$	$^{+0.32}_{-0.32}$
E_T^{miss} - cluster	$^{+0.21}_{-0.23}$	$^{+0.68}_{-0.67}$	$^{+0.22}_{-0.21}$	$^{+0.44}_{-0.45}$	$^{+0.36}_{-0.36}$
E_T^{miss} - pileUp	$^{+0.10}_{-0.12}$	$^{+0.34}_{-0.34}$	$^{+0.11}_{-0.11}$	$^{+0.33}_{-0.34}$	$^{+0.20}_{-0.20}$
μ - Trigger	$^{+0.32}_{-0.34}$	$^{+0.23}_{-0.23}$	$^{+0.11}_{-0.11}$	$^{+0.00}_{-0.00}$	$^{+0.20}_{-0.20}$
Generator	$^{+0.40}_{-0.41}$	$^{+0.40}_{-0.40}$	$^{+0.40}_{-0.40}$	$^{+0.40}_{-0.40}$	$^{+0.40}_{-0.40}$
PDF	$^{+1.22}_{-1.20}$	$^{+1.21}_{-1.18}$	$^{+1.21}_{-1.18}$	$^{+1.22}_{-1.20}$	$^{+1.21}_{-1.18}$
Scale	$^{+0.40}_{-0.41}$	$^{+0.40}_{-0.40}$	$^{+0.40}_{-0.40}$	$^{+0.40}_{-0.40}$	$^{+0.40}_{-0.40}$
Signal stat. (MC)	$^{+0.86}_{-0.86}$	$^{+1.07}_{-1.05}$	$^{+0.93}_{-0.91}$	$^{+1.31}_{-1.28}$	$^{+0.50}_{-0.50}$
Bkg stat. (MC)	$^{+0.11}_{-0.12}$	$^{+1.59}_{-1.59}$	$^{+0.16}_{-0.16}$	$^{+1.70}_{-1.71}$	$^{+0.43}_{-0.42}$
Bkg stat. (Data Driven)	$^{+4.52}_{-4.51}$	$^{+4.30}_{-4.29}$	$^{+2.78}_{-2.78}$	$^{+5.06}_{-5.11}$	$^{+2.31}_{-2.21}$
Data Driven method - Z+jets	$^{+4.42}_{-4.44}$	$^{+3.85}_{-3.85}$	$^{+2.46}_{-2.46}$	$^{+4.54}_{-4.57}$	$^{+3.06}_{-3.02}$
Data Driven method - top	$^{+1.26}_{-1.27}$	$^{+1.75}_{-1.75}$	$^{+1.25}_{-1.25}$	$^{+0.48}_{-0.49}$	$^{+1.26}_{-1.25}$
Total (no lumi)	$^{+6.76}_{-6.77}$	$^{+6.81}_{-6.78}$	$^{+5.47}_{-5.37}$	$^{+9.00}_{-8.86}$	$^{+4.85}_{-4.76}$

10.6 Results

The final results for the fiducial and total cross-section measurement in each channel and for the combined measurement are shown in Tables 10.11 and 10.12. The systematic uncertainties include all sources except luminosity, which is listed separately.

Table 10.11: Measured fiducial cross sections for each channel and combined.

Channel	Cross-Section [fb]
$\mu\mu\mu$	$23.03^{+2.84}_{-2.66}(\text{stat})\ ^{+1.53}_{-1.53}(\text{syst})\ ^{+0.46}_{-0.45}(\text{lumi})$
$e\mu\mu$	$21.46^{+3.46}_{-3.20}(\text{stat})\ ^{+1.43}_{-1.43}(\text{syst})\ ^{+0.44}_{-0.43}(\text{lumi})$
$ee\mu$	$24.98^{+3.57}_{-3.25}(\text{stat})\ ^{+1.33}_{-1.31}(\text{syst})\ ^{+0.49}_{-0.48}(\text{lumi})$
eee	$22.53^{+4.29}_{-3.85}(\text{stat})\ ^{+2.01}_{-1.97}(\text{syst})\ ^{+0.46}_{-0.44}(\text{lumi})$
Combined	$92.31^{+6.66}_{-6.33}(\text{stat})\ ^{+4.31}_{-4.26}(\text{syst})\ ^{+1.85}_{-1.79}(\text{lumi})$

Table 10.12: Measured total cross sections for each channel and combined.

Channel	Cross-Section [pb]
$\mu\mu\mu$	$18.74^{+2.31}_{-2.17}(\text{stat})\ ^{+1.27}_{-1.27}(\text{syst})\ ^{+0.38}_{-0.36}(\text{lumi})$
$e\mu\mu$	$17.72^{+2.86}_{-2.64}(\text{stat})\ ^{+1.21}_{-1.20}(\text{syst})\ ^{+0.37}_{-0.35}(\text{lumi})$
$ee\mu$	$20.69^{+2.97}_{-2.69}(\text{stat})\ ^{+1.13}_{-1.11}(\text{syst})\ ^{+0.41}_{-0.39}(\text{lumi})$
eee	$18.78^{+3.58}_{-3.20}(\text{stat})\ ^{+1.69}_{-1.66}(\text{syst})\ ^{+0.38}_{-0.37}(\text{lumi})$
Combined	$19.00^{+1.38}_{-1.30}(\text{stat})\ ^{+0.92}_{-0.90}(\text{syst})\ ^{+0.38}_{-0.37}(\text{lumi})$

Chapter 11

Anomalous Triple Gauge Couplings

Standard Model electroweak theory predicts the existence of triple gauge couplings, including vertices in which the W and Z bosons couple to each other. New interactions or new particles could modify the couplings of these vertices. As discussed in Section 2.5, we express the WZ triple gauge couplings with an effective Lagrangian with three independent coupling parameters: g_1^Z, κ_Z, and λ_Z. In the Standard Model, $g_1^Z = \kappa_Z = 1$, and $\lambda_Z = 0$. We look for physics beyond the standard by looking for deviations in the couplings from their predicted value. Couplings that differ from the Standard Model prediction are called *anomalous triple gauge couplings* (aTGCs). We model WZ production with any value of each anomalous coupling by reweighting Monte Carlo events after production with a technique described in Section 11.1.

The existence of aTGCs would modify both the cross section and kinematics of WZ production. Contributions to WZ production from diagrams with the g_1^Z and λ_Z couplings are proportional to $\hat{s}$, where $\hat{s}$ is the square of the center-of-mass energy of the WZ production vertex. Contributions from κ_Z terms are proportional

to $\sqrt{\hat{s}}$. Kinematic distributions that are sensitive to the $\hat{s}$ of the WZ system are therefore sensitive to the presence of anomalous couplings. Section 11.2 discusses the dependence of several observables on anomalous couplings. We find that studying the transverse momentum of the Z boson in WZ events gives us the greatest sensitivity to the presence of aTGCs.

Using the differential p_T^Z distribution of the selected WZ sample, we extract limits on Δg_1^Z, $\Delta\kappa_Z$, and λ_Z, where $\Delta g_1^Z \equiv g_1^Z - 1$ and $\Delta\kappa_Z \equiv \kappa_Z - 1$ are deviations from the Standard Model values. In the effective Lagrangian approach, a form-factor can be introduced to ensure unitary at all energies. We set limits in two cases: 1) with a form factor $\Lambda = 2$ TeV, and 2) with no form factor, $\Lambda = \infty$. The form factor is discussed in Section 2.5.

We model the background as a function of the Z transverse momentum and calculate systematic uncertainties that reflect our knowledge of the shape of the p_T^Z distribution as well as the overall WZ signal normalization, as discussed in Sections 11.4 and 11.5, respectively. Our limits are presented in Section 11.7.2.

11.1 aTGC Simulation and Event Reweighting

We model WZ events with anomalous triple gauge couplings using MC@NLO version 4.0 [88]. With this generator, it is possible to generate $W^{\pm}Z$ events with any value of the anomalous TGC parameters Δg_1^Z, $\Delta\kappa_Z$, and λ_Z. We simulate two sets of events: the first set models Standard Model WZ production, and the second set simulates WZ events with one particular set of anomalous couplings (see Section 7.1). Each event stores a vector of 10 weights $\{w_0 \ldots w_9\}$, with which every event can be

reweighed to any other aTGC phase space point.

The weight at a new point is given by

$$\begin{aligned} w(\Delta g_1^Z, \Delta\kappa_Z, \lambda_Z) = w_0 &+ (\Delta g_1^Z)^2 w_1 + (\Delta\kappa_Z)^2 w_2 + (\lambda_Z)^2 w_3 \\ &+ 2\Delta g_1^Z w_4 + 2\Delta\kappa_Z w_5 + 2\lambda_Z w_6 \\ &+ 2\Delta g_1^Z \Delta\kappa_Z w_7 + 2\Delta g_1^Z \lambda_Z w_8 + 2\Delta\kappa_Z \lambda_Z w_9. \end{aligned} \quad (11.1)$$

The reweighting procedure relies on the fact that we can factorize each event amplitude into parts that are dependent on the event kinematics and parts that are dependent on the values of the anomalous couplings. Specifically, we can write the event amplitude for a general WZ event, A, as a linear function of the Standard Model amplitude A_0 and the amplitudes $A_{\Delta g_1^Z}$, $A_{\Delta\kappa_Z}$, and A_{λ_Z} containing the anomalous vertices associated with the couplings:

$$A = A_0 + \Delta g_1^Z \times A_{\Delta g_1^Z} + \Delta\kappa_Z \times A_{\Delta\kappa_Z} + \lambda_Z \times A_{\lambda_Z} \quad (11.2)$$

Here, the anomalous coupling parameters have been factored out, and the amplitudes $A_{\Delta g_1^Z}$, $A_{\Delta\kappa_Z}$, and A_{λ_Z} do not depend on the values of the couplings. Event weights are in general determined by the cross section of the process, which is in turn calculated using the square amplitudes. The square amplitude includes 9 terms that multiply the aTGC parameters and one overall event weight. The 9 event weights $\{w_1 \ldots w_9\}$ are these aTGC square amplitudes for the simulated event, and the w_0 weight is the Standard Model weight, a function of the final state kinematics. The reweighting procedure described by equation 11.1 takes these weights and multiplies them by the value of any set of aTGC parameters to give an event-by-event weight for any possible set of anomalous couplings. Since all kinematic information is also stored for each

event, any kinematic distribution can be calculated with any set of aTGC parameters.

As a result of the reweighting capability, we can produce one WZ sample and use it to scan the full range of aTGC space when setting limits. The other WZ sample is used to validate the reweighting procedure.

The WZ aTGC Monte Carlo events are produced with a form factor of 100 TeV. It is also possible to reweigh each event to any other form factor. Let Λ_{FF} be the original form factor and $\Lambda\prime_{FF}$ be the new value of the cut-off scale. For each aTGC parameters multiplying a weight, the weight must be multiplied by $(1 + \hat{s}/\Lambda^2_{FF})^2$ to remove the old form factor and divided by $(1 + \hat{s}/\Lambda\prime^2_{FF})^2$ to add in the new form factor. This is equivalent to adjusting the event weights $\{w_0 \dots w_9\}$ as

$$w_i \to \begin{cases} w_i & \text{for } i = 0 \\ w_i \frac{(1+\hat{s}/\Lambda^2_{FF})^2}{(1+\hat{s}/\Lambda\prime^2_{FF})^2} & \text{for } i = 4, 5, 6 \\ w_i \frac{(1+\hat{s}/\Lambda^2_{FF})^4}{(1+\hat{s}/\Lambda\prime^2_{FF})^4} & \text{for } i = 1, 2, 3, 7, 8, 9 \end{cases} \tag{11.3}$$

To remove the form factor, Λ is set to infinity.

11.2 Sensitivity of Kinematic Distributions to aTGCs

If new physics produces anomalous triple gauge couplings, both the cross section of inclusive WZ production as well as the kinematics of the final state W and Z bosons would differ from the Standard Model predictions. Distributions that are sensitive to the center-of-mass energy of the interaction are particularly sensitive to the presence of aTGCs, including the leading lepton p_T spectrum, the mass of the

WZ system, and the Z boson transverse momentum distribution. The dependence of these distributions, as well as the dependence of the inclusive $W^{\pm}Z$ cross section, on the values of aTGC parameters are shown in Figure 11.1 at truth level in simulation.

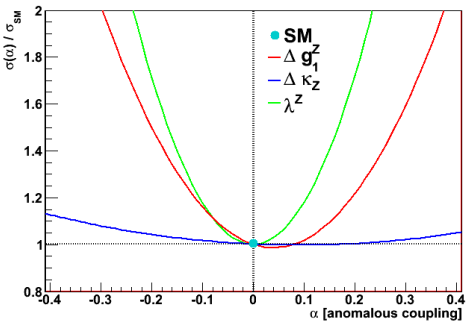

(a) Anomalous cross section

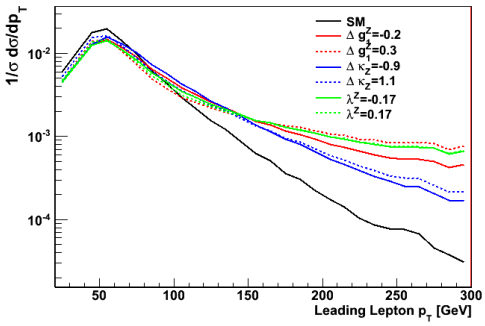

(b) Anomalous leading lepton p_T

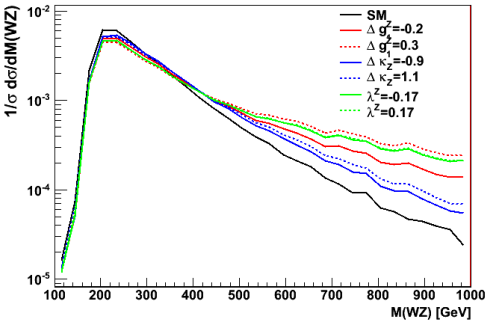

(c) Anomalous m_{WZ}

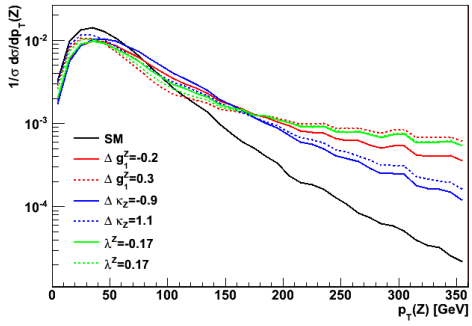

(d) Anomalous p_T^Z

Figure 11.1: The effect of aTGCs on WZ production in simulation, at the truth level. A form factor with $\Lambda = 2$ TeV is used in these distributions. The cross section (upper left) is shown as a function of each anomalous coupling, while the other couplings are set to zero. The differential distributions are shown for two specific values of each anomalous parameter; the values of the aTGCs correspond to the limits found in the previous analysis. The kinematic distributions have been normalized to the same area; only shape comparisons are shown here.

As can be seen in Figure 11.1(a), the $W^{\pm}Z$ cross section is a quadratic function of the anomalous TGCs. For most values of anomalous couplings, the cross

section increases. However, interference terms between the three different couplings can produce smaller cross sections than the Standard Model for particular values of the couplings. The WZ cross section has a stronger dependence on the values of Δg_1^Z and λ_Z than on $\Delta\kappa_Z$ because the terms in the Lagrangian with g_1^Z and λ_Z are proportional to $\hat{s}$ while the κ_Z term is proportional to $\sqrt{\hat{s}}$. As a result, the limits we can set on $\Delta\kappa_Z$ are weaker than the limits we can set on Δg_1^Z and λ_Z.

In Figures 11.1(b), 11.1(c), and 11.1(d), the leading lepton p_T distribution, the mass of the WZ system, and the Z boson p_T spectrum all show large deviations from the Standard Model distributions at high mass or momentum. These distributions have been normalized to show only shape comparisons. If we include the number of expected WZ events as well as their differential distribution, the distribution of these observables can be considerably more sensitive to the presence of aTGCs than the cross section alone. In particular, with 1 fb^{-1} of data, we found that, on average, the limits on Δg_1^Z, $\Delta\kappa_Z$, and λ_Z improve by 42%, 23%, and 41% when moving from using the cross section to using the Z boson p_T distribution to set limits on the aTGC parameters.

We perform a study in Monte Carlo to compare the expected sensitivity from studying different differential distributions. We calculate the range of 95% confidence intervals we would expect to set on each aTGC parameter, assuming that there are no anomalous couplings, for several differential distributions. To extract the limits in this study, we use a simplified version of the limit setting extraction detailed in Section 11.6. The actual limit extraction uses a frequentist approach to determine the 95% confidence interval based on a likelihood function describing how likely the

data is given a particular value of an aTGC parameter. While this limit extraction gives exact coverage, it is computationally slow. To approximate the limit extraction for analysis optimization, the 95% confidence interval is calculated using the best fit value plus and minus the errors computed by setting the delta log-likelihood to 1.92. Compared to the frequentist limit-setting approach, the delta log-likelihood method undercovers the frequentist 95% confidence interval. However, it still can be used to compare the limits found by studying different variables and binnings.

The differential distributions we examine are the reconstructed WZ invariant mass, the leading lepton p_T, the invariant mass of the three leptons in the event, and the Z boson transverse momentum. The WZ mass is reconstructed using a constraint on the W mass as described in Section 10.2. The expected limits are very sensitive to the binning of the differential distribution. We divide each of the four distributions into four bins. Since aTGC dependence is largest at high momentum or high mass, the sensitivity to the presence of aTGCs depends strongly on the ratio of Standard Model WZ events to aTGC WZ events in the last bin, which in turn depends on the number of expected Standard Model events in the highest p_T^Z bin. To exclude a potential bias due to different binnings, the binning for each distribution is selected to ensure a uniform number of expected Standard Model WZ events across all observables (ie: bin 1 does not have to have the same number of events as bin 2, but bin 1 for all observables has the same number of expected WZ events.)

For each aTGC parameter and for each observable, the width of the 95% confidence interval is calculated in 5000 toy experiments using the delta log-likelihood = 1.92 method described above. The width of the confidence interval is the distance be-

tween the lower and upper bound. In each toy experiment, the number of "observed" data events in each bin is randomly sampled from a Poisson distribution with mean equal to the number of data + background events in each bin. The signal/background ratio is assumed to be the same for each kinematic distribution, and the limits are calculated only considering statistical uncertainty. The cut-off scale is set to 3 TeV for this comparison.

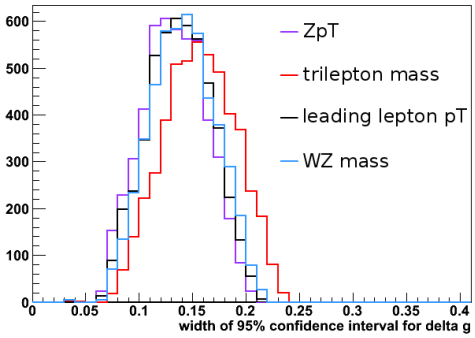

(a) Δg_1^Z

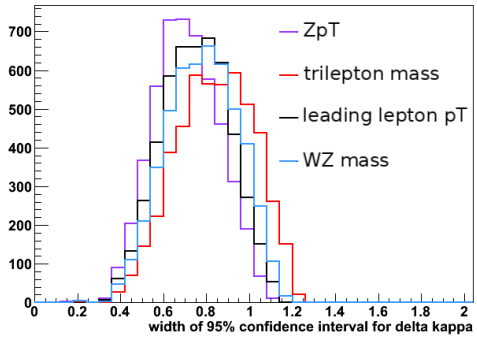

(b) $\Delta\kappa_Z$

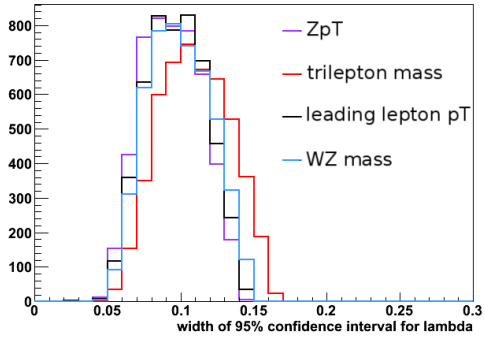

(c) λ_Z

Figure 11.2: Expected aTGC limits from different observables. The 95% confidence interval widths corresponding to limits extracted by setting delta log-likelihood = 1.92 in 5000 toy experiments for each aTGC parameter. The distribution of widths extracted from different observables are compared.

The comparisons of the widths of expected aTGC limits in the absence of any aTGC signal is shown in Figure 11.2. Different kinematic distributions have different sensitivities to the presence of aTGCs. The smaller the width of the expected limits, the better the limits are. In particular, the best sensitivity is obtained from studying the transverse momentum of the Z boson.

The fact that the measured p_T^Z distribution is most sensitive to aTGCs makes qualitative sense as well. The Z boson momentum is a proxy for the WZ mass, which is directly sensitive to $\sqrt{\hat{s}}$. However, the reconstructed WZ mass suffers from our inability to directly reconstruct the W boson momentum. In this analysis, the W momentum is reconstructed by solving for the z component of the momentum, given the lepton momentum, the E_T^{miss}, and assuming the mass of the W boson. In the case of two real solutions, the lower value is selected. In case of an imaginary solution, the imaginary piece is set to zero. In this way, information is lost in reconstructing the WZ mass. The p_T^Z distribution, however, is built directly from the measurement of leptons.

As observed in Figure 11.1, the p_T^Z distribution also has advantages in the case that there are non-zero aTGC parameters. Qualitatively, the p_T^Z distribution shows the largest shape different for positive and negative values of the aTGC parameters. Thus, if we do measure aTGCs, the transverse momentum of the Z boson could be sensitive to the sign of the parameter.

Due to the narrowness of the expected limits in the absence of aTGC signal, the possibility to distinguish the sign of aTGC parameters if they exist, and the good experimental resolution, the transverse momentum of the Z boson is chosen as the

distribution in which to search for the presence of aTGCs.

11.3 Binning Optimization

The effect of anomalous couplings is most pronounced for events with Z bosons with large transverse momentum, as visible in Figure 11.1. Moreover, the ratio of the number of expected Standard Model to anomalous coupling events varies as the binning of the p_T^Z distribution changes. In this way, the expected sensitivity to the presence of anomalous couplings is dependent on the binning we chose.

In order to choose a binning for the extraction of aTGC limits, several studies are performed. The first study optimizes the bin boundaries while restricting the number of bins to four. This study is performed using only statistical uncertainties. Once the optimized four bin distribution is found, the systematic uncertainties and data-driven backgrounds are evaluated for those four bins. The backgrounds and uncertainties are then used to re-optimize the binning, again restricting the number of bins to four. The systematic uncertainties and data-driven backgrounds are smoothly varied as the binning changes for the bin optimization study. Finally, the last optimization allows the number of bins to change.

The initial four bin optimization is performed using simulation and only considers statistical uncertainties. The sensitivity to different p_T^Z binnings is tested using the delta log-likelihood = 1.92 method, as described in Section 11.2. For each aTGC parameter and for each observable, the width of the 95% confidence interval is calculated in 5000 toy experiments. In each toy experiment, the number of "observed" data events in each bin is randomly sampled from a Poisson distribution with mean

equal to the number of data + background events in each bin.

Several constraints are placed on the last bin in the first four bin optimization. Specifically, the last bin is required to have greater than or equal to 10% of the total number of expected events, which keeps the statistical uncertainty on the last bin below 25%. There is no estimate of systematic uncertainty in the last bin at this point; we choose to keep the statistical uncertainty under control by keeping the number of expected SM events above 10%. Additionally, the last bin is conservatively restricted to an upper boundary of 500 GeV, as the ability to estimate systematic uncertainties for higher Z transverse momentum values is not yet tested.

The initial optimization finds a maximum in expected sensitivity for a binning of (0,30,60,120,500) GeV. This is called the "nominal" binning.

Once a nominal binning is chosen, all systematic uncertainties are calculated using this binning, as described in Section 11.5. Additionally, the data-driven background estimates are calculated for this nominal binning. There are sufficient events in WZ simulation above 500 GeV to calculate systematic uncertainties, so the upper boundary of the differential distribution is allowed to go to 2 TeV, above which there are no more WZ simulated events.

For the second round of optimization, the expected background and the systematic uncertainties are used as inputs. The expected sensitivity to aTGC couplings is tested by comparing the distribution of expected limits for different binnings. The systematic uncertainties are kept at the same relative size in each bin, even as the bin boundaries are changed. For the data-driven backgrounds, the size of the background in the new binning is smoothly varied from the nominal binning by assuming that the

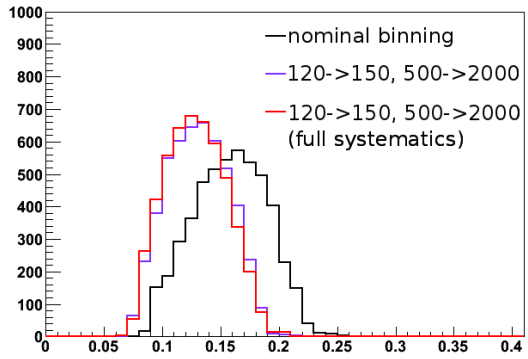

(a) Δg_1^Z

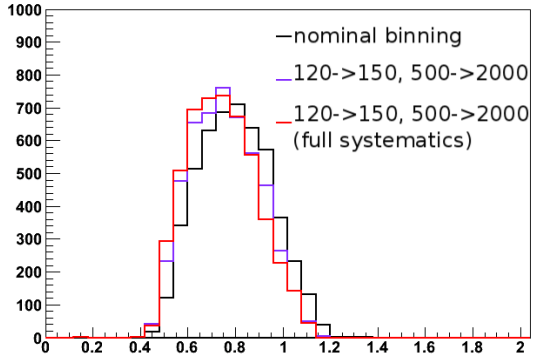

(b) $\Delta\kappa_Z$

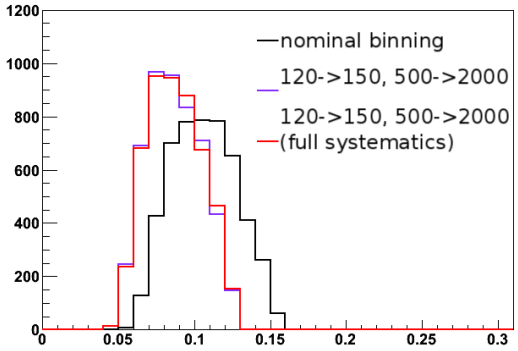

(c) λ_Z

Figure 11.3: Expected aTGC limits from different bin boundaries. The 95% confidence interval widths corresponding to limits extracted by setting delta log-likelihood = 1.92 in 5000 toy experiments for each aTGC parameter. The distribution of widths extracted from the nominal (black) and optimized p_T^Z binnings are compared. For the optimized binning, the expected limits predicted in the simplified study (purple) are shown along with the limits expected after the full systematics and new data-driven background estimates are computed for the new binning (red). The cut-off scale is 100 TeV for this comparison.

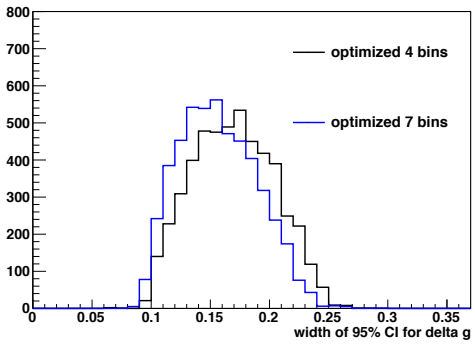

(a) Δg_1^Z

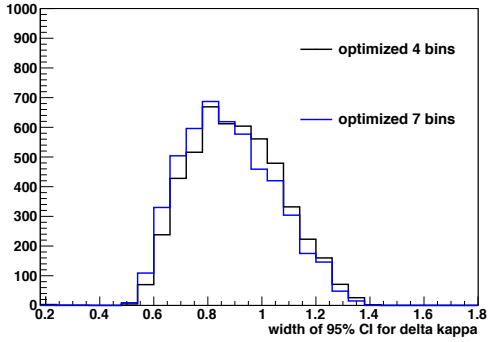

(b) $\Delta\kappa_Z$

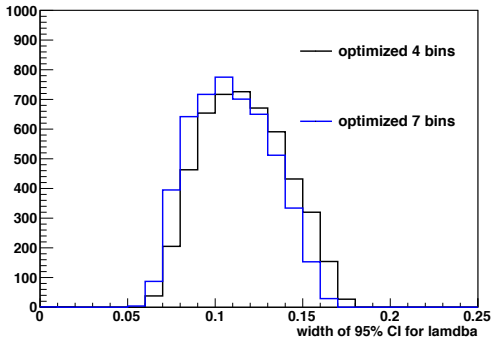

(c) λ_Z

Figure 11.4: Expected aTGC limits from 7 versus 4 bins. The 95% confidence interval widths corresponding to limits extracted by setting delta log-likelihood = 1.92 in 5000 toy experiments for each aTGC parameter. The distribution of widths extracted from the optimized 4 bin (black) and optimized 7 bin (blue) p_T^Z binnings are compared. The cut-off scale is 2 TeV for this comparison.

backgrounds follow the same shape as the signal. The actual data driven backgrounds are based on control regions with limited statistics in data, and there could be significant statistical fluctuations in the estimates as the binning is varied. Smoothly varying the data driven estimates from their nominal values, rather than recalculating them, prevents optimizing based on false minimums from real data fluctuations. The expected number of signal events is calculated for each new binning from simulation, for both Standard Model WZ production and production with anomalous couplings.

The sensitivity to the presence of aTGC is found to increase for all three couplings as the upper bin boundary is moved from 500 GeV to 2 TeV. No new Standard Model WZ events fall into the bin, but anomalous TGC points continue to contribute events up until 2 TeV. After 2 TeV, there are no additional aTGC events, so the sensitivity does not increase any further. We choose to limit the upper bin to 2 TeV, rather than infinity, so we can test the acceptance and efficiency of simulated events in the full last bin. The limits do not change if the upper bin boundary is moved above 2 TeV, as there are no additional simulated events.

Moving the boundaries at 30 and 60 GeV has no effect on the expected sensitivity. Moving the lower boundary of the last bin to 180 improves the expected limits significantly and still keeps > 5 Standard Model WZ events expected in all bins. The fewer events expected in the last bin, the more the observed limits can differ from the average expected limits. Moreover, the systematic uncertainties on both the signal acceptance and on the data driven background estimates grow as the number of events in the last bin drops. The second round of optimization finds an optimal four bin binning of (0,30,60,120,180,2000 GeV). The systematic uncertainties and data driven

backgrounds are re-estimated for this binning.

The comparisons of the widths of expected aTGC limits in the absence of aTGC signal is shown in Figure 11.3 for the nominal binning and the optimized binning with four bins. The optimized binning is shown with both the "simulated", smoothly-varied systematics and data-driven background estimates, along with the actual systematics and background estimates which were recalculated once the binning was chosen.

Initially, the analysis was optimized using 4 bins, as described above. However, adding additional bins increases the expected sensitivity to aTGCs. The upper limit on the number of bins is set by two considerations: 1) the ability to calculate estimated backgrounds in data in all bins with reasonable uncertainty, and 2) the amount of computational time taken to perform a fit. Since the 2D limits and the expected limits require large number of pseudo experiments, increasing the number of bins significantly drastically slows down the turn around time of the analysis. We find that seven bins is an optimum between the expected sensitivity, visual presentation, ability to do data-driven background estimates, and time required to perform the fits. Moving from four to seven bins improves the expected limits by 5%-15%, depending on the anomalous parameter.

After optimizing the expected sensitivity of the bin boundaries with seven bins, a final binning of (0,30,60,90,120,150,180,2000) GeV is chosen. This binning minimizes the width of the expected limits (assuming the Standard Model) and keeps enough events in all bins to estimate the background from data and to keep systematic uncertainties under control. Figure 11.4 compares the width of expected aTGC limits

for the optimized binning with 4 bins and the optimized binning with 7 bins.

11.4 Differential Background Estimates, Signal Expectation, and Observed Events

The expected background is calculated as a function of the Z boson transverse momentum. For backgrounds estimated from simulation, the procedure is straightforward. For backgrounds estimated from data, the control regions are studied in each bin and independent estimations are performed bin-by-bin.

Details of the data background estimation technique for events with top quarks can be found in Section 9.3 and the data estimation for Z+jets events is described in Section 9.1. For the Z+jets estimate, the fake-factor estimate uses the ratio of two control regions, times the product of a third control region in data. When these control regions are evaluated bin-by-bin, the total estimate will not necessarily agree exactly with the total estimate evaluated channel by channel. The two total estimates should agree within the statistical uncertainty, which they do.

The number of expected background events, expected signal events, and observed events in data in each bin of the differential Z transverse momentum distribution is shown in Table 11.1.

Table 11.1: Differential observed and expected events. Summary of observed events and expected signal and background contributions in different $p_{\mathrm{T}}(Z)$ ranges used for anomalous Triple Gauge Coupling limit setting and combined. The first error is statistical while the second is systematic.

$p_{\mathrm{T}}(Z)$ (GeV)	[0, 30]	[30, 60]	[60, 90]	[90, 120]	[120, 150]	[150, 180]	[180, 2000]	Combined
Observed	73	111	69	24	14	13	13	317
ZZ	$4.8\pm0.1\pm0.3$	$7.4\pm0.1\pm0.5$	$4.3\pm0.1\pm0.3$	$2.1\pm0.1\pm0.2$	$1.0\pm0.0\pm0.1$	$0.6\pm0.0\pm0.1$	$0.8\pm0.0\pm0.1$	$21.0\pm0.2\pm0.7$
W/Z+jets	$12.2\pm4.0^{+2.6}_{-2.6}$	$11.5\pm2.4^{+2.1}_{-2.1}$	$3.3\pm1.9^{+0.6}_{-0.6}$	$1.5\pm1.0^{+0.3}_{-0.3}$	$0.5\pm0.5^{+0.2}_{-0.2}$	$0.4\pm0.5^{+0.1}_{-0.1}$	$0.6\pm0.6^{+0.2}_{-0.2}$	$30.0\pm5.2^{+7.5}_{-7.5}$
Top	$1.4\pm0.4\pm0.5$	$2.9\pm0.5\pm0.9$	$2.9\pm0.4\pm0.9$	$1.8\pm0.4\pm0.5$	$0.9\pm0.2\pm0.2$	$0.4\pm0.1\pm0.04$	$1.1\pm0.1\pm0.1$	$11.5\pm0.9\pm3.4$
$W/Z+\gamma$	$0.4\pm0.4\pm0.0$	$2.0\pm0.8\pm0.1$	$0.3\pm0.3\pm0.0$	$1.0\pm0.6\pm0.1$	$0.0\pm0.0\pm0.0$	$0.0\pm0.0\pm0.0$	$0.0\pm0.0\pm0.0$	$3.7\pm1.1\pm0.1$
Bkg (total)	$18.7\pm4.0^{+2.6}_{-2.6}$	$23.8\pm2.6^{+2.4}_{-2.4}$	$10.8\pm2.0^{+1.2}_{-1.2}$	$6.4\pm1.2^{+0.6}_{-0.6}$	$2.4\pm0.5^{+0.3}_{-0.3}$	$1.5\pm0.5^{+0.2}_{-0.2}$	$2.5\pm0.6^{+0.2}_{-0.2}$	$68.1\pm5.5^{+8.2}_{-8.2}$
Expected signal	$52.1\pm0.6\pm3.0$	$76.3\pm0.7\pm4.8$	$49.4\pm0.5\pm3.9$	$24.7\pm0.4\pm2.5$	$12.0\pm0.3\pm1.0$	$7.2\pm0.2\pm0.7$	$9.4\pm0.2\pm0.9$	$231.2\pm1.1\pm7.8$
Expected S/B	2.8	3.2	4.6	3.8	4.9	4.9	3.8	3.4

11.5 Differential Systematic Uncertainties

We calculate the systematic uncertainties which reflect the accuracy of our estimates of the number of expected background and signal events per bin of p_T^Z. The fractional systematic uncertainties are calculated from the raw shifts in the number of expected signal or background events, per bin, as each systematic source is varied by one sigma. The systematic uncertainties are calculated for all four flavor channels inclusively and are calculated from Standard Model WZ events. The correlation between bins is calculated from the shifts in the number of events. A systematic which is fully correlated across all bins produces the same relative shift in the number of expected events in each bin. The systematic uncertainties which affect both signal and background predictions are listed below, along with a qualitative comment about the level of correlation between bins of p_T^Z:

- Trigger (*almost fully correlated*)
- Electron identification, reconstruction, smearing, and isolation (*almost fully correlated*)
- Muon efficiency, smearing, scale, and isolation (*almost fully correlated*)
- E_T^{miss} resolution and scale (*large correlation*)
- PDF systematics (*large correlation*)
- Generator systematics (*some correlation*)
- Renormalization / factorization scale (*some correlation*)

- Data driven background estimates (*some correlation*)
- Luminosity (*full correlation*)

Section 10.4 describes in detail the calculation of the systematics which affect the efficiency of selecting WZ events, and the data driven background estimate systematic uncertainties are described in Section 9.1 and 9.3. The calculation of differential systematic uncertainties follows the same procedures used in calculating the inclusive systematic uncertainties, for those uncertainties which affect the efficiency of selecting WZ events. As discussed above, the shift in the number of expected events is calculated for each bin for each systematic uncertainty source, and the fractional uncertainty and correlation between bins is used in the calculation of aTGC limits.

We calculate limits on the anomalous couplings using the number of expected signal events in each p_T^Z bin. Therefore, we rely on the signal simulation to model the efficiency C_{WZ} of accepting WZ events, given that they are within the fiducial acceptance of the detector and selection cuts (see Section 10.3.2.) We model the number of expected events as a function of the anomalous couplings, and the number of expected events takes into account changes in the efficiency. It is important that the efficiency for selecting WZ events is not significantly different in events with anomalous couplings than in Standard Model WZ events, however, to ensure that the systematic uncertainties we calculate for Standard Model events also apply in the case of non-zero anomalous couplings.

The fiducial efficiency C_{WZ} is shown as a function of the Z boson transverse momentum in Figure 11.5 for Standard Model WZ events as well as for events with three values of non-zero aTGCs. The values of the anomalous couplings shown are

the limits found by the 1 fb^{-1} WZ analysis and they represent the largest values of anomalous couplings that we can hope to observe. The efficiency C_{WZ} is not flat as a function of p_T^Z, which is the reason we need to calculate systematics on the efficiency as a function of p_T^Z. However, over the full range of Z transverse momentum, the efficiency of accepting WZ events is the same for Standard Model events and events with non-zero aTGCs, within the statistical uncertainty of the simulated sample. This confirms that we can use the systematic uncertainties on signal efficiency calculated with Standard Model events for events with anomalous couplings as well. As a result, the systematic uncertainties are not a function of the anomalous couplings.

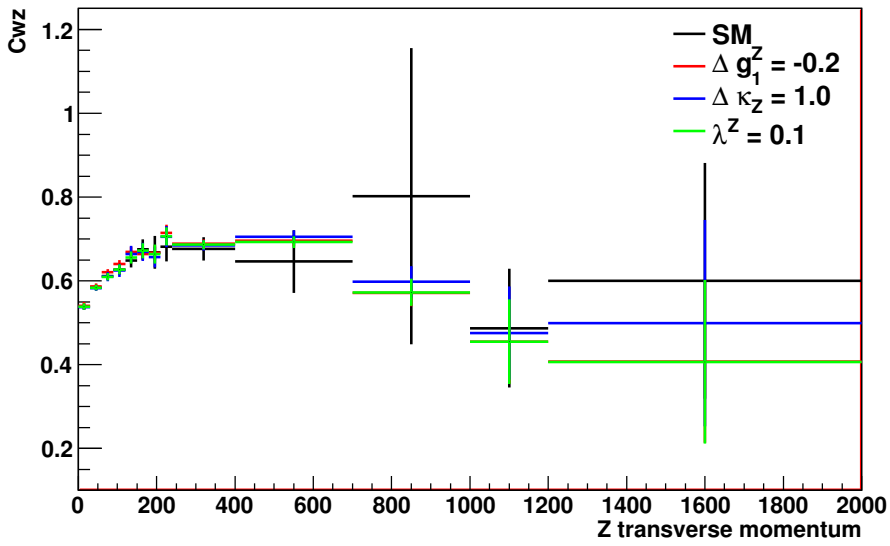

Figure 11.5: Efficiency as a function of p_T^Z. The efficiency C_{WZ} of reconstructing WZ events, given that they are within the fiducial acceptance volume, as a function of the true p_T^Z in simulation. The efficiency is shown for Standard Model WZ events (black) as well as for events with three different anomalous couplings (colors.)

In addition to systematic uncertainties on the efficiency of accepting signal events, it is important to consider uncertainties on the overall shape and normalization of the

expected WZ signal. These systematics do not affect the cross section calculation, because in calculating the cross section, we are measuring the signal normalization directly. However, in calculating limits on anomalous couplings, we take the number of expected Standard Model events as an input, and deviations from the expected number give us sensitivity to the couplings.

The systematic uncertainties on the normalization of the expected WZ signal come from our uncertainty on the theoretical WZ cross section and are discussed in Section 10.1. The major contributions to the uncertainty on the theoretical cross section are from PDFs and from the QCD renormalization and factorization scale used in simulating the events. We re-calculate these systematic uncertainties in bins of p_T^Z. The uncertainty on the normalization due to PDFs is between 4% and 5% across the full Z boson transverse momentum distribution. The uncertainty on the number of expected WZ events due to the QCD renormalization and factorization scale varies from 2.6% in the lowest p_T^Z bin to 8% for events with high p_T^Z.

The uncertainty on the shape of the simulated WZ signal distribution is evaluated by comparing events simulated with MC@NLO with events simulated with POWHEG BOX [121]. The generator uncertainty is taken as the relative difference in the number of signal events simulated by each generator, in each bin. The distributions are normalized before calculating the uncertainty to only test for shape differences, as normalization uncertainties are already covered by the systematic uncertainties due to PDF and scale.

The full list of differential systematic uncertainties is shown in Table 11.2. The systematic uncertainties on the shape and normalization of the expected WZ Stan-

dard Model signal are shown in Figure 11.6 as a function of Z transverse momentum.

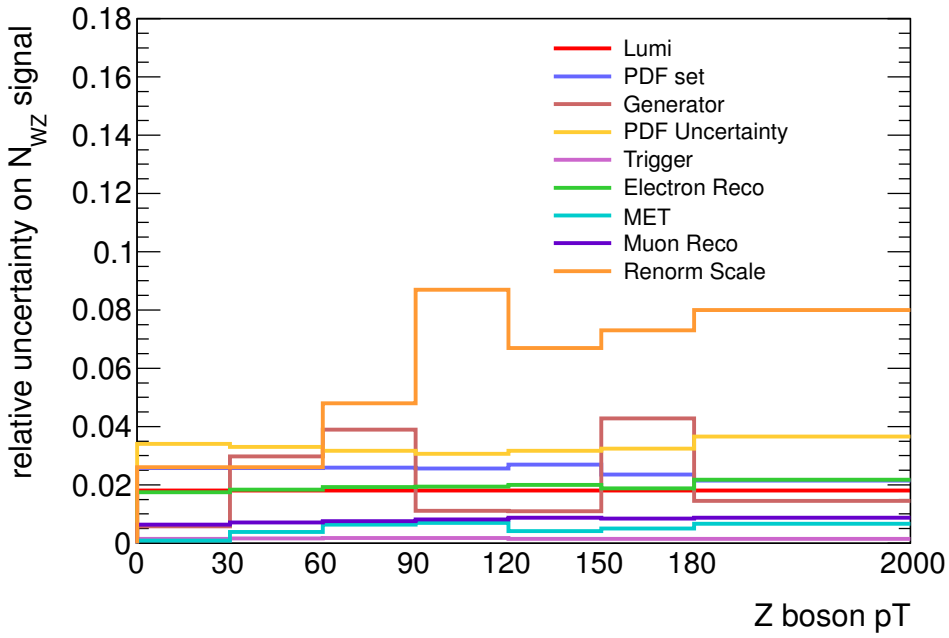

Figure 11.6: Shape and normalization systematic uncertainties on WZ signal. Full details are available in Table 11.2.

Table 11.2: Differential systematic uncertainties. Summary of all acceptance and efficiency uncertainties (%) used in the aTGC limit extraction.

Source	0-30 GeV	30-60 GeV	60-90 GeV	90-120 GeV	120-150 GeV	150-180 GeV	180-2000 GeV
μ reconstruction efficiency	0.55	0.56	0.57	0.58	0.59	0.61	0.63
μ p_{T} scale &resolution	0.07	0.03	0.07	0.18	0.35	0.15	0.25
μ isolation & impact parameter efficiency	0.32	0.43	0.49	0.53	0.55	0.57	0.55
e reconstruction efficiency	0.97	0.97	1.19	1.03	1.06	0.10	1.13
e identification efficiency	1.35	1.44	0.94	1.44	1.37	0.55	1.30
e isolation & impact parameter efficiency	0.41	0.56	0.79	0.70	0.70	0.03	0.73
e energy scale	-0.16	0.16	0.10	0.38	0.40	-0.43	1.10
e energy resolution	0.05	0.02	-0.28	-0.07	0.09	0.51	-0.14
E_T^{miss} cluster energy scale	-0.00	0.20	0.41	0.47	0.19	0.06	-0.12
E_T^{miss} jet energy scale	-0.07	-0.09	-0.23	0.04	-0.16	0.35	0.04
E_T^{miss} jet energy resolution	-0.01	0.01	0.27	0.36	-0.07	0.05	0.61
E_T^{miss} pileup	0.04	0.10	0.35	0.36	0.08	0.04	-0.21
Trigger - μ	0.14	0.16	0.16	0.16	0.15	0.14	0.14
Trigger - e	0.02	0.03	0.03	0.03	0.02	0.02	0.02
Generator	-0.58	-2.97	3.90	1.11	1.10	4.28	-1.45
PDF	4.28	4.19	4.09	4.00	4.16	4.02	4.24
Scale	2.60	2.60	4.80	8.70	6.70	7.30	8.00
Luminosity	1.8	1.8	1.8	1.8	1.8	1.8	1.8

11.6 Limit Setting Procedure

We wish to quantify what values of anomalous couplings are compatible with the observed data sample. We do so by using a frequentist limit approach [78, 86, 129] to determine the 95% confidence interval (C.I.) for each aTGC parameter. In the frequentist approach, the 95% confidence interval is the interval which, if we redo the experiment many times and recalculate the C.I. for each experiment, will contain the true values of the anomalous coupling parameters in 95% of the experiments [77].

We calculate the 95% C.I. by constructing a likelihood function which expresses the likelihood of observing a given number of events given the signal and background expectation. The number of expected signal events is parametrized as a function of the values of the anomalous couplings. We generate a large number of pseudo experiments for each hypothetical value of the anomalous coupling. In each pseudo experiment, the "observed" number of events is drawn randomly from a Poisson distribution whose mean is equal to the number of signal+background events for that value of anomalous coupling. Each pseudo experiment is ranked, where the rank function is the ratio of the likelihood of the "observed" number of events given the value of the anomalous coupling under consideration to the maximum likelihood for the "observed" number of events, maximized across all possible values of the anomalous coupling. After pseudo experiments have been ranked, the rank is calculated for the actual number of observed data events for each value of anomalous coupling. At a given value of the anomalous coupling, if greater than 95% of the pseudo experiments have a larger rank than observed in the actual experiment, that value of anomalous coupling is rejected at the 95% level.

While the frequentist approach requires generating a large number of pseudo experiments and is computationally slow, the approach is robust and the brute-force calculation of the 95% confidence interval guarantees statistical coverage.

As for the calculation of the cross section, systematic uncertainties are treated as nuisance parameters with Gaussian constraints.

The likelihood is built on the number of expected signal events, which is expressed as a function of the anomalous couplings. The number of expected signal events is calculated for each anomalous coupling point using the reweighting procedure described in Section 11.1. In addition to the weights from the aTGC value, a few other multiplicative weights are applied to the MC sample:

- MC generator weights (+1 or −1) from MC@NLO
- Pile-up weights
- Trigger scale factors
- Reconstruction scale factors

These weights are the same as used in the cross section calculation and are described in Section 7.2. After applying these factors, we accumulate the event weights for the MC signal events that pass our selection. The end result is the expected number of signal events in bin i, N_s^i, which takes the form:

$$\begin{aligned} N_s^i(\Delta g_1^Z, \Delta\kappa_Z, \lambda_Z) = W_0^i &+ (\Delta g_1^Z)^2 W_1^i + (\Delta\kappa_Z)^2 W_2^i + (\lambda_Z)^2 W_3^i \\ &+ 2\Delta g_1^Z W_4^i + 2\Delta\kappa_Z W_5^i + 2\lambda_Z W_6^i \\ &+ 2\Delta g_1^Z \Delta\kappa_Z W_7^i + 2\Delta g_1^Z \lambda_Z W_8^i + 2\Delta\kappa_Z \lambda_Z W_9^i \end{aligned} \quad (11.4)$$

for each bin of p_T^Z. It is these coefficients $\{W_j^i\}$ that are used in the limit setting procedure.

The detailed procedure for determining the 95% C.I. is as follows [108].

1. The likelihood function described in Section 10.5 is modified by replacing the cross section σ with one of the aTGC parameters $\alpha = \Delta g_1^Z$, $\Delta\kappa_Z$, or λ_Z. Additionally, the sum over flavor bins $i = 1...4$ is replaced by a sum over p_T^Z bins $i = 1...7$. The likelihood of observing a given number of events given a particular value of anomalous coupling α is therefore:

$$-\ln L(N_{obs}|\alpha,\{\beta_k\}) = \sum_{i=1}^{7} -\ln\left(\frac{e^{-(N_s^i(\alpha,\{\beta_k\})+N_b^i(\{\beta_k\}))}\times(N_s^i(\alpha,\{\beta_k\})+N_b^i(\{\beta_k\}))^{N_{obs}^i}}{(N_{obs}^i)!}\right)+\sum_{k=1}^{n}\frac{\beta_k^2}{2} \tag{11.5}$$

The number of signal events N_s^i in p_T^Z bin i is expressed as a quadratic function of α using the reweighting method. The symbol N_{obs} stands for the observed numbers of data events, and β are the nuisance parameters which represent the n Gaussian constrained systematics.

2. A test statistic $q(\alpha)$ is built by taking the ratio of the profile maximum likelihood at a test aTGC parameter value α to the full maximum likelihood. The test statistic takes the form:

$$q(\sigma) = \frac{L(n|\alpha,\hat{\hat{\beta}})}{L(n|\hat{\alpha},\hat{\beta})} \tag{11.6}$$

where $\hat{\hat{\beta}}$ is the maximum likelihood estimator of β that maximizes the numerator for the fixed test value of α, and $\hat{\alpha}$ and $\hat{\beta}$ are the values of α and β which maximize the denominator.

3. The observed value of the test statistic, $q_{\text{obs}}(\alpha)$, is found using the observed data n_{obs} for each value of the test aTGC parameter. This is done by scanning a range of values of α and determining the value of the test statistic for each α.

4. To determine how often an outcome at least as unlikely as the actual observation is expected, we generate a large number of pseudo experiments for each test value of α, compute the test statistic $q_{\text{pe}}(\alpha)$, and compare them with the observed $q_{\text{obs}}(\alpha)$. To generate each pseudo experiment, the nuisance parameters β are Gaussian fluctuated around the mean value of $\hat{\hat{\beta}}(\alpha)$. The numbers of "observed" events N^i_{pe} is drawn randomly from a Poisson distribution whose mean is computed from the value of α and β.

5. The p-value at each value of α is calculated as the fraction of pseudo experiments whose test statistic $q_{\text{pe}}(\alpha)$ is smaller than the observed value $q_{\text{obs}}(\alpha)$.

6. By scanning α, all values of the aTGC parameter for which $p(\alpha) \geq 5\%$ can be determined and these define the 95% C.I. of α for the observed data.

The number of pseudo experiments, 10,000, in step 4 is chosen to ensure that a p-value of 5% can be determined to a reasonable statistical precision of $\pm 0.2\%$.

Because the expected number of signal events N^i_s is a quadratic function of α, $N^i_s(\alpha)$ has a minimum near $\alpha = 0$, and increases in both positive and negative directions of α. As a result, there may be either one or two optimum values of α that best describe the observed data, depending on whether N_{obs} is smaller or larger than the minimum expected value. This results in two possibilities for the 95% C.I. of α: it may be a single continuous region or two disjoint regions.

The limits are obtained in two separate scenarios. In the first scenario, limits are set on each parameter by setting the value of the other two aTGC parameters to zero. These limits are called "1D" limits.

In the second scenario, one aTGC parameter is set to zero, and the 95% confidence contour for the other two parameters are fit simultaneously, allowing for a confidence interval in a "2D" phase space. In the 2D case, the best-fit value can have non-zero couplings in two parameters.

The 2D limits are extracted following the same method as for the 1D limits. First, the best-fit value in the 2D aTGC parameter space is found. From that point, 1D limits are extracted along radial lines moving out from the best-fit value. The 95% confidence contour is the contour connecting the set of points which correspond to the 95% limits on the many radial spokes.

11.7 Results

11.7.1 Expected Limits from WZ production

To evaluate the expected sensitivity of our measurement, we generate a large number (5,000) of toy Monte Carlo data sets assuming all anomalous couplings are zero. We evaluate the 95% confidence interval for each toy data set, and record the upper limit, the lower limit, and the width of the interval. The expected limits are taken as the interval spanning the average upper limit and the average lower limit across all toy data sets. Figure 11.7 shows the distributions of the 95% C.I. obtained from the toy experiments, as well as the actual C.I. from the data. Figure 11.8 shows

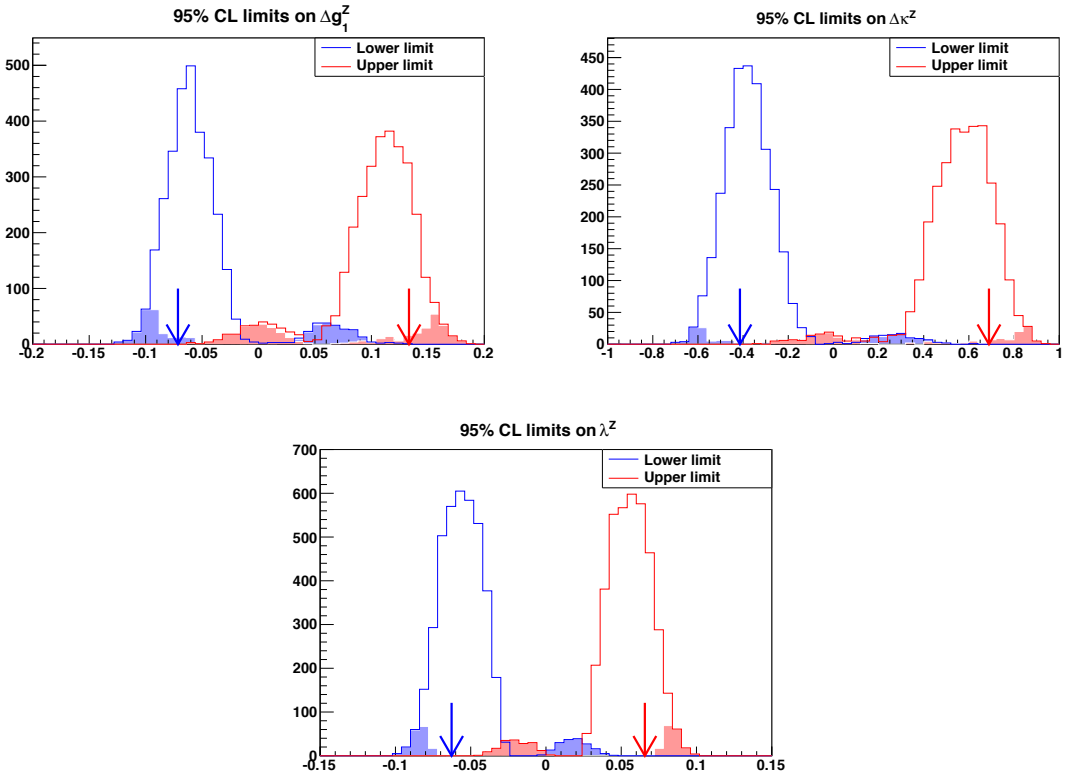

Figure 11.7: Expected upper and lower limits of the 95% aTGC confidence intervals. Upper (red) and lower (blue) limits of the 95% C.I. of Δg_1^Z (top-left), $\Delta\kappa_Z$ (top-right), and λ_Z (bottom), obtained from toy MC samples. The shaded area indicate the cases in which two split C.I. were found. The blue and red arrows show the actual limits obtained from data. These limits are for a cut-off scale of 2 TeV.

the widths of the 95% C.I. If a toy experiment gives two separate C.I., the sum of the two widths is plotted. Table 11.3 shows the 95% C.I. of the expected aTGC limits.

11.7.2 Observed Limits from WZ production

Figure 11.9 shows the Z boson transverse momentum distribution for the Standard Model alongside the distribution expected for values of the three anomalous couplings that correspond to the upper limit of the 99% expected confidence interval (assuming

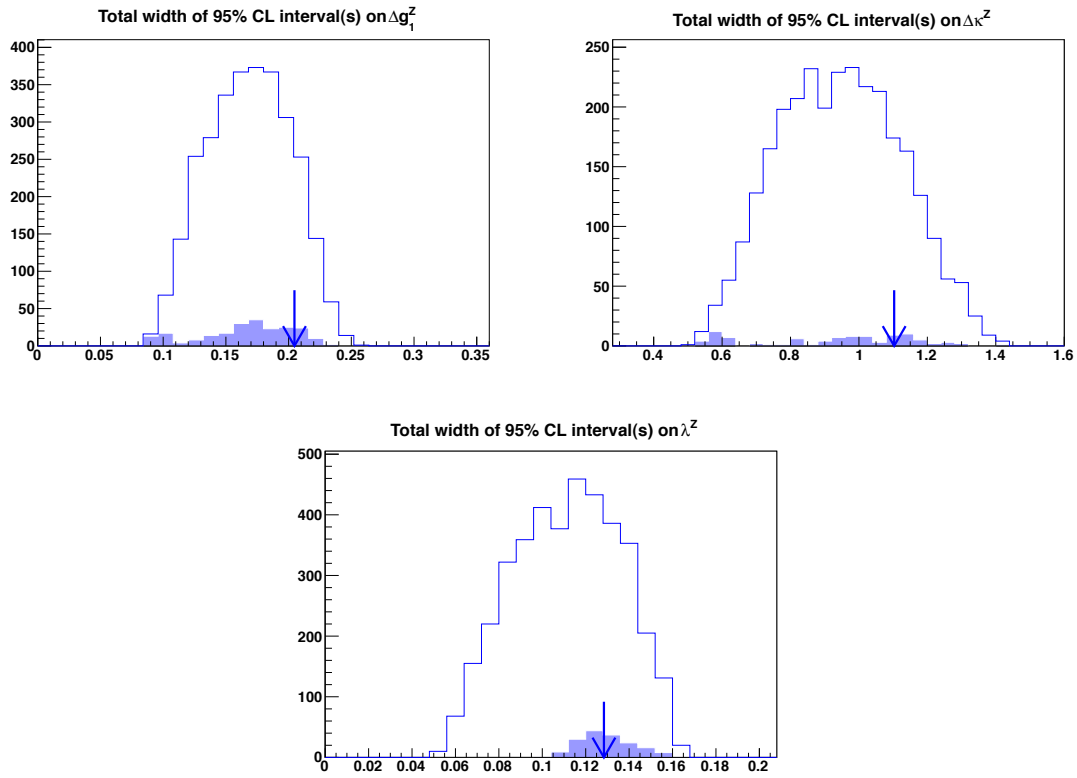

Figure 11.8: Expected widths of the 95% C.I. on anomalous couplings. Total widths of the 95% C.I. of Δg_1^Z (top-left), $\Delta\kappa_Z$ (top-right), and λ_Z (bottom), obtained from toy MC samples. The shaded areas indicate the cases in which two split confidence intervals were found. The blue arrows show the width of the actual limits obtained from data. These limits are for a cut-off scale of 2 TeV.

no anomalous signal). The 99% expected limits are shown to emphasis the effect of anomalous couplings. The sensitivity in the last bin of p_T^Z to anomalous couplings is evident. It is also apparent that if there were anomalous couplings, each coupling would have a slightly different differential p_T^Z distribution. Depending on the size of the anomalous coupling, we might have the sensitivity to tell apart the contribution of different couplings.

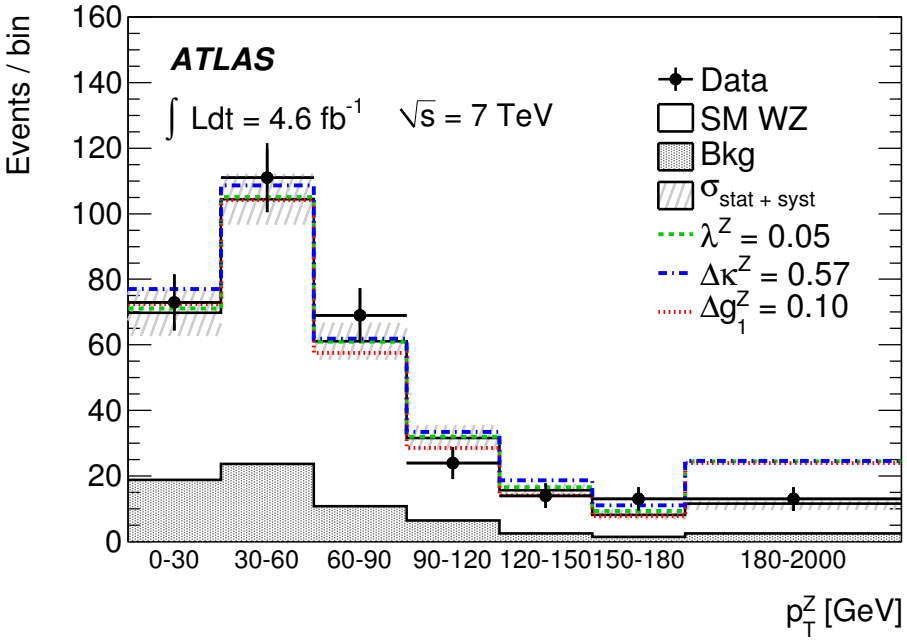

Figure 11.9: p_T^Z of WZ events used to obtain aTGC limits. Data is shown alongside expected background and signal events, assuming the Standard Model. Expected events in the case of anomalous TGC parameters are also shown, for values for each of the three couplings that correspond to the upper limit of the expected 99% confidence intervals. The sensitivity to the presence of aTGCs is clear in the last bin. Additionally, the three anomalous couplings have different shapes in p_T^Z. The last bin is shortened for display purposes; it includes events up to 2 TeV. The aTGC values shown are calculated with a cut-off scale of 2 TeV.

Table 11.3 summarizes the observed 95% confidence interval (C.I.) on the anomalous couplings Δg_1^Z, $\Delta\kappa_Z$, and λ_Z at two different values of the cut-off scale Λ: $\Lambda = 2$

Table 11.3: Expected and observed 95% confidence intervals on the anomalous couplings Δg_1^Z, $\Delta\kappa_Z$, and λ_Z. Limits are 1D; each coupling is fit independently while the other couplings are fixed to zero.

	Observed 95% C.I. $\Lambda = 2$ TeV	Expected 95% C.I. $\Lambda = 2$ TeV	Observed 95% C.I. $\Lambda = \infty$	Expected 95% C.I. $\Lambda = \infty$
Δg_1^Z	$[-0.074, 0.133]$	$[-0.059, 0.110]$	$[-0.057, 0.093]$	$[-0.046, 0.080]$
$\Delta\kappa_Z$	$[-0.42, 0.69]$	$[-0.37, 0.57]$	$[-0.37, 0.57]$	$[-0.33, 0.47]$
λ_Z	$[-0.064, 0.066]$	$[-0.056, 0.055]$	$[-0.046, 0.047]$	$[-0.041, 0.040]$

TeV, and no form-factor (equivalent to setting $\Lambda \to \infty$). These limits are 1D limits obtained by setting the other aTGC parameters to zero.

The 95% confidence interval for the 2D fitting scenario are shown as contours in Figure 11.10. The limits for the scenario with a 2 TeV cut-off scale and with no form factor are both shown.

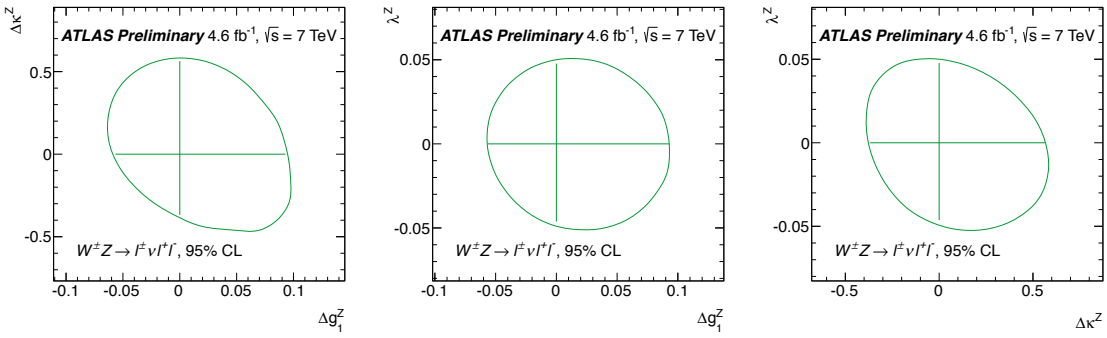

Figure 11.10: Observed 2D 95% Confidence Contours. The cut-off scale is 2 TeV for the limits shown with a fine line and no cut-off for the limits shown with a thick line. The horizontal and vertical lines inside each contour correspond to the limits found in the 1D fit procedure.

Figure 11.11 compares the observed limit with the Tevatron results. While the ATLAS limits are the most stringent direct limits on all three WZ couplings, the limits are only a slight improvement over the limits from the D0 experiment. There

are two reasons why the ATLAS limits are not a significant improvement. First, WZ production at the Tevatron is dominated by leading order terms, including the term with the WWZ triple gauge coupling vertex. At the LHC, the next-to-leading order terms contribute nearly as much as the leading order terms, as discussed in Section 2.4. This has the effect of obscuring events from the vertex with the triple gauge couplings by producing significant number of energetic WZ events from QCD production. Second, the D0 experiment observed significantly fewer events at high p_T^Z than expected; as a result, the observed limits are better than their expected limits. This explains why the D0 limits are more stringent than the CDF limits, even though the luminosity is lower. In the ATLAS data, we observe a slight excess of events at high p_T^Z, resulting in slightly worse observed limits than expected limits.

11.7.3 Observed Limits from WW, ZZ, and $W/Z+\gamma$ production

Final states with other pairs of vector bosons are also sensitive to anomalous triple gauge couplings. As described in Section 2.5, after requiring that C and P are conserved by each term in the Lagrangian, there are 5 couplings in the effective Lagrangian description of the WWZ and $WW\gamma$ vertex: κ_Z, λ_Z, g_1^Z, λ_γ, and κ_γ. WZ production is sensitive to the first 3 couplings, but the WW final state is sensitive to all 5.

The ATLAS WW analysis with 4.6 fb^{-1} at $\sqrt{s} = 7$ TeV is detailed in Reference [64]. Limits are set by studying the reconstructed leading lepton p_T distribution, shown in Figure 11.12. Limits on anomalous parameters are set using a likelihood test

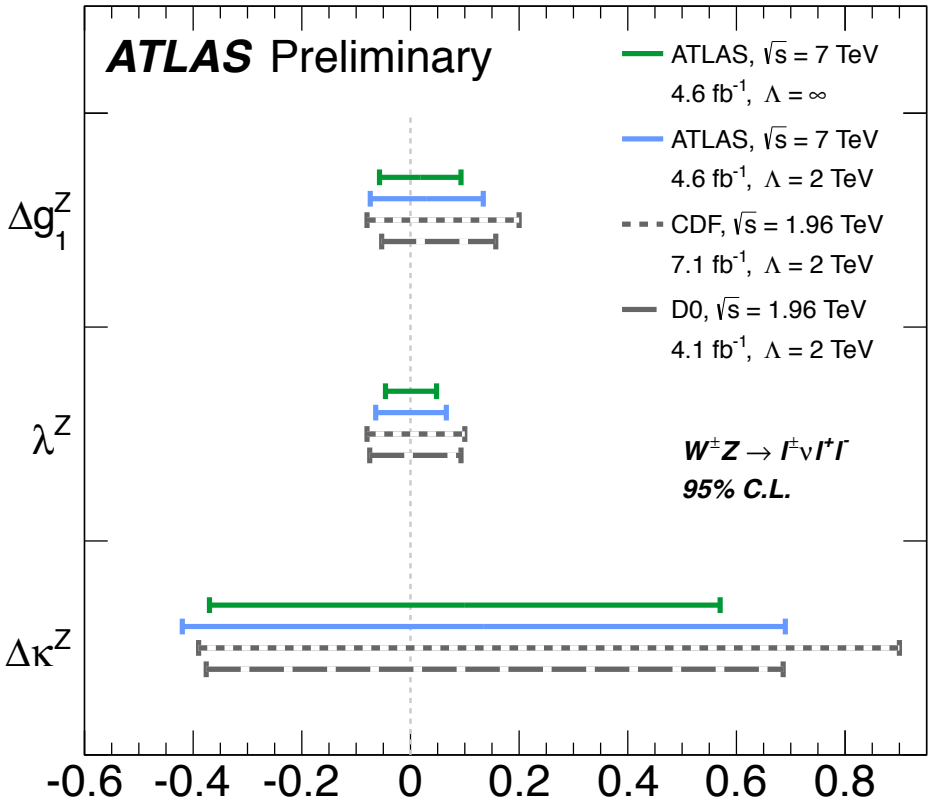

Figure 11.11: Comparison of aTGC limits from WZ production, shown for ATLAS and Tevatron experiments. Luminosities, centre of mass energy and cut-off Λ for each experiment are shown and the limits are for 95% confidence interval.

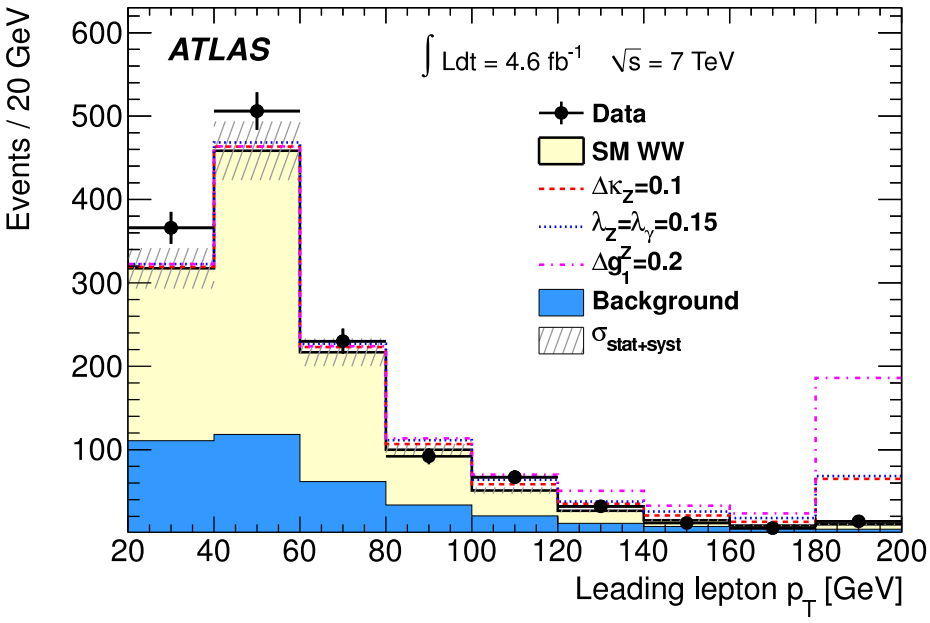

Figure 11.12: WW leading lepton p_T distribution. Data is shown along side expected background and signal events, assuming the Standard Model. Expected events in the case of anomalous TGC parameters are also shown, for values for each of the three couplings. The last bin is shortened for display purposes; it includes all events above 180 GeV.

Table 11.4: Limits on aTGC parameters from WW production, assuming no relationship amongst the five couplings. The 95% C.L. expected and observed limits on anomalous TGCs are shown for $\Lambda = \infty$. Except for the coupling under study, all other anomalous couplings are set to zero [64].

Parameter	Expected ($\Lambda = \infty$)	Observed ($\Lambda = \infty$)
$\Delta\kappa_Z$	$[-0.077, 0.086]$	$[-0.078, 0.092]$
λ_Z	$[-0.071, 0.069]$	$[-0.074, 0.073]$
λ_γ	$[-0.144, 0.135]$	$[-0.152, 0.146]$
Δg_1^Z	$[-0.449, 0.546]$	$[-0.373, 0.562]$
$\Delta\kappa_\gamma$	$[-0.128, 0.176]$	$[-0.135, 0.190]$

incorporating the observed number of candidate events, the expected signal as a function of aTGCs, and the estimated background in each p_T bin. The 95% confidence interval includes all values of aTGC parameters for which the negative log-likelihood increases by no more than 1.92 units above the minimum.

The WW final state can not distinguish between the WWZ and the $WW\gamma$ vertex. If no relation is assumed between the five couplings, the sensitivity to λ_Z and g_1^Z is significantly worse in WW production than in WZ production – the observed limits on Δg_1^Z are an order of magnitude worse in WW production than found in WZ production, and the limits on λ_Z are a factor 2 worse in WW production. The WW production contribution from $\Delta\kappa_Z$ scales as $\hat{s}$, while the WZ cross section contribution from $\Delta\kappa_Z$ scales as $\sqrt{\hat{s}}$), so WW production sets better limits on $\Delta\kappa_Z$ even when no assumption about the relationship between couplings is made. The limits set on the five anomalous couplings from WW production, assuming no relations amongst them, is shown in Table 11.4.

If assumptions are made about the relationship between the anomalous parameters, the limits from WW production improve significantly. The WW analysis stud-

Table 11.5: Limits on aTGC parameters from WW production, with assumptions on the relationship between the five couplings. The 95% C.L. expected and observed limits on anomalous TGCs in the LEP, HISZ and Equal Couplings scenarios are shown for two scales $\Lambda = 6$ TeV and $\Lambda = \infty$. Except for the coupling under study, all other anomalous couplings are set to zero [64].

Scenario	Parameter	Observed ($\Lambda = 6$ TeV)	Observed ($\Lambda = \infty$)
LEP	$\Delta\kappa_Z$	$[-0.045, 0.044]$	$[-0.043, 0.043]$
	$\lambda_Z = \lambda_\gamma$	$[-0.062, 0.065]$	$[-0.062, 0.059]$
	Δg_1^Z	$[-0.036, 0.066]$	$[-0.039, 0.052]$
HISZ	$\Delta\kappa_Z$	$[-0.039, 0.057]$	$[-0.036, 0.057]$
	$\lambda_Z = \lambda_\gamma$	$[-0.066, 0.065]$	$[-0.063, 0.063]$
Equal Couplings	$\Delta\kappa_Z$	$[-0.061, 0.093]$	$[-0.061, 0.083]$
	$\lambda_Z = \lambda_\gamma$	$[-0.062, 0.065]$	$[-0.062, 0.059]$

ies three sets of relationships (called "scenarios"). In the "Equal Couplings scenario", $\Delta\kappa_Z = \Delta\kappa_\gamma$, $\lambda_Z = \lambda_\gamma$, and $g_1^Z = 1$. The "LEP scenario" is motivated by $SU(2) \times U(1)$ gauge invariance and assumes $\Delta\kappa_\gamma = (\cos^2\theta_W / \sin^2\theta_W)(\Delta g_1^Z - \Delta\kappa_Z)$, and $\lambda_Z = \lambda_\gamma$. The final scenario, called the "HISZ scenario", assumes $\Delta g_1^Z = \Delta\kappa_Z/(\cos^2\theta_W - \sin^2\theta_W)$, $\Delta\kappa_\gamma = 2\Delta\kappa_Z \cos^2\theta_W/(\cos^2\theta_W - \sin^2\theta_W)$, and $\lambda_Z = \lambda_\gamma$. The observed limits for the 5 anomalous parameters are shown for these three scenarios in Table 11.5.

The limits from WW production obtained on ATLAS are compared to the limits from CMS, the Tevatron, and LEP in the LEP scenario in Figure 11.13. While the limits from ATLAS are more stringent than the limits from the Tevatron, the LEP limits remain the strongest constraint on anomalous couplings in WW production.

The ZZ final state is sensitive to neutral triple gauge couplings involving the ZZZ and $ZZ\gamma$ vertices with two on-shell Z bosons and one off-shell Z or γ. Anomalous neutral couplings describing these vertices can be parametrized by two CP-violating

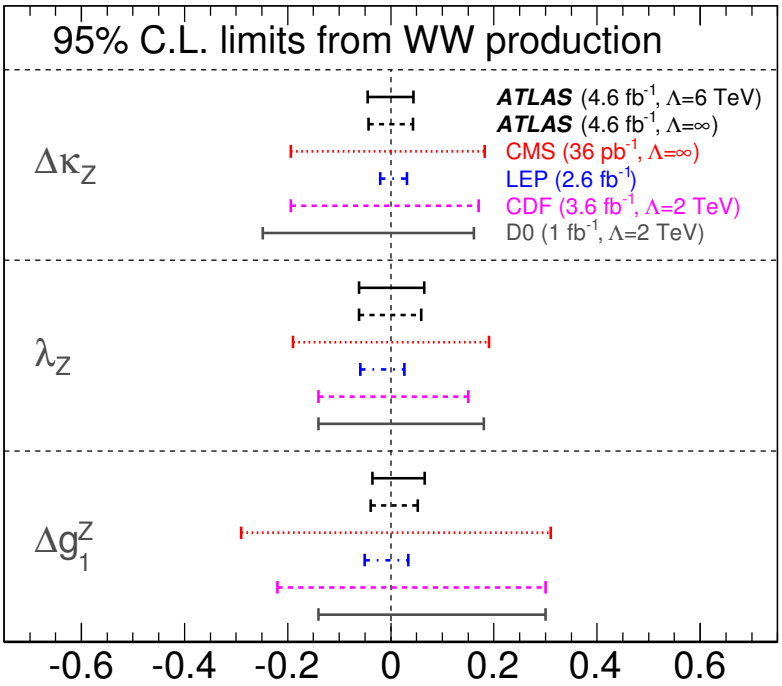

Figure 11.13: Comparison of aTGC limits from WW production at different experiments. Limits are shown from ATLAS [64], Tevatron and LEP experiments. Luminosities, centre of mass energy and cut-off Λ for each experiment are shown and the limits are for 95% confidence interval.

terms, f_4^Z and f_4^γ, and two CP-conserving complex parameters, f_5^Z and f_5^γ. All neutral triple gauge couplings are zero in the Standard Model.

The ATLAS ZZ analysis with 4.6 fb^{-1} at $\sqrt{s} = 7$ TeV is detailed in Reference [65]. Limits are set by studying the differential distribution of the transverse momentum of the leading Z boson in both $ZZ \to \ell\ell\ell\ell$ and $ZZ \to \ell\ell\nu\nu$ final states. The leading Z is defined as the Z boson with the higher transverse momentum for ZZ events with four leptons, and as the Z boson decaying to a charged lepton pair in $ZZ \to \ell\ell\nu\nu$ events. The leading Z p_T distribution is shown for four lepton events in Figure 11.14.

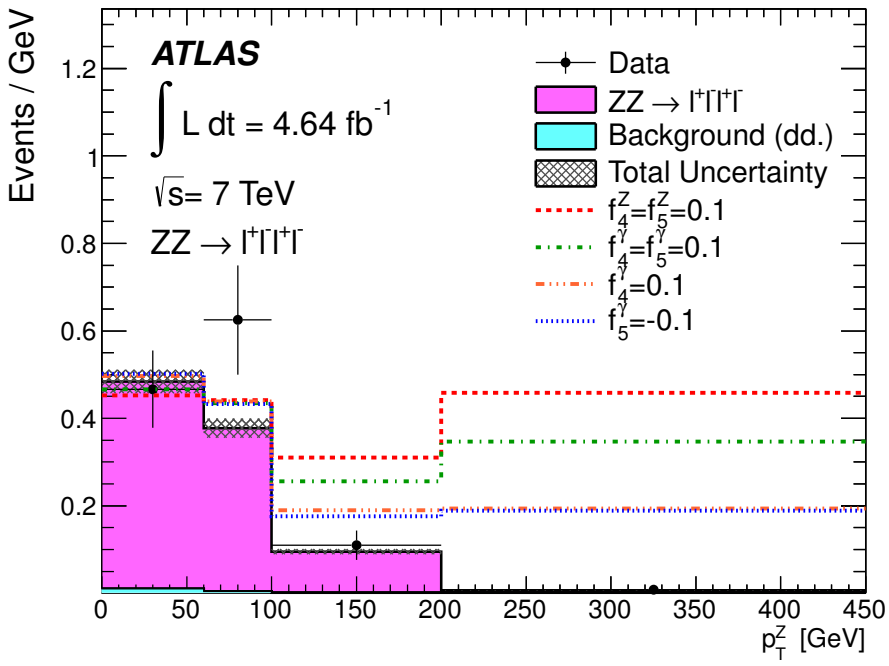

Figure 11.14: ZZ p_T^Z distribution. Data is shown along side expected background and signal events, assuming the Standard Model. Expected events in the case of anomalous TGC parameters are also shown, for values for each of the three couplings [65].

Limits on the values of anomalous neutral couplings are calculated using the same Frequentist approach that is used for the WZ analysis. The observed limits from AT-

LAS are shown in Figure 11.15, along with the limits obtained in other experiments. The ATLAS and CMS limits, which are comparable with each other, are an order of magnitude better than the limits from the Tevatron and from LEP.

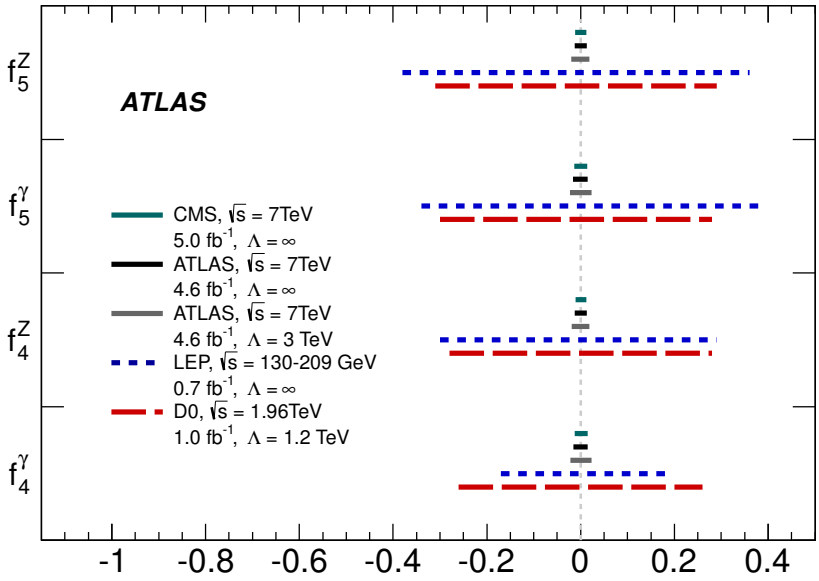

Figure 11.15: Comparison of aTGC limits from ZZ production at different experiments. Limits are shown from ATLAS [65], Tevatron and LEP experiments. Luminosities, centre of mass energy and cut-off Λ for each experiment are shown and the limits are for 95% confidence interval.

Finally, final states involving an on-shell photon and either a W or Z boson are also sensitive to anomalous couplings vertices with photon couplings. The $W\gamma$ final state is sensitive to the $WW\gamma$ vertex, involving the κ_γ and λ_γ couplings. The $Z\gamma$ final state is sensitive t to neutral triple gauge couplings involving the $ZZ\gamma$ and $Z\gamma\gamma$ vertices with one on-shell Z boson, one on-shell photon, and one off-shell Z or photon. Anomalous neutral couplings describing these vertices can be parametrized by the h_3^Z,

h_3^γ, h_4^Z, and h_4^γ parameters. All neutral triple gauge couplings are zero in the Standard Model.

The ATLAS $W/Z\gamma$ analysis with 4.6 fb^{-1} at $\sqrt{s} = 7$ TeV is detailed in Reference [66]. Limits are set with the sample of $W\gamma$ and $Z\gamma$ events in which the photon has missing transverse energy greater than 100 GeV and there are no reconstructed jets with $E_T > 30$ GeV. Limits on the values of anomalous neutral couplings are calculated using the same frequentist approach that is used for the WZ analysis. The observed limits from ATLAS, along with the limits obtained in other experiments, are shown in Figures 11.16 and 11.17 for the couplings studied in $W\gamma$ and $Z\gamma$ production.

The ATLAS limits are the most stringent for the neutral couplings in $Z\gamma$ production. LEP obtained tighter limits for $\Delta\kappa_\gamma$ and λ_γ, but these limits were obtained by studying the WW final state, as the LEP accelerator could not produce the charged $W\gamma$ final state.

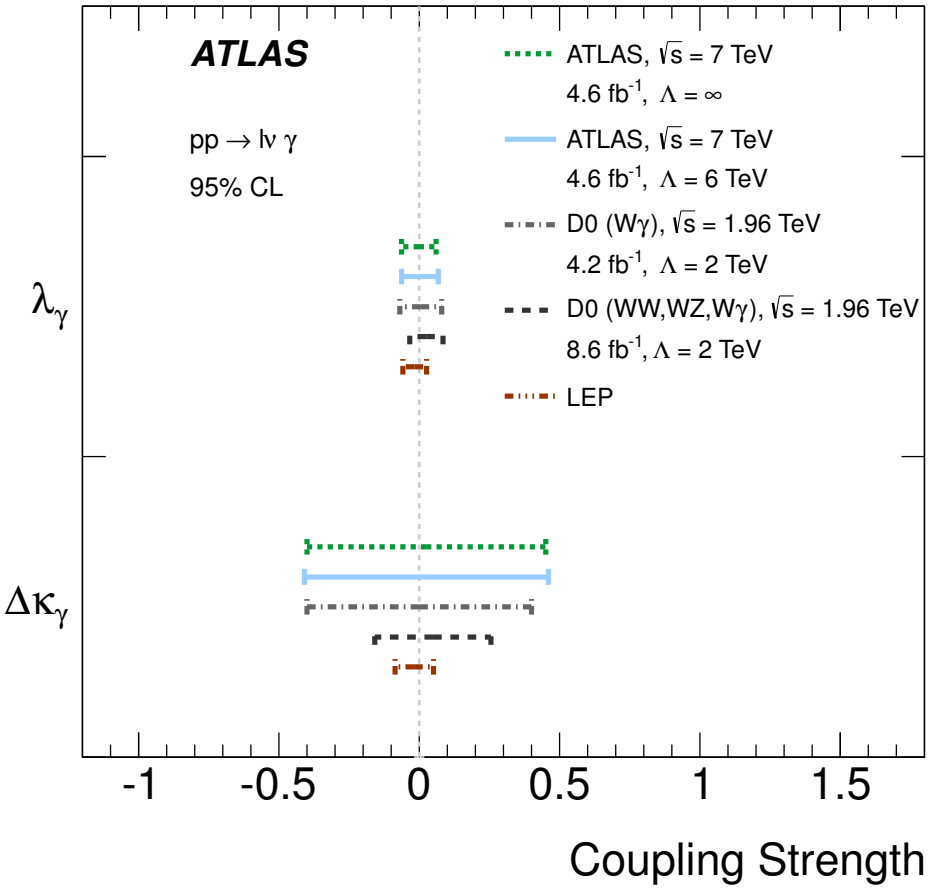

Figure 11.16: Comparison of aTGC limits from $W\gamma$ production at different experiments. Limits are shown from ATLAS [66], Tevatron and LEP [7] experiments. Luminosities, centre of mass energy and cut-off Λ for each experiment are shown and the limits are for 95% confidence interval.

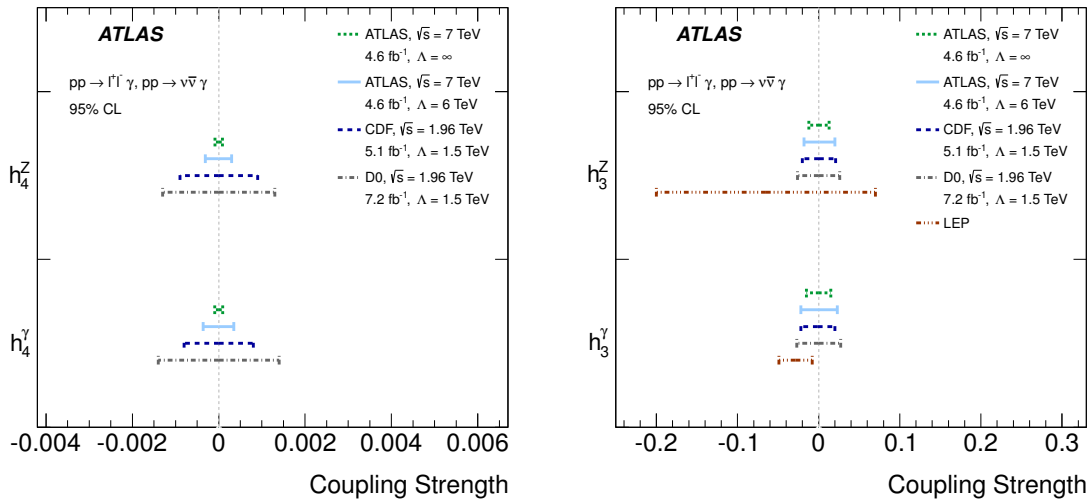

Figure 11.17: Comparison of aTGC limits from $Z\gamma$ production at different experiments. Limits are shown from ATLAS [66], Tevatron [] and LEP [7] experiments. Luminosities, centre of mass energy and cut-off Λ for each experiment are shown and the limits are for 95% confidence interval.

Chapter 12

Conclusion and Outlook

We observe 317 $WZ \to \ell\nu\ell\ell$ candidate events, with an expected background of 68 ± 10 events, in 4.6 fb^{-1} of proton-proton collisions collected with the ATLAS detector. We determine the WZ production cross section to be $19.0^{+1.4}_{-1.3}$ (stat) ± 0.9 (syst) ± 0.4 (lumi) pb, which is consistent with the next-to-leading Standard Model prediction of $17.6^{+1.1}_{-1.0}$ pb. By studying the transverse momentum distribution of the Z boson in selected WZ events, we extract the following 95% confidence intervals for anomalous triple gauge boson couplings which could contribute to WZ production:

$$\begin{aligned} \Delta g_1^Z &: [-0.057, 0.093] \\ \Delta\kappa_Z &: [-0.37, 0.57] \\ \lambda_Z &: [-0.046, 0.047] \end{aligned} \tag{12.1}$$

Our limits on these couplings are the tightest to date for couplings measured in WZ production, and the most stringent model-independent limits on Δg_1^Z and λ_Z.

The study of WZ production at the LHC will continue to be interesting. The data collected by the ATLAS detector in 2012 has a center-of-mass energy of $\sqrt{s} = 8$

TeV and has an integrated luminosity of 23 fb^{-1}. With this dataset, the measurement of the WZ production cross section at 8 TeV will continue to test the high energy behavior of electroweak physics. Moreover, with 23 fb^{-1}, the measurement of the cross section will no longer be limited by statistics. We expect the measurement of the WZ cross section at $\sqrt{s} = 8$ TeV with the full 2012 dataset will have around a 3% statistical uncertainty. In the analysis presented here, the largest systematic uncertainty, which was due to the expected Z+jets background contribution, was around 5%. However, with more data, the number of events in data control regions grows, and we expect the systematic uncertainty on the Z+jets background to drop to 3% without changing the method for estimating the background. To further improve the precision of the measurement, it will be necessary to find a way to estimate the expected Z+jets contribution with higher precision. However, even if the analysis were to be repeated with no changes except the new dataset, the total expected uncertainty on the measurement will be equivalent to or slightly smaller than the uncertainty on the theoretical prediction, which is 6%.

We also expect that the limits on anomalous triple gauge couplings will improve with the 2012 data. The precision of the limits improves roughly with $L^{1/4}$; we expect roughly a 30% improvement in our limits from increasing our data sample to 23 fb^{-1}. The increase in the center-of-mass energy from 7 TeV to 8 TeV also improves our expected limits by 30%. In addition to the expected improvements in the limits on Δg_1^Z, $\Delta\kappa_Z$, and λ_Z obtained from studying WZ production with the 2012 data, the ATLAS collaboration has plans to extract tighter limits on the couplings by combining information from both the WZ and WW final states.

The LHC expects to begin colliding protons again in early 2015 at $\sqrt{s} = 14$ TeV. With this energy and the hundreds of fb^{-1} of integrated luminosity we hope to collect within a few years of data taking, we expect to improve the limits on anomalous triple gauge couplings by an order of magnitude [61]. At that level, the limits will be sensitive to most of the predictions of anomalous couplings by current theoretical models [83]. Additionally, we will be able to measure WZ and WW scattering precisely enough to test whether or not the Higgs boson behaves as expected in regularizing diboson scattering.

Bibliography

[1] Measurement of the top quark-pair production cross section with ATLAS in pp collisions at $\sqrt{s} = 7$ TeV. *Eur. Phys. J.*, C 71:1577, 2011.

[2] Combined CDF and D0 measurement of WZ and ZZ production in final states with b-tagged jets. 2012.

[3] T. Aaltonen et al. Measurement of the WZ Cross Section and Triple Gauge Couplings in $p\bar{p}$ Collisions at $\sqrt{s} = 1.96$ TeV. *Phys.Rev.*, D86:031104, 2012.

[4] D. Adams et al. Track reconstruction in the ATLAS Muon Spectrometer with MOORE 007. ATLAS Technical Report ATL-SOFT-2003-007, 2003.

[5] S. Agostinelli et al. GEANT4: A simulation toolkit. *Nucl. Instrum. Meth.*, A506:250–303, 2003.

[6] H. Aihara et al. Anomalous Gauge Boson Interactions. arXiv:9503425 [hep-ph], 1995.

[7] J. Alcaraz et al. A Combination of preliminary electroweak measurements and constraints on the standard model. 2006.

[8] ALEPH Collaboration. Precision electroweak measurements on the Z resonance. *Phys.Rept.*, 427:257–454, 2006.

[9] ALICE Collaboration. ALICE Technical Design Report. `http://alice.web.cern.ch/Alice/TDR/`.

[10] Benjamin C. Allanach, Farvah Mahmoudi, Jordan P. Skittrall, and K. Sridhar. Gluon-initiated production of a Kaluza-Klein gluon in a Bulk Randall-Sundrum model. *JHEP*, 1003:014, 2010.

[11] J. Alwall et al. MadGraph/MadEvent v4: The New Web Generation. *JHEP*, 09:028, 2007.

[12] AMS Collaboration. First result from the alpha magnetic spectrometer on the international space station: Precision measurement of the positron fraction in primary cosmic rays of 0.5˘350 gev. *Phys. Rev. Lett.*, 110:141102, Apr 2013.

[13] G Anders et al. Study of the relative lhc bunch populations for luminosity calibration. Feb 2012.

[14] G. Arnison et al. Experimental observation of isolated large transverse energy electrons with associated missing energy at s=540 gev. *Physics Letters B*, 122(1):103 – 116, 1983.

[15] ATLAS Collaboration. Approved Muon Spectrometer Plots. `https://twiki.cern.ch/twiki/pub/AtlasPublic/ApprovedPlotsMuon/RPC_singlePanelPlateauEff_EtaPhi.gif`.

[16] ATLAS Collaboration. Athena Computing Framework ATLAS Internal Webpage. `https://twiki.cern.ch/twiki/bin/viewauth/Atlas/AthenaFramework`.

[17] ATLAS Collaboration. ATLAS Photos. `http://www.atlas.ch/photos/`.

[18] ATLAS Collaboration. ATLAS Public Luminosity Plots. `https://twiki.cern.ch/twiki/bin/view/AtlasPublic/LuminosityPublicResults`.

[19] ATLAS Collaboration. Egamma Isolation Twiki. `https://twiki.cern.ch/twiki/bin/viewauth/AtlasProtected/EgammaIsolation#Cell_Based_Isolation_Etcone`.

[20] ATLAS Collaboration. Electron/Gamma Public Results. ATLAS note `https://twiki.cern.ch/twiki/bin/view/AtlasPublic/ElectronGammaPublicCollisionResults`.

[21] ATLAS Collaboration. Expected Performance of the ATLAS Experiment - Detector, Trigger and Physics. arXiv:0901.0512 [hep-ex].

[22] ATLAS Collaboration. Performance of primary vertex reconstruction in proton-proton collisions at $\sqrt{s} = 7$ tev in the atlas experiment. ATLAS Conference Note: ATLAS-CONF-2010-069, `https://cdsweb.cern.ch/record/1281344?ln=en`.

[23] ATLAS Collaboration. Public Egamma Trigger Plots for Collision Data. ATLAS note `https://twiki.cern.ch/twiki/bin/view/AtlasPublic/EgammaTriggerPublicResults`.

[24] ATLAS Collaboration. Reconstruction and Calibration of Missing Transverse Energy and Performance in Z and W events in ATLAS Proton-Proton Collisions

at $\sqrt{s} = 7$ TeV. ATLAS conference note ATLAS-CONF-2011-080 `https://cdsweb.cern.ch/record/1355703?ln=en`.

[25] ATLAS Collaboration. Single Boson and Diboson Production Cross Sections in pp Collisions at $\sqrt{s} = 7$ TeV. ATLAS Internal Communication ATL-COM-PHYS-2010-695(2010).

[26] ATLAS Collaboration. Z+jets Status Update, W and Z Physics Plenary 30 August 2011. `https://indico.cern.ch/conferenceDisplay.py?confId=141396`.

[27] ATLAS Collaboration. *ATLAS Muon Spectrometer Technical Design Report*. CERN, Geneva, 1997.

[28] ATLAS Collaboration. The ATLAS Experiment at the CERN Large Hadron Collider. *JINST*, 3:S08003, 2008.

[29] ATLAS Collaboration. Determination of the muon reconstruction efficiency in atlas at the z resonance in proton-proton collisons at sqrt(s)=7 tev. Technical Report ATLAS-CONF-2011-008, CERN, Geneva, Feb 2011.

[30] ATLAS Collaboration. Luminosity Determination in *pp* Collisions at $\sqrt{s} = 7$ TeV using the ATLAS Detector at the LHC. *European Physics Journal C*, 71:1630, 2011.

[31] ATLAS Collaboration. Muon combined performance plots for hcp. Technical Report ATLAS-COM-PHYS-2011-1504, CERN, Geneva, Nov 2011.

[32] ATLAS Collaboration. Muon momentum resolution in first pass reconstruction of pp collision data recorded by atlas in 2010. Technical Report ATLAS-CONF-2011-046, CERN, Geneva, Mar 2011.

[33] ATLAS Collaboration. Muon reconstruction efficiency in reprocessed 2010 lhc proton-proton collision data recorded with the atlas detector. Technical Report ATLAS-CONF-2011-063, CERN, Geneva, Apr 2011.

[34] ATLAS Collaboration. A Measurement of WZ Production in Proton-Proton Collisions at sqrt(s) = 7 TeV with the ATLAS Detector. Technical Report ATL-COM-PHYS-2012-488, CERN, Geneva, May 2012.

[35] ATLAS Collaboration. Electron performance measurements with the ATLAS detector using the 2010 LHC proton-proton collision data. *Eur. Phys. J. C*, 72:1909, 2012.

[36] ATLAS Collaboration. Measurement of the combined ww and wz production cross section in the semileptonic final state in proton-proton collisions at s = 7 tev with the atlas detector. Technical Report ATLAS-CONF-2012-157, CERN, Geneva, Nov 2012.

[37] ATLAS Collaboration. Measurement of WZ production in proton-proton collisions at $\sqrt{s} = 7$ TeV with the ATLAS detector. *Eur.Phys.J.*, C72:2173, 2012.

[38] ATLAS Collaboration. Observation of a new particle in the search for the Standard Model Higgs boson with the ATLAS detector at the LHC. *Phys.Lett.*, B716:1–29, 2012.

[39] ATLAS Collaboration. Performance of missing transverse momentum reconstruction in atlas with 2011 proton-proton collisions at $sqrts = 7$ tev. Technical Report ATLAS-CONF-2012-101, CERN, Geneva, Jul 2012.

[40] ATLAS Collaboration. Performance of Missing Transverse Momentum Reconstruction in Proton-Proton Collisions at 7 TeV with ATLAS. *Eur.Phys.J.*, C72:1844, 2012.

[41] ATLAS Collaboration. Performance of the ATLAS Inner Detector Track and Vertex Reconstruction in the High Pile-Up LHC Environment. Technical Report ATLAS-CONF-2012-042, CERN, Geneva, Mar 2012.

[42] ATLAS Collaboration. Performance of the atlas muon trigger in 2011. Technical Report ATLAS-CONF-2012-099, CERN, Geneva, Jul 2012.

[43] ATLAS Collaboration. Improved luminosity determination in pp collisions at sqrt(s) = 7 TeV using the ATLAS detector at the LHC. 2013.

[44] Howard Baer, Vernon Barger, Sabine Kraml, Andre Lessa, Warintorn Sreethawong, et al. WZ plus missing-ET signal from gaugino pair production at LHC7. *JHEP*, 1203:092, 2012.

[45] M. Banner et al. Observation of single isolated electrons of high transverse momentum in events with missing transverse energy at the cern pp collider. *Physics Letters B*, 122(56):476 – 485, 1983.

[46] U. Baur, Tao Han, and J. Ohnemus. WZ production at hadron colliders: Effects of nonstandard WWZ couplings and QCD corrections. *Phys.Rev.*, D51:3381–3407, 1995.

[47] M. Benedikt and others (eds.). The LHC design report v.3 : the LHC Injector Chain. CERN-2004-003-V-3, `http://cdsweb.cern.ch/record/823808`.

[48] Gianfranco Bertone. *Particle dark matter observations, models and searches*. Cambridge University Press, Cambridge, UK New York, 2010.

[49] Thomas Binoth, C. Buttar, P.J. Clark, and E.W. Nigel Glover. Proceedings of 65th Scottish Universities Summer School in Physics: LHC Physics (SUSSP65). 2012.

[50] R. W. Brown, D. Sahdev, and K. O. Mikaelian. $W^{\pm}z^0$ and $w^{\pm}\gamma$ pair production in νe, pp, and $\overline{p}p$ collisions. *Phys. Rev. D*, 20:1164–1174, Sep 1979.

[51] O.S. Bruning and others (eds.). The LHC design report v.1 : the LHC Main Ring. CERN-2004-003-V-1, `http://cdsweb.cern.ch/record/782076`.

[52] O.S. Bruning and others (eds.). The LHC design report v.2 : the LHC Infrastructure and General Services. CERN-2004-003-V-2, `http://cdsweb.cern.ch/record/815187`.

[53] W Buttinger. The atlas level-1 trigger system. Technical Report ATL-DAQ-PROC-2012-024, CERN, Geneva, Jun 2012.

[54] Robert N. Cahn. The eighteen arbitrary parameters of the standard model in your everyday life. *Rev. Mod. Phys.*, 68:951–959, Jul 1996.

[55] J.M. Campbell et al. Next-to-leading order QCD predictions for W + 2jet and Z + 2jet production at the CERN LHC. *Phys. Rev.*, D68:094021, 2003.

[56] John M. Campbell, R. Keith Ellis, and Ciaran Williams. Vector boson pair production at the LHC. *JHEP*, 1107:018, 2011.

[57] CDF Collaboration. Observation of WZ Production. *Phys.Rev.Lett.*, 98:161801, 2007.

[58] CDF Collaboration. Precise measurement of the W-boson mass with the CDF II detector. *Phys.Rev.Lett.*, 108:151803, 2012.

[59] CMS Collaboration. CMS Physics Technical Design Report, Volume I and II. `http://cmsdoc.cern.ch/cms/cpt/tdr/`.

[60] CNGS Collaboration. CNGS Experiment. `http://proj-cngs.web.cern.ch/proj-cngs/`.

[61] ATLAS Collaboration. *ATLAS Detector and Physics Performance Technical Design Report*. CERN, Geneva, 1999.

[62] ATLAS Collaboration. The ATLAS Experiment at the Large Hadron Collider. *JINST*, 3:S08003, 2008.

[63] ATLAS Collaboration. Measurement of the WZ production cross section and limits on anomalous triple gauge couplings in proton-proton collisions at $\sqrt{s} = 7$ TeV with the ATLAS detector. *Phys.Lett.*, B709:341–357, 2012.

[64] ATLAS Collaboration. Measurement of w^+ w^-production in pp collisions at sqrt {s}= 7 tev with the atlas detector and limits on anomalous wwz and wwgamma couplings. *arXiv preprint arXiv:1210.2979*, 2012.

[65] ATLAS Collaboration. Measurement of zz production in pp collisions at sqrt (s)= 7 tev and limits on anomalous zzz and zzgamma couplings with the atlas detector. *arXiv preprint arXiv:1211.6096*, 2012.

[66] ATLAS Collaboration. Measurements of wgamma and zgamma production in pp collisions at sqrt {s}= 7 tev with the atlas detector at the lhc. *arXiv preprint arXiv:1302.1283*, 2013.

[67] CDF Collaboration. Measurement of the $WW + WZ$ Production Cross Section Using a Matrix Element Technique in Lepton + Jets Events. *Phys.Rev.*, D82:112001, 2010.

[68] CMS Collaboration. Measurement of the sum of WW and WZ production with W+dijet events in pp collisions at $\sqrt{s} = 7$ TeV. *Eur. Phys. J. C*, 73:2283, 2013.

[69] D0 Collaboration. Measurement of the $WZ \to \ell\nu\ell\ell$ cross section and limits on anomalous triple gauge couplings in $p\bar{p}$ collisions at $\sqrt{s} = 1.96$ TeV. *Phys.Lett.*, B695:67–73, 2011.

[70] D0 Collaboration. A measurement of the WZ and ZZ production cross sections using leptonic final states in 8.6 fb^{-1} of $p\bar{p}$ collisions. *Phys.Rev.*, D85:112005, 2012.

[71] D0 Collaboration. Measurements of WW and WZ production in W + jets final states in $p\bar{p}$ collisions. *Phys.Rev.Lett.*, 108:181803, 2012.

[72] CMS Collaborations. Observation of a new boson at a mass of 125 GeV with the CMS experiment at the LHC. *Phys.Lett.*, B716:30–61, 2012.

[73] COMPASS Collaboration. COMPASS Experiment. `http://wwwcompass.cern.ch/`.

[74] G. Corcella et al. HERWIG 6: an event generator for Hadron Emission Reactions With Interfering Gluons. *JHEP*, 010:0101, 2001.

[75] Gennaro Corcella, Ian G Knowles, Giuseppe Marchesini, Stefano Moretti, Kosuke Odagiri, Peter Richardson, Michael H Seymour, and Bryan R Webber. Herwig 6.5 release note. *arXiv preprint hep-ph/0210213*, 2002.

[76] T Cornelissen et al. Concepts, design and implementation of the atlas new tracking (newt). ATLAS Technical Report ATL-SOFT-PUB-2007-007, `https://cdsweb.cern.ch/record/1020106`, 2007.

[77] G. Cowan. *Statistical Data Analysis*. Oxford University Press, 1998.

[78] G. Cowan, K. Cranmer, E. Gross, and O. Vitells. Asymptotic Formulae for Likelihood-Based Tests of New Physics. *Eur. Phys. J. C*, 71:1554, 2011.

[79] R. Decker, S. Jadach, J. Kuhn, and Z. Was. The Tau Decay Library Tauola: Version 2.4. *Comput. Phys. Commun.*, 76:361, 1993.

[80] DELPHI Collaboration. First WW event at LEP. `http://www-d0.fnal.gov/~mulders/linkWWevent.html`, 1996.

[81] C. Carli (ed.). Chamonix 2011 LHC Performance Workshop. `http://indico.cern.ch/conferenceOtherViews.py?view=standard&confId=103957`.

[82] N. Van Eldik. *The ATLAS Muon Spectrometer: Calibration and Pattern Recognition*. PhD thesis, University of Amsterdam, Amsterdam, 2007.

[83] J. Ellison and J. Wudka. Study of Trilinear Gauge Boson Couplings at the Tevatron Collider. arXiv:9804322 [hep-ph], 1998.

[84] L. Evans and P. Bryant. LHC Machine. *JINST*, 3:S08001, 2008.

[85] E. Farhi and L. Susskind. Technicolour. *Phys. Rept.*, 74:277, 1981.

[86] Gary J. Feldman and Robert D. Cousins. A Unified Approach to the Classical Statistical Analysis of Small Signals. *Phys. Rev. D*, 57:3873–3889, 1998.

[87] S. Frixione, P. Nason, and C. Oleari. Matching NLO QCD computations with Parton Shower simulations: the POWHEG method. *JHEP*, 11:070, 2007.

[88] S. Frixione and B.R. Webber. Matching NLO QCD computations and parton shower simulations. *JHEP*, 06:029, 2002.

[89] Daniel Froidevaux and Paris Sphicas. General-purpose detectors for the large hadron collider. *Annual Review of Nuclear and Particle Science*, 56(1):375, 2006.

[90] R. Fruhwirth et al. Application of Kalman Filtering to Track and Vertex Fitting. *Nucl. Inst. Meth. A*, 262, 1987.

[91] Howard Georgi and S. L. Glashow. Unity of all elementary-particle forces. *Phys. Rev. Lett.*, 32:438–441, Feb 1974.

[92] Sheldon L. Glashow. Partial-symmetries of weak interactions. *Nuclear Physics*, 22(4):579–588, 1961.

[93] Stephen Godfrey and Heinz König. Atomic parity violation as a probe of anomalous gauge-boson couplings. *Phys. Rev. D*, 45:3196–3200, May 1992.

[94] Y. A. Golfand and E. P. Likhtman. Extension of the Algebra of Poincare Group Generators and Violation of P invariance. *JETP Lett.*, 13:323, 1971.

[95] M.C. Gonzalez-Garcia and Yosef Nir. Neutrino masses and mixing: Evidence and implications. *Rev.Mod.Phys.*, 75:345–402, 2003.

[96] G. J. Gounaris, J. Layssac, and F. M. Renard. Off-shell structure of the anomalous z and γ self-couplings. *Phys. Rev. D*, 62:073012, Sep 2000.

[97] D. Griffiths. *Introduction to Elementary Particles*. Wiley-VCH, 2008.

[98] M. Groll. Associated production of weak bosons at the LHC with the ATLAS detector. *J. Phys.Conf. Ser.*, 171:012086, 2009.

[99] Claus Grupen and Boris Shwartz. *Particle detectors*, volume 26. Cambridge University Press, 2008.

[100] K. Hagiwara, S. Ishihara, R. Szalapski, and D. Zeppenfeld. Low energy effects of new interactions in the electroweak boson sector. *Phys. Rev. D*, 48:2182–2203, Sep 1993.

[101] F. Halzen and A.D. Martin. *Quarks & Leptons: An Introductory Course in Modern Particle Physics*. Wiley, 1984.

[102] D. Hanneke, S. Fogwell, and G. Gabrielse. New Measurement of the Electron Magnetic Moment and the Fine Structure Constant. *Phys.Rev.Lett.*, 100:120801, 2008.

[103] F.J. Hasert et al. Observation of Neutrino Like Interactions Without Muon Or Electron in the Gargamelle Neutrino Experiment. *Phys.Lett.*, B46:138–140, 1973.

[104] P. W. Higgs. Broken Symmetries and the Masses of Gauge Bosons. *Physical Review Letters*, 13:508–509, October 1964.

[105] J. Nielsen. W/Z+Jet Cross Section Measurements at the Large Hadron Collider. *ATLAS proceedings*, pages ATL–COM–PHYS–2009–324, 2009.

[106] F. James. MINUIT - Function Minimization and Error Analysis. CERN Program Library entry D506, Geneva, 1998.

[107] Sunghoon Jung and James D. Wells. Comparison of electric dipole moments and the Large Hadron Collider for probing CP violation in triple boson vertices. *Phys.Rev.*, D80:015009, 2009.

[108] Michael Aaron Kagan. *Measurement of the W+/-Z production cross section and limits on anomalous triple gauge couplings at s= 7 TeV using the ATLAS detector*. PhD thesis, HARVARD UNIVERSITY, 2012.

[109] Hung-Liang Lai, Marco Guzzi, Joey Huston, Zhao Li, Pavel M Nadolsky, Jon Pumplin, and C-P Yuan. New parton distributions for collider physics. *Physical Review D*, 82(7):074024, 2010.

[110] W Lampl, S Laplace, D Lelas, P Loch, H Ma, S Menke, S Rajagopalan, D Rousseau, S Snyder, and G Unal. Calorimeter clustering algorithms: Description and performance. Technical Report ATL-LARG-PUB-2008-002. ATL-COM-LARG-2008-003, CERN, Geneva, Apr 2008.

[111] P. Langacker. The physics of heavy Z′ gauge bosons. *Rev. Mod. Phys.*, 81:1199, 2009.

[112] J.F. Laporte. Muonboy documentation. `https://twiki.cern.ch/twiki/bin/view/AtlasProtected/MuonboyDocumentation`.

[113] J.P. Lees et al. Evidence for an excess of $\bar{B} \to D^{(*)}\tau^-\bar{\nu}_\tau$ decays. *Phys.Rev.Lett.*, 109:101802, 2012.

[114] D. Levin. Muonrecpedia. `https://twiki.cern.ch/twiki/bin/view/AtlasProtected/MuonRecoPedia`.

[115] LHCb Collaboration. LHCb Technical Design Report, Volumes 1-11. `http://lhcb.web.cern.ch/lhcb/TDR/TDR.htm`.

[116] Maalpu. LHC Main Images Directory. `http://maalpu.org/lhc/images/directory.htm`.

[117] M.L. Mangano et al. ALPGEN, a generator for hard multiparton processes in hadronic collisions. *JHEP*, 07:001, 2003.

[118] Mark I Collaboration. Archives and History Office. `http://www.slac.stanford.edu/history/mark.shtml`.

[119] A.D. Martin et al. Parton distributions for the LHC. arXiv:0901.0002 [hep-ph].

[120] Stephen P. Martin. A Supersymmetry primer. 1997.

[121] T. Melia, P. Nason, R. Rontsch, and G. Zanderighi. W+W-, WZ and ZZ production in the POWHEG BOX. arXiv:1107.5051 [hep-ph].

[122] F Meloni et al. Vertexing Performance Data vs MC comparison for LPCC. Technical Report ATL-COM-PHYS-2011-1312, CERN, Geneva, Sep 2011.

[123] MiniBooNE Collaboration. Event Excess in the MiniBooNE Search for $\bar{\nu}_\mu \to \bar{\nu}_e$ Oscillations. *Phys.Rev.Lett.*, 105:181801, 2010.

[124] Vasiliki A. Mitsou. The ATLAS transition radiation tracker. pages 497–501, 2003.

[125] NA61 Collaboration. NA61 Experiment. `https://na61.web.cern.ch/na61/xc/index.html`.

[126] NA62 Collaboration. NA62 Experiment. `http://na62.web.cern.ch/na62/`.

[127] K. Nakamura et al. Review of Particle Physics. *Journal of Physics G*, 37, 2010.

[128] A. Neveu and J. H. Schwarz. Quark Model of Dual Pions. *Phys. Rev. D*, 4:1109, 1971.

[129] J. Neyman. Outline of a Theory of Statistical Estimation Based on the Classical Theory of Probability. *Philosophical Transactions of the Royal Society of London A*, 236:333–380, 1937.

[130] R Nicolaidou, L Chevalier, S Hassani, J F Laporte, E Le Menedeu, and A Ouraou. Muon identification procedure for the ATLAS detector at the LHC using Muonboy reconstruction package and tests of its performance using cosmic rays and single beam data. *Journal of Physics: Conference Series*, 219(3):032052, 2010.

[131] Particle Data Group Collaboration. W prime-Boson Searches. `pdg.web.cern.ch/.../reviews/rpp2011-rev-wprime-searches.pdf`, 2011.

[132] Particle Data Group Collaboration. Higgs Bosons: Theory and Searches. `pdg.lbl.gov/2012/reviews/rpp2012-rev-higgs-boson.pdf`, 2012.

[133] D.H. Perkins. *Introduction to High Energy Physics*. Cambridge University Press, 2000.

[134] M.E. Peskin and D. V. Schroeder. *An Introduction to Quantum Field Theory*. Westview Press, 1995.

[135] P. Ramond. Dual Theory for Free Fermions. *Phys. Rev. D*, 3:2415, 1971.

[136] A. Salam. Elementary particle theory: Relativistic groups and analyticity (Nobel Symposium No. 8), 1968.

[137] Julian Schwinger. A theory of the fundamental interactions. *Annals of Physics*, 2(5):407 – 434, 1957.

[138] Paolo Spagnolo. Boson gauge couplings at LEP. 2005.

[139] S. Torbjorn et al. PYTHIA 6.4 Physics and Manual. *JHEP*, 05:026, 2006.

[140] V. Trimble. Existence and nature of dark matter in the universe. *Annual Review of Astronomy and Astrophysics*, 25:425–472, 1987.

[141] V Cindro and others. The atlas beam conditions monitor. *Journal of Instrumentation*, 3(02):P02004, 2008.

[142] S. van der Meer. Calibration of the effective beam height in the ISR. CERN note: CERN-ISR-PO-68-31, `https://cdsweb.cern.ch/record/296752`, 1968.

[143] M Villa. The luminosity monitor of the atlas experiment. In *Nuclear Science Symposium Conference Record (NSS/MIC), 2009 IEEE*, pages 1028–1033. IEEE, 2009.

[144] D. V. Volkov and V. P. Akulov. Possible Universal Neutrino Interaction. *JETP Lett.*, 16:438, 1972.

[145] Steven Weinberg. A model of leptons. *Phys. Rev. Lett.*, 19(21):12641266, 1967.

[146] J. Wess and B. Zumino. Supergauge transformations in four dimensions. *Nucl. Phys. B*, 70:39, 1974.

[147] Wikimedia Commons. Crystal Ball Function. `http://en.wikipedia.org/wiki/Crystal_Ball_function`.

[148] J. Wudka. A short course in effective Lagrangians. arXiv:0002180 [hep-ph], 2000.

[149] Dieter Zeppenfeld and Scott Willenbrock. Probing the three-vector-boson vertex at hadron colliders. *Phys. Rev. D*, 37:1775–1786, Apr 1988.